

# Topological analysis of chaotic dynamical systems

Robert Gilmore

*Department of Physics & Atmospheric Science, Drexel University, Philadelphia, Pennsylvania 19104*

Topological methods have recently been developed for the analysis of dissipative dynamical systems that operate in the chaotic regime. They were originally developed for three-dimensional dissipative dynamical systems, but they are applicable to all “low-dimensional” dynamical systems. These are systems for which the flow rapidly relaxes to a three-dimensional subspace of phase space. Equivalently, the associated attractor has Lyapunov dimension  $d_L < 3$ . Topological methods supplement methods previously developed to determine the values of metric and dynamical invariants. However, topological methods possess three additional features: they describe how to model the dynamics; they allow validation of the models so developed; and the topological invariants are robust under changes in control-parameter values. The topological-analysis procedure depends on identifying the stretching and squeezing mechanisms that act to create a strange attractor and organize all the unstable periodic orbits in this attractor in a unique way. The stretching and squeezing mechanisms are represented by a caricature, a branched manifold, which is also called a template or a knot holder. This turns out to be a version of the dynamical system in the limit of infinite dissipation. This topological structure is identified by a set of integer invariants. One of the truly remarkable results of the topological-analysis procedure is that these integer invariants can be extracted from a chaotic time series. Furthermore, self-consistency checks can be used to confirm the integer values. These integers can be used to determine whether or not two dynamical systems are equivalent; in particular, they can determine whether a model developed from time-series data is an accurate representation of a physical system. Conversely, these integers can be used to provide a model for the dynamical mechanisms that generate chaotic data. In fact, the author has constructed a doubly discrete classification of strange attractors. The underlying branched manifold provides one discrete classification. Each branched manifold has an “unfolding” or perturbation in which some subset of orbits is removed. The remaining orbits are determined by a basis set of orbits that forces the presence of all remaining orbits. Branched manifolds and basis sets of orbits provide this doubly discrete classification of strange attractors. In this review the author describes the steps that have been developed to implement the topological-analysis procedure. In addition, the author illustrates how to apply this procedure by carrying out the analysis of several experimental data sets. The results obtained for several other experimental time series that exhibit chaotic behavior are also described. [S0034-6861(98)00304-3]

## CONTENTS

I. Introduction	1456	3. Duffing dynamics	1475
A. Laser with modulated losses	1456	4. van der Pol–Shaw dynamics	1476
B. Objectives of a new analysis procedure	1459	5. Cusp catastrophe dynamics	1476
C. Preview of results	1460	V. Invariants from Templates	1477
II. Preliminaries	1460	A. Locating periodic orbits	1477
A. Some basic results	1461	B. Topological invariants	1478
B. Change of variables	1462	1. Linking numbers	1478
1. Differential coordinates	1462	2. Relative rotation rates	1478
2. Delay coordinates	1462	C. Dynamical invariants	1479
C. Qualitative properties	1463	D. Inflating a template	1480
1. Poincaré program	1463	VI. Unfolding a Template	1480
2. Stretching and squeezing	1463	A. Topological restrictions	1481
D. The problem	1463	B. Forcing diagram	1482
III. Topological Invariants	1464	1. Zero-entropy orbits	1483
A. Linking numbers	1464	2. Positive-entropy orbits	1484
B. Relative rotation rates	1465	C. Basis sets of orbits	1484
C. Knot holders or templates	1467	D. Routes to chaos	1485
IV. Templates as Flow Models	1468	E. Coexisting basins	1485
A. The Birman-Williams theorem in $R^3$	1468	F. Other template unfoldings	1485
B. The Birman-Williams theorem in $R^n$	1469	VII. Topological-Analysis Algorithm	1486
C. Templates	1470	A. Construct an embedding	1486
D. Algebraic description of templates	1471	B. Identify periodic orbits	1486
E. Control-parameter variation	1472	C. Compute topological invariants	1487
F. Examples of templates	1474	D. Identify a template	1487
1. Rössler dynamics	1474	E. Validate the template	1487
2. Lorenz dynamics	1474	F. Model the dynamics	1488
		G. Validate the model	1488
		VIII. Data	1488

A. Data requirements	1489	XIV. Conclusions	1524
1. $\sim 100$ cycles	1489	Acknowledgments	1526
2. $\sim 100$ samples/cycle	1489	References	1526
B. Fast look at data	1489		
C. Processing in the frequency domain	1489		
1. High-frequency filter	1489		
2. Low-frequency filter	1489		
3. Derivatives and integrals	1490		
4. Hilbert transform	1490		
5. Fourier interpolation	1491		
6. Hilbert transform and interpolation	1491		
D. Processing in the time domain	1492		
1. Singular-value decomposition for data fields	1492		
2. Singular-value decomposition for scalar time series	1492		
IX. Unstable Periodic Orbits	1493		
A. Close returns in flows	1493		
1. Close-returns plot	1493		
2. Close-returns histogram	1493		
3. Tests for chaos	1494		
B. Close returns in maps	1494		
1. First-return plot	1494		
2. $p$ th-return plot	1494		
C. Metric methods	1494		
X. Embedding	1496		
A. Time-delay embedding	1496		
B. Differential phase-space embedding	1497		
1. $x, \dot{x}, \ddot{x}$	1497		
2. $\int x, x, \dot{x}$	1497		
C. Embeddings with symmetry	1498		
D. Coupled-oscillator embeddings	1498		
E. Singular-value decomposition embeddings	1499		
F. Singular-value decomposition projections	1499		
XI. Horseshoe Mechanism ( $A_2$ )	1499		
A. Belousov-Zhabotinskii reaction	1500		
1. Embedding	1500		
2. Periodic orbits	1500		
3. Template identification	1501		
4. Template verification	1502		
5. Basis set of orbits	1502		
6. Modeling the dynamics	1503		
7. Model validation	1505		
B. Laser with saturable absorber	1506		
C. Laser with modulated losses	1506		
1. Poincaré section mappings	1506		
2. Projection to a Poincaré section	1507		
3. Result	1508		
D. Other systems exhibiting $A_2$ dynamics	1508		
E. "Invariant" versus "robust"	1508		
F. Why $A_2$ ?	1510		
XII. Lorenz Mechanism ( $A_3$ )	1511		
A. Optically pumped molecular laser	1511		
1. Models	1511		
2. Amplitudes	1512		
3. Intensities	1515		
B. Fluids	1515		
C. Induced attractors and templates	1516		
D. Why $A_3$ ?	1517		
XIII. Duffing Oscillator	1517		
A. Background	1517		
B. Flow approach	1517		
C. Template	1518		
D. Orbit organization	1520		
1. Nonlinear oscillator	1520		
2. Duffing template	1522		
E. Levels of structure	1524		

## I. INTRODUCTION

The subject of this review is the analysis of data generated by a dynamical system operating in a chaotic regime. More specifically, this review describes how to extract, from chaotic data, topological invariants that determine the stretching and squeezing mechanisms responsible for generating these chaotic data.

In this introductory section we briefly describe, for purposes of motivation, a laser that has been operated under conditions in which it behaved chaotically (see Sec. I.A). The topological tools that we describe in this review were developed in response to the challenge of analyzing the chaotic data sets generated by this laser. In Sec. I.B we list a number of questions that we want to be able to answer when analyzing a chaotic signal. None of these questions can be addressed by the older tools for analyzing chaotic data, which include dimension calculations and estimates of Lyapunov exponents. In Sec. I.C we preview the results that will be presented during the course of this review. It is astonishing that the topological-analysis tools that we shall describe have provided answers to more questions than we had originally asked. This analysis procedure has also raised more questions than we have answered in this review.

### A. Laser with modulated losses

The possibility of observing deterministic chaos in lasers was originally demonstrated by *Arecchi et al.* (1982) and *Gioggia and Abraham* (1983). The use of lasers as a testbed for generating deterministic chaotic signals has two major advantages over fluid systems, which had until that time been the principle source for chaotic data:

- (i) The time scales intrinsic to a laser ( $10^{-7}$  to  $10^{-3}$  sec) are much shorter than the time scales for fluid experiments.
- (ii) Reliable laser models exist in terms of a small number of ordinary differential equations whose solutions show close qualitative similarity to the behavior of the lasers that are modeled (*Puccioni et al.*, 1985; *Tredicce et al.*, 1986).

We originally studied in detail the laser with modulated losses. A schematic of this laser is shown in Fig. 1. A Kerr cell is placed within the cavity of a  $\text{CO}_2$  gas laser. The electric field within the cavity is polarized by Brewster angle windows. The Kerr cell allows linearly polarized light to pass through it. An electric field across the Kerr cell rotates the plane of polarization. As the polarization plane of the Kerr cell is rotated away from the polarization plane established by the Brewster angle windows, controllable losses are introduced into the cavity. If the Kerr cell is periodically modulated, the output intensity is also modulated. When the modulation amplitude is small, the output modulation is locked to the

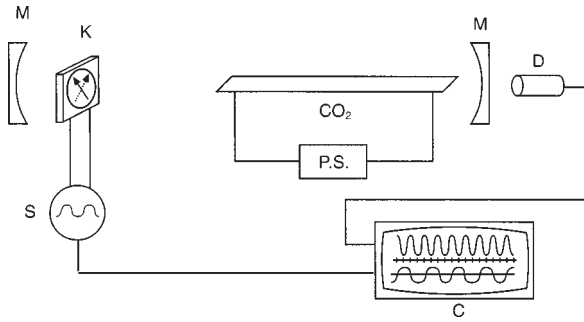


FIG. 1. Schematic representation of a laser with modulated losses. CO<sub>2</sub>: laser tube containing CO<sub>2</sub> with Brewster windows; *M*: mirrors forming cavity; *P.S.*: power source; *K*: Kerr cell; *S*: signal generator; *D*: detector; *C*: oscilloscope and recorder. A variable electric field across the Kerr cell varies its polarization direction and modulates the electric-field amplitude within the cavity.

modulation of the Kerr cell. When the modulation amplitude is sufficiently large and the modulation frequency is comparable to the cavity-relaxation frequency, or one of its subharmonics, the laser-output intensity no longer remains locked to the signal driving the Kerr cell, and can even become chaotic.

The laser with modulated losses has been studied extensively both experimentally (Arecchi *et al.*, 1982; Gioggia and Abraham, 1983; Puccioni *et al.*, 1985; Tredicce, Abraham *et al.*, 1985; Tredicce, Arecchi *et al.*, 1985; Midavaine, Dangoisse, and Glorieux, 1986; Tredicce *et al.*, 1986) and theoretically (Matorin, Pikoovskii, and Khanin, 1984; Solari *et al.*, 1987; Solari and Gilmore, 1988). The rate equations governing the laser intensity *S* and the population inversion *N* are

$$\begin{aligned} dS/dt &= -k_0 S[(1-N) + m \cos(\omega t)], \\ dN/dt &= -\gamma[(N-N_0) + (N_0-1)SN]. \end{aligned} \quad (1.1)$$

Here *m* and  $\omega$  are the modulation amplitude and angular frequency, respectively, of the Kerr cell; *N*<sub>0</sub> is the pump parameter, normalized to *N*<sub>0</sub>=1 at the laser threshold; and *k*<sub>0</sub> and  $\gamma$  are loss rates. In scaled form, this equation is

$$\begin{aligned} du/d\tau &= [z - T \cos(\Omega\tau)]u, \\ dz/d\tau &= (1 - \epsilon_1 z) - (1 + \epsilon_2 z)u, \end{aligned} \quad (1.2)$$

where the scaled variables are  $u=S$ ,  $z=k_0\kappa(N-1)$ ,  $t=\kappa\tau$ ,  $T=k_0m$ ,  $\Omega=\omega\kappa$ ,  $\epsilon_1=\kappa\gamma$ ,  $\epsilon_2=1/\kappa k_0$ , and  $\kappa^2=1/\gamma k_0(N_0-1)$ . The bifurcation behavior exhibited by the simple models (1.1) and (1.2) is qualitatively, if not quantitatively, in agreement with the experimentally observed behavior of this laser.

A bifurcation diagram for the laser, and the model (1.2), is shown in Fig. 2. The bifurcation diagram is constructed by varying the modulation amplitude *T* and keeping all other parameters fixed. This bifurcation diagram is similar to experimentally observed bifurcation diagrams.

This diagram shows that a period-one solution exists above the laser threshold (*N*<sub>0</sub>>1) for *T*=0 and remains

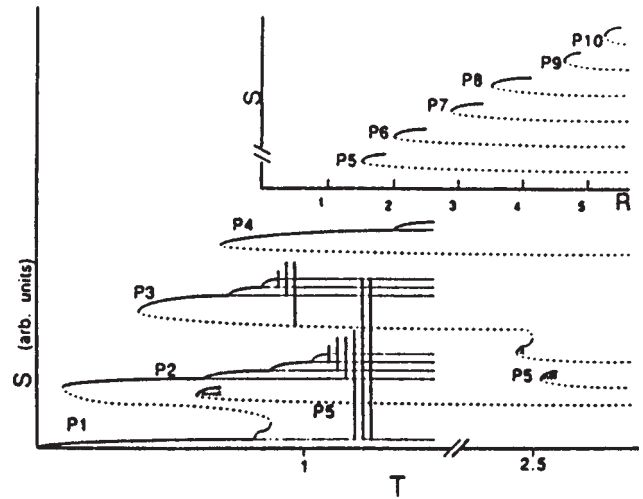


FIG. 2. Bifurcation diagram for model (1.2) of the laser with modulated losses, with  $\epsilon_1=0.03$ ,  $\epsilon_2=0.009$ ,  $\Omega=1.5$ . Stable periodic orbits (solid lines), regular saddles (dashed lines), and strange attractors are shown. Period-*n* branches ( $P_n \geq 2$ ) are created in saddle-node bifurcations and evolve through the Feigenbaum period-doubling cascade as the modulation amplitude *T* increases. Two additional period-5 branches are shown as well as a "snake" based on the period-three regular saddle. The period-two saddle orbit created in a period-doubling bifurcation from the period-one orbit ( $T \sim 0.8$ ) is related by a snake to the period-two saddle orbit created at *P*<sub>2</sub>.

stable as *T* is increased until  $T \sim 0.8$ . It becomes unstable at  $T \sim 0.8$ , with a stable period-two orbit emerging from it in a period-doubling bifurcation. Contrary to what might be expected, this is not the early stage of a period-doubling cascade, for the period-two orbit is annihilated at  $T \sim 0.85$  in an inverse saddle-node bifurcation with a period-two regular saddle. This saddle-node bifurcation destroys the basin of attraction of the period-two orbit. Any point in that basin is dumped into the basin of a period  $4=2 \times 2^1$  orbit, even though there are two other coexisting basins of attraction for stable orbits of periods  $6=3 \times 2^1$  and 4.

Subharmonics of period *n* ( $P_n, n \geq 2$ ) are created in saddle-node bifurcations at increasing values of *T* and *S* (*P*<sub>2</sub> at  $T \sim 0.1$ , *P*<sub>3</sub> at  $T \sim 0.3$ , *P*<sub>4</sub> at  $T \sim 0.7$ , *P*<sub>5</sub> and higher shown in inset). All subharmonics in this series to period *n*=11 have been seen both experimentally and in simulations of (1.2). The evolution ("perestroika," Arnol'd, 1986) of each subharmonic follows a standard scenario as *T* increases (Eschenazi, Solari, and Gilmore, 1989):

- (i) A saddle-node bifurcation creates an unstable saddle and a node which is initially stable.
- (ii) Each node becomes unstable and initiates a period-doubling cascade as *T* increases. The cascade follows the standard Feigenbaum (1978, 1980) scenario. The ratios of *T* intervals between successive bifurcations, and of geometric sizes of the stable nodes of periods  $n \times 2^k$ , have been estimated up to  $k \leq 6$  for some of these subharmon-

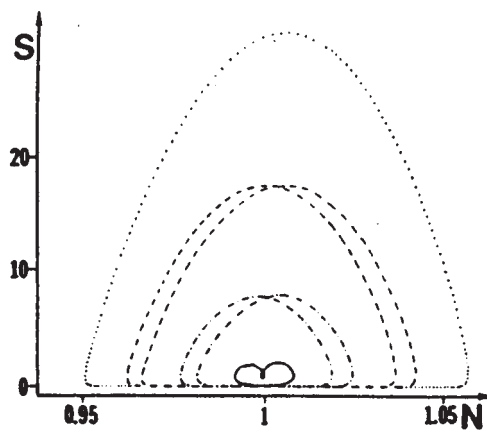


FIG. 3. Multiple basins of attraction coexisting over a broad range of control-parameter values. The stable orbits or strange attractors within these basins have a characteristic organization. The coexisting orbits shown above are, from inside to outside: period two bifurcated from period-one branch, period two, period three, period four. The two inner orbits are separated by an unstable period-two orbit (not shown); all three are part of a “snake.”

ics, both from experimental data and from the simulations. These ratios are compatible with the universal scaling ratios.

- (iii) Beyond accumulation, there is a series of noisy orbits of period  $n \times 2^k$  that undergo inverse period-halving bifurcations. This scenario has been predicted by Lorenz (1980).

We have observed additional systematic behavior shared by the subharmonics shown in Fig. 2. Higher subharmonics are generally created at larger values of  $T$ . They are created with smaller basins of attraction. The range of  $T$  values over which the Feigenbaum scenario is played out becomes smaller as the period ( $n$ ) increases. In addition, the subharmonics show an ordered pattern in space. In Fig. 3 we show four stable periodic orbits that coexist under certain operating conditions. Roughly speaking, the larger-period orbits exist “outside” the smaller-period orbits. These orbits share many other systematics, which have been described by Eschenazi, Solari, and Gilmore (1989).

In Fig. 4 we show an example of a chaotic time series taken for  $T \sim 1.3$  after the chaotic attractor based on the period-two orbit has collided with the period-three regular saddle.

The period-doubling, accumulation, inverse noisy period-halving scenario described above is often interrupted by a crisis (Grebogi, Ott, and Yorke, 1983) of one type or another:

*Boundary crisis:* A regular saddle on a period- $n$  branch in the boundary of a basin of attraction surrounding either the period- $n$  node or one of its periodic or noisy periodic granddaughter orbits collides with the attractor. The basin is annihilated or enlarged.

*Internal crisis:* A flip saddle of period  $n \times 2^k$  in the boundary of a basin surrounding a noisy period  $n$

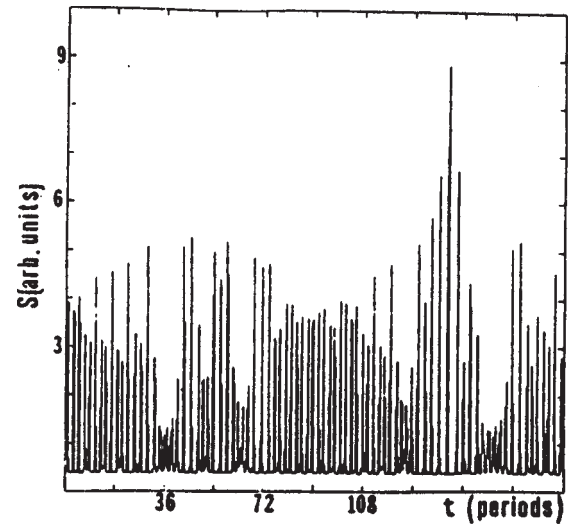


FIG. 4. Time series from laser with modulated losses showing alternation between noisy period-two and noisy period-three behavior ( $T \sim 1.3$  in Fig. 2).

$\times 2^{k+1}$  orbit collides with the attractor to produce a noisy period-halving bifurcation.

*External crisis:* A regular saddle of period  $n'$  in the boundary of a period- $n$  ( $n' \neq n$ ) strange attractor collides with the attractor, thereby annihilating or enlarging the basin of attraction.

Figure 5(a) provides a schematic representation of the bifurcation diagram shown in Fig. 2. The different kinds of bifurcations encountered in both experiments and simulations are indicated here. These include direct and inverse saddle-node bifurcations, period-doubling bifurcations, and boundary and external crises. As the laser-operating parameters ( $k_0, \gamma, \Omega$ ) change, the bifurcation diagram changes. In Figs. 5(b) and 5(c) we show schematics of bifurcation diagrams obtained for slightly different values of these operating (or control) parameters.

In addition to the subharmonic orbits of period  $n$  created at increasing  $T$  values (Fig. 2), there are orbits of period  $n$  that do not appear to belong to that series of subharmonics. The clearest example is the period-two orbit, which bifurcates from period one at  $T \sim 0.8$ . Another is the period-three orbit pair created in a saddle-node bifurcation, which occurs at  $T \sim 2.45$ . These bifurcations were seen in both experiments and simulations. We were able to trace the unstable orbits of period two ( $0.1 < T < 0.85$ ) and period three ( $0.4 < T < 2.5$ ) in simulations and found that these orbits are components of an orbit “snake” (Alligood, 1985; Alligood, Sauer, and Yorke, 1997). This is a single orbit that folds back and forth on itself in direct and inverse saddle-node bifurcations as  $T$  increases. The unstable period-two orbit ( $0.1 < T < 0.85$ ) is part of a snake. By changing operating conditions, both snakes can be eliminated [see Fig. 5(c)]. As a result, the “subharmonic  $P2$ ” is really nothing other than the period-two orbit, which bifurcates from the period-one branch  $P1$ . Furthermore, instead of having saddle-node bifurcations creating four inequivalent period-three orbits (at  $T \sim 0.4$  and  $T \sim 2.45$ ) there is re-

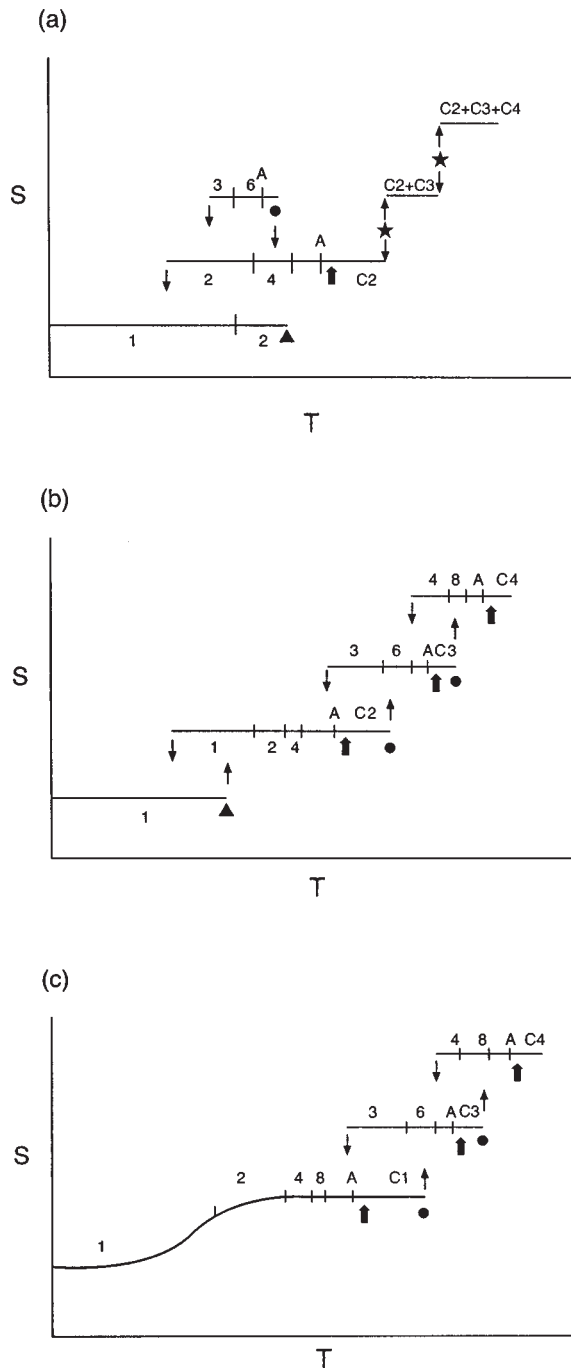


FIG. 5. (a) Schematic of bifurcation diagram shown in Fig. 2. Various bifurcations are indicated:  $\downarrow$ , saddle node;  $\blacktriangle$ , inverse saddle node;  $\bullet$ , boundary crisis;  $\star$ , external crisis. Period-doubling bifurcations are identified by a small vertical line separating stable orbits of periods differing by a factor of two. Accumulation points are identified by A. Strange attractors based on period  $n$  are indicated by  $C_n$ . As control parameters change, the bifurcation diagram is modified, as in (b) and (c). The sequence (a) to (c) shows the unfolding of the “snake” in the period-two orbit.

ally only one pair of period-three orbits, the other pair being components of a snake.

Topological tools (relative rotation rates, Solari and Gilmore, 1988) were developed to determine which orbits might be equivalent, or components of a snake, and

which are not. These tools suggested that the Smale (1967) horseshoe mechanism was responsible for generating the nonlinear phenomena obtained in both the experiments and the simulations. This mechanism predicts that additional inequivalent subharmonics of period  $n$  can exist for  $n \geq 5$ . Since we observed that the size of a basin of attraction decreases rapidly with  $n$ , we searched for the two additional saddle-node bifurcations involving period-five orbits that are allowed by the horseshoe mechanism. Both were located in simulations. Their locations are indicated in Fig. 2 at  $T \sim 0.6$  and  $T \sim 2.45$ . One was also located experimentally. The other may also have been seen, but the basin was too small to be certain of its existence.

Bifurcation diagrams have been obtained for a variety of physical systems: other lasers (Wedding, Gasch, and Jaeger, 1984; Waldner *et al.*, 1986; Roldán *et al.*, 1997); electric circuits (Bocko, Douglas, and Frutchy, 1984; Klinker, Meyer-Ilse, and Lauterborn, 1984; Satija, Bishop, and Fesser, 1985; van Buskirk and Jeffries, 1985); a biological model (Schwartz and Smith, 1983); a bouncing ball (Tufillaro, Abbott, and Reilly, 1992); and a stringed instrument (Tufillaro *et al.*, 1995). These bifurcation diagrams are similar, but not identical, to the ones shown above. This raised the question of whether similar processes were governing the description of this large variety of systems.

During these analyses, it became clear that standard tools (dimension calculations and Lyapunov exponent estimates) were not sufficient for a satisfying understanding of the stretching and squeezing processes that occur in phase space and which are responsible for generating chaotic behavior. In the laser we found many coexisting basins of attraction, some containing a periodic attractor, others a strange attractor. The rapid alternation between periodic and chaotic behavior as control parameters (e.g.,  $T$  and  $\Omega$ ) were changed meant that dimension and Lyapunov exponents varied at least as rapidly.

For this reason, we sought to develop additional tools that were invariant under control parameter changes for the analysis of data generated by dynamical systems that exhibit chaotic behavior.

## B. Objectives of a new analysis procedure

In view of the experiments just described, and the data that they generated, we hoped to develop a procedure for analyzing data that achieved a number of objectives. These included an ability to answer the following questions:

(i) Is it possible to develop a procedure for understanding dynamical systems *and their evolution* (“*perestroika*”) as the operating parameters (e.g.,  $m$ ,  $k_0$ , and  $\gamma$ ) change?

(ii) Is it possible to identify a dynamical system by means of topological invariants, following suggestions proposed by Poincaré (1892)?

(iii) Can selection rules be constructed under which it is possible to determine the order in which periodic or

bits can be created and/or annihilated by standard bifurcations? Or when different orbits might belong to the same snake?

(iv) Is it possible to determine when two strange attractors are (a) equivalent (one can be transformed into the other, by changing parameters, for example, without creating or annihilating any periodic orbits); (b) adiabatically equivalent (one can be deformed into the other, by changing parameters, and only a small number of orbit pairs below any period are created or destroyed); or (c) inequivalent (there is no way to transform one into the other)?

### C. Preview of results

A procedure for analyzing chaotic data has been developed that addresses many of the questions presented above. This procedure is based on computing the topological invariants of the unstable periodic orbits that occur in a strange attractor. These topological invariants are the orbits' linking numbers and their relative rotation rates. Since these are defined in  $R^3$ , we originally thought this topological analysis procedure was restricted to the analysis of three-dimensional dissipative dynamical systems. However, it is applicable to higher-dimensional dynamical systems, provided points in phase space relax sufficiently rapidly to a three-dimensional manifold contained in the phase space. Such systems can have any dimension, but they are "strongly contracting" and have Lyapunov dimension (Kaplan and Yorke, 1979)  $d_L < 3$ .

The results are as follows:

(i) The stretching and squeezing mechanisms responsible for creating a strange attractor and organizing all unstable periodic orbits in it can be identified by a particular kind of two-dimensional manifold ("branched manifold"). This is an attractor that is obtained in the "infinite dissipation" limit of the original dynamical system.

(ii) All such manifolds can be identified and classified by topological indices. These indices are integers.

(iii) Dynamical systems classified by inequivalent branched manifolds are inequivalent. They cannot be deformed into each other.

(iv) In particular, the four most widely cited examples of low-dimensional dynamical systems exhibiting chaotic behavior [Lorenz equations (Lorenz, 1963), Rössler equations (Rössler, 1976a), Duffing oscillator (Thompson and Stewart, 1986; Gilmore, 1981), and van der Pol-Shaw oscillator (Thompson and Stewart, 1986; Gilmore, 1984)] are associated with different branched manifolds, and are therefore intrinsically inequivalent.

(v) The characterization of a branched manifold is unchanged as the control parameters are varied.

(vi) The branched manifold is identified by (a) identifying segments of the time series that can act as surrogates for unstable periodic orbits by the method of close returns; (b) computing the topological invariants (linking numbers and relative rotation rates) of these surrogates for unstable periodic orbits; and (c) comparing

these topological invariants for surrogate orbits to the topological invariants for corresponding periodic orbits on branched manifolds of various types.

(vii) The identification of a branched manifold is confirmed or rejected by using the branched manifold to predict topological invariants of additional periodic orbits extracted from the data and comparing these predictions with those computed from the surrogate orbits.

(viii) Topological constraints derived from the linking numbers and the relative rotation rates provide selection rules for the order in which orbits can be created and must be annihilated as control parameters are varied.

(ix) A basis set of orbits can be identified that defines the spectrum of all unstable periodic orbits in a strange attractor, up to any period.

(x) The basis set determines the maximum number of coexisting basins of attraction that a small perturbation of the dynamical system can produce.

(xi) As control parameters change, the periodic orbits in the dynamical system are determined by a sequence of different basis sets. Each such sequence represents a "route to chaos."

The information described above can be extracted from time-series data. Experience shows that the data need not be exceptionally clean and the data set need not be exceptionally long.

There is now a doubly discrete classification for strange attractors generated by low-dimensional dynamical systems. The gross structure is defined by an underlying branched manifold. This can be identified by a set of integers that is robust under control-parameter variation. The fine structure is defined by a basis set of orbits. This basis set changes as control parameters change. A sequence of basis sets can represent a route to chaos. Different sequences represent distinct routes to chaos.

## II. PRELIMINARIES

A dynamical system is a set of ordinary differential equations,

$$\frac{d\mathbf{x}}{dt} = \dot{\mathbf{x}} = \mathbf{F}(\mathbf{x}, \mathbf{c}), \quad (2.1)$$

where  $\mathbf{x} \in R^n$  and  $\mathbf{c} \in R^k$  (Arnol'd, 1973; Gilmore, 1981). The variables  $\mathbf{x}$  are called state variables. They evolve in time in the space  $R^n$ , called a state space or a phase space. The variables  $\mathbf{c} \in R^k$  are called control parameters. They typically appear in ordinary differential equations as parameters with fixed values. In Eq. (1.1) the variables  $S$ ,  $N$ , and  $t$  are state variables and the "constants"  $k_0$ ,  $\gamma$ ,  $\omega$ ,  $m$ , and  $N_0$  are control parameters.

Ordinary differential equations arise quite naturally to describe a wide variety of physical systems. The surveys by Cvitanovic (1984) and Hao (1984) present a broad spectrum of physical systems that are described by nonlinear ordinary differential equations of the form (2.1).

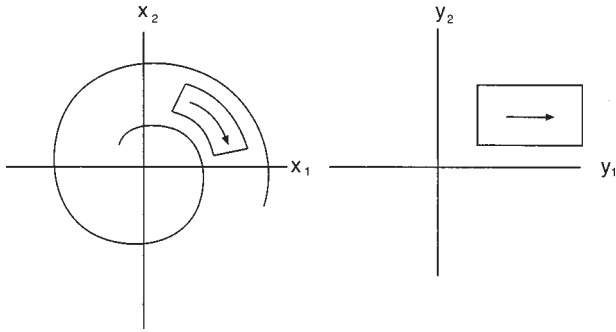


FIG. 6. Smooth transformation that reduces the flow to the very simple normal form (2.4) locally in the neighborhood of a nonsingular point.

### A. Some basic results

We review a few fundamental results that lie at the heart of dynamical systems.

The existence and uniqueness theorem (Arnol'd, 1973) states that through any point in phase space there is a solution to the differential equations, and that the solution is unique:

$$\mathbf{x}(t) = \mathbf{f}(t; \mathbf{x}(t=0), \mathbf{c}). \quad (2.2)$$

This solution depends on time  $t$ , the initial conditions  $\mathbf{x}(t=0)$ , and the control-parameter values  $\mathbf{c}$ .

It is useful to make a distinction between singular points  $\mathbf{x}^*$  and nonsingular points in the phase space. A singular point  $\mathbf{x}^*$  is a point at which the forcing function  $\mathbf{F}(\mathbf{x}^*, \mathbf{c}) = 0$  in Eq. (2.1). Since  $d\mathbf{x}/dt = \mathbf{F}(\mathbf{x}, \mathbf{c}) = 0$  at a singular point, a singular point is also a fixed point,  $d\mathbf{x}^*/dt = 0$ :

$$\mathbf{x}(t) = \mathbf{x}(0) = \mathbf{x}^*. \quad (2.3)$$

The distribution of the singular points of a dynamical system provides more information about a dynamical system than we have learned to exploit (Gilmore, 1981, 1996), even when these singularities are "off the real axis" (Eschenazi, Solari, and Gilmore, 1989). That is, even before these singularities come into existence, there are canonical precursors that indicate their imminent creation.

A local normal-form theorem (Arnol'd, 1973) guarantees that at a nonsingular point  $\mathbf{x}_0$  there is a smooth transformation to a new coordinate system  $\mathbf{y} = \mathbf{y}(\mathbf{x})$  in which the flow (2.1) assumes the canonical form

$$\begin{aligned} \dot{y}_1 &= 1, \\ \dot{y}_j &= 0, \quad j=2,3,\dots,n. \end{aligned} \quad (2.4)$$

This transformation is illustrated in Fig. 6. The local form (2.4) tells us nothing about how phase space is stretched and squeezed by the flow. To this end, we present a version of this normal-form theorem that is much more useful for our purposes. If  $\mathbf{x}_0$  is not a singular point, there is an orthogonal (volume-preserving) transformation centered at  $\mathbf{x}_0$  to a new coordinate system  $\mathbf{y} = \mathbf{y}(\mathbf{x})$  in which the dynamical system equations assume the following local canonical form in a neighborhood of  $\mathbf{x}_0$ :

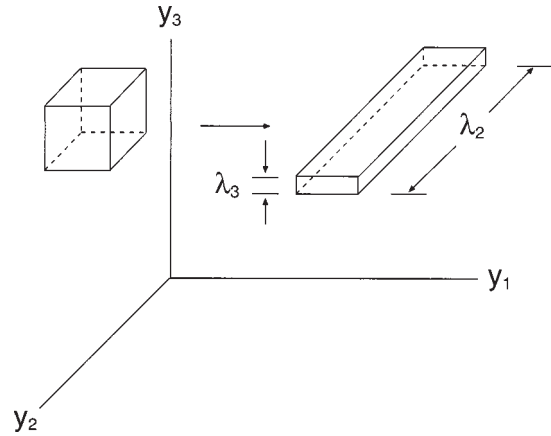


FIG. 7. Orthogonal transformation that reduces the flow to the local normal form (2.5) in the neighborhood of a nonsingular point.

$$\begin{aligned} \dot{y}_1 &= |\mathbf{F}(\mathbf{x}_0, \mathbf{c})| = \left| \sum_{k=1}^n \mathbf{F}_k(\mathbf{x}_0, \mathbf{c})^2 \right|^{1/2}, \\ \dot{y}_j &= \lambda_j y_j \quad j=2,3,\dots,n. \end{aligned} \quad (2.5)$$

The local eigenvalues  $\lambda_j$  depend on  $\mathbf{x}_0$  and describe how the flow deforms the phase space in the neighborhood of  $\mathbf{x}_0$ . This is illustrated in Fig. 7. The constant associated with the  $y_1$  direction shows how a small volume is displaced by the flow in a short time  $\Delta t$ . If  $\lambda_2 > 0$  and  $\lambda_3 < 0$ , the flow stretches the initial volume in the  $y_2$  direction and shrinks it in the  $y_3$  direction. The eigenvalues  $\lambda_j$  are called local (they depend on  $\mathbf{x}_0$ ) Lyapunov exponents. We remark here that one eigenvalue of a flow at a nonsingular point always vanishes, and the associated eigenvector is in the flow direction.

The divergence theorem relates the time rate of change of a small volume of the phase space to the divergence of the function  $\mathbf{F}(\mathbf{x}; \mathbf{c})$ . We assume a small volume  $V$  is surrounded by a surface  $S = \partial V$  at time  $t$  and ask how the volume changes during a short period of time. The volume will change because the flow will displace the surface. The change in the volume is equivalent to the flow through the surface, which can be expressed as (Gilmore, 1981)

$$V(t+dt) - V(t) = \oint_{\partial V} dx_i \wedge dS_i. \quad (2.6)$$

Here  $dS_i$  is an element of surface area orthogonal to the displacement  $dx_i$  and  $\wedge$  is the standard mathematical generalization in  $R^n$  of the cross product in  $R^3$ . The time rate of change of volume is

$$\frac{dV}{dt} = \oint_{\partial V} \frac{dx_i}{dt} \wedge dS_i = \oint_{\partial V} F_i \wedge dS_i. \quad (2.7)$$

The surface integral is related to the divergence of the flow  $\mathbf{F}$  by (Gilmore, 1981)

$$\lim_{V \rightarrow 0} \frac{1}{V} \frac{dV}{dt} = \lim_{V \rightarrow 0} \frac{1}{V} \oint_{\partial V} F_i \wedge dS_i \stackrel{\text{def}}{=} \text{div } \mathbf{F} = \nabla \cdot \mathbf{F}. \quad (2.8)$$

In a locally cartesian coordinate system,  $\text{div } \mathbf{F} = \nabla \cdot \mathbf{F} = \sum_{i=1}^n \partial F_i / \partial x_i$ . The divergence can also be expressed in terms of the local Lyapunov exponents,

$$\nabla \cdot \mathbf{F} = \sum_{j=1}^n \lambda_j, \tag{2.9}$$

where  $\lambda_1 = 0$  (flow direction) and  $\lambda_j$  ( $j > 1$ ) are the local Lyapunov exponents in the direction transverse to the flow (see Fig. 7). This is a direct consequence of the local normal form result (2.5).

**B. Change of variables**

We present here two examples of changes of variables that are important for the analysis of dynamical systems, but which are not discussed in generic differential equations texts. The authors of such texts typically study only point transformations  $\mathbf{x} \rightarrow \mathbf{y}(\mathbf{x})$ . The coordinate transformations we discuss are particular cases of contact transformations and nonlocal transformations. We treat these transformations because they are extensively used to construct embeddings of scalar experimental data into multidimensional phase spaces. This is done explicitly for three-dimensional dynamical systems. The extension to higher-dimensional dynamical systems is straightforward.

1. Differential coordinates

If the dynamical system is

$$\frac{d\mathbf{x}}{dt} = \mathbf{F}(\mathbf{x}) \quad \mathbf{x} = (x_1, x_2, x_3), \tag{2.10}$$

then we define  $\mathbf{y}$  as follows:

$$\begin{aligned} y_1 &= x_1, \\ y_2 &= \dot{x}_1 = dy_1/dt = F_1, \\ y_3 &= dy_2/dt = \ddot{x}_1 = \dot{F}_1 = \frac{\partial F_1}{\partial x_i} \frac{dx_i}{dt} = (\mathbf{F} \cdot \nabla) F_1. \end{aligned} \tag{2.11}$$

The equations of motion assume the form

$$\begin{aligned} \frac{dy_1}{dt} &= y_2, \\ \frac{dy_2}{dt} &= y_3, \\ \frac{dy_3}{dt} &= G(y_1, y_2, y_3) = (\mathbf{F} \cdot \nabla)^2 F_1. \end{aligned} \tag{2.12}$$

In this coordinate system, modeling the dynamics reduces to constructing the single function  $G$  of three variables, rather than three separate functions, each of three variables.

To illustrate this idea, we consider the Lorenz (1963) equations:

$$\begin{aligned} \frac{dx}{dt} &= -\sigma x + \sigma y, \\ \frac{dy}{dt} &= rx - y - xz, \\ \frac{dz}{dt} &= -bz + xy. \end{aligned} \tag{2.13}$$

Then the differential coordinates  $(X, Y, Z)$  can be related to the original coordinates by

$$\begin{aligned} X &= x, \\ \frac{dX}{dt} &= Y, \\ \frac{dY}{dt} &= Z, \\ \frac{dZ}{dt} &= (YZ + \sigma Y^2 + Y^2 - \sigma XZ - XZ - X^3 Y - \sigma X^4 \\ &\quad - bXZ - \sigma bXY + \sigma brX^2 - bXY - \sigma bX^2)/X. \end{aligned} \tag{2.14}$$

2. Delay coordinates

In this case we define the new coordinate system as follows:

$$\begin{aligned} y_1(t) &= x_1(t), \\ y_2(t) &= x_1(t - \tau), \\ y_3(t) &= x_1(t - 2\tau), \end{aligned} \tag{2.15}$$

where  $\tau$  is some time that can be specified by various criteria. In the delay coordinate system, the equations of motion do not have the simple form (2.12). Rather, they are

$$\frac{dy_i}{dt} = H_i(\mathbf{y}), \tag{2.16}$$

where it is probably impossible to construct the functions  $H_i(\mathbf{y})$  explicitly in terms of the original functions  $F_i(\mathbf{x})$ .

When attempting to develop three-dimensional models for dynamical systems that generate chaotic data, it is necessary to develop models for the driving functions [the  $\mathbf{F}(\mathbf{x})$  on the right-hand side of Eq. (2.10)]. When the variables used are differential coordinates [see Eq. (2.11)], two of the three functions that must be modeled in Eq. (2.12) are trivial and only one is nontrivial. On the other hand, when delay coordinates [see Eq. (2.15)] are used, all three functions [the  $H_i(\mathbf{y})$  on the right-hand side of Eq. (2.16)] are nontrivial. This is one of the reasons that we prefer to use differential coordinates—rather than delay coordinates—when analyzing chaotic data, if it is possible.

## C. Qualitative properties

### 1. Poincaré program

The original approach to the study of differential equations involved searches for exact analytic solutions. If they were not available, one attempted to use perturbation theory to approximate the solutions. While this approach is useful for determining explicit solutions, it is not useful for determining the general behavior predicted by even simple nonlinear dynamical systems. Poincaré realized the poverty of this approach over a century ago (Poincaré, 1892). His approach involved studying how an ensemble of nearby initial conditions (an entire neighborhood in phase space) evolved. Poincaré's approach to the study of differential equations evolved into the mathematical field we now call topology.

Topological tools are useful for the study of both conservative and dissipative dynamical systems. In fact, Poincaré was principally interested in conservative (Hamiltonian) systems. However, the most important tool—the Birman-Williams theorem—on which our topological analysis method is based is applicable to dissipative dynamical systems. It is for this reason that the tools presented in this review are applicable to three-dimensional dissipative dynamical systems. At present, they can be extended to “low” ( $d_L < 3$ ) dimensional dissipative dynamical systems, where  $d_L$  is the Lyapunov dimension of the strange attractor.

### 2. Stretching and squeezing

In this review we are principally interested in dynamical systems that behave chaotically. Chaotic behavior is defined by two properties:

- (a) sensitivity to initial conditions and
- (b) recurrent nonperiodic behavior.

Sensitivity to initial conditions means that nearby points in phase space typically “repel” each other. That is, the distance between the points increases exponentially, at least for a sufficiently small time:

$$d(t) = d(0)e^{\lambda t} \quad (\lambda > 0, 0 < t < \tau). \quad (2.17)$$

Here  $d(t)$  is the distance separating two points at time  $t$ ,  $d(0)$  is the initial distance separating them at  $t=0$ ,  $t$  is sufficiently small, and the “Lyapunov exponent”  $\lambda$  is positive. To put it graphically, the two initial conditions are “stretched apart.”

If two nearby initial conditions diverged from each other exponentially in time for all times, they would eventually wind up at opposite ends of the universe. If motion in phase space is bounded, the two points will eventually reach a maximum separation and then begin to approach each other again. To put it graphically again, the two initial conditions are then “squeezed together.”

We illustrate these concepts in Fig. 8 for a process that develops a strange attractor in  $R^3$ . We take a set of initial conditions in the form of a cube. As time in-

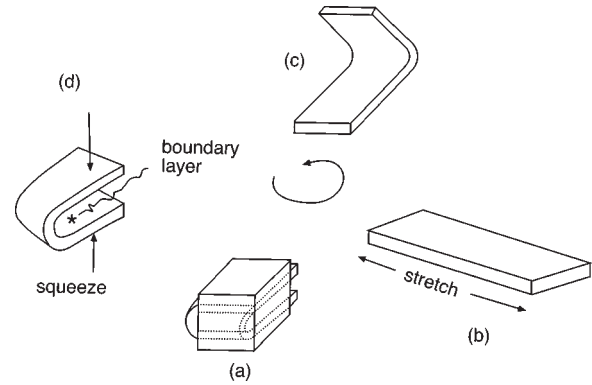


FIG. 8. Stretching and squeezing under a flow. A cube of initial conditions (a) evolves under the flow. The cube moves in the direction of the flow [see Eq. (2.5)]. The sides stretch in the directions of the positive Lyapunov exponents and shrink along the directions of the negative Lyapunov exponents (b). Eventually, two initial conditions reach a maximum separation (c) and begin to get squeezed back together (d). A boundary layer (d) separates two distant parts of phase space that are being squeezed together.

creases, the cube stretches in directions with positive local Lyapunov exponents and shrinks in directions with negative local Lyapunov exponents. Two typical nearby points (a) separate at a rate determined by the largest positive local Lyapunov exponent (b). Eventually these two points reach a maximum separation (c), and thereafter are squeezed to closer proximity (d). We make a distinction between “shrinking,” which must occur in a dissipative system since some eigenvalues must be negative ( $\sum_{j=1}^n \lambda_j < 0$ ), and “squeezing,” which forces distant parts of phase space together. When squeezing occurs, the two parts of phase space being squeezed together must be separated by a boundary layer, which is indicated in Fig. 8(d). Boundary layers in dynamical systems are important but have not been extensively studied.

If a dynamical system is dissipative ( $\nabla \cdot \mathbf{F} < 0$  everywhere) all volumes in phase space shrink to zero asymptotically in time. If the motion in phase space is bounded and exhibits sensitivity to initial conditions, then almost all initial conditions will asymptotically gravitate to a strange attractor.

Repeated applications of the stretching and squeezing mechanisms build up an attractor with a self-similar (fractal) structure. Knowing the fractal structure of the attractor tells us nothing about the mechanism that builds it up. On the other hand, knowing the mechanism allows us to determine the fractal structure of the attractor and to estimate its invariant properties.

Our efforts in this review are concentrated on determining the stretching and squeezing mechanisms that generate strange attractors, rather than determining the fractal structures of these attractors.

### D. The problem

Beginning with equations for a low-dimensional dynamical system [see Eq. (2.1)], it is possible, sometimes

with difficulty, to determine the stretching and squeezing mechanisms that build up strange attractors and to determine the properties of these strange attractors.

In experimental situations, we usually have available measurements on only a subset of coordinates in the phase space. More often than not, we have available only a single (scalar) coordinate:  $x_1(t)$ . Furthermore, the available data are discretely sampled at times  $t_i$ ,  $i = 1, 2, \dots, N$ .

The problem we discuss is how to determine, using a finite length of discretely sampled scalar time-series data, (a) the stretching and squeezing mechanisms that build up the attractor and (b) a dynamical system model that reproduces the experimental data set to an “acceptable” level.

### III. TOPOLOGICAL INVARIANTS

Every attempt to classify or characterize strange attractors should begin with a list of the invariants that attractors possess. These invariants fall into three classes: (a) metric invariants, (b) dynamical invariants, and (c) topological invariants.

Metric invariants include dimensions of various kinds (Grassberger and Procaccia, 1983) and multifractal scaling functions (Halsey *et al.*, 1986). Dynamical invariants include Lyapunov exponents (Oseledec, 1968; Wolf *et al.*, 1985). The properties of these invariants have been discussed in recent reviews (Eckmann and Ruelle, 1985; Abarbanel *et al.*, 1993), so they will not be discussed here. These real numbers are invariant under coordinate transformations but not under changes in control-parameter values. They are therefore not robust under perturbation of experimental conditions. Finally, these invariants provide no information on “how to model the dynamics” (Gunaratne, Linsay, and Vinson, 1989).

Although metric invariants play no role in the topological-analysis procedure that we present in this review, the Lyapunov exponents do play a role. In particular, it is possible to define an important dimension, the Lyapunov dimension  $d_L$ , in terms of the Lyapunov exponents. We assume an  $n$ -dimensional dynamical system has  $n$  Lyapunov exponents ordered according to

$$\lambda_1 \geq \lambda_2 \geq \dots \geq \lambda_n. \quad (3.1)$$

We determine the integer  $K$  for which

$$\sum_{i=1}^K \lambda_i \geq 0 \quad \sum_{i=1}^K \lambda_i + \lambda_{K+1} < 0. \quad (3.2)$$

We now ask: Is it possible to characterize subsets of the phase space whose volume decreases under the flow? To provide a rough answer to this question, we construct a  $p$ -dimensional “cube” in the  $n$ -dimensional phase space, with edge lengths along  $p$  eigendirections  $i_1, i_2, \dots, i_p$  and with eigenvalues  $\lambda_{i_1}, \lambda_{i_2}, \dots, \lambda_{i_p}$ . Then the volume of this cube will change over a short time  $t$  according to [see Eqs. (2.8) and (2.9)]

$$V(t) \sim V(0) e^{(\lambda_{i_1} + \lambda_{i_2} + \dots + \lambda_{i_p})t}. \quad (3.3)$$

It is clear that there is some  $K$ -dimensional cube ( $i_1 = 1, i_2 = 2, \dots, i_K = K$ ) whose volume grows in time, for a short time, but that every  $K+1$  dimensional cube decreases in volume under the flow.

We can provide a better characterization if we replace the cube with a fractal structure. In this case, a conjecture by Kaplan and Yorke (1979) (see also Alligood, Sauer, and Yorke, 1997), states that every fractal whose dimension is greater than  $d_L$  is volume decreasing under the flow, and that this dimension is

$$d_L = K + \frac{\sum_{i=1}^K \lambda_i}{|\lambda_{K+1}|}. \quad (3.4)$$

If  $\lambda_1 = 0$ , then  $K = 1$  and  $d_L = 1$ ; if  $K = n$ , then  $d_L = n$ . This dimension obeys the inequalities  $K \leq d_L < K + 1$ .

Topological invariants generally depend on the periodic orbits that exist in a strange attractor. Unstable periodic orbits exist in abundance in a strange attractor; they are dense in hyperbolic strange attractors (Devaney and Nitecki, 1979). In nonhyperbolic strange attractors their numbers grow exponentially with their period according to the attractor’s topological entropy. From time to time, as control parameters are varied, new periodic orbits are created. Upon creation, some orbits may be stable, but they are surrounded by open basins of attraction that insulate them from the attractor (Eschenazi, Solari, and Gilmore, 1989). Eventually, the stable orbits usually lose their stability through a period-doubling cascade.

The stretching and squeezing mechanisms that act to create a strange attractor also act to uniquely organize all the unstable periodic orbits embedded in the strange attractor. Therefore the organization of the unstable periodic orbits within the strange attractor serves to identify the stretching and squeezing mechanisms that build up the attractor. It might reasonably be said that the organization of period orbits provides the skeleton on which the strange attractor is built (Auerbach *et al.*, 1987; Cvitanovic, Gunaratne, and Procaccia, 1988; Solari and Gilmore, 1988; Gunaratne, Linsay, and Vinson, 1989; Lathrop and Kostelich, 1989).

In three dimensions the organization of unstable periodic orbits can be described by integers or rational fractions. In higher dimensions we do not yet know how to make a topological classification of orbit organization. As a result, we confine ourselves to the description of dissipative dynamical systems that are three dimensional, or “effectively” three dimensional. For such systems, we describe three kinds of topological invariants: (a) linking numbers, (b) relative rotation rates, and (c) knot holders or templates.

#### A. Linking numbers

Linking numbers were introduced by Gauss to describe the organization of vortex tubes in the “ether.” Given two closed curves  $\mathbf{x}_A$  and  $\mathbf{x}_B$  in  $R^3$  that have no points in common, Gauss proved that the integral (Rolfson, 1976)

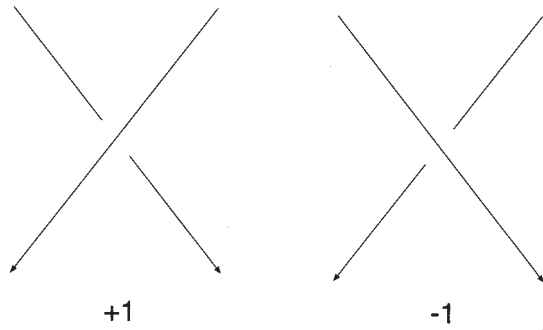


FIG. 9. Projections of curves in  $R^3$  into a two-dimensional subspace. A sign is associated with each nondegenerate crossing, corresponding to whether the crossing is “right handed” or “left handed.”

$$L(A, B) = \frac{1}{4\pi} \oint_A \oint_B \frac{(\mathbf{x}_A - \mathbf{x}_B) \cdot (d\mathbf{x}_A \times d\mathbf{x}_B)}{|\mathbf{x}_A - \mathbf{x}_B|^3} \quad (3.5)$$

is an integer. This integer is called the linking number of the curves  $A$  and  $B$ . It remains invariant as the orbits are deformed, so long as the deformation does not involve the orbits crossing through each other.

These results are directly applicable to the unstable periodic orbits in a strange attractor. Two different periodic orbits can never intersect, for that would violate the uniqueness theorem.

It is not necessary to compute the Gaussian integral to evaluate the integer  $L(A, B)$ . A much simpler algorithm involves projecting the knots onto a two-dimensional subspace. In the projection it is typical for nondegenerate crossings to occur (see Fig. 9). Degenerate crossings (see Fig. 10) can be removed by a perturbation. Linking numbers and self-linking numbers are constructed as follows (Rolfson, 1976; Kaufman, 1987; Atiyah, 1990; Adams, 1994):

(1) Tangent vectors to the two crossings are drawn in the direction of the flow.

(2) The tangent vector to the upper segment (in the projection) is rotated into the tangent vector to the lower segment through the smaller angle.

(3) If the rotation is “right handed,” the crossing is assigned a value  $+1$ . If the rotation is “left handed,” it is assigned a value  $-1$ .

(4) The linking number  $L(A, B)$  is half the sum of the signed crossings of  $A$  and  $B$ .

(5) The self-linking number of an orbit with itself,  $SL(A) = L(A, A)$ , is the sum (not half sum) of the signed crossings of  $A$  with itself.

In Fig. 11 we show how to compute the linking number of a period-two and a period-three orbit found in the strange attractor that is constructed from data from the Belousov-Zhabotinskii reaction. In Fig. 12 we compute the self-linking numbers for each of these two orbits.

**B. Relative rotation rates**

These topological invariants were originally introduced (Solari and Gilmore, 1988) to help describe peri-

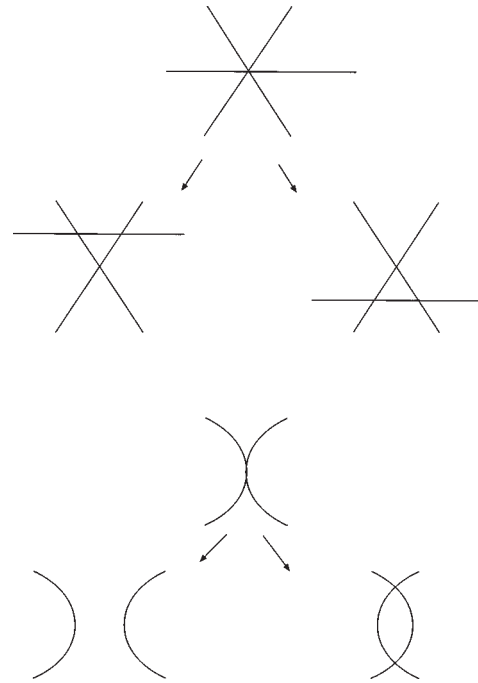


FIG. 10. Degenerate crossings. Degeneracies can be removed by perturbation.

odically driven two-dimensional dynamical systems, such as periodically driven nonlinear oscillators. However, these invariants can also be constructed for a large class of autonomous dynamical systems in  $R^3$ : those for which a Poincaré section can be constructed. More specifically, whenever we find a strange attractor with a “hole” in the middle (see Fig. 57), a family of Poincaré sections exists. Relative rotation rates can be defined for all such dynamical systems.

The construction of relative rotation rates proceeds as follows: Assume that a periodically driven dynamical system has two periodic orbits  $A$  and  $B$  in  $R^3$  with periods  $p_A$  and  $p_B$ . The orbit  $A$  intersects a Poincaré sec-

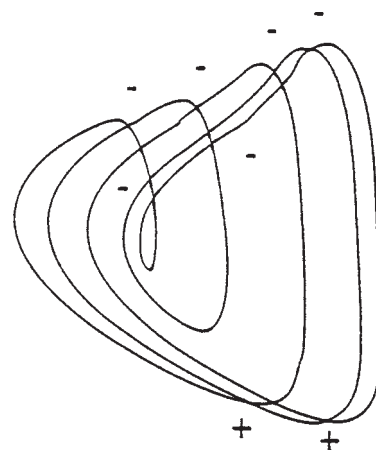


FIG. 11. Computing linking numbers. The linking number of a period-two and a period-three orbit extracted from experimental data is computed by counting half the number of signed crossings. Do not count the self-crossings. The linking number is  $-2$ .

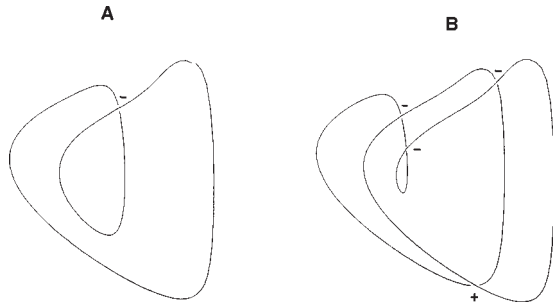


FIG. 12. Computing self-linking numbers. The self-linking numbers of the period-two and period-three orbits shown in Fig. 11 are computed simply by counting the signed self-crossings. The self-linking numbers are  $-1$  and  $-2$ .

tion in  $p_A$  points  $a_1, a_2, \dots, a_{p_A}$ , while  $B$  intersects this section at  $p_B$  points  $b_j, j=1, 2, \dots, p_B$ . Choose any pair of points (initial conditions)  $(a_i, b_j)$  in the Poincaré section and connect these points by a directed line segment (an arrow). If this line segment is evolved under the flow, it will return to its original orientation after  $p_A \times p_B$  periods. This means that the line segment rotates through an integer number of full rotations ( $2\pi$  radians) in the plane perpendicular to the flow in  $p_A \times p_B$  periods. The average rotation, per period, during these  $p_A \times p_B$  periods, is

$$R_{ij}(A, B) = \frac{1}{2\pi p_A p_B} \oint \frac{\mathbf{n} \cdot (\Delta \mathbf{r} \times \mathbf{d}(\Delta \mathbf{r}))}{\Delta \mathbf{r} \cdot \Delta \mathbf{r}} \quad (3.6)$$

This integral depends on the initial points  $(a_i, b_j)$  in the Poincaré section. For the orbits  $A$  and  $B$ , a total of  $p_A \times p_B$  relative rotation rates can be computed, since  $1 \leq i \leq p_A, 1 \leq j \leq p_B$ . These rational fractions are typically not all equal.

The linking number  $L(A, B)$  can easily be constructed from the relative rotation rates  $R_{ij}(A, B)$ :

$$L(A, B) = \sum_{i,j} R_{ij}(A, B) \quad (3.7)$$

(but not vice versa). The proof of Eq. (3.7) is given by Solari and Gilmore (1988).

The relative rotation rates of an orbit with itself can be constructed in the same way. The only technical point which should be mentioned is that  $R_{ii}(A, A)$  is not defined by the integral (3.6). We define  $R_{ii}(A, A) = 0$ . Then the set of self-linking numbers of  $A$  is

$$SL(A) = L(A, A) = \sum_{1 \leq i, j \leq p_A} R_{ij}(A, A). \quad (3.8)$$

The self-relative rotation rates provide a surprising amount of information. For example, two orbits with the same period and self-linking number may have different self-relative rotation rates. The two orbits are then inequivalent. In addition, the spectrum of fractions in  $R_{ij}(A, A)$  provides information about how the flow deforms a neighborhood of the orbit. Self-relative rotation rates were used to identify orbits belonging to the different “snakes” shown in Fig. 2.

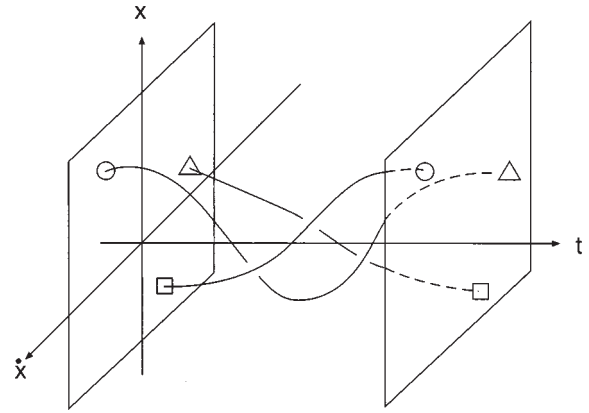


FIG. 13. The  $x-\dot{x}-t$  phase space for a driven nonlinear oscillator. A period-three orbit is shown.

Relative rotation rates are rather easily computed for a driven dynamical system. We illustrate this by computing the self-relative rotation rates for a period-four orbit extracted from NMR laser data (Tuffiaro *et al.*, 1991). The space in which the orbit is embedded is shown in Fig. 13. The projection into the  $x-t$  plane is shown in Fig. 14. This projection is usually what is measured, and the  $x-\dot{x}-t$  embedding is constructed from it. In Fig. 14 each tick represents one period. The original period-four orbit is shown repeated twice in each of the four panels for convenience. A second copy of the period-four orbit is shown superposed on the first orbit, shifting one period in passing from Fig. 14(a) to Fig. 14(d). The self-relative rotation rates are computed by counting the crossings and dividing by  $4 \times 2$ . All crossings are negative in this projection by the left-hand rule. The set of self-relative rotation rates for this orbit is  $(-\frac{1}{2})^8 (-\frac{1}{4})^4 (0)^4$ . That is,  $(-\frac{1}{2})$  occurs 8 times, etc. In presenting relative-rotation-rate information, we present only the ratios of these fractions. In tabular form, these results are presented as  $(-\frac{1}{2})^2 (-\frac{1}{4}) 0$ .

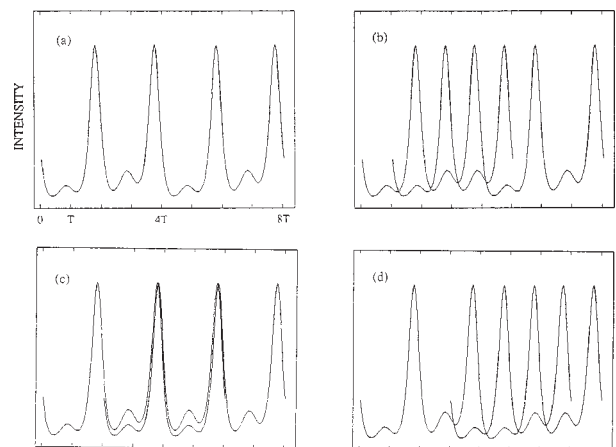
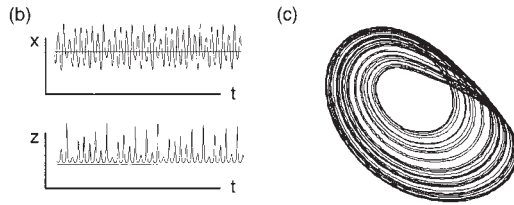


FIG. 14. A period-four orbit is superposed on itself (repeated twice for convenience), shifted by one period in progressing from (a) to (d). The signed number of crossings is: 0,  $-4$ ,  $-2$ ,  $-4$  in (a), (b), (c), (d) (respectively). The relative rotation rates are  $(-\frac{1}{2})^8 (-\frac{1}{4})^4 (0)^4$ .

(a) Rössler Equations

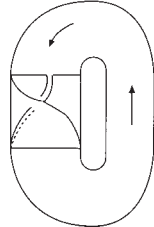
$$\begin{aligned} \frac{dx}{dt} &= -y - z \\ \frac{dy}{dt} &= x + ay \\ \frac{dz}{dt} &= b + z(x - c) \end{aligned}$$



(f)

$$\begin{pmatrix} -1 & 0 \\ 0 & 0 \end{pmatrix} \\ \begin{pmatrix} 0 & +1 \end{pmatrix}$$

(e)



(d)

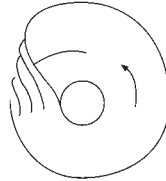


FIG. 15. (a) Rössler equations. (b)  $x(t)$  and  $z(t)$  plotted after transients have died out and the trajectory has relaxed to the strange attractor. Control parameter values:  $(a,b,c) = (0.398,2.0,4.0)$ . (c) Projection of the strange attractor into the  $x$ - $y$  plane. (d) Caricature of the flow on the attractor. (e) Birman-Williams knot holder for this attractor. (f) Algebraic representation of this template.

C. Knot holders or templates

Knot holders were constructed by Birman and Williams (1983a, 1983b) to describe the ensemble of unstable periodic orbits in a strange attractor, as well as the topological organization of those periodic orbits. The first knot holder was constructed for the strange attractor generated by the Lorenz equations. Knot holders for other dynamical systems were subsequently constructed.

That knot holders should exist at all is suggested by Figs. 15 and 16. These figures are for the “hydrogen atom” and “hydrogen molecule” problems of dynamical-systems theory. The two most widely studied low-dimensional dynamical systems are the Rössler equations (Rössler, 1976a, 1976b) and the Lorenz equations (Lorenz, 1963). Each figure consists of six parts. The first presents the equations of motion. The second presents time traces of two of the state variables:  $x(t)$  and  $z(t)$  in both cases. The third part is a projection of the strange attractor into a two-dimensional subspace of

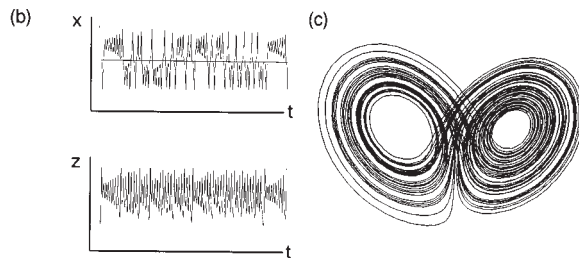
the three-dimensional phase space. Part four is a caricature of this projection, showing crossing information. Part five is the Birman-Williams knot holder, which can be used to describe unstable periodic orbits in the attractor, as well as their topological organization. Finally, part six provides the algebraic description of these topological objects. The algebraic description consists of a set of integers that describe the stretching and squeezing mechanisms, which act on phase space to generate the strange attractor and to organize all the unstable periodic orbits in it in a unique way.

It is remarkable that these integers can be extracted from chaotic data. Our objective is to describe how to extract these integers from chaotic data, which is usually a single scalar time series.

The caricature [Figs. 15(d), 16(d)] is apparent because the strange attractor is “thin.” That is, it looks like a two-dimensional manifold in most places, but it actually has some thickness in the transverse direction. In fact, in both cases the attractor is a fractal with a Lyapunov

(a) Lorenz Equations

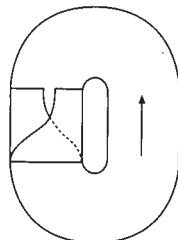
$$\begin{aligned} \frac{dx}{dt} &= -\sigma x + \sigma y \\ \frac{dy}{dt} &= rx - y - zy \\ \frac{dz}{dt} &= -bz + xy \end{aligned}$$



(f)

$$\begin{pmatrix} 0 & 0 \\ 0 & 0 \end{pmatrix} \\ \begin{pmatrix} +1 & -1 \end{pmatrix}$$

(e)



(d)

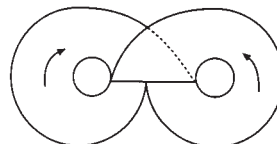


FIG. 16. (a) Lorenz equations. (b)  $x(t)$  and  $z(t)$  plotted after transients have died out and the trajectory has relaxed to the strange attractor. Control parameter values:  $(b,\sigma,r) = (8/3,10.0,30.0)$ . (c) Projection of the strange attractor into the  $x=y-z$  plane. (d) Caricature of the flow on the attractor. (e) Birman-Williams knot holder for this attractor. (f) Algebraic representation of this template.

dimension close to 2. Specifically, the Lyapunov dimension is  $d_L = 2 + \epsilon$ ,  $\epsilon = \lambda_1 / |\lambda_3|$ , where  $\lambda_1 + \lambda_2 + \lambda_3 = \nabla \cdot \mathbf{F}$  is very negative ( $\leq -5$ ; both systems are highly dissipative). For both attractors,  $\lambda_1 > 0$  (sensitivity to initial conditions),  $\lambda_2 = 0$  (flow direction), and  $\lambda_3 \ll 0$  (very dissipative).

Knot holders contain all the crossing information required in order to construct the two previously introduced topological invariants: linking numbers and relative rotation rates.

Linking numbers and relative rotation rates are invariant under smooth coordinate transformations. They are also invariant under control-parameter changes. That is, over the range of control-parameter values in which the orbits  $A$  and  $B$  exist, their linking numbers and relative rotation rates do not change. These numbers do not depend on the stability of the orbits. Thus, even for nonhyperbolic attractors, for which one or both orbits  $A, B$  may be stable (i.e., just created in saddle-node or period-doubling bifurcations),  $L(A, B)$  and  $R_{ij}(A, B)$  do not change as  $A$  (or  $B$ ) undergoes bifurcations and/or changes in stability, as long as they exist.

A knot holder is invariant under smooth (point) change of variables. As defined below, knot holders are also invariant under changes in control-parameter values. Inequivalent knot holders, those with different algebraic descriptions, cannot be smoothly deformed into each other. This means in particular that strange attractors with inequivalent knot holders are inequivalent.

Since knot holders summarize the stretching and squeezing mechanisms that generate strange attractors, they are currently the best tool available for the study of strange attractors in low-dimensional dynamical systems.

#### IV. TEMPLATES AS FLOW MODELS

The caricatures of the Rössler and Lorenz flows presented in Figs. 15(d) and 16(d) are convenient ways to summarize the stretching and squeezing mechanisms responsible for generating their strange attractors. It is remarkable that a caricature of this type exists for all dissipative flows in  $R^3$  that generate strange attractors. The existence of such a caricature is made rigorous by the Birman-Williams Theorem (1983a, 1983b).

##### A. The Birman-Williams theorem in $R^3$

Birman and Williams assume that there is a dissipative flow in  $R^3$  that generates a hyperbolic strange attractor. Already this assumption presents a problem for us: we have yet to see a set of dissipative ordinary differential equations or a dissipative physical system with this property. Such attractors are “nongeneric” (Gilmore, 1981) in Nature. Nevertheless, this is a very useful theorem, which we shall pursue and whose outcome we shall modify to a form in which it is useful for applications.

For such attractors there are three Lyapunov exponents  $\lambda_1 > \lambda_2 > \lambda_3$ , which obey the following conditions:

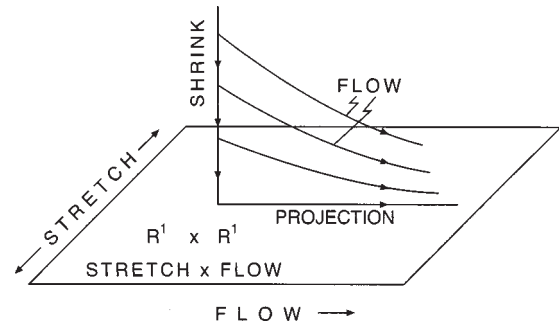


FIG. 17. Birman-Williams projection. Identifying all points with the same asymptotic future amounts to projecting down along a stable direction to a point in a space that is a two-dimensional manifold “almost everywhere.”

$$\begin{aligned} \lambda_1 &> 0 && \text{(sensitivity to initial conditions),} \\ \lambda_2 &= 0 && \text{(flow direction),} \\ \lambda_3 &< -|\lambda_1| && \text{(dissipative).} \end{aligned} \quad (4.1)$$

Birman and Williams then identify two points in phase space,  $\mathbf{x}_1$  and  $\mathbf{x}_2$ , if they have the same future:

$$\mathbf{x}_1 \sim \mathbf{x}_2 \quad \text{if} \quad \lim_{t \rightarrow \infty} |\mathbf{f}(t, \mathbf{x}_1(t=0), \mathbf{c}) - \mathbf{f}(t, \mathbf{x}_2(t=0), \mathbf{c})| = 0. \quad (4.2)$$

This results in a projection along stable one-dimensional manifolds (the  $\lambda_3$  direction) onto a space that is essentially two-dimensional “almost everywhere.” The two dimensions correspond to the flow direction ( $\lambda_2$ ) and the stretching direction ( $\lambda_1$ ). This projection is illustrated in Fig. 17. The places in this projection where “almost everywhere” fails (i.e., “almost nowhere”) are where we focus our attention. These are precisely the places that describe stretching and squeezing.

In Fig. 18 we show how the identification defined by Eq. (4.2) and illustrated in Fig. 17 fails to generate a two-dimensional manifold. On the left of this figure we show a cube of initial conditions in phase space. After some finite time, shrinking occurs in one dimension, stretching in another. In addition, a gap appears in the outflow direction. Under the projection (4.2) this space becomes a two-dimensional manifold everywhere but at the “tear point,” which separates regions heading off to different parts of phase space. The tear point is one type of singularity that keeps this space of projected flows from being a two-dimensional manifold. This point is actually an initial condition for a trajectory that goes asymptotically to a singular point.

On the right in Fig. 18 we show two cubes in different parts of phase space that will be squeezed together by the flow. After some finite time the cubes are deformed to the Y-shaped structure, with a boundary layer separating the deformed parallelepipeds at the junction. Under the identification (4.2), the two inflowing regions meet at a branch line and give rise to a single outflowing two-dimensional region. This Y-shaped structure fails to be a manifold because of the junction at the branch line.

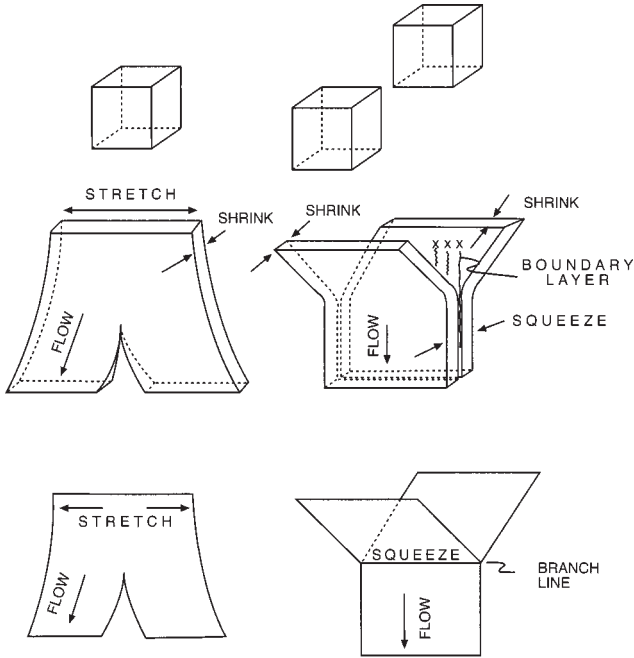


FIG. 18. Left: A cube of initial conditions (top) is deformed under the stretching part of the flow (middle). A gap begins to form for two parts of the flow heading to different parts of phase space. Under further shrinking, a two-dimensional structure is formed that is not a manifold because of the tear point, which is an initial condition for a trajectory to a singular point. Right: Two cubes of initial conditions (top) in distant parts of phase space are squeezed together and deformed by the flow (middle). A boundary layer separates the deformed parallelepipeds at their junction. Under the projection the two inflow regions are joined to the outflow region by a branch line.

The branch line is the other type of singularity that keeps the space of projected flows from being a two-dimensional manifold.

The Birman-Williams theorem states that, under the identification (4.2), the strange attractor projects down to a two-dimensional branched manifold. Every branched manifold is built up from two basic building blocks that represent “stretch” and “squeeze” by connecting outflows to inflows. Every outflow is connected to some inflow, and vice versa: there are no free ends. Figure 19 shows a possible branched manifold. In Fig. 20 we show branched manifolds representing the Rössler and Lorenz systems, even though hyperbolicity has

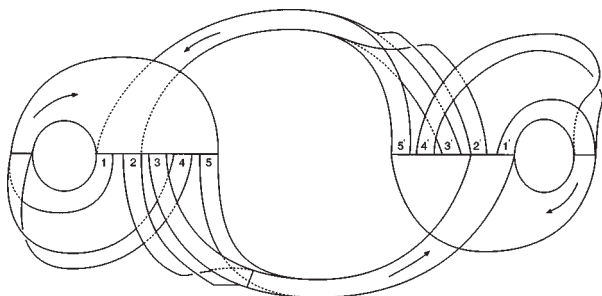


FIG. 19. One possible branched manifold for a flow.

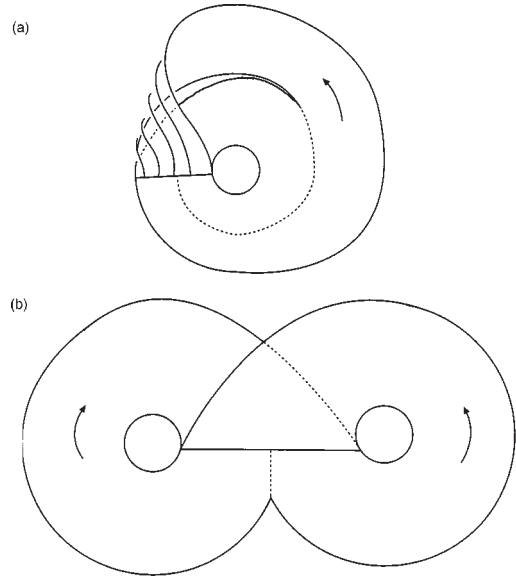


FIG. 20. Branched manifolds describing stretching and squeezing for (a) the Rössler and (b) the Lorenz equations.

never been demonstrated for either attractor for any control-parameter values.

The Birman-Williams theorem also states that, under the projection (4.2), no orbits cross through each other. Their topological organization is invariant under the projection. In particular, topological invariants (linking numbers, relative rotation rates) of the periodic orbits are the same in the attractor as in its caricature, the two-dimensional branched manifold. It is this property—the comparison of topological invariants for periodic orbits “extracted from data” with the invariants of corresponding orbits in a branched manifold—that allows us to determine stretching and squeezing mechanisms from chaotic data.

The Birman-Williams theorem can be interpreted from a more physically motivated viewpoint. Imagine that we are able to vary the control parameters so that (a) no new periodic orbits are created in saddle-node bifurcations and (b)  $\lambda_1$  remains positive and finite while  $\lambda_3 \rightarrow -\infty$ . Under these conditions the “thickness” of the strange attractor decreases, and its Lyapunov dimension approaches 2:

$$d_L = 2 + \frac{\lambda_1}{|\lambda_3|} \rightarrow 2. \tag{4.3}$$

The projection (4.2) is equivalent to increasing the dissipation without bound. For this reason we sometimes refer to the projection (4.2) as a “deflation.” Conversely, once the two-dimensional branched manifold describing a flow has been determined, it can be “inflated” (thickened up) to more accurately represent the geometric properties of the original attractor, which are destroyed by deflation.

### B. The Birman-Williams theorem in $R^n$

The very first application of the Birman-Williams theorem to a physical system (Mindlin *et al.*, 1991) ran

into an unexpected and fortuitous problem. The problem was that any theoretical description of the underlying physical mechanism involved more than three variables (Scott, 1991). Knots fall apart in dimensions greater than three, so the Birman-Williams theorem, as originally proved, was not applicable. In spite of this, we were able to compute knot invariants from experimental data.

This serendipitous result led to a deeper understanding of the Birman-Williams theorem. We imagine a dynamical system in  $R^n$  ( $n > 3$ ) with a hyperbolic strange attractor having only one unstable direction:

$$\lambda_1 > \lambda_2 = 0 > \lambda_3 > \lambda_4 \cdots > \lambda_n. \quad (4.4)$$

If the attractor is strongly contracting,

$$|\lambda_3| > \lambda_1, \quad (4.5)$$

then the identification (4.2) acts to project the attractor to a two-dimensional branched manifold. In this projection an  $(n-2)$ -dimensional stable manifold is projected onto a point in a two-dimensional manifold “almost everywhere” with coordinates in the  $\lambda_1$  (stretching) and  $\lambda_2$  (flow) directions.

If the projection is carried out along the  $\lambda_4, \dots, \lambda_n$  directions first, the projected flow lies in a three-dimensional submanifold of  $R^n$ . In this space the topological organization of unstable periodic orbits is determined by the standard topological invariants (linking numbers, relative rotation rates), since these are defined for periodic orbits in three-dimensional spaces. Then the last projection along the least strongly contracting ( $\lambda_3$ ) direction preserves the topological organization of the unstable periodic orbits in the strange attractor.

For strongly contracting flows, the local Lyapunov dimension

$$d_L = 2 + \frac{\lambda_1}{|\lambda_3|} < 3 \quad (4.6)$$

is less than three everywhere. If  $d_L(\mathbf{x})$  is the local Lyapunov dimension of the attractor and  $\text{Max} d_L(\mathbf{x}) < 3$  is its maximum over the attractor, then Eq. (4.2) provides a projection of the flow in the strange attractor down to a branched manifold with dimension  $[\text{Max} d_L(\mathbf{x})] = 2$ , where  $[*]$  is the integer part of  $*$ .

### C. Templates

For purposes of computing topological invariants, it is useful to transform branched manifolds into some standard form. These standard forms are called templates. Several closely related standard forms have been proposed (Holmes, 1988; Mindlin *et al.*, 1990; Tufillaro, Abbott, and Reilly, 1992), which are discussed below. All standard forms depend on projections of the two-dimensional branched manifolds, which are embedded in  $R^3$ , into a two-dimensional subspace. Crossing information must be preserved in these projections. We dis-

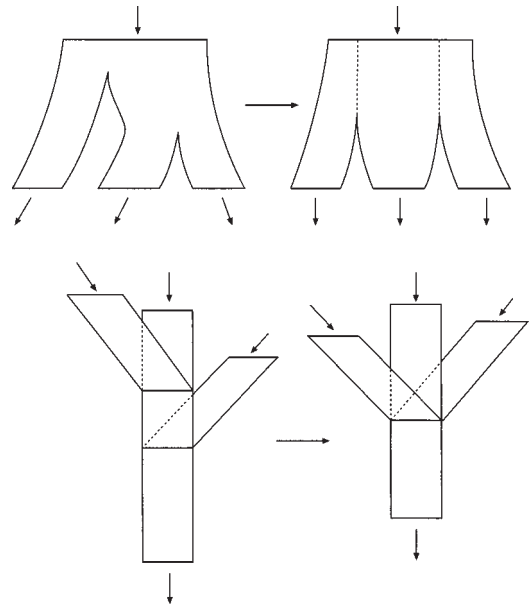


FIG. 21. Simplifying branched manifolds. This can be done by redrawing the concatenation of stretches with stretches or squeezes with squeezes. The resulting structures are nongeneric in branched manifolds, but convenient.

cuss now several steps which are useful in transforming two-dimensional branched manifolds into a standard template form.

Branched manifolds are constructed from the stretch and squeeze building blocks in “Lego”<sup>®</sup> fashion by connecting outflow to inflow. We can simplify our description of templates when stretches are connected to stretches, or squeezes to squeezes, as suggested in Fig. 21. After this simplification, (a) stretches have one inflow and  $n (\geq 2)$  outflows separated by  $n-1$  tear points, and (b) squeezes have  $n (\geq 2)$  inflows and one outflow joined at a branch line  $B$ .

A branched manifold then has  $k$  branch lines  $B_j$  ( $1 \leq j \leq k$ ). Each branch line has  $n_k$  preimages, one in each of the  $n_k$  rectangles feeding it. These can be determined by locating the preimage of each tear point on the nearest branch in the flow-reversed direction. For example, the preimages for the Rössler and Lorenz branched manifolds are identified by following the dashed lines from the tear points, backward against the flow direction, to the first branch line (see Fig. 20).

In this way each branch line is divided into two or more segments. The branch lines are then separated and deformed, as shown in Fig. 22 for the Rössler system. In this representation of Rössler dynamics, the stretching and squeezing processes are summarized between the lines marked “top” and “bottom.” A phase-space point flows either through branch 0 or branch 1. Branch 0 is orientation preserving; branch 1 is orientation reversing. The flow is returned from the branch line at the bottom to its preimage at the top by a flow that performs neither stretching nor squeezing. The stretching and squeezing is then repeated.

All stretching and squeezing occurs as the flow progresses through this region (from top to bottom).

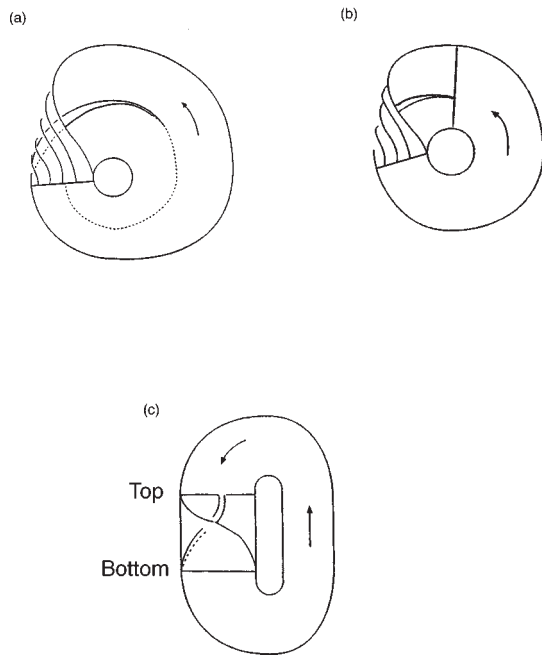


FIG. 22. (a) Branched manifold for Rössler flow. The preimage (follow the dashed lines) of the tear point on the branched manifold divides the branch line into two segments. (b) These segments are rotated around to the point of the flow where stretching and squeezing begin. (c) The entire flow is deformed to the standard form shown. All interesting processes occur between the branch line (bottom of figure) and its preimages (top of figure). The flow caricature between these two lines is the template. We often include the return flow with the template.

This segment of the standard form for the projection of a two-dimensional branched manifold onto  $R^2$  is called a template. A template summarizes all the stretching and squeezing processes that act on the phase space to create the strange attractor. We usually include the return flow with the template.

Following this procedure, it is not difficult to see that any branched manifold can be transformed, after projection to  $R^2$ , into the standard form shown in Fig. 23. (Franks and Williams, 1985; Kocarev, Tasev, and Dimovski, 1994). Each branch line is divided into segments by locating preimages of each tear point on the branch lines. The return flow from each branch line (bottom) feeds the segments of the branch lines (top). The stretch and squeeze mechanisms are described as follows:

- The signed number of twists in each branch of the flow is indicated in the region labeled A1. This is just the signed number of half turns:  $0, \pm 1, \pm 2, \dots$
- Branches cross but do not twist in the region labeled A2. Each branch crossing is assigned an integer in exactly the same way as is done for knots (see Fig. 11).
- In the region labeled B the various branches are squeezed together. An array is introduced (Mindlin *et al.*, 1990) to indicate the order in which they are squeezed. By convention, the integers indicating ordering are larger the further from the observer (increasing

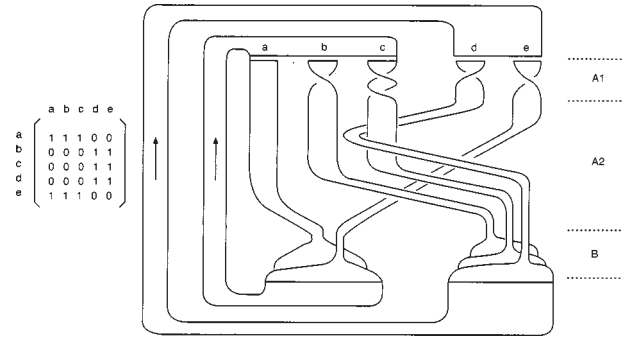


FIG. 23. Standard form for templates. A template can be constructed for any branched manifold by following the procedures described in the text and illustrated in Fig. 22. The template is characterized by branch-twisting (A1) and crossing (A2) information, the order in which branches are squeezed together (B), and the branch transition matrix.

from top to bottom).

- A transition matrix (Markov matrix) is introduced to identify which branches are connected to which.

#### D. Algebraic description of templates

The template shown in Fig. 23 defines a stretching and squeezing mechanism similar to, but simpler than, those responsible for creating the strange attractor generated by a nonlinear electric circuit (Kocarev, Tasev, and Dimovski, 1994). The branch-twisting and -crossing information is summarized by a  $5 \times 5$  matrix  $T(i,j)$ . The integer in the  $(i,i)$  position is the local torsion information. It is easily determined by counting the signed crossings of the edges of the  $i$ th branch (from region A1). The integer  $T(i,j)$  is the signed number of crossings of the  $i$ th and  $j$ th branches. This is equivalent to twice the linking number of the period-one orbits in these two branches. This information comes from region A2. If  $T(i,j)=0$ , the branches do not cross. The  $1 \times 5$  array indicates the order in which the branches are joined at the branch lines (from region B). In the projection, branches with larger integer values are behind branches with smaller values. Since there are two branch lines, the order of the integers for each branch is important. Finally, the  $5 \times 5$  transition matrix shows how the flow can move from branch to branch (from region B). This is equivalent to giving a prescription for the symbolic dynamics of allowed periodic orbits. For example, the period-four orbit  $acde acde \dots$  is allowed, but  $adde adde \dots$  is not allowed [ $M(a,d)=0$ ].

Two other representations of templates have been proposed. In both representations all branches are connected on the bottom line. The templates so constructed are called “fully expansive.” In the representation proposed by Mindlin *et al.* (1990), the order in which the branches are squeezed together is represented by a set of integers in an array. In the projection considered, the smaller the integer, the closer to the observer is the branch. In the representation proposed by Tufillaro, Abbott, and Reilly (1992), the branches are reordered so

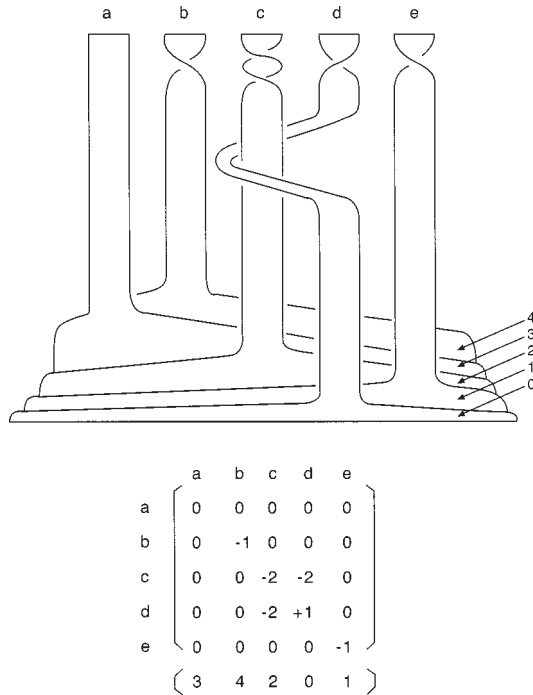


FIG. 24. Alternative representation of the template shown in Fig. 23. This representation is fully expansive. Each branch contains a period-one orbit. The template matrix *now contains information* about the period-one orbits.  $T(i,i)$  is the local torsion of orbit  $i$ , and  $T(i,j) = 2L(i,j)$ . The array describes the order in which the branches are squeezed together. Information in the array can be extracted from linking numbers for period-two orbits.

that the projection is in some standard order. The order chosen is this: the further to the right a branch appears at the bottom of flow region A2, the closer to the front it is in the projection of the squeezing region. In all cases a Markov matrix describes which branches flow to which other branches.

We now describe in more detail the template representation used by Mindlin *et al.* (1990). If the branches are labeled  $A, B, \dots, N$ , then a general period- $p$  orbit is a sequence of  $p$  symbols that indicates which branches the periodic orbit traverses, as well as in which order. For fully expansive templates, each branch contains a period-one orbit. These exist in a 1-1 correspondence with the branches, and the same symbol is used to label both the branch and the period-one orbit in it. The template matrix  $T(i,j)$  contains information about these orbits. In fact, the template matrix is constructed out of topological invariants of these orbits. More specifically, the diagonal matrix elements  $T(i,i)$  are the local torsions of the period-one orbits  $i$ , and the off-diagonal elements  $T(i,j) = T(j,i)$  are twice the linking numbers of the period-one orbits  $i$  and  $j$ . The array obeys the convention described above. In Fig. 24 we show this representation for the template shown in Fig. 23.

Remark: In this representation, the template matrix  $T(i,j)$  can be obtained by determining the linking numbers and local torsions of only the period-one orbits in the flow. The array matrix can be determined from the

linking numbers of only  $N-1$  appropriate pairs of period-one and/or period-two orbits.

The three representations each change as the projection of the branched manifold in  $R^3$  down to different two-dimensional subspaces  $R^2$  changes. It hardly matters which algebraic representation is chosen to describe the dynamics: the differences are choices of convention. What matters is that the topological invariants (linking numbers, relative rotation rates) depend only on the orbits involved and not on the representation used for the computation.

Any of these representations can be used to compute topological invariants. Therefore the integers that characterize templates algebraically are in fact topological invariants of the branched manifold that describes the strange attractor. That is to say, these integers are topological invariants of the strange attractor itself. It is these integers that we shall extract from data in order to identify the stretching and squeezing mechanisms responsible for generating chaos.

### E. Control-parameter variation

The metric and dynamical invariants of strange attractors are independent of coordinate transformations and initial conditions. However, they are not independent of control-parameter variation.

Topological invariants of orbits and orbit pairs are unchanged under control-parameter variation as long as the orbits exist. However, as control parameters are varied, periodic orbits are created and/or annihilated. Therefore it is not obvious that the topological description of a strange attractor is invariant under control-parameter variation.

In fact, there are two options, which will be illustrated with respect to both the Rössler and Lorenz attractors. Suppose the Rössler equations are integrated for parameter values for which there is a strange attractor, and that all the unstable periodic orbits in the strange attractor are constructed from the alphabet with two symbols 0 and 1. If every possible symbol sequence is allowed, the attractor is hyperbolic. We have never encountered such an attractor, either in simulations of dissipative systems or in the analysis of experimental data. In our experience, it is always the case that some symbol sequences are forbidden.

For example, if the symbol sequence 00 is the only symbol sequence that is forbidden, then every periodic orbit is constructed from the two-letter alphabet 01 and 1. A template for the strange attractor is shown in Fig. 25(a). In this template there are two branches: A, corresponding to the symbol sequence 01, and B, corresponding to 1. The stretching and squeezing are as indicated in this template, which can be constructed as a subtemplate (Ghrist, Holmes, and Sullivan, 1996) of the Rössler template. There is a 1-1 correspondence between periodic orbits in the template shown in Fig. 25(a) and those in the strange attractor.

In general, the alphabet required to describe a nonhyperbolic strange attractor for the Rössler equations con-

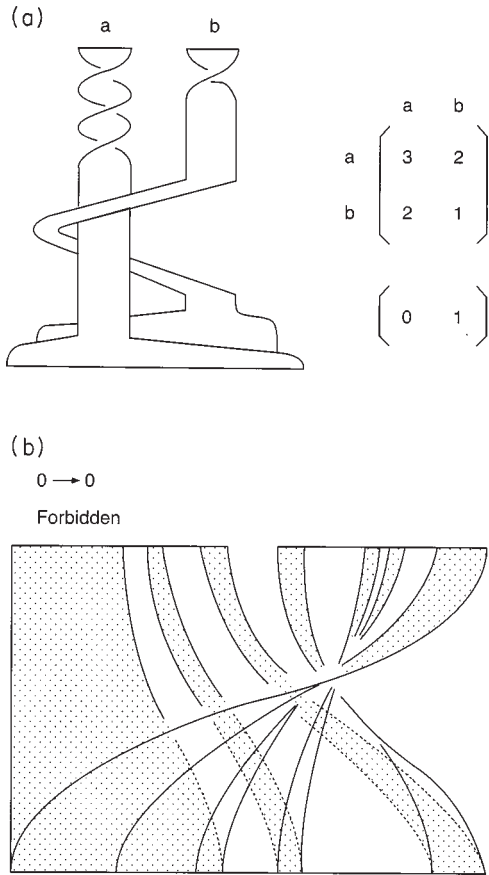


FIG. 25. Rössler template. (a) Template describing a strange attractor generated by the Rössler equations, but containing only unstable periodic orbits built up from the symbols 01 and 1. (b) For this attractor the flow is restricted to a portion of the original template. This subset is obtained by removing the pieces of the branch corresponding to forbidden transitions, in this case  $0 \rightarrow 0$ , that correspond to the left quarter of the branch line. All parts of the branch line that eventually flow into this segment must also be removed. They are determined by finding all preimages of this segment.

sists of a large number of symbol sequences. This number grows with the length of the sequence. For example, to length four the alphabet might be 01, 011, and 0111. In general, as longer and longer symbol sequences occur, new inadmissible sequences appear. We can take this into account by increasing the number of letters in the alphabet of allowed symbols as the length of the symbol sequence grows (an alternative possibility, involving Markov partitions, is indicated below). Each letter in the alphabet (A,B,C, . . . ) then corresponds to one branch of a template. In this representation (a) every possible sequence of letters is allowed, (b) a template typically has an infinite number of branches, and (c) the number of branches corresponding to symbol sequences of length  $\leq P$  is finite. We do not regard this as an elegant or even convenient way to describe strange attractors for dynamical systems.

We now describe an alternative way to describe the dynamics. This is shown in Fig. 25(b) for the Rössler strange attractor, for which the symbol sequence 00 is

$$\begin{array}{c}
 a \quad b \\
 \left( \begin{array}{cc}
 3 & 2 \\
 2 & 1
 \end{array} \right) \\
 \left( \begin{array}{cc}
 0 & 1
 \end{array} \right)
 \end{array}$$

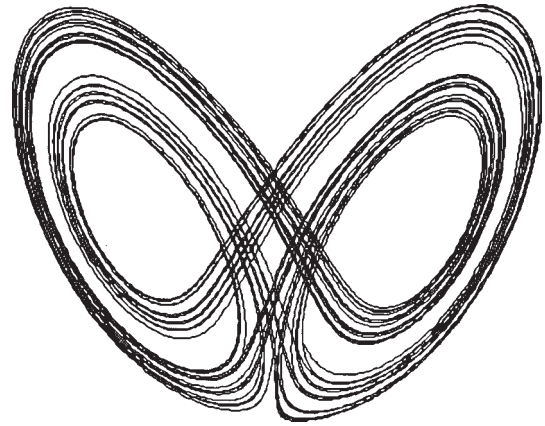


FIG. 26. Lorenz-like strange attractor generated by integrating the Shimizu-Morioka (1980) equations.

forbidden. Here we begin with the Rössler template and impose the condition that the transition  $0 \rightarrow 0$  is forbidden [ $M(0,0)=0$ ]. This requires that the flow not even reach the left quarter of the branch at the bottom. To ensure this condition, we propagate this quarter branch backwards 1,2, . . . iterations, and eliminate those parts of the template that eventually feed this segment. Each backward iteration has two preimages, since two branches join at the branch line. In this way, we interpret the flow as confined to what is left of the original template (shown in white). That is, the template description (template matrix and array) remains unchanged, but the Markov transition matrix changes

$$\text{from } M = \begin{bmatrix} 1 & 1 \\ 1 & 1 \end{bmatrix} \text{ to } M = \begin{bmatrix} 0 & 1 \\ 1 & 1 \end{bmatrix}. \tag{4.7}$$

In this interpretation we regard the simple Rössler template with branches 0, 1 as generating a “covering” symbolic dynamics. That is, there is a 1-1 correspondence between all the unstable periodic orbits in the hyperbolic Rössler attractor and all the unstable periodic orbits in the template. There is a 1-1 correspondence between the unstable periodic orbits in a typical nonhyperbolic strange attractor for the Rössler equations and a *subset* of unstable periodic orbits in the template with two branches. The missing orbits have been “pruned away” (Cvitanovic, Gunaratne, and Procaccia, 1988).

A second example involves the Lorenz template. Integrating the Lorenz-like Shimizu-Morioka (1980) equations (Shil’nikov, 1993)

$$\begin{aligned}
 \dot{x} &= y, \\
 \dot{y} &= x - \lambda y - xz, \\
 \dot{z} &= -\alpha z + x^2,
 \end{aligned} \tag{4.8}$$

for  $(\alpha, \lambda) = (0.5, 0.85)$  produces the attractor shown in Fig. 26. The two options are again: (a) To construct the template for the attractor, as shown in Fig. 27(a) (it is a subtemplate of the Lorenz template) and (b) to regard the flow as restricted to a subset of the Lorenz template [this interpretation is shown in Fig. 27(b)].

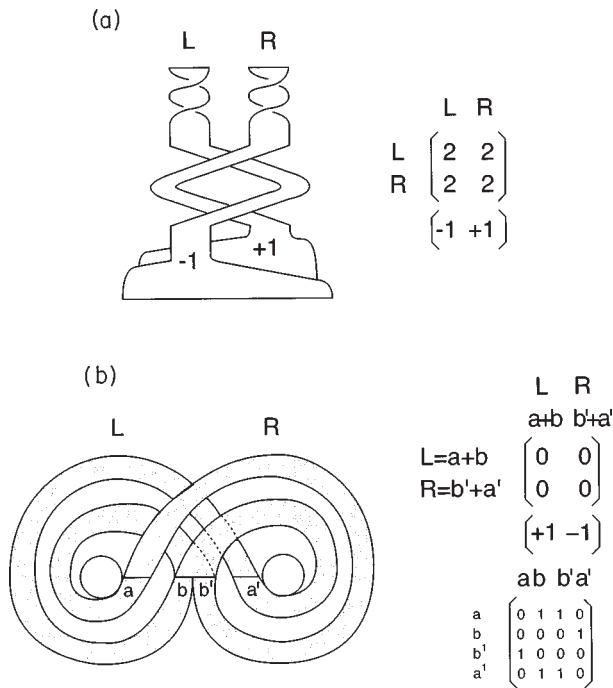


FIG. 27. (a) Template for the attractor shown in Fig. 26. (b) Restriction of the flow shown in Fig. 26 to the Lorenz template.

We have the following two choices as control parameters are varied: (a) identify and exhibit the appropriate branched manifold and template as a subtemplate of the original system [Figs. 25(a) and 27(a)]; and (b) identify a single template and restrict the flow to a subset of it [Figs. 25(b) and 27(b)]. Without hesitation we adopt the second option, for the following reasons:

- (1) The template is then invariant under control parameter variations.
- (2) It is much easier to see how the flow gets “pushed around” on a template than to work out how one subtemplate changes to another as control parameters vary.
- (3) With only one template to work with, the topological invariants of all orbits and orbit pairs need to be computed only once. As long as those orbits remain embedded in the strange attractor as the attractor changes with control parameters, these quantities remain invariant.
- (4) It makes no sense to force an interpretation in terms of subtemplates to preserve the idea of hyperbolicity, when this is nongeneric in dissipative physical systems in the first place.
- (5) The global organization of a flow is largely determined by the fixed points and their insets and outsets, and by some low period orbits and their stable and unstable manifolds. Since these are robust under large variations in parameters, we also want the caricature (template) describing the flow to be robust. This suggests a single-template interpretation.

With this interpretation, templates are topological invariants under change of coordinates, initial conditions,

and control-parameter values. The changing nature of the flow, as control parameters are changed, is encapsulated in the Markov transition matrix. For example, in the Lorenz flow it is possible to subdivide the two segments of the branch line  $L$  and  $R$  into  $n_1$  and  $n_2$  adjacent intervals  $L_1, L_2, \dots, L_{n_1}$  and  $R_1, R_2, \dots, R_{n_2}$ . Then linking numbers (topology) depend only on the symbol sequence ( $LRLL\dots$ ), but the dynamics depend on the  $(n_1+n_2) \times (n_1+n_2)$  Markov transition matrix, which describes, to some extent (the better, the larger  $n_1$  and  $n_2$ ), which orbits are allowed in the flow and which have been “pruned” (Cvitanovic, Gunaratne, and Procaccia, 1988) from the flow.

## F. Examples of templates

Although there are very many three-dimensional dissipative dynamical systems with strange attractors, their characterization requires only a relatively small number of templates. We present some here.

### 1. Rössler dynamics

As the parameters of the Rössler equations are varied, the attractor changes shape, from “fold” chaos to “funnel” chaos to “spiral” chaos (Rössler, 1976b). Some of these changes involve the creation of periodic orbits for which a two symbol (0,1) encoding is not possible. For example, in the transition to funnel chaos a new branch is “created.” In fact, it is preferable to state that this branch was always present, but not visited by the flow at all for smaller control-parameter values. The three-branched template for funnel chaos is shown in Fig. 28(a). For small parameter values the flow is restricted to branches 0 and 1. For larger values it extends over three branches: 0, 1, and 2. For yet larger values it extends over four branches [Fig. 28(b)]. In general, there is an infinite number of branches that exist and wind around each other in a tightening spiral. This information has been used to build up a systematic template description for some physical processes (Gilmore and McCallum, 1995). Usually the flow is confined to only a small number of branches for any control-parameter values, but the branches are organized in a systematic way with respect to each other.

### 2. Lorenz dynamics

Here also the standard template [see Fig. 16(e)] is what is seen at smaller values of the control-parameter  $r$ . As  $r$  is increased past a threshold  $r \sim 60$ , the flow extending from the extreme left or right to the opposite lobe is folded over onto itself (Sparrow, 1982). It is then no longer possible to find a unique correspondence between unstable periodic orbits and a two-symbol alphabet: four symbols are required. A caricature of this flow is given in Fig. 29(a), along with a template in Fig. 29(b).

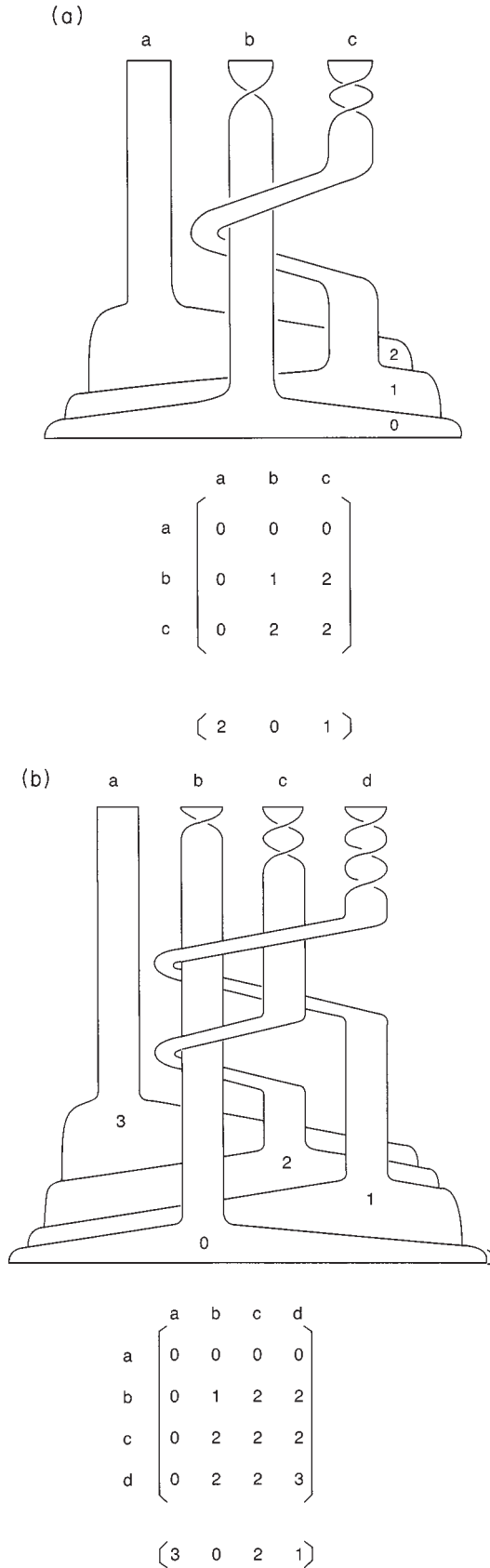


FIG. 28. Rössler template bifurcations. (a) As control parameters in the Rössler equations increase, the flow begins to explore a third template branch. (b) A fourth branch is explored for yet larger values of control parameters. Branches are organized in a systematic way with respect to each other.

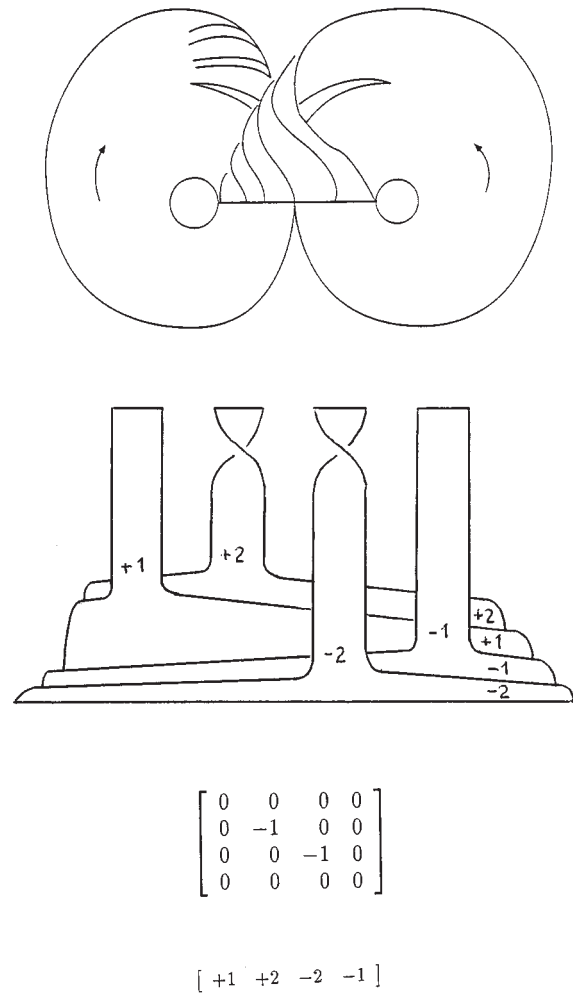


FIG. 29. Lorenz template perestroika. For larger values of the Rayleigh number  $r$  in the Lorenz model, the return flow folds back on itself in a way shown by this caricature. Top: Caricature. Bottom: Template for this flow.

### 3. Duffing dynamics

The attractor generated by the dynamical system

$$\begin{aligned} \dot{x} &= y, \\ \dot{y} &= -\delta y - \partial V / \partial x + b \sin(\phi), \\ \dot{\phi} &= \omega = 2\pi/T \end{aligned} \tag{4.9}$$

will be discussed at length in Sec. XIII. Here,  $V = -1/2 x^2 + 1/4 x^4$  is a function that represents a potential with two minima, or wells, one on the left ( $L$ ), the other on the right ( $R$ ). For a limited range of control parameters there is a  $9 = 3^2$  branch template. That is, the template has an infinite number of branches, only nine of which are explored by the flow. We present a caricature of this flow in Fig. 30(a) and unwind this caricature to produce the template, which is shown in Fig. 30(b). Each symbol consists of a pair [e.g.,  $(\hat{a}\hat{b})$ ], with  $\hat{a}$  indicating a branch in the left well [branches  $(a, b, c)$ ] and  $\hat{b}$  representing a branch in the right well [branches  $(\hat{a}, \hat{b}, \hat{c})$ ]. The template matrix and array are shown for this template.

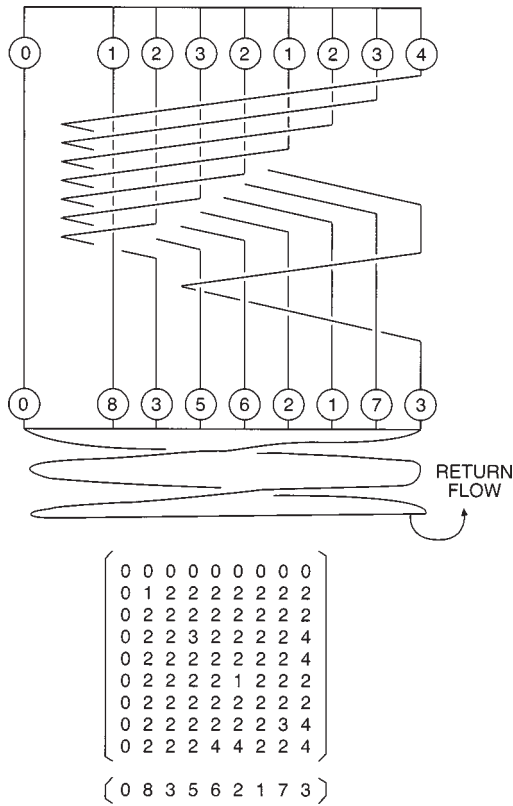


FIG. 30. Top: Caricature for the flow development in the Duffing equations over range of control-parameter values (principally  $T=2\pi/\omega$ ). Bottom: Template for this flow.

4. van der Pol–Shaw dynamics

A modification of the van der Pol equations proposed by Shaw (1981) is

$$\begin{aligned} \dot{x} &= 0.7y + (1.0 - 10y^2)x, \\ \dot{y} &= -x + 0.25 \sin(\phi), \\ \dot{\phi} &= \omega = \pi. \end{aligned} \tag{4.10}$$

Before the attractor is formed, the equations exhibit a Hopf bifurcation (Thompson and Stewart, 1986). This means that the invariant set is a torus  $T^2 = S^1 \times S^1$ . As the nonlinearity is increased, the torus becomes deformed. The action of the flow on the phase space can be described as follows: Part of the torus is pinched out, stretched around the outside of the torus, and then squeezed back into the surface [see Fig. 31(a) for a caricature]. The template associated with this mechanism is shown in Fig. 31(b). With some practice, the discontinuity in the template matrix (0,2,3) can be interpreted in terms of the boundary condition on the original invariant surface ( $T^2 \times R^1$ ) for this equation, as opposed to ( $S^1 \times R^2$ ) for the Duffing oscillator (Mindlin *et al.*, 1990).

5. Cusp catastrophe dynamics

A simple electric circuit originally proposed by Shiriki, Yamamoto, and Mori (1981) was modified and extensively studied by King and Gaito (1992) (see also

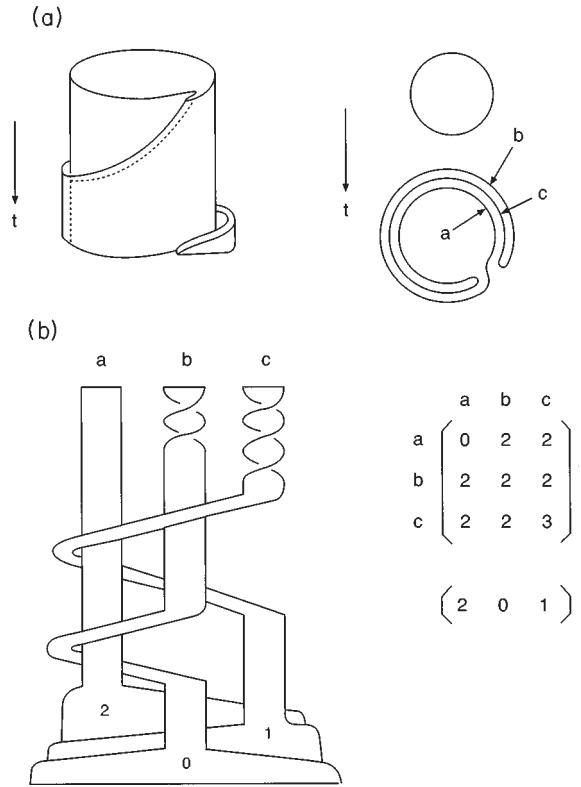


FIG. 31. (a) Caricature of the flow for the van der Pol–Shaw equations in a certain range of parameter values (Thompson and Stewart, 1986). (b) Template.

Gaito and King, 1990). King and Gaito studied the nonlinear circuit shown in the inset to Fig. 32. The voltages  $V_1$  and  $V_2$  are measured across the capacitors  $C_1$  and  $C_2$ ; the current  $I_L$  flows through the resistanceless inductor  $L$ . The resistor  $R$  is linear, while the resistor  $N$  is nonlinear with  $I-V$  characteristic

$$I_N(V) = v + aV + bV^3 \quad a < 0 < b.$$

In terms of scaled variables  $x, y, z$ , defined by

$$\begin{pmatrix} x \\ y \\ z \end{pmatrix} = \sqrt{bR} \begin{pmatrix} V_1 \\ V_2 \\ RI_L \end{pmatrix}, \quad \tau = t/RC_2, \tag{4.11}$$

the dynamical equations of motion are

$$\frac{d}{d\tau} \begin{pmatrix} x \\ y \\ z \end{pmatrix} = \begin{pmatrix} -\frac{1}{m} \left( \frac{d\Phi}{dx} - y \right) \\ x - y - z \\ \beta y \end{pmatrix}. \tag{4.12}$$

The function  $\Phi(x; \alpha, \mu)$  is the cusp catastrophe function

$$\Phi(x; \alpha, \mu) = \frac{1}{4} x^4 - \frac{1}{2} \alpha x^2 + \mu x.$$

This represents a symmetric double-well potential for  $\alpha > 0, \mu = 0$ .

A sequence of bifurcations leading to chaotic behavior that explores both wells in the phase space  $(x, y, z)$  was studied both theoretically and experimentally. The theoretical part of the study involved a qualitative de-

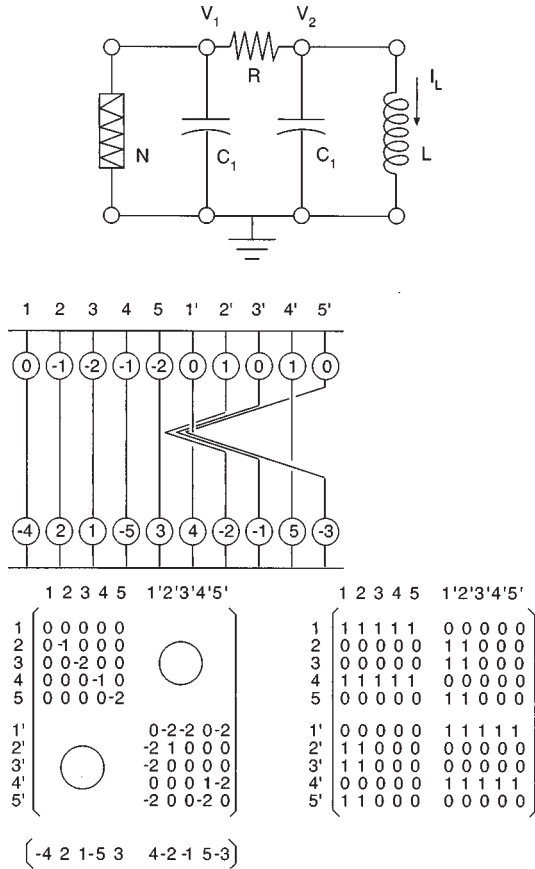


FIG. 32. Template for the branched manifold shown in Fig. 19. The template matrix and array are shown below it (left). The Markov transition matrix is also shown (right).

scription of the dynamical behavior in each of the two wells, as well as a determination of how the motion evolves when the top of the barrier between the two wells is not sufficiently high to isolate each well from the other. On the basis of qualitative arguments backed up by phase-space plots, surfaces of section, and return maps, King and Gaito were able to construct a branched manifold describing the symmetric strange attractor that stretches between the two wells. Their theoretical predictions were supported by experiments carried out on the electric circuit. The branched manifold that they identified is shown in Fig. 19. The corresponding template is shown in Fig. 32.

V. INVARIANTS FROM TEMPLATES

A. Locating periodic orbits

In the construction of branched manifolds by the projection (4.2), the uniqueness theorem is preserved in the forward-time direction. It is lost in the backward-time direction. This remains true in the rearrangement (isotopy) that leads from the branched manifold to its standard representation, the template. Therefore each point in the top branch line of a template (see Fig. 19) is an initial condition for a unique future trajectory. The trajectory is uniquely defined by the template branches that

it evolves through. For example, if a template has branches  $A, B, C, D$ , an initial condition on  $A$  might lead to a trajectory such as  $ABADC\dots$ , which is built from the alphabet  $(A, B, C, D)$ . The following possibilities occur:

- (a) The trajectory consists of an infinite sequence of letters drawn from the small alphabet that labels template branches. This is typical.
- (b) The trajectory is labeled by a finite sequence. This is atypical (nongeneric, a measure zero occurrence). It corresponds to a trajectory in phase space that asymptotically approaches a fixed point in the attractor, or, correspondingly, a tear point in the branched manifold.

In the former case there are again two possibilities:

- (a) The orbit is periodic, of period  $p$ . That is, there is a smallest positive integer  $p$  for which the symbol sequence repeats itself, or has the form  $(\sigma_1\sigma_2\dots\sigma_p)^{\infty}$ , where  $\sigma_i \in \text{alphabet}$ . This is not typical.
- (b) The orbit is not periodic. This is typical.

We concentrate our attention on periodic orbits, since the Birman-Williams theorem guarantees that their topological properties are unchanged under the projection (4.2), and we understand how to compute these properties for periodic orbits in flows.

To compute the topological invariants of periodic orbits in templates we must first locate them on the template. This is relatively easy. The template acts as a one-dimensional map from the top branch to the bottom branch. Periodic orbits for one-dimensional unimodal maps are well understood (Metropolis, Stein, and Stein, 1973; Collet and Eckmann, 1980). Periodic orbits for one-dimensional multimodal maps are more complicated (Block and Coppel, 1992; Alsedà, Llibre, and Misiurewicz, 1993; De Melo and Van Strien, 1993). Their organization can be determined by constructing  $n$ -ary trees (Tuffillaro, Abbott, and Reilly, 1992) or by Kneading Theory (Milnor and Thurston, 1987). We briefly review how Kneading Theory is used to locate orbits on templates.

Assume a template has  $k + 1$  branches, which we label for convenience  $0, 1, 2, \dots, k$  from left to right along the top branch of the template. We define an order along branches:  $a < b$  if  $a$  is to the left of  $b$ . Branch  $i$  is orientation (order) preserving or orientation reversing, depending on whether its local torsion  $T(i, i)$  is even or odd. Passage of two points through a branch of a template preserves or reverses the order of the images  $I(a)$  and  $I(b)$ , depending on whether the branch is orientation preserving [ $a < b \Rightarrow I(a) < I(b)$ ] or orientation reversing [ $a < b \Rightarrow I(a) > I(b)$ ].

An orbit of period  $p$  has symbol sequence

$$\sigma_1\sigma_2\dots\sigma_p \quad \sigma_1\sigma_2\dots\sigma_p \quad \dots \tag{5.1}$$

After one period it advances to

$$\sigma_2\dots\sigma_p\sigma_1 \quad \sigma_2\dots\sigma_p\sigma_1 \quad \dots \tag{5.2}$$

To find the “address” of the initial condition for Eq. (5.1), we conjugate each symbol ( $\sigma_i \rightarrow \bar{\sigma}_i$ ) following any orientation-reversing branch. Conjugation is equivalent to reading from right to left, and given explicitly by

$$\sigma_i + \bar{\sigma}_i = k. \tag{5.3}$$

For example, suppose a template has four branches 0, 1, 2, 3, and branch 1 is orientation reversing. To find the address of 0213 along branch 0, we perform the following simple calculation:

$$\begin{aligned} 0213 \ 0213 \ 0213 \ \dots &\rightarrow 021\bar{3} \ \bar{0}2\bar{1}\bar{3} \ \bar{0}21\bar{3} \ \dots \\ &= 0210 \ 3123 \ 0210 \ \dots \end{aligned} \tag{5.4}$$

The address of (0213) “ $\infty$ ” along branch 0 is given by the infinite sequence (0210 3123) “ $\infty$ ”, which is of period 8. In general, the address of a period- $p$  orbit is a sequence of period  $p$  or  $2p$ , depending on whether the orbit traverses an even or odd number of orientation-reversing branches of the template (i.e., has even or odd parity).

Following this procedure, an address can be computed for each of the  $p$  initial conditions for a period- $p$  orbit:  $\sigma_1\sigma_2\cdots\sigma_p, \sigma_2\cdots\sigma_p\sigma_1, \dots, \sigma_p\sigma_1\sigma_2\cdots$ . The relative location of initial conditions along a template branch is then determined by the order of their addresses in a way whose obviousness would be diminished by additional explanation.

To illustrate, we consider the orbits 01 and 011 on the horseshoe template (Fig. 33):

$$\begin{aligned} 01 &\rightarrow 01 \ 01 \rightarrow 01 \ \bar{0}\bar{1} \rightarrow 01 \ 10 \\ 10 &\rightarrow 10 \ 10 \rightarrow \bar{1}\bar{0} \ \bar{1}\bar{0} \rightarrow 11 \ 00 \\ 011 &\rightarrow 011 \ 011 \rightarrow 01\bar{1} \ 01\bar{1} \rightarrow 010 \ 010 \\ 110 &\rightarrow 110 \ 110 \rightarrow 1\bar{1}\bar{0} \ 1\bar{1}\bar{0} \rightarrow 100 \ 100 \\ 101 &\rightarrow 101 \ 101 \rightarrow 1\bar{0}\bar{1} \ 1\bar{0}\bar{1} \rightarrow 110 \ 110 \end{aligned}$$

In Fig. 33 we show how the five strands of these two orbits of period two and three are draped over the horseshoe template.

**B. Topological invariants**

The addresses of initial conditions are used to locate orbits on templates. This information is then used to compute the topological invariants of these orbits.

**1. Linking numbers**

To compute the linking numbers for two orbits, it is sufficient to compute the signed number of crossings of these two orbits on their knot holder and divide by two. Computation of self-linking numbers is even easier: it is sufficient to add the local torsion for each symbol in the sequence.

This algorithm for computing addresses and counting crossings has been reduced to a FORTRAN code (available from the author on request). The inputs to this code are template information (a template matrix and array)

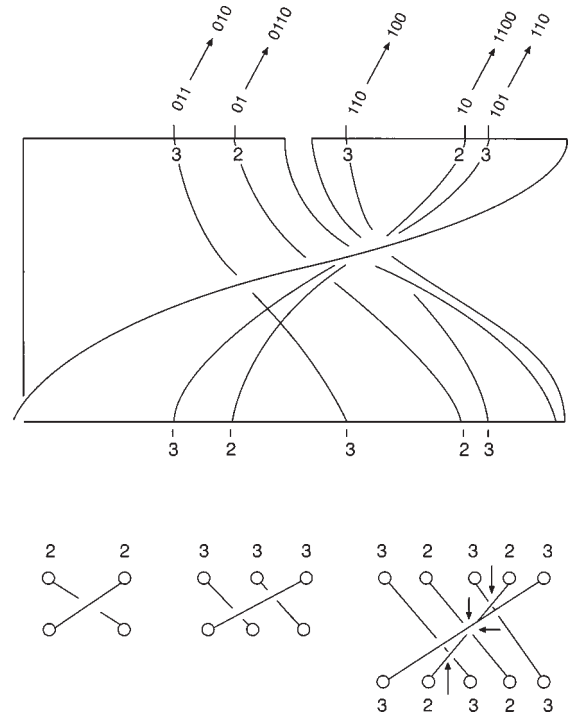


FIG. 33. Period-two and period-three orbits on the horseshoe template. Their locations are determined by comparing their addresses. By inspection,  $SL(01) = +1$ ,  $SL(011) = +2$ , and  $L(01,011) = +2$ .

and orbit information (a list of periodic orbits identified by period and symbolic dynamics). The output consists of a table of linking numbers.

In Table I we present the linking and self-linking numbers for orbits of period up to five on a right-handed horseshoe (Rössler) template. The branches are labeled 0,1. There are two orbits of period one (0,1), one of period two (01), two of period three (001,011), and three, six, . . . of periods four, five, . . .

Right-handed Horseshoe	Right-handed Lorenz	
$\begin{bmatrix} 0 & 0 \\ 0 & +1 \\ 0 & -1 \end{bmatrix}$	$\begin{bmatrix} 0 & 0 \\ 0 & 0 \\ 0 & -1 \end{bmatrix}$	(5.5)

In Table II we present the linking and self-linking numbers for orbits of period up to five on a right-handed Lorenz template. The branches are labeled  $L,R$ . Both are orientation preserving. Therefore the address is identical to the orbit symbol. The number of orbits of any period is the same in both templates, under the correspondence  $0 \leftrightarrow L, 1 \leftrightarrow R$ . However, addresses and therefore linking numbers are not the same because branch 1 in the horseshoe template is orientation reversing.

**2. Relative rotation rates**

Computation of relative rotation rates follows a very similar algorithm. Two orbits of periods  $p_A$  and  $p_B$  are

TABLE I. Linking numbers for orbits to period 5 on the right-handed Smale horseshoe template.

		1 <sub>1</sub>	1 <sub>1</sub>	2 <sub>1</sub>	3 <sub>1</sub>	3 <sub>1</sub>	4 <sub>1</sub>	4 <sub>2</sub>	4 <sub>2</sub>	5 <sub>1</sub>	5 <sub>1</sub>	5 <sub>2</sub>	5 <sub>2</sub>	5 <sub>3</sub>	5 <sub>3</sub>
1 <sub>1</sub>	0	0	0	0	0	0	0	0	0	0	0	0	0	0	0
1 <sub>1</sub>	1	0	0	1	1	1	2	1	1	2	2	2	2	1	1
2 <sub>1</sub>	01	0	1	1	2	2	3	2	2	4	4	3	3	2	2
3 <sub>1</sub>	011	0	1	2	2	3	4	3	3	5	5	5	5	3	3
3 <sub>1</sub>	001	0	1	2	3	2	4	3	3	5	5	4	4	3	3
4 <sub>1</sub>	0111	0	2	3	4	4	5	4	4	8	8	7	7	4	4
4 <sub>2</sub>	0011	0	1	2	3	3	4	3	4	5	5	5	5	4	4
4 <sub>2</sub>	0001	0	1	2	3	3	4	4	3	5	5	5	5	4	4
5 <sub>1</sub>	01111	0	2	4	5	5	8	5	5	8	10	9	9	5	5
5 <sub>1</sub>	01101	0	2	4	5	5	8	5	5	10	8	8	8	5	5
5 <sub>2</sub>	00111	0	2	3	5	4	7	5	5	9	8	6	7	5	5
5 <sub>2</sub>	00101	0	2	3	5	4	7	5	5	9	8	7	6	5	5
5 <sub>3</sub>	00011	0	1	2	3	3	4	4	4	5	5	5	5	4	5
5 <sub>3</sub>	00001	0	1	2	3	3	4	4	4	5	5	5	5	5	4

draped over the template. Two initial conditions are joined by an oriented line segment, and the number of half twists that this segment undergoes as it evolves through  $p_A \times p_B$  forward iterations is counted. This integer is divided by  $2p_A \times p_B$ . This calculation is then repeated for all other initial conditions. This bookkeeping has also been reduced to a FORTRAN code, which is available from the author on request. The inputs are the same as for the linking-number computation. The output is a table of relative rotation rates. The relative rotation rates for all orbits to period five on a right-handed horseshoe template are presented in Table III.

The relative rotation rates and linking numbers of orbits generated in a period-doubling cascade based on a period- $p$  orbit have systematic properties, which have been described by Solari and Gilmore (1988). Their systematics account for many previously derived results (Uezu and Aizawa, 1982; Beiersdorfer, Wersinger, and Treve, 1983; Uezu, 1983). In Table IV we present the relative rotation rates for the orbits to period 16 in the

cascade based on the period-one orbit (1) in the Smale horseshoe. In Table V we present the linking numbers for these orbits.

C. Dynamical invariants

Topological entropy estimates the rate of growth in the number of orbits of period  $p$ ,  $N(p)$ , as  $p$  increases. For a fully expansive template on  $K$  branches,

$$N(p) \sim \frac{1}{p} K^p \sim e^{ph_T}.$$

As a result

$$h_T = \lim_{p \rightarrow \infty} \frac{1}{p} \ln N(p) = \ln K.$$

For example, the topological entropy of the two-branched Rössler and Lorenz templates is  $\ln 2$ .

TABLE II. Linking numbers for orbits to period 5 on the right-handed Lorenz template.

		1 <sub>1</sub>	1 <sub>1</sub>	2 <sub>1</sub>	3 <sub>1</sub>	3 <sub>1</sub>	4 <sub>1</sub>	4 <sub>2</sub>	4 <sub>2</sub>	5 <sub>1</sub>	5 <sub>1</sub>	5 <sub>2</sub>	5 <sub>2</sub>	5 <sub>3</sub>	5 <sub>3</sub>
1 <sub>1</sub>	<i>L</i>	0	0	0	0	0	0	0	0	0	0	0	0	0	0
1 <sub>1</sub>	<i>R</i>	0	0	0	0	0	0	0	0	0	0	0	0	0	0
2 <sub>1</sub>	<i>LR</i>	0	0	1	1	1	1	2	1	1	2	2	2	2	1
3 <sub>1</sub>	<i>LRR</i>	0	0	1	2	1	2	2	1	2	3	3	2	2	1
3 <sub>1</sub>	<i>LLR</i>	0	0	1	1	2	1	2	2	1	2	2	3	3	2
4 <sub>1</sub>	<i>LRRR</i>	0	0	1	2	1	3	2	1	3	3	3	2	2	1
4 <sub>2</sub>	<i>LLRR</i>	0	0	2	2	2	2	3	2	2	4	3	4	3	2
4 <sub>2</sub>	<i>LLLRR</i>	0	0	1	1	2	1	2	3	1	2	2	3	3	3
5 <sub>1</sub>	<i>LRRRR</i>	0	0	1	2	1	3	2	1	4	3	3	2	2	1
5 <sub>1</sub>	<i>LRRLR</i>	0	0	2	3	2	3	4	2	3	6	5	4	4	2
5 <sub>2</sub>	<i>LLRRR</i>	0	0	2	3	2	3	3	2	3	5	4	4	3	2
5 <sub>2</sub>	<i>LLRLR</i>	0	0	2	2	3	2	4	3	2	4	4	6	5	3
5 <sub>3</sub>	<i>LLLRR</i>	0	0	2	2	3	2	3	3	2	4	3	5	4	3
5 <sub>3</sub>	<i>LLLLR</i>	0	0	1	1	2	1	2	3	1	2	2	3	3	4

TABLE III. Relative rotation rates for orbits to period 5 on the right-handed Smale horseshoe template.

	1 <sub>1</sub>	2 <sub>1</sub>	3 <sub>1</sub>	3 <sub>1</sub>	4 <sub>1</sub>	4 <sub>2</sub>	4 <sub>2</sub>	5 <sub>1</sub>	5 <sub>1</sub>	5 <sub>2</sub>	5 <sub>2</sub>	5 <sub>3</sub>	5 <sub>3</sub>
	1	01	011	001	0111	0011	0001	01111	01101	00111	00101	00011	00001
1 <sub>1</sub>	0												
2 <sub>1</sub>	$\frac{1}{2}$	$\frac{1}{2}0$											
3 <sub>1</sub>	$\frac{1}{3}$	$\frac{1}{3}$	$(\frac{1}{3})^2 0$										
3 <sub>1</sub>	$\frac{1}{3}$	$\frac{1}{3}$	$\frac{1}{3}$	$(\frac{1}{3})^2 0$									
4 <sub>1</sub>	$\frac{1}{2}$	$\frac{11}{24}$	$\frac{1}{3}$	$\frac{1}{3}$	$(\frac{1}{2})^2 \frac{1}{4} 0$								
4 <sub>2</sub>	$\frac{1}{4}$	$\frac{1}{4}$	$\frac{1}{4}$	$\frac{1}{4}$	$\frac{1}{4}$	$(\frac{1}{4})^3 0$							
4 <sub>2</sub>	$\frac{1}{4}$	$\frac{1}{4}$	$\frac{1}{4}$	$\frac{1}{4}$	$\frac{1}{4}$	$\frac{1}{4}$	$(\frac{1}{4})^3 0$						
5 <sub>1</sub>	$\frac{2}{5}$	$\frac{2}{5}$	$\frac{1}{3}$	$\frac{1}{3}$	$\frac{2}{5}$	$\frac{1}{4}$	$\frac{1}{4}$	$(\frac{2}{5})^4 0$					
5 <sub>1</sub>	$\frac{2}{5}$	$\frac{2}{5}$	$\frac{1}{3}$	$\frac{1}{3}$	$\frac{2}{5}$	$\frac{1}{4}$	$\frac{1}{4}$	$\frac{2}{5}$	$(\frac{2}{5})^4 0$				
5 <sub>2</sub>	$\frac{2}{5}$	$\frac{3}{10}$	$\frac{1}{3}$	$\frac{4}{15}$	$\frac{7}{20}$	$\frac{1}{4}$	$\frac{1}{4}$	$(\frac{2}{5})^4 \frac{1}{5}$	$(\frac{2}{5})^3 \frac{1}{5}^2$	$(\frac{2}{5})^2 (\frac{1}{5})^2 0$			
5 <sub>2</sub>	$\frac{2}{5}$	$\frac{3}{10}$	$\frac{1}{3}$	$\frac{4}{15}$	$\frac{7}{20}$	$\frac{1}{4}$	$\frac{1}{4}$	$(\frac{2}{5})^4 \frac{1}{5}$	$(\frac{2}{5})^3 (\frac{1}{5})^2$	$(\frac{2}{5})^2 (\frac{1}{5})^3$	$(\frac{2}{5})^2 (\frac{1}{5})^2 0$		
5 <sub>3</sub>	$\frac{1}{5}$	$\frac{1}{5}$	$\frac{1}{5}$	$\frac{1}{5}$	$\frac{1}{5}$	$\frac{1}{5}$	$\frac{1}{5}$	$\frac{1}{5}$	$\frac{1}{5}$	$\frac{1}{5}$	$\frac{1}{5}$	$(\frac{1}{5})^4 0$	
5 <sub>3</sub>	$\frac{1}{5}$	$\frac{1}{5}$	$\frac{1}{5}$	$\frac{1}{5}$	$\frac{1}{5}$	$\frac{1}{5}$	$\frac{1}{5}$	$\frac{1}{5}$	$\frac{1}{5}$	$\frac{1}{5}$	$\frac{1}{5}$	$\frac{1}{5}$	$(\frac{1}{5})^4 0$

Strange attractors almost always are not hyperbolic and the flow is not fully expansive on the template. Under these conditions, the flow is described by a Markov transition matrix  $M$ . The number of orbits of period  $p$  is then estimated by

$$N(p) \sim \frac{1}{p} \text{Tr } M^p. \tag{5.6}$$

If the eigenvalues of the matrix  $M$  are  $\lambda_1 \geq \lambda_2 \geq \dots$ , then the trace is well approximated by  $\text{Tr } M^p \sim \lambda_1^p$ . As a result, the topological entropy is the logarithm of the largest eigenvalue of the transition matrix  $M$ . For fully expansive templates, all matrix elements of the transition matrix are +1 and the matrix has rank 1 with eigenvalues  $K$  and 0 ( $K-1$  fold degenerate). In the general case the eigenvalues can be computed using the subroutine HQR in *Numerical Recipes* (Press *et al.*, 1986).

D. Inflating a template

It is sometimes useful to “inflate” a template to get a better approximation of the original dynamics. This is

TABLE IV. Relative rotation rates for the period-doubling cascade in the Smale horseshoe template, assuming zero global torsion. The fractions are  $t_1 = \frac{1}{2}$ ,  $t_2 = \frac{1}{4}$ ,  $t_3 = \frac{3}{8}$ ,  $t_4 = \frac{5}{16}$ . This table can be extended in the obvious way with  $t_5 = \frac{11}{32}$ ,  $t_6 = \frac{21}{64}$ . The torsions obey the Fibonacci relation  $2t_{n+1} = t_n + t_{n-1}$ .

$k$	Period	0	1	2	3	4
		1	2	4	8	16
0	1	0	$t_1$	$t_1$	$t_1$	$t_1$
1	2	$t_1$	$t_1 0$	$t_1 t_2$	$t_1 t_2$	$t_1 t_2$
2	4	$t_1$	$t_1 t_2$	$t_1^2 t_2 0$	$t_1^2 t_2 t_3$	$t_1^2 t_2 t_3$
3	8	$t_1$	$t_1 t_2$	$t_1^2 t_2 t_3$	$t_1^4 t_2^2 t_3 0$	$t_1^4 t_2^2 t_3 t_4$
4	16	$t_1$	$t_1 t_2$	$t_1^2 t_2 t_3$	$t_1^4 t_2^2 t_3 t_4$	$t_1^8 t_2^4 t_3^2 t_4 0$

done by expanding the branch lines to “branch rectangles” in the strongly contracting direction. In Fig. 34 a two-branch template is expanded to a mapping  $R^2 \rightarrow R^2$ . To do this, the negative Lyapunov exponent  $\lambda_3$ , whose limit is  $-\infty$  in the template construction, is allowed to be finite. The Lyapunov exponents for the map  $R^2 \rightarrow R^2$  are then  $\mu \sim \pm e^{\lambda_1 T}$  and  $\nu \sim \pm e^{\lambda_3 T}$ , with  $|\mu| > 1 > |\nu| > 0$  and  $T$  as the return-flow time.

Periodic orbits in the mapping  $R^2 \rightarrow R^2$  can be located by a method somewhat more involved than the Kneading Theory construction: forward and backward iterates are constructed. Their intersection defines a fractal in  $R^2$ . The construction is carried out explicitly for the two-branch mapping associated with a Smale (1967) horseshoe in great detail by Guckenheimer and Holmes (1983). The intersections of the forward and backward iterates provide addresses for all orbits in the flow and map. Needless to say, topological invariants remain invariant under inflation.

VI. UNFOLDING A TEMPLATE

“Unfolding” is a technical term for a beautiful idea. An unfolding summarizes all possible consequences of

TABLE V. Linking numbers for the period-doubling cascade in the Smale horseshoe template, assuming zero global torsion.

		0	1	2	3	4	5
$k$	Period	1	2	4	8	16	32
0	1	0	1	2	4	8	16
1	2	1	1	3	6	12	24
2	4	2	3	5	13	26	52
3	8	4	6	13	23	51	102
4	16	8	12	26	51	97	205
5	32	16	24	52	102	205	399

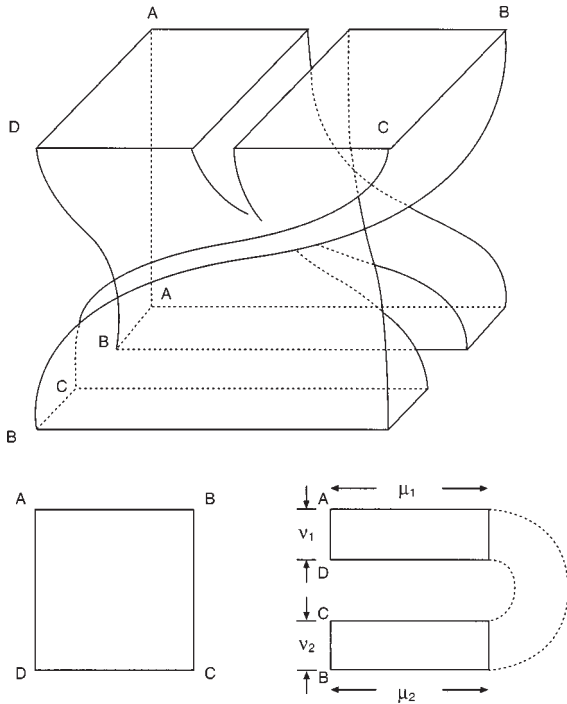


FIG. 34. Template inflation. A two-branch template is inflated by expanding against the strongly contracting direction. The result provides a map  $R^2 \rightarrow R^2$ .

the most general possible perturbation. The concept is fundamental to the discussion of singularities (Arnol'd, 1968, 1975; Golubitsky and Guillemin, 1973; Thom, 1975; Zeeman, 1977; Poston and Stewart, 1978; Gilmore, 1981). We give a simple example: The potential  $V(x) = \frac{1}{4}x^4$  is singular at  $x=0$  because  $\partial V/\partial x=0$  and  $\partial^2 V/\partial x^2=0$  at  $x=0$ . An arbitrary perturbation of this potential, in the neighborhood of  $x=0$ , has the form

$$V(x) + \text{arbitrary perturbation} = \frac{1}{4}x^4 + \frac{1}{2}ax^2 + bx = V(x;a,b). \quad (6.1)$$

The two-parameter function  $\frac{1}{2}ax^2 + bx$  is called the universal perturbation of the singular function  $\frac{1}{4}x^4$  and the two-parameter family of functions  $V(x;a,b)$  is called the unfolding of the singular potential.

What does unfolding have to do with templates? We shall use the spirit behind this concept to enrich our understanding of dynamical systems. Templates have been introduced to describe hyperbolic attractors. We have stretched the interpretation of template so that these structures actually represent nonhyperbolic attractors. A  $K$ -branched template supports all periodic orbits that can be constructed from  $K$  symbols. A strange attractor does not typically support this complete spectrum of unstable periodic orbits. Many orbits have been "pruned" away (Cvitanovic, Gunaratne, and Procaccia, 1988). However, this pruning is subject to strict rules of a topological nature. More specifically, if some periodic orbits are present in an attractor, they force the presence of others. Unfolding a template amounts to constructing the forcing rules for the periodic orbits that the

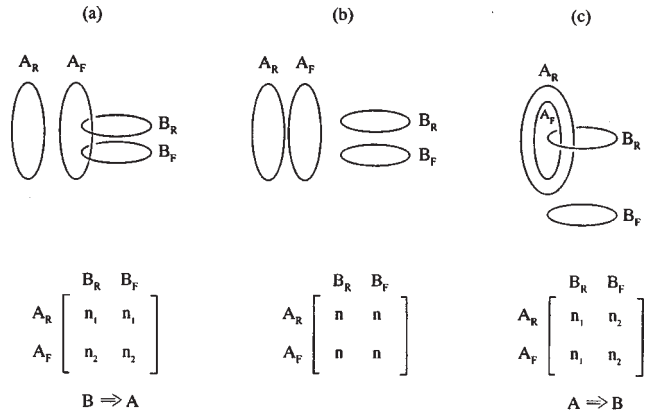


FIG. 35. Topological nature of forcing. Linking numbers of two saddle-node pairs can be used to determine if one pair of orbits forces another.

template contains. We illustrate this idea for the Smale horseshoe template, where the results are the most complete.

### A. Topological restrictions

As control parameters for a dynamical system are varied, periodic orbits are created (or annihilated) in either saddle-node or period-doubling bifurcations. Suppose we have two saddle-node pairs of orbits  $\{A_R, A_F\}$  and  $\{B_R, B_F\}$ . Here  $R$  refers to the regular saddle and  $F$  to the flip saddle. These saddles have even and odd parity, respectively.

In computing the linking numbers of the orbit pair  $\{A_R, A_F\}$  with the orbit pair  $\{B_R, B_F\}$ , three possibilities occur. These are summarized in Fig. 35. Since linking numbers cannot change while the orbits exist, the three possibilities in Fig. 35 show the following:

- (a) The pair  $\{A_R, A_F\}$  cannot undergo an inverse saddle-node bifurcation until the orbit pair  $\{B_R, B_F\}$  does. Conversely,  $\{B_R, B_F\}$  cannot be created in a saddle-node bifurcation until the orbit pair  $\{A_R, A_F\}$  already exists. We summarize this situation by saying  $B$  "forces"  $A$  and writing  $B \Rightarrow A$ .
- (b) Neither orbit pair forces the other.
- (c)  $A \Rightarrow B$ .

Period-doubling bifurcations can be treated similarly. If  $M$  and  $D$  are a mother-daughter pair of orbits, then  $M$  has period  $p$  and  $D$  has period  $2p$ . Both have odd parity. The orbits  $M^2 = MM$  (the  $p$  symbols of  $M$  are repeated twice) and  $D$  can then be treated like  $A_R$  and  $A_F$  in the procedure described above.

The forcing relationship is transitive:

$$\text{if } A \Rightarrow B \text{ and } B \Rightarrow C \text{ then } A \Rightarrow C. \quad (6.2)$$

This is suggested in Fig. 36.

However, there are some complications. If the two orbit pairs  $\{B_R, B_F\}$  and  $\{C_R, C_F\}$  have the same braid type (Birman, 1975; Rolfson, 1976; Kaufman, 1987; Hall,

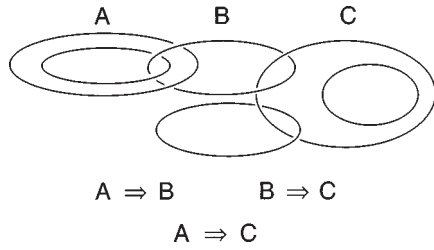


FIG. 36. Transitive nature of forcing. If  $A \Rightarrow B$  and  $B \Rightarrow C$ , then  $A \Rightarrow C$ .

1991, 1993, 1994a, 1994b; Tufillaro, Abbott, and Reilly, 1992), then it is possible for these orbits to rearrange themselves as control parameters are varied and for  $\{B_R, C_F\}$  and  $\{C_R, B_F\}$  to undergo saddle-node bifurcations. That is, if  $A \Rightarrow B$  and  $A \Rightarrow C$  but  $B$  and  $C$  have the same braid type, it is possible that  $A$  forces neither  $B$  nor  $C$  by exchange elimination (Mindlin *et al.*, 1993). This process is summarized in Fig. 37.

**B. Forcing diagram**

The topological arguments outlined above can be applied to periodic orbits on any template. They have been carried out in detail only for the Smale horseshoe tem-

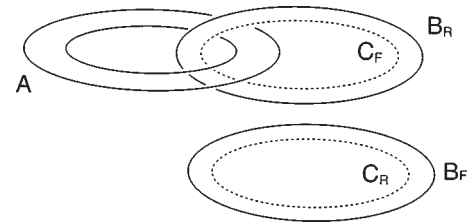


FIG. 37. Complicated nature of forcing. If orbits  $B$  and  $C$  have the same braid type, the orbit pairs may exchange partners. Then  $A$  forces neither  $B$  nor  $C$  if both exist, while it forces one saddle-node pair if the other does not exist.

plate. This is in part because the calculations are very difficult, but also in part because this particular template occurs so often in physical systems.

The forcing diagram for orbits up to period eight on the horseshoe template is shown in Fig. 38. All orbits to period eight have been summarized in Table VI, along with their salient properties. These orbits are identified as  $P_j$ , where  $P$  is the period of the orbit and  $j$  indicates the order of occurrence of this orbit in unimodal maps of the interval, including the logistic map (Metropolis, Stein, and Stein, 1973). The orbits in the Smale horseshoe template exist in 1-1 correspondence with periodic orbits in the logistic map  $x' = \lambda x(1-x)$  for  $\lambda = 4$ . As a

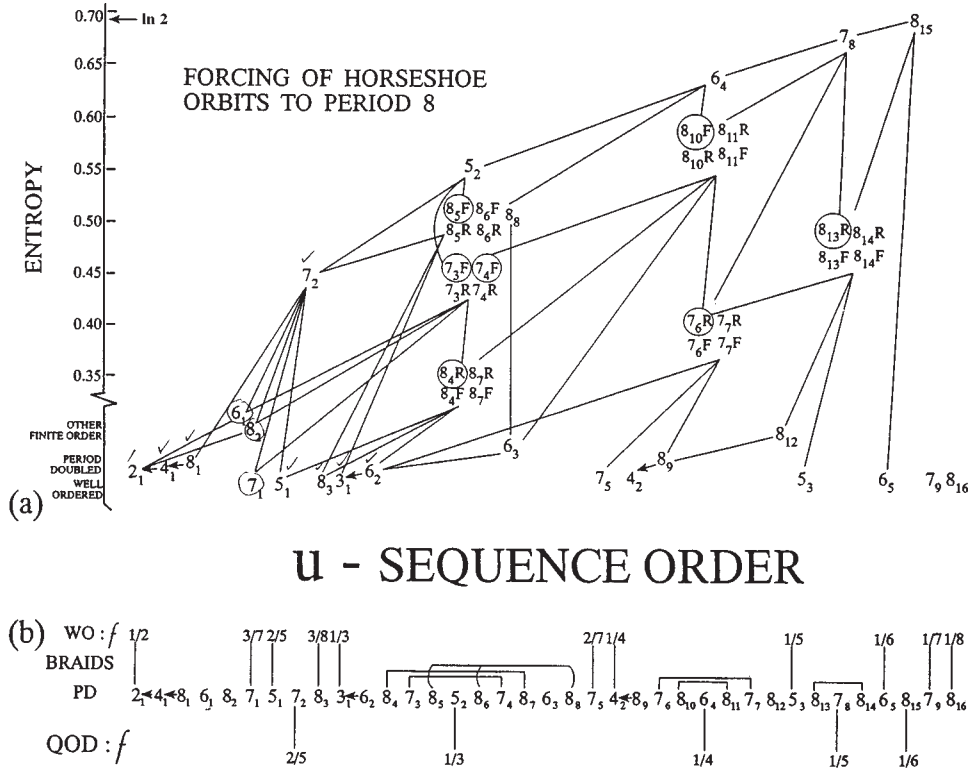


FIG. 38. (a) Orbit-forcing diagram for horseshoe dynamics. The orbits and their properties are described in Table VI. Orbits are organized (approximately) by one-dimensional entropy (horizontal axis) and topological entropy (vertical axis). Small distortions are present to make the diagram more readable. Well-ordered, period-doubled, and finite-order orbits all have zero topological entropy, but are slightly offset at the bottom of the figure, again for clarity. The backbone of the diagram consists of well-ordered orbits and quasi-one-dimensional orbits, both of which exist in 1-1 correspondence with rational fractions  $f$  in the interval  $0 < f < 1/2$ . Only first-order forcing is shown. (b) Orbits in order of their appearance in one-dimensional maps of the interval. Also shown: fractional values for well-ordered orbits, for quasi-one-dimensional orbits, and for orbits with same braid type.

TABLE VI. Horseshoe orbits to period 8. Orbits are identified as  $P_j$ , where  $P$  is the period and  $j$  is the order of appearance of the orbit in unimodal maps of the interval. Underlined symbols are 1 or 0 for regular saddles (even parity) or flip saddles (odd parity). PD=period doubled; WO=well ordered; FO=finite order; PE=positive entropy; QOD=quasi one dimensional.

Orbit	Symbol sequence	Type	Fraction	One-dimensional entropy	Topological entropy
1 <sub>1</sub>	1	1F		0	0
2 <sub>1</sub>	01	PD of 1F		0	0
3 <sub>1</sub>	0 <u>1</u> 1	WO	1/3	0.481 212	0
4 <sub>1</sub>	0111	PD of 2 <sub>1</sub>		0	0
4 <sub>2</sub>	00 <u>1</u> 1	WO	1/4	0.609 378	0
5 <sub>1</sub>	011 <u>1</u> 1	WO	2/5	0.414 013	0
5 <sub>2</sub>	001 <u>1</u> 1	QOD	1/3	0.543 535	0.543 535
5 <sub>3</sub>	000 <u>1</u> 1	WO	1/5	0.656 256	0
6 <sub>1</sub>	011 <u>1</u> <u>1</u> 1	FO		0.240 606	0
6 <sub>2</sub>	001 0 <u>1</u> 1	PD of 3 <sub>1</sub>		0.481 212	0
6 <sub>3</sub>	001 <u>1</u> <u>1</u> 1	FO		0.583 557	0
6 <sub>4</sub>	00 <u>1</u> <u>1</u> 1	QOD	1/4	0.632 974	0.632 974
6 <sub>5</sub>	000 <u>0</u> <u>1</u> 1	WO	1/6	0.675 975	0
7 <sub>1</sub>	011 1 <u>1</u> <u>1</u> 1	WO	3/7	0.382 245	0
7 <sub>2</sub>	011 0 <u>1</u> <u>1</u> 1	QOD	2/5	0.442 138	0.442 138
7 <sub>3</sub>	001 0 <u>1</u> <u>1</u> 1	PE		0.522 315	0.476 818
7 <sub>4</sub>	001 1 <u>1</u> <u>1</u> 1	PE		0.562 400	0.476 818
7 <sub>5</sub>	001 10 <u>1</u> 1	WO	2/7	0.601 001	0
7 <sub>6</sub>	000 10 <u>1</u> 1	PE		0.618 362	0.382 245
7 <sub>7</sub>	000 1 <u>1</u> <u>1</u> 1	PE		0.645 710	0.382 245
7 <sub>8</sub>	000 <u>0</u> <u>1</u> <u>1</u> 1	QOD	1/5	0.666 215	0.666 215
7 <sub>9</sub>	000 <u>0</u> <u>0</u> <u>1</u> 1	WO	1/7	0.684 905	0
8 <sub>1</sub>	0111 0 <u>1</u> 01	PD of 4 <sub>1</sub>		0	0
8 <sub>2</sub>	011 1 <u>1</u> 1 <u>1</u> 1	FO		0.304 688	0
8 <sub>3</sub>	011 0 <u>1</u> 1 <u>1</u> 1	WO	3/8	0.468 258	0
8 <sub>4</sub>	001 0 <u>1</u> 1 <u>1</u> 1	PE		0.499 747	0.346 034
8 <sub>5</sub>	001 0 <u>1</u> 0 <u>1</u> 1	PE		0.539 792	0.498 093
8 <sub>6</sub>	001 1 <u>1</u> 0 <u>1</u> 1	PE		0.547 612	0.498 093
8 <sub>7</sub>	001 1 <u>1</u> 1 <u>1</u> 1	PE		0.574 865	0.346 034
8 <sub>8</sub>	001 10 <u>1</u> <u>1</u> 1	PE		0.591 718	0.498 093
8 <sub>9</sub>	0001 0 <u>0</u> 11	PD of 4 <sub>2</sub>		0.609 378	0
8 <sub>10</sub>	000 10 <u>1</u> <u>1</u> 1	PE		0.626 443	0.568 666
8 <sub>11</sub>	000 1 <u>1</u> 1 <u>1</u> 1	PE		0.639 190	0.568 666
8 <sub>12</sub>	000 1 <u>1</u> 0 <u>1</u> 1	FO		0.651 766	0
8 <sub>13</sub>	000 <u>0</u> <u>1</u> 0 <u>1</u> 1	PE		0.660 791	0.458 911
8 <sub>14</sub>	000 <u>0</u> <u>1</u> 1 <u>1</u> 1	PE		0.671 317	0.458 911
8 <sub>15</sub>	000 <u>0</u> <u>0</u> <u>1</u> <u>1</u> 1	QOD	1/6	0.680 477	0.680 477
8 <sub>16</sub>	000 <u>0</u> <u>0</u> <u>0</u> <u>1</u> 1	WO	1/8	0.689.121	0

result, an enormous amount is known about the properties of these orbits.

The orbits in the logistic map are created in a particular order, which is determined by Kneading Theory. This order is called the  $U$ -sequence (universal) order (Metropolis, Stein, and Stein, 1973). As a result, an entropy can be associated with every orbit—this is called the orbit’s one-dimensional entropy. An entropy can also be associated with each orbit as an orbit in a two-dimensional map or three-dimensional flow. This is the topological entropy. It has been defined earlier [see (5.6)]. The one-dimensional entropy is an upper bound

on an orbit’s topological entropy; they are different except for a set of orbits identified by rational fractions  $m/n$  in the interval  $0 < m/n < \frac{1}{2}$  (Hall, 1993).

Five classes of orbits occur in Table VI and Fig. 38. These can be distinguished by their topological entropy, as follows.

1. Zero-entropy orbits

*Well-ordered orbits.* These do not force any other orbits except  $1R, 1F$ . These orbits are torus knots (Holmes, 1986). Each well-ordered orbit is identified by

an irreducible rational fraction  $0 < p/(q+2p) < \frac{1}{2}$  (irreducible means that  $p$  and  $q+2p$  have no common factors larger than 1). The orbit has period  $P=q+2p$  and is built up from a symbol sequence

$$W(1)W(2)\cdots W(q+p)$$

$$W(i) = \begin{cases} 0 \\ 11 \end{cases} \text{ if } [im] - [(i-1)m] = \begin{cases} 0 \\ 1 \end{cases}, \quad (6.3)$$

where  $m=p/(q+p)$ ,  $1 \leq i \leq q+p$ , and  $[x]$  is the integer part of  $x$ . For example, the well-ordered orbits of period eight correspond to the rational fractions  $\frac{1}{8}$  and  $\frac{3}{8}$  ( $\frac{2}{8}$  is not irreducible) and are ( $\frac{3}{8}$ :  $8_3=011\ 011\ \underline{11}$ ) and ( $\frac{1}{8}$ :  $8_{16}=000\ 000\ \underline{11}$ ). The symbol sequence for the regular saddle is given. It has even parity. The symbol sequence for its saddle partner in one-dimensional maps is obtained by changing the symbol  $\underline{1}$  to 0. This node or flip saddle has odd parity. Well-ordered orbits are easily recognized by their self-relative rotation rates, all of which have the same fractional value  $p/(q+2p)$ .

*Period-doubled orbits.* Each daughter orbit forces its mother, grandmother, . . . , and its regular saddle grand patriarch. By the transitivity result (Fig. 36), it is sufficient to indicate only daughter-mother forcing, as in the cases  $8_1 \Rightarrow 4_1 \Rightarrow 2_1$ ,  $6_3 \Rightarrow 3_1$ , and  $8_9 \Rightarrow 4_2$  shown in the forcing diagram. Period-doubled orbits can also easily be recognized by their relative and self-relative rotation rates. The systematics of these fractions have been discussed in detail by Solari and Gilmore (1988).

*Finite-order orbits.* These orbits have zero topological entropy because the number of orbits that they force grows only algebraically (not exponentially) with increasing period. These orbits, to period eight in Fig. 38, are  $6_1$ ,  $8_2$ ,  $6_3$ , and  $8_{12}$ .

2. Positive-entropy orbits

*Quasi-one-dimensional orbits.* These orbits force exactly the same spectrum of orbits in two-dimensional maps as they do in one-dimensional maps (Hall, 1991, 1993). Therefore their topological entropy is exactly equal to their one-dimensional entropy. Like well-ordered orbits, there is a 1-1 correspondence between quasi-one-dimensional orbits and irreducible rational fractions  $0 < f = m/n < \frac{1}{2}$ . To each such fraction there is a saddle-node pair of quasi-one-dimensional orbits of period  $n+2$ , with symbolic dynamics

$$0^{\kappa_1(f)}11 \quad 0^{\kappa_2(f)}11\cdots \quad 0^{\kappa_m(f)}111,$$

$$\kappa_1(f) = [1/f] - 1 = [n/m] - 1,$$

$$\kappa_i(f) = [i/f] - [(i-1)/f] - 2, \quad 2 \leq i \leq m. \quad (6.4)$$

For example, for period eight,  $n=6$ , the only irreducible fraction is  $1/6$ , and the quasi-one-dimensional orbit for  $f = \frac{1}{6}$  is ( $\frac{1}{6}$ :  $8_{15}=000\ 001\ \underline{11}$ ).

*All the rest.* All other orbits not described so far obey  $0 < h_T < \text{one-dimensional entropy}$ .

For these orbits, two or more saddle-node pairs belong to the same braid type and can therefore undergo exchange elimination. Orbits that belong to the same

braid type are identified by their spectrum of self-relative rotation rates. They also have the same period and topological entropy. To period eight, there are six such groupings:  $\{8_4, 8_7\}$ ,  $\{7_6, 7_7\}$ ,  $\{8_{13}, 8_{14}\}$ ,  $\{7_3, 7_4\}$ ,  $\{8_5, 8_6, 8_8\}$ , and  $\{8_{10}, 8_{11}\}$ . The self-relative rotation rates are sufficient to distinguish braid type to period 10 but not period 11.

Through period eight, orbit forcing in the horseshoe is shown in Fig. 38. The orbits are located in this figure according to their  $U$ -sequence order (one-dimensional entropy) along the horizontal axis and their topological entropy along the vertical axis. Only the ‘‘first-order’’ forcings have been indicated. This is sufficient by transitivity. This shows, for example,  $6_4 \Rightarrow 8_{10} F \Rightarrow 8_4 R \Rightarrow 5_1$ . The one-dimensional entropy was computed using an algorithm by Block *et al.* (1980). The topological entropy was computed using algorithms developed by Bestvina and Handel (1992) and Los (1993).

In Fig. 38(b) we list all orbits to period eight by increasing one-dimensional entropy. We also indicate the rational fractional value for the well-ordered orbits and the quasi-one-dimensional orbits. Finally, we indicate orbit multiplets of the same braid type.

The forcing diagram is the unfolding of the horseshoe template to period eight. This diagram describes all possible combinations of orbits that can be found in the horseshoe template under a perturbation that prunes away orbits in a way allowed by topological constraints.

C. Basis sets of orbits

The spectrum of unstable periodic orbits in a nonhyperbolic strange attractor must be consistent with the unfolding of the Smale horseshoe template represented in Fig. 38. Any set of allowed orbits can be represented simply by a basis set of orbits. This is a minimal set of orbits that forces all the orbits in the spectrum.

The construction of a basis set is simple and algorithmic. The orbits in the spectrum, up to some maximum period, are listed (left to right) according to increasing topological entropy. Those with the same topological entropy are organized by increasing one-dimensional entropy. The right-most orbit is in the basis set. It is removed, along with all the orbits which it forces. Of the remaining orbits, the right-most is again a basis orbit. It and its consequents are removed. The process is repeated until the list is exhausted. This procedure results in a minimal, ordered set of orbits that force all orbits, up to the maximum period, present in the initial list. This minimal set is called a basis set of orbits (to that period).

For example, suppose the unstable periodic orbits in a strange attractor are those forced by  $7_6$  in one-dimensional maps of the interval. The orbits involved can easily be read from Fig. 38(b). Organizing them by topological and one-dimensional entropy as just described, we find, to period eight,

$$\underline{2_1 4_1 8_1 6_1 8_2 7_1 5_1 8_3 3_1 6_2 6_3 7_5 4_2 8_9 8_4 8_7 6_7 2_7 3_7 4_8 5_8 6_8 8_8 5_2}. \quad (6.5)$$

The underlined orbits are those forced by  $5_2$ . Then  $5_2$  is the first basis orbit. When  $5_2$  and the underlined orbits are removed, the list becomes

$$\underline{6}_3 \underline{7}_5 4_2 8_9 8_7 R 7_6 7_4 F 8_6 F 8_8. \quad (6.6)$$

The orbit  $8_8$  is a basis orbit. It and  $6_3$  are removed from the list. Continuing in this way, the basis set of orbits which force all those initially present is (reading right to left)

$$8_7 R 7_6 7_4 F 8_6 F 8_8 5_2. \quad (6.7)$$

A lower bound on the topological entropy of the flow can be obtained by computing the topological entropy of the braid containing the basis set of orbits.

A forcing diagram exists for any template. It can be computed explicitly up to any period  $p$ . Then any flow can be described by a basis (to period  $p$ ). This allows a discrete topological classification of strange attractors by template and basis.

#### D. Routes to chaos

As control parameters of a dynamical system [see Eq. (2.1)] are varied, periodic orbits are created and/or annihilated by saddle-node and period-doubling bifurcations. At one extreme, there may be a single stable periodic orbit. It is also possible that several stable periodic orbits coexist, each with its own basin of attraction. At the other extreme, a hyperbolic attractor may exist that contains a full set of unstable periodic orbits built of  $K$  letters with a full transition matrix (“complete chaos”). It is of great interest to us to know how it is possible to get from one extreme (regular motion) to the other. These are called “routes to chaos.”

Routes to chaos are identified by specifying a sequence of basis sets. The basis sets are related by first-order implications. For example, the sequence

$$\begin{aligned} 2_1 \rightarrow 4_1 \rightarrow 8_1 \rightarrow (8_1, 7_1) \rightarrow (8_1, 7_1, 8_3) \rightarrow (7_2, 8_3) \rightarrow 5_2 \\ \rightarrow (5_2, 8_8) \rightarrow 6_4 \rightarrow (6_4, 8_{12}) \rightarrow (6_4, 8_{12}, 5_3) \rightarrow (6_4, 8_{14}) \\ \rightarrow 7_8 \rightarrow (7_8, 6_5) \rightarrow 8_{15} \rightarrow (8_{15}, 7_9) \rightarrow (8_{15}, 7_9, 8_{16}) \end{aligned} \quad (6.8)$$

is one possible route to chaos. By this procedure we have a discrete classification of the routes to chaos in horseshoe dynamics. In fact, to any finite period the number of distinct routes to chaos is finite.

#### E. Coexisting basins

Whenever a pair of periodic orbits is created by a saddle-node bifurcation, the saddle appears initially as a stable orbit. Its basin of attraction “eats a hole” in the strange attractor. This means that motion in the strange attractor is bounded away from the newly created stable periodic orbit. As control parameters vary, the stable periodic orbit may undergo a series of period-doubling bifurcations that ultimately destroy the basin (Eshchenazi, Solari, and Gilmore, 1989).

It is sometimes useful to know how many basins of attraction can coexist with a strange attractor. This kind of information is outside the scope of most studies, which are confined to the attractor itself. However, we can provide an answer.

Suppose an attractor is identified by a basis set of  $t$  unstable periodic orbits up to period  $p$ . Then there is a perturbation that neither creates nor annihilates orbits by saddle-node bifurcations, but which moves each of the basis orbits to the verge of saddle-node annihilation. At this point, each node periodic orbit is stable and surrounded by its own basin of attraction. Therefore, under a perturbation,  $t$  basins of attraction can coexist, each surrounding a stable node from the basis set.

#### F. Other template unfoldings

It might seem that the unfolding results for templates presented in this section are limited in that they are available only for the horseshoe template. While there is merit to this viewpoint, the situation is not quite so bleak. Many templates consist of contiguous branches  $A, B, C, \dots$ , each of which is related to the next by a fold. In this case orbits confined to only two adjacent branches exhibit the systematics of unfoldings presented in Fig. 38.

When orbits extend over three adjacent branches of such templates, the level of difficulty in creating an unfolding increases dramatically, for two reasons. First, the number of orbits of period  $p$  based on three symbols increases much faster than for the two-branch case. Second, while a two-branch template with a fold is unique up to global torsion (Solari and Gilmore, 1988), there are essentially three different templates with three branches related by folds. These are shown in Fig. 39. This means that a larger number of orbits must be unfolded for three different cases. The fact that there is a symbol conjugacy between two of these templates, and that the third is self-conjugate, would help only slightly in the construction of these unfoldings.

In principle, an unfolding for the Lorenz template can be carried out as demonstrated for the horseshoe template. However, there is an intriguing relationship between the two templates that simplifies this problem. The Lorenz template is a “double cover” of the horseshoe template. That is, there is a  $2 \rightarrow 1$  mapping of dynamics on the Lorenz template to dynamics on the horseshoe template. This can be seen from the phase-space plot in Fig. 16(c) and its caricature in Fig. 16(d). By passing a curve through the two holes, straightening it out, and then projecting the dynamics down onto a plane perpendicular to this axis, Lorenz dynamics is projected down onto Rössler-like dynamics. The relationship between symbol sequences in the Lorenz system, with alphabet  $(L, R)$  (left, right), and the Rössler system, with alphabet  $(0, 1)$  (orientation preserving, reversing), is as follows:

Lorenz	Rössler	
$LL$ or $RR$	0	(6.9)
$LR$ or $RL$	1.	

A period- $p$  Lorenz orbit projects to a period- $p$  or period- $p/2$  Rössler orbit:

$LLRL \rightarrow 0110$	
$LLRR \rightarrow 0101 = 01.$	(6.10)

Conversely, a period- $p$  Rössler orbit lifts to either a period- $2p$  or two period- $p$  Lorenz orbits:

$001 \rightarrow LLLRRR$	
$011 \rightarrow \begin{matrix} LLR \\ RRL. \end{matrix}$	(6.11)

With these identifications, the horseshoe unfolding in Fig. 38 can be transformed to an unfolding of the Lorenz template. There are two drawbacks to this construction: (a) The unfolding produced is not “up to” period  $p (=8)$ . (b) The unfolding is valid only for symmetry-preserving perturbations. It is not generic.

## VII. TOPOLOGICAL-ANALYSIS ALGORITHM

We now describe the method developed for the topological-analysis of strange attractors generated by dynamical systems operating in a chaotic regime. The method consists of a number of steps. These are summarized in Fig. 40 and described in some detail below. At present, these methods are applicable to low-dimensional dynamical systems—that is, systems whose effective dimension is three.

### A. Construct an embedding

The strange attractor must be embedded in a three-dimensional space. If the dynamical system is given analytically [see Eq. (2.1)] and is already three dimensional, this problem is already solved. If the dynamical system is given analytically but is of dimension greater than three, it is necessary to compute the local Lyapunov dimension  $d_L(\mathbf{x})$  on the attractor. If  $\text{Max}[d_L(\mathbf{x})] = 2$  then the Birman-Williams theorem is applicable. The projection of the attractor into a three-dimensional subspace of phase space then provides the appropriate embedding.

When the chaotic dynamics is generated by a physical system, the analysis becomes more interesting. If three or more independent time series  $x(t), y(t), z(t), \dots$  are available, then the situation is as previously described. In many cases, only a single time series is available. This time series is always discretely sampled and may not have an optimum signal-to-noise ratio. In this case we must construct an embedding from this single time series. In other instances, we have an entire data field sampled at each time and must reduce this to a small number of time series. These two situations occur in laser experiments. In one case only the integrated output intensity on a cross section may be available. In another, a succession of frames (for example,  $120 \times 240$  pixels of

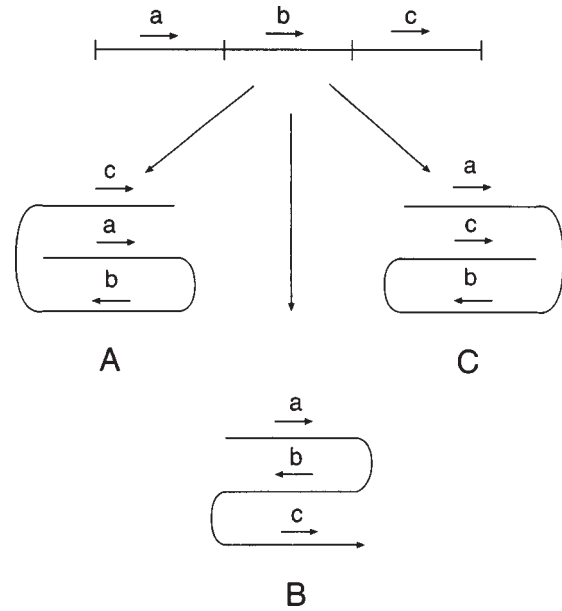


FIG. 39. Three inequivalent templates whose branches are related by a smooth deformation of the flow (a fold). A and C are dual while B is self-dual.

16 bit data/pixel) may be available. In both cases we wish to generate a small number ( $n=3$ ) of time series so that a  $d_L = 2 + \epsilon$  ( $0 < \epsilon < 1$ ) dimensional strange attractor can be embedded in  $R^3$ .

We discuss embedding procedures in more detail in Sec. X.

### B. Identify periodic orbits

We have already pointed out that unstable periodic orbits are abundant in strange attractors and dense in hyperbolic strange attractors. If an initial condition enters the neighborhood of an unstable periodic orbit, then it will evolve in the neighborhood of the unstable periodic orbit for a while. If this initial condition falls close enough to the unstable periodic orbit along its unstable manifold, and its unstable Lyapunov exponent is not too large, the initial condition may evolve all the way around the attractor and return to a neighborhood of its starting point. If this happens, it will evolve in a neighborhood of phase space that it has previously visited. When this occurs, the difference  $|\mathbf{x}(t) - \mathbf{x}(t + \tau)|$  remains small for a while. This signature is used to locate segments in a chaotic data set that can be used as surrogates for unstable periodic orbits. That is, the segment lies in a neighborhood of the unstable periodic orbit and so behaves to some extent like the unstable periodic orbit. This method of finding unstable periodic orbits in data is called the method of close returns.

It is not sufficient simply to locate surrogates for unstable periodic orbits. The name of each orbit must be identified by a symbol sequence. This is necessary because we eventually need to identify orbits in the flow with orbits on a template in a 1-1 way. Identifying the symbolic dynamics of an orbit in a flow can often be

done with a low error rate, which decreases as the dissipation increases. If a Poincaré section exists (as it does for all one-dimensional embeddings that we use), so that a return map can be constructed, identification of an orbit's symbolic dynamics becomes much easier. A data file of the successive encounters with the Poincaré section is created. Then a  $p$ th return map is generated, and those intersections closest to the diagonal are interesting candidates for the end points of an unstable orbit of period  $p$  (or  $p/2, \dots$ ).

At this stage, the identification of a symbol sequence with an unstable periodic orbit must be regarded as tentative.

### C. Compute topological invariants

The topological invariants for periodic orbits embedded in a three-dimensional phase space are linking numbers. We have already described how to compute linking numbers and self-linking numbers for periodic orbits by counting crossings in a projection onto a two-dimensional subspace. In the event that a one-parameter family ( $0 \leq \theta \leq 2\pi$ ,  $0$  and  $2\pi$  identified) of Poincaré sections can be constructed, relative rotation rates can also be computed. These invariants are computed for all surrogate unstable periodic orbits extracted from the data by the method of close returns.

At the present time, the only topological invariants we can construct for the unstable periodic orbits in strange attractors are the linking numbers and relative rotation rates, which can be constructed for knots in  $R^3$ . In higher dimensions links fall apart. The only impediment to extending this topological-analysis method to higher dimensions is the construction of topological invariants for strange attractors in  $R^n$  for  $n > 3$ .

### D. Identify a template

By this stage, the first step in identifying a template has already been taken. The alphabet required to identify all unstable periodic orbits "in" the attractor has been established. If the alphabet has  $K$  letters  $A, B, \dots$ , then the template has  $K$  branches. The algebraic description of the template is constructed as follows:

- (a) The linking numbers and local torsions of all the period-one orbits are sufficient to construct the template matrix

$$\begin{aligned} T(i,i) &= LT(i), \\ T(i,j) &= 2L(i,j). \end{aligned} \tag{7.1}$$

- (b) The linking numbers of  $K-1$  adjacent pairs of period-two orbits  $L(A,B), L(B,C), \dots$  are sufficient to determine the order in the array.

The total number of pieces of information required is  $\frac{1}{2}K(K+1) + (K-1)$ .

In most instances not all period-one and period-two orbits are available, in which case other low-period or-

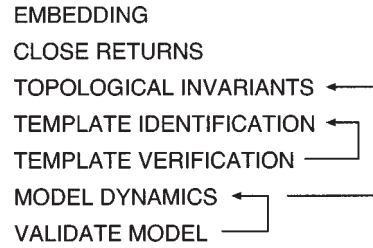


FIG. 40. Steps in the topological-analysis procedure. Vertical arrows indicate loop-closing procedures.

bits from the attractor can be used to extract the information necessary to identify the template. As an example, in horseshoe dynamics the orbit 0 is often not available. The period-one orbit 1, the period-two orbit 01, and either of the period-three orbits 001 or 011 can be used to extract the four necessary pieces of information from the chaotic signal.

### E. Validate the template

A template is tentatively identified using topological information from a minimal set of the low-period orbits. This identification must then be validated. This is done by using the template to construct a table of topological invariants for all the periodic orbits that it supports. If the original template identification was correct, these numbers must be identical to the topological invariants determined for the unstable periodic orbits extracted from the strange attractor. If the two sets of numbers do not agree, either the original template identification was incorrect or the symbolic names attributed to some surrogate orbits were in error. We have usually found complete agreement between the topological invariants computed from the surrogate data and from the corresponding orbits on a template. In a few cases there was not complete agreement. This has always been due to a questionable symbol assignment to some part of a surrogate orbit. In all cases this validation step has helped to refine the identification of a few surrogate orbits.

Orbit labeling and template identification are not isolated problems. They constitute one global problem, which must be resolved so that the table of topological invariants computed from the data is identical to that computed for corresponding orbits on the template.

We remark that the template-identification step provides a "loop closing" step, or self-consistency check. Loop closings are represented by the return arrows in Fig. 40. This process is analogous to the process involved in the statistical evaluation of experimental data. For example, a least-squares fit of *any* model will *always* converge to *some* result. The follow-up question, "is this best fit model any good?" must then be answered by additional tests (see Press *et al.*, 1986). Such loop-closing tests are absent from the older metric methods for analyzing chaotic data.

## F. Model the dynamics

In the end, a branched manifold or its template provides only a caricature for a flow. It identifies the stretching and squeezing mechanisms generating chaos. But it provides more unstable periodic orbits than are actually present, and it is more dissipative than the actual dynamics.

In some cases it is useful to attempt a better model of the dynamics. The art of model building falls into two broad categories: building analytical models and thinking the unthinkable.

In the traditional approach, a model of the form (2.1) is proposed, and one attempts to estimate the forcing functions as linear superpositions of basis functions  $\Phi_j(\mathbf{x}; \mathbf{c})$ :

$$F_i(\mathbf{x}; \mathbf{c}) = \sum_{j=1}^N A_j \Phi_j(\mathbf{x}; \mathbf{c}). \quad (7.2)$$

Many criteria exist for choosing the basis functions  $\Phi_j(\mathbf{x}; \mathbf{c})$  and estimating the coefficients  $A_j$ . This field has been extensively discussed in a recent beautiful review (Abarbanel *et al.*, 1993) and monograph (Abarbanel, 1996). We have only one contribution to provide, which deals with estimating the coefficients  $A_j$ .

We have found it useful to consider the vector  $(B_0, B_1, B_2, \dots, B_N)$  coupled to the functions  $(\Phi_0 = dx_i/dt, \Phi_1, \Phi_2, \dots, \Phi_N)$ . A singular-value decomposition of the  $(1+N) \times T$  ( $T$  = number of measurements) matrix  $\Phi_j(\mathbf{x}_i; \mathbf{c})$  produces a series of eigenvectors  $[B_0(\alpha), \dots, B_N(\alpha)]$ , with eigenvalues  $\lambda(\alpha)$ ,  $\alpha = 0, 1, 2, \dots, N$  (Press *et al.*, 1986). The square of each eigenvalue provides a “noise” estimate. We search for the minimum value of  $[\lambda(\alpha)/B_0(\alpha)]^2$  and identify the coefficients  $A_j$  in Eq. (7.2) with  $-B_j(\alpha)/B_0(\alpha)$ . This eigenvector analysis avoids the singularities that occur when one attempts to normalize functions  $\Phi_j$  with respect to the measure on the strange attractor.

The second approach is based on the spirit that motivated a remarkable paper entitled “Computers and the theory of statistics: thinking the unthinkable” (Efron, 1979). We ask the question, “Even if we have an analytic expression of the form (2.1), does that really help us to understand the dynamics?” Usually: No!

For this reason, we partition the phase space into a small number of “flow tubes,” which are essentially inflations of branches of a branched manifold. We then provide a numerical algorithm for the flow through each region. In this way the physical nature of the flow is apparent, and the lack of a (global) analytic expression for the dynamics is no great drawback.

## G. Validate the model

Once again, an estimation step must be followed by a loop-closing (validation) step. Two ways exist to validate a model of a chaotic system: compare invariants and test for entrainment.

In the first method the topological, dynamical, and metric invariants of the experimental strange attractor are compared with those generated by the model. In particular, the templates must be identical and the spectrum of unstable periodic orbits, as represented by a basis set of orbits, should be close. In addition, the average Lyapunov exponents and the Lyapunov dimensions should be close. If sufficient data are available (often not the case), metric properties determined from the data can be compared with those computed from the model.

The second method is based on a beautiful idea due to Fujisaka and Yamada (1983) and (independently) to Brown, Rulkov, and Tracy (1994). This idea in turn is based on one of the oldest observations in the field of nonlinear dynamics: The 17th century observation by Huyghens that two clocks will synchronize when placed sufficiently close together on a wall that provides coupling between them (Jackson, 1990). Synchronization between two physical systems has been studied in some detail (Pecora and Carroll, 1990). The idea of Brown, Rulkov, and Tracy is that if a model is a sufficiently good representation of a physical process, then the model can be entrained by the data. If  $y_i^m$  are model variables and  $y_i^d$  are data variables, then one cannot expect the model

$$\frac{dy_i^m}{dt} = F_i(\mathbf{y}^m; \mathbf{c}) \quad (7.3)$$

to reproduce the data in the sense  $y_i^m(t) = y_i^d(t)$ , no matter how good the model is. However, one might expect that a small coupling between model and data variables

$$\frac{dy_i^m}{dt} = F_i(\mathbf{y}^m; \mathbf{c}) - \sum_j \lambda_{ij} (y_j^m - y_j^d) \quad (7.4)$$

will entrain the model output to the data. In the case of entrainment, a plot of  $y_i^m(t) - y_i^d(t)$  vs  $t$  is zero. This test already provides a useful method for model validation, even though it has not yet been made quantitative.

## VIII. DATA

Data sets generated by a number of physical systems have been subjected to topological analysis. These include the Belousov-Zhabotinskii reaction, the laser with modulated losses, the laser with saturable absorber, the CO<sub>2</sub> laser, a dye laser, the NMR laser, a catalytic reaction, a model of a collapsing globular cluster, and a musical instrument. In most cases the data collected consisted of a single (scalar) time series. However, some data sets consisted of entire data fields—an amplitude or intensity distribution in one, two, or three dimensions as well as time. In this section we describe the data characteristics and the processing methods that have been useful for implementing topological analyses.

Data processing can be carried out in the frequency domain, the time domain, or a combination of time and frequency domains. Frequency-domain processing for linear systems has a long history and is well understood.

Reliable tools (fast Fourier transform, see Press *et al.*, 1986; Oppenheim and Schaffer, 1989) are easily available for such processing. Time-domain processing of data generated by chaotic systems is a more recent development (Hammel, 1990). Some tools are robust; others are in the development stage. Much more recently a combination of time- and frequency-domain methods has been developed for processing chaotic data (Sauer, 1992). For the most part, we have found that frequency-domain methods have been sufficient for processing chaotic data. In some instances, time-domain processing with singular-value methods has been useful (Broomhead and King, 1986).

We emphasize strongly that the topological-analysis procedure is carried out in the time domain only. However, time-domain, frequency-domain, or singular-value methods may be used to construct the embeddings on which the topological analysis method is based.

We assume throughout that the data sample the entire strange attractor. That is all transients have died out and motion is not confined to a subset of the attractor during the data-acquisition process.

#### A. Data requirements

Data requirements for a topological analysis can conveniently be expressed in terms of “cycles” and “cycle time.” Roughly, a cycle is a trip “around” the strange attractor, and cycle time is the time it takes to make this trip. Usually the meaning of “around” is clear once an embedding is available. This time scale can often be estimated by direct inspection of the data: it is the average peak-to-peak separation. If necessary, it can be estimated as the inverse of the highest frequency peak in the power spectrum or the lowest time-delay peak in a close-returns histogram.

##### 1. ~100 cycles

From experience, ~100 cycles is more than enough for a topological analysis. When data are plotted in a suitable embedding, the first dozen cycles outline the shape of the attractor, the next 20 to 50 cycles fill in the details, and beyond 100 cycles no additional detail is provided (Fig. 41).

##### 2. ~100 samples/cycle

From experience, ~100 samples/cycle provides a convenient sampling rate. More than 100 samples/cycle provides redundant information. Fewer than 50 samples/cycle usually means that the data must be smoothed or interpolated in some way. We have analyzed data sets with as many as 200 samples/cycle and as few as 12 samples/cycle. In the former case we carried the overhead of larger-than-necessary data sets. In the latter we had relatively short data sets, but paid the price of being forced to interpolate the data. We have found frequency-domain methods fast and efficient for data-interpolation purposes.

Our preference has been to deal with shorter rather than longer data sets. Many of our analyses have been

carried out on a subset (often a small subset) of the available data. An optimum file for a topological analysis contains 8K ( $8192=2^{13}$ ) scalar measurements with sampling parameters in the range recommended above.

#### B. Fast look at data

It is always useful to look at the data before embarking on an analysis. In some instances a fast look is sufficient to identify the stretching and squeezing processes involved. There are two very simple ways to view the data: plot  $x(t)$  versus  $t$  and plot  $dx/dt$  versus  $x(t)$ . The first way is simply a plot of the data itself. In many cases it is possible to identify the fixed points and their stability type simply by inspection. In the second method, the difference  $x(t_{i+1})-x(t_i)$  is used as an estimate for  $dx(t_i)/dt$ . The plot of  $x(t_{i+1})-x(t_i)$  vs  $x(t_i)$  is then a projection of the strange attractor onto the  $x-\dot{x}$  plane. This projection can indicate the number of fixed points in phase space and localize the region of phase space where squeezing occurs. In Fig. 42 we indicate four possible types of folding behavior that can easily be recognized, in both the  $x$  vs  $t$  and  $\dot{x}$  vs  $x$  plots.

#### C. Processing in the frequency domain

Very clean data sets can sometimes be used directly for topological analysis, without any processing. This is not usual. Data processing is very conveniently carried out in the frequency domain using Fourier techniques. Most of the procedures described below depend on the fast Fourier transform.

##### 1. High-frequency filter

Experimental data sets often consist of two components: a signal on top of which is superposed noise. Even very clean data sets that have been recorded and stored in digital form have a noise component induced by round-off or truncation. An extensive industry has arisen to deal with the separation of signal from noise. For our purposes, it is usually sufficient to remove the high-frequency components in the Fourier transform of the data set.

Typically, it is sufficient to filter out components whose frequency is more than a factor of ten greater than the frequency corresponding to the cycle time.

##### 2. Low-frequency filter

Most of the important information in a chaotic signal is contained in the low frequencies. It is therefore usually a very bad idea to filter frequencies any smaller than those corresponding to the cycle time.

However, exceptions do exist. When performing an integral-differential embedding, one of the three variables created from the scalar data set is the integral of the data:

$$y_1(t) = \int_{-\infty}^t x(t') dt'. \quad (8.1)$$

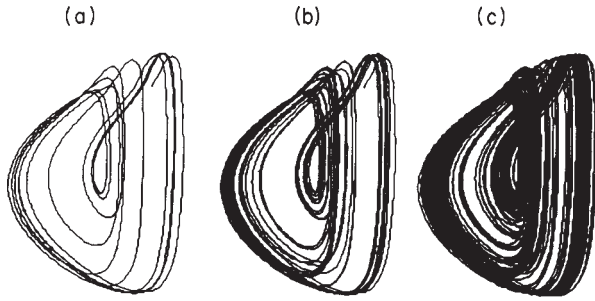


FIG. 41. Optimal length of data sets. Too much data are not useful for a topological analysis. (a) A dozen cycles outline the skeleton of the attractor, (b) 20–50 more cycles fill in the details, (c) and more begin to obscure the details.

In some cases, when plotting the projection  $y_1(t)$  vs  $x(t)$ , we are able to see the “attractor” drift in the  $y_1$ - $y_2$  plane along the  $y_1$  axis [see Fig. 56(b)]. This drift can be traced to secular and long-term variability in the data set. This is not atypical of experiments that last longer than a substantial fraction of a day due to slow variations in the electrical grid. When these slow variations are removed by low-frequency filtering of the data, the attractor remains stationary (Fig. 57). We can provide no hard and fast rules for the low-frequency cutoff. We can only suggest that the cutoff be gradually increased until the projection of the attractor ceases to wander in phase space.

The low-frequency filter can be implemented in the time domain by introducing a decaying memory function in the integral:

$$y_1(t) = \int_{-\infty}^t x(t') e^{-(t-t')/\tau} dt'. \quad (8.2)$$

Here  $\tau$  is a memory time. We have found it useful to use a multiple of the cycle time for  $\tau$  ( $\sim 10$ ).

### 3. Derivatives and integrals

To carry out a topological analysis, an embedding of the data must first be constructed. One way to create an embedding is to use derivatives and/or integrals of the original scalar data set as components of the embedding vector. These can be constructed directly from the data.

Derivatives and integrals can also be constructed using Fourier methods. The fast Fourier transform analog of the relation

$$x(t) = \int \hat{x}(\omega) e^{i\omega t} d\omega, \quad (8.3)$$

$$\frac{dx}{dt} = \int i\omega \hat{x}(\omega) e^{i\omega t} d\omega.$$

is shown in Fig. 43. To compute the derivative: (a) Take the fast Fourier transform of the data; (b) interchange the real and imaginary components, with phase information, and multiply by  $|\omega|$ , as shown in Fig. 43; and (c) take the inverse transform. In this process, the zero frequency terms should be zeroed out. If the power spec-

trum is not small near the Nyquist frequency, frequency-domain processing is a bad idea and should be abandoned.

The integral is computed in much the same way. The difference is that the phase change is opposite that shown in Fig. 43, and the Fourier coefficients are divided by  $|\omega|$ , rather than multiplied by  $|\omega|$ .

Generalized derivatives and integrals of degree  $d$  can also be computed. These are constructed by the algorithm described above, except that the Fourier coefficients are multiplied by  $|\omega|^d$  instead of  $|\omega|^1$ . Generalized derivatives of experimental data are shown in Fig. 44 for  $d = -\frac{1}{2}$  (“square root of the integral”),  $d = 0$  (Hilbert transform), and  $d = \frac{1}{2}$  (“square root of the derivative”).

### 4. Hilbert transform

The scalar data set  $x(t)$  can be regarded as the real part of a complex data set  $z(t)$ :

$$x(t) = \text{Re}[x(t) + iy(t)] = \text{Re } z(t).$$

If  $z(t)$  is analytic in the upper half plane, the imaginary part  $y(t)$  is the Hilbert transform of  $x(t)$ . The Hilbert transform of  $x(t)$  is related to  $x(t)$  by an integral that is an immediate result of Cauchy’s theorem

$$y(t) = \frac{1}{\pi} \int_{-\infty}^{+\infty} \frac{x(t')}{t-t'} dt'. \quad (8.4)$$

However, it is a simple matter to construct  $y(t)$  from  $x(t)$  using the Fourier transform (Oppenheim and Schaffer, 1989). Essentially,  $y(t)$  is the “noise free” derivative of  $x(t)$ . Its construction, illustrated in Fig. 43, is as follows:

- (1) Compute the FFT of  $x(t)$ .
- (2) Interchange the real and imaginary parts of  $\hat{x}(\omega)$ , with phase as shown in Fig. 43. Multiply by  $|\omega|^{d=0} = 1$  (optional).
- (3) Compute the inverse fast Fourier transform.

The output is the real signal  $y(t)$ . It is the generalized derivative with  $d=0$ .

This algorithm can be implemented more efficiently by computing  $y(t)$  as an imaginary signal. If the array that results in step 2 above is multiplied by  $i$ , then it is no longer necessary to interchange the real and imaginary parts of the Fourier coefficients. The positive-frequency coefficients are multiplied by  $-1$  and the negative-frequency components are multiplied by  $+1$ . If this array is now added to the original array representing  $\hat{x}(\omega)$ , all positive-frequency terms are zero and all negative-frequency terms are doubled in value. For bookkeeping purposes, it is simpler to construct  $\hat{x}(\omega) - i\hat{y}(\omega)$ . This is done by zeroing out all negative-frequency terms and leaving the positive-frequency terms unchanged. The inverse fast Fourier transform is then  $\frac{1}{2}[x(t) - iy(t)]$ .

The Hilbert transform of the Belousov-Zhabotinskii data is shown in Fig. 44(b). The beginning and end of the time series diverge from the projected attractor [ $y(t)$  vs  $x(t)$ ] because of the Gibbs’ phenomenon. We did not

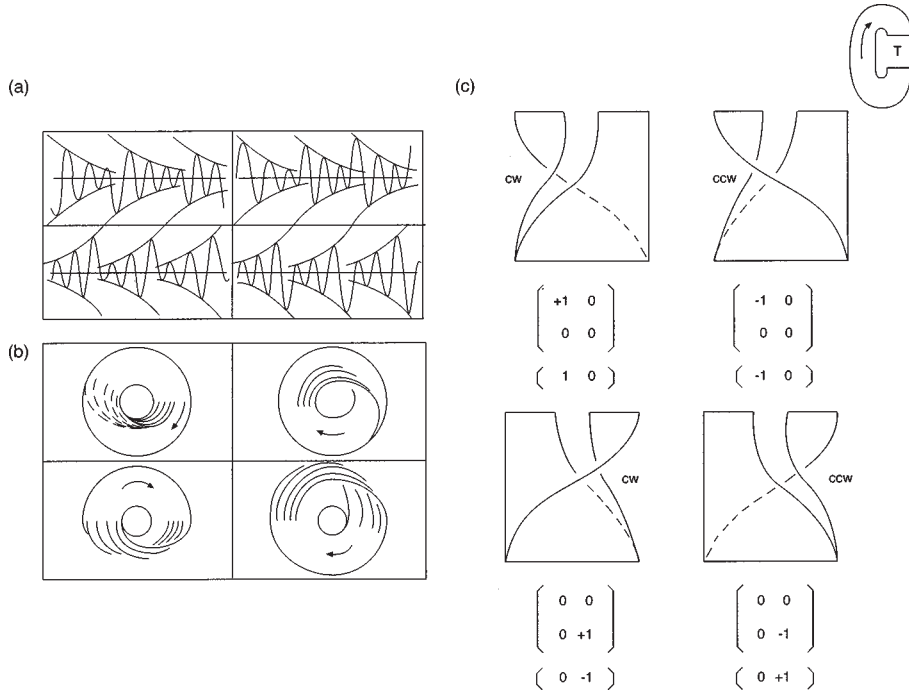


FIG. 42. Simple method for identifying Smale horseshoe templates. Morphology of a time series is sometimes sufficient to determine the stretching and folding mechanism responsible for creation of the strange attractor.

make an effort to match values at the beginning and end of the data segment that was used.

5. Fourier interpolation

In some cases data sets are undersampled. It is then useful to interpolate between data points. A number of interpolation schemes are available and discussed in *Numerical Recipes* (Press *et al.*, 1986). We find these time-domain schemes time consuming since they require interpolation between successive small subsets of data in a long data set.

We prefer fast Fourier transform-based interpolation method, which is shown schematically in Fig. 45. This method can be used whenever the power spectrum drops to zero or to an acceptable noise level at the Nyquist frequency. The data set of length  $N$  is placed in an array of length  $2N$  in the usual way. The fast Fourier transform is then performed in the usual way. The output array is then extended to an array of length  $4N$  by inserting  $2N$  zeros at the Nyquist frequency  $N_Q$ . The inverse fast Fourier transform is an array of length  $4N$ , which is real, so that only  $2N$  values are nonzero. These  $2N$  values include the original data set consisting of  $N$  values together with  $N$  additional values, which are interpolations between each of the original data values. The interpolation of  $1, 3, \dots, 2^k - 1$  data values between each observation can be achieved using the same method, except that  $(2^k - 1) \times 2N$  zeroes must be inserted at the Nyquist frequency. In Fig. 46 we show how this method has been used to clean up an undersampled time series.

6. Hilbert transform and interpolation

The algorithms described above for computing a Hilbert transform and for interpolating a data set can be

combined into a single algorithm that does both and that is more efficient than either algorithm singly. Given a data set of length  $N$ :

- (1) Take the fast Fourier transform of  $x(t)$ , expressed as a data file of length  $2N$ .
- (2) Zero out all terms except the positive-frequency terms between the low-frequency and high-frequency thresholds. Extend the length of the data file to  $2^k \times 2N$  by padding the end of the data file with zeros.
- (3) Take the inverse fast Fourier transform.

The output file contains a complex data set of length  $2^k \times N$ . The real part contains the original signal with  $2^k - 1$  points interpolated between each of the observations. The imaginary part is the Hilbert transform of the interpolated real part. In Fig. 47 we use this method both to plot  $dx/dt$  vs  $x(t)$  for a real signal that is undersampled and the interpolated Hilbert transform against the interpolated signal.

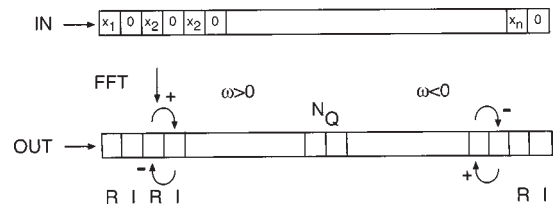


FIG. 43. Organization of the arrays representing input data set and output Fourier coefficients in a widely available fast Fourier transform code. In computing derivatives, the real and imaginary parts of the coefficients must be interchanged (multiplication by  $i$ ) and the coefficients multiplied by  $\omega$ . Positive frequencies occur between 0 and  $N_Q$ , the Nyquist frequency. Negative frequencies occur between  $N_Q$  and the end of the file.

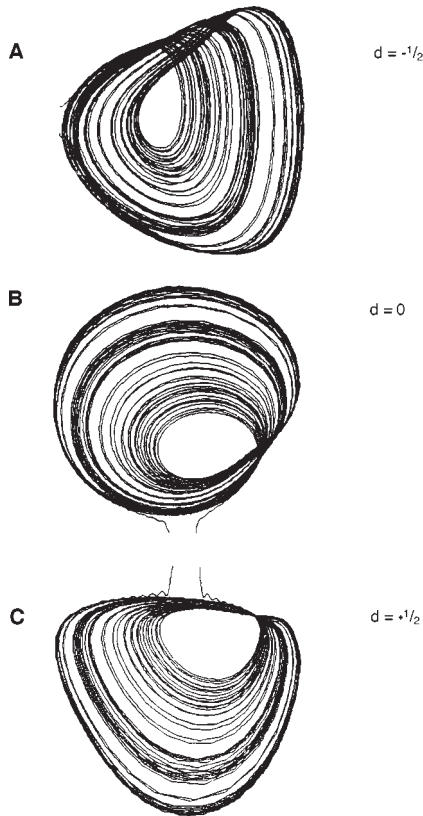


FIG. 44. Generalized derivatives computed for an experimental data set. (a)  $d = -\frac{1}{2}$ ; (b)  $d = 0$ ; (c)  $d = +\frac{1}{2}$ .

**D. Processing in the time domain**

A large number of smoothing and interpolation methods exist for processing data in the time domain. They include classical techniques, such as those summarized in *Numerical Recipes* (Press *et al.*, 1986). They also include a number of methods that have been developed specifically for chaotic data, and that make heavy use of the existence of stable and unstable manifolds (Hammel, 1990). The only smoothing method that we have used extensively is the singular-value decomposition (Lorenz, 1956; Broomhead and King, 1986).

**1. Singular-value decomposition for data fields**

The singular-value decomposition is a statement that a data matrix  $Z(i, j)$ ,  $1 \leq i \leq m, 1 \leq j \leq n$  can be decomposed as an outer product of orthonormal vectors  $u(i, \alpha)$  and  $v(j, \alpha)$  in complementary spaces of dimensions  $m$  and  $n$  as follows:

$$Z(i, j) = \sum_{\alpha=1}^{\min(m, n)} \lambda_{\alpha} u(i, \alpha) v(j, \alpha). \tag{8.5}$$

In the applications that we have in mind,  $j$  is a time index and  $i$  is a space index. If the data set is in  $1+1$  dimensions, the singular-value decomposition expresses the data matrix as an outer product of one-dimensional spatial modes with one-dimensional temporal modes. If the data set is in  $2+1$  or  $3+1$  dimensions, then the spatial index  $i$  becomes more interesting.

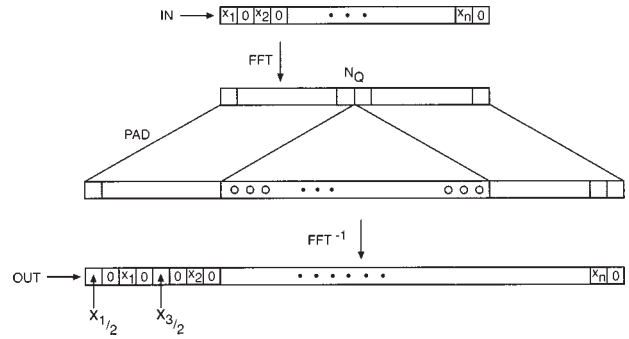


FIG. 45. Fourier interpolation. A real data set of length  $N$  is easily interpolated by inserting  $2N$  zeroes at the Nyquist frequency ( $N_Q$ ).

The beauty of the singular-value decomposition is that the squares of the eigenvalues ( $\lambda_{\alpha}^2$ ) represent the relative importance of mode  $\alpha$  in the decomposition. Therefore we can compute the value of

$$\frac{\sum_{\alpha=1}^k \lambda_{\alpha}^2}{\sum_{\alpha=1}^{\min(m, n)} \lambda_{\alpha}^2} \tag{8.6}$$

to find the percentage contribution of the  $k$ -most-important modes in this decomposition. In this expression the eigenvalues are ordered by decreasing magnitude ( $\lambda_1^2 \geq \lambda_2^2 \geq \dots$ ). Truncation at  $k$  modes provides  $k$  time series for analysis. Each is coupled to a conjugate spatial mode. If  $k=3$ , a topological analysis can be carried out on the temporal amplitudes  $v(j, \alpha)$  ( $\alpha=1,2,3$ ) for the three most important spatial modes  $u(i, \alpha)$  ( $\alpha=1,2,3$ ).

A beautiful analysis of fluid data has been carried out by Chauve and LeGal (1992) using the singular-value decomposition. The analysis was carried out on data contained in a  $512 \times 256$  data field. The values of 16 maxima in the spatial direction (512) were located for each time value (256). This information was stored in a  $16 \times 256$  data matrix. Three complex amplitudes were extracted from this  $1+1$  data field, and the system generating the data was shown to be compatible with a set of complex Ginzburg-Landau equations.

**2. Singular-value decomposition for scalar time series**

Singular-value decomposition methods can be used on a single time series  $x(i)$  (Broomhead and King, 1986) to smooth it and to create a  $p$ -dimensional embedding. The procedure is to create a data matrix  $Z(i, j)$  using a standard  $P$ -dimensional embedding

$$x(i) \rightarrow Z(i, j) = x(i+j-1), \quad 1 \leq j \leq P. \tag{8.7}$$

A singular-value decomposition is performed on  $Z(i, j)$  and the complementary eigenvectors used to construct matrices:

$$Z_{\alpha}(i, j) = \lambda_{\alpha} u(i, \alpha) v(j, \alpha). \tag{8.8}$$

Then a  $p$ -dimensional embedding of the scalar data set  $x(i)$  is created by defining the  $p$  components of a vector  $y$  as follows ( $p \leq P$ ):

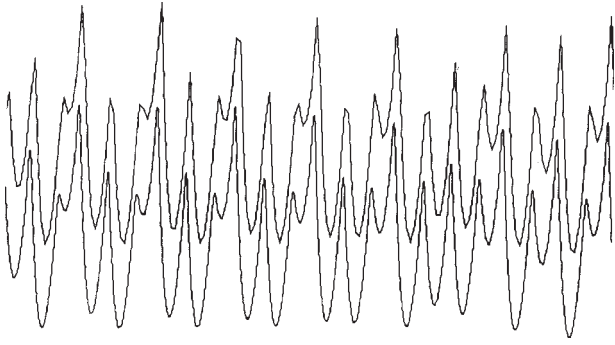


FIG. 46. An undersampled time series and an 8:1 interpolation of the time series. The two are offset for clarity.

$$y_\alpha(k) = \langle Z_\alpha(i, j) \rangle_{i+j=k-1}. \quad (8.9)$$

In this expression  $\alpha = 1, 2, \dots, p$  and the average is taken over the matrix elements of  $Z_\alpha(i, j)$ , subject to the condition  $i + j = k - 1$ . A smoothing of the data is obtained by summing over the coordinates,

$$\bar{x}(k) = \sum_{\alpha=1}^p y_\alpha(k), \quad (8.10)$$

where the sum is truncated to exclude the least important modes (“noise”).

## IX. UNSTABLE PERIODIC ORBITS

Unstable periodic orbits that reside in a strange attractor can be located by the method of close returns. Segments can then be extracted from the data set and used as surrogates for the unstable periodic orbits. These surrogates are used to compute topological invariants: linking numbers and, if a Poincaré section can be constructed, relative rotation rates. The topological invariants are used as fingerprints of strange attractors (Tuffillaro, Solari, and Gilmore, 1990).

### A. Close returns in flows

#### 1. Close-returns plot

Close-returns plots are based on the observation that the difference  $|\mathbf{x}(t) - \mathbf{x}(t + \tau)|$  remains small over some time interval  $t_i \leq t \leq t_j$  when  $\mathbf{x}(t)$  is near a periodic orbit of period  $\tau$ . Searches for periodic orbits based on this observation were first proposed by Eckmann and Ruelle (1987) in terms of recurrence plots, which are plots of  $\Theta(\epsilon - |\mathbf{x}(t_i) - \mathbf{x}(t_j)|)$  as a function of the times  $t_i$  and  $t_j$ . In such plots the  $(i, j)$  pixel is plotted black if  $|\mathbf{x}(t_i) - \mathbf{x}(t_j)| < \epsilon$  and white otherwise. The parameter  $\epsilon$  is usually chosen as about 1% of the diameter of the strange attractor. In such plots the diagonal  $t_i = t_j$  is black. Close-returns segments appear as line segments parallel to the diagonal.

We have modified recurrence plots and instead plot  $\Theta(\epsilon - |\mathbf{x}(t) - \mathbf{x}(t + \tau)|)$  as a function of  $t$ , the location in the data set, and  $\tau$ , the period. Close-returns segments

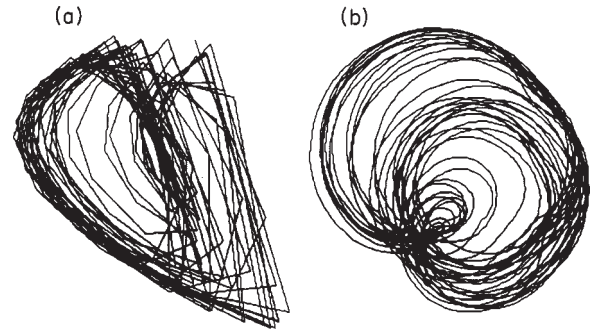


FIG. 47. (a) Phase-space reconstruction  $\dot{x}$  vs  $x$  for an undersampled real signal. (b) Hilbert transform vs interpolated signal when both are computed using the interpolation-transformation algorithm.

appear as horizontal line segments, from which the location in the data set as well as the period are easily recognized.

Close-returns plots and recurrence plots are normally carried out on vectors  $\mathbf{x}(t) \in R^n$  that traverse a strange attractor. If only a scalar data set is available, it might seem that an embedding of the data is required before a close-returns plot can be constructed. This is not so. Since an embedding of a scalar data set contains no more information than the original data set, close-returns plots on scalar time series are effective in locating unstable periodic orbits. In Fig. 48 we show a close-returns plot obtained from the Belousov-Zhabotinskii data. The horizontal line segments indicating periodic orbits stand out clearly. The upward-curving segments occur as rising ( $\dot{x} > 0$ ) parts of the data set cross descending ( $\dot{x} < 0$ ) parts. Such artifacts are examples of “false nearest neighbors” (Abarbanel *et al.*, 1993; Abarbanel, 1996). They are easily removed by embedding the data.

Close-returns plots are very insensitive to additive noise (Mindlin *et al.*, 1991). In fact, they degrade gracefully as the noise level is increased far beyond what is acceptable for standard metric calculations.

In order to emphasize that periodic orbits can be extracted from scalar time series before an embedding has been constructed, this section (IX) on locating periodic orbits appears before the section (X) describing embedding methods.

#### 2. Close-returns histograms

A time-delay histogram can be constructed by counting close returns as a function of delay (Lathrop and Kostelich, 1989; Tuffillaro, Solari, and Gilmore, 1990)

$$H(t_j) = \sum_i \Theta(\epsilon - |\mathbf{x}(t_i) - \mathbf{x}(t_i - t_j)|). \quad (9.1)$$

In Fig. 49(a) we present the close-returns histogram for the close returns plot shown in Fig. 48 (Mindlin and Gilmore, 1992). The peaks in the histogram clearly indicate the “cycle time” and the approximate periods of the unstable periodic orbits.

### 3. Tests for chaos

Close-returns histograms have been used to distinguish chaotic from stochastic behavior (Gilmore, 1993a, 1993b). By inspection, the close-returns histogram for a chaotic signal [Fig. 49(a)] differs from the close-returns histogram for a stochastic signal [Fig. 49(b)]. For the latter,  $H(t_j)$  is essentially a uniform distribution. Standard statistical tests (Press *et al.*, 1986) can then be used to test the null hypothesis  $H_0$  that the histogram  $H(t_j)$  is uniform. These tests cannot be used to prove that a data set is chaotic, but they can be used to reject the alternative hypothesis that it is stochastic. At the present time, the most convincing way to prove that a data set is chaotic is to identify at least one unstable periodic orbit with positive topological entropy.

#### B. Close returns in maps

##### 1. First-return plot

Close-returns searches can be applied to maps. In fact, they are implemented more easily for maps than for flows.

To create a map from flow data, it is necessary to construct a Poincaré section. For our preferred embedding of scalar data (the differential phase space method), a Poincaré section always exists. In fact, it is simply defined by  $\dot{x}=0$  for  $x>0$  (where  $\langle x \rangle_t=0$ ). From a long file of flow data, we construct a small file  $(M_i, t_i)$  containing the values of the  $i$ th local maximum,  $M_i$ , and the location in the data set,  $t_i$ , at which this maximum occurs. For a data file of length  $10^4$  and a sampling rate of about 100 samples/cycle, the file of local maxima contains  $10^2$  local maxima, along with their locations in the data file.

A first-return plot of  $M_{i+1}$  vs  $M_i$  can be constructed to identify period-one orbits in the map. These correspond to points closest to the diagonal in the first-return map (Fig. 50). The unstable period-one orbit in the flow is then represented by the segment of data in the original data set between  $t_i$  and  $t_{i+1}$ , where the point  $(M_i, M_{i+1})$  is closest to the diagonal.

The first-return plot can often be used to identify an alphabet of symbols to label the orbits. Critical points, or their approximations, separate parts of the return map that are labeled by different letters. The return map for a data set from the Belousov-Zhabotinskii reaction is shown in Fig. 50. For this return map two symbols suffice. The more dissipative the system is, the easier it is to make an error-free identification between data segments and symbols. Ultimately, orbit identification by symbol sequence must be consistent with template identification.

##### 2. $p$ th return plot

Surrogates for unstable period- $p$  orbits can be obtained in the same way from  $p$ th return plots. All values of  $t_i$  for which  $|M_i - M_{i+p}|$  is sufficiently small are candidates for initial conditions for unstable period- $p$  orbits.

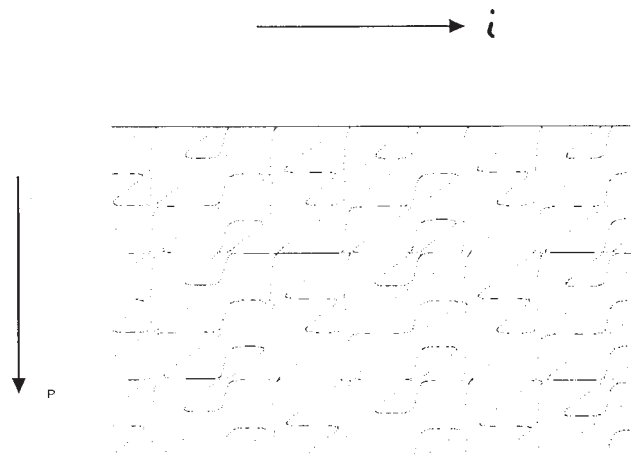


FIG. 48. Close-returns plot  $\Theta(\epsilon - |x(i) - x(i+p)|)$  of Belousov-Zhabotinskii data. Horizontal line segments indicate regions of data set that are near unstable periodic orbits.

When possible, the symbol sequence for these orbits should be determined, since many topologically inequivalent period- $p$  orbits can exist.

By this method it is possible to find a period- $p/2$  orbit that “goes around twice.” Finding such orbits is not useless, for they make computation of the local torsion of the period- $p/2$  orbit very simple.

By slowly increasing the rejection threshold for  $|M_i - M_{i+p}|$ , it is possible to find several representatives of a period- $p$  orbit. Usually, we choose the best (smallest  $|M_i - M_{i+p}|$ ) as the surrogate orbit. However, we can often use the other surrogates to determine the local torsion of this orbit.

#### C. Metric methods

In order for the close-returns procedure to work, the unstable Lyapunov exponent cannot be too large. A useful rule of thumb for period- $p$  orbits is  $\lambda(t_{i+p} - t_i) < 1$ , where  $\lambda$  is the positive Lyapunov exponent. If the Lyapunov exponent is too large, it is not very likely that an initial condition near a period- $p$  orbit will evolve in the neighborhood of that orbit for the entire time interval  $t_{i+p} - t_i$ . In this case it is still possible to find surrogates for period  $p$  orbits. We have used the following method successfully when necessary, but prefer to avoid it when possible. The basic idea is to push the search for periodic orbits into the symbol-sequence space. The first step is to encode the entire time series by a symbol sequence  $\sigma_1 \sigma_2 \sigma_3 \cdots \sigma_N$ , where the data between  $t_i$  and  $t_{i+1}$  is encoded by the symbol  $\sigma_i$ . As above,  $t_i$  is the time of the  $i$ th intersection with a Poincaré section. As mentioned above, the identification of a symbol with a data segment is often simple after a first-return map has been created.

Suppose now that the symbols are drawn from a small alphabet  $A, B, C, \dots$  and that the branches are ordered (lexigraphically) in a template ( $A < B < C \cdots$ ). To find a period-two orbit  $AB$  we proceed as follows. The future of  $A$  is  $(A)BABAB \cdots$ . We identify a symbol  $A$  in the

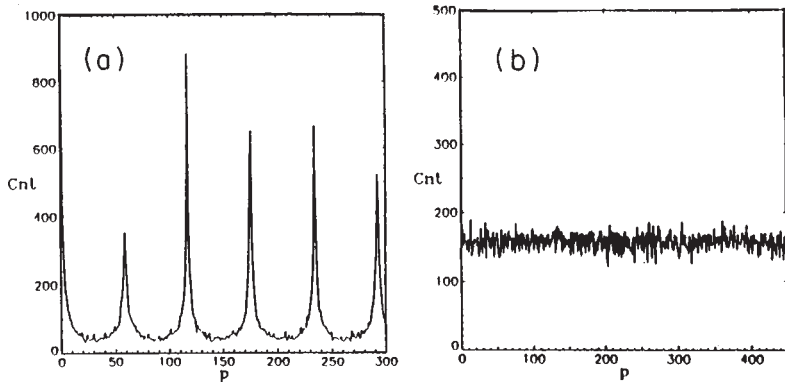


FIG. 49. (a) Close-returns histogram for the close-returns plot shown in Fig. 48. The peak at the smallest time delay provides a good estimate of the “cycle time.” (b) Close-returns histogram for a stochastic data set. This distribution is compatible with a uniform distribution.

symbol sequence representing the data, and compare the future of that symbol with the future of  $A$  in the periodic orbit:

data  $\hat{A} B A B C \tilde{A} B A B B \dots$   
 period 2  $A B A B A \dots$   
 period 2  $A B A B A \dots$  (9.2)

The segment of data starting from  $\hat{A}$  agrees with the period-two orbit for the next three periods, but is different ( $C$  vs  $A$ ) at the fourth period in the future. On the other hand, the segment of data starting from  $\tilde{A}$  is also different ( $B$  vs  $A$ ) starting at the fourth place, but is less different ( $B$  vs  $C$ ) than the future of  $\hat{A}$ . On this basis the data segment starting from  $\tilde{A}$  would be more like  $A$  in the period-two orbit  $AB$  than the data segment starting from  $\hat{A}$ . Forward and backward objective functions measuring degree of similarity can be defined. By optimizing these objective functions in some useful way, it is possible to choose from the data set the best approximation to each of the  $p$  symbols in a period- $p$  orbit.

Another way to perform this same function is to introduce a metric in the space of symbols (Collet and Eckmann, 1980; Tuffillaro, Abbott, and Reilly, 1992). The distance between two symbol sequences  $\mu_1 \mu_2 \dots \mu_N$  and  $\nu_1 \nu_2 \dots \nu_N$  at symbol  $i$  can be defined by

$$d(\mu, \nu) = \sum_{k=0, \pm 1, \pm 2, \dots} \frac{1}{2^{|k|}} f^{|k|}(\mu_{i+k}, \nu_{i+k}), \quad (9.3)$$

where  $f(\mu_j, \nu_j) = 0$  if  $\mu_j = \nu_j$  and has some nonzero value otherwise, depending on how far apart  $\mu_i$  and  $\nu_i$  are. There are many closely related ways to impose a metric on the space of symbols.

If implemented correctly, objective functions and metrics lead to the same results. If suitable thresholds are satisfied for all symbols in the symbol name for a period- $p$  orbit, then it is possible to string the associated  $p$  segments of data together to get a reasonable surrogate for the period- $p$  orbit. One should plot the orbit  $x_{\sigma_i}(t)$  vs  $t$  to verify that it is a suitable surrogate (for example, all discontinuities between adjacent segments are “small”). If one (or more) of the thresholds is not satisfied, no surrogate for the period- $p$  orbit can be constructed by this method, and we can assume that this unstable periodic orbit is “not in the data.”

We have used this method to construct surrogates for periodic orbits ( $p=6,7,8$ ) predicted to exist in the Belousov-Zhabotinskii data set but not recovered by the method of close returns. These orbits will be discussed more fully in Sec. XI.A.5.

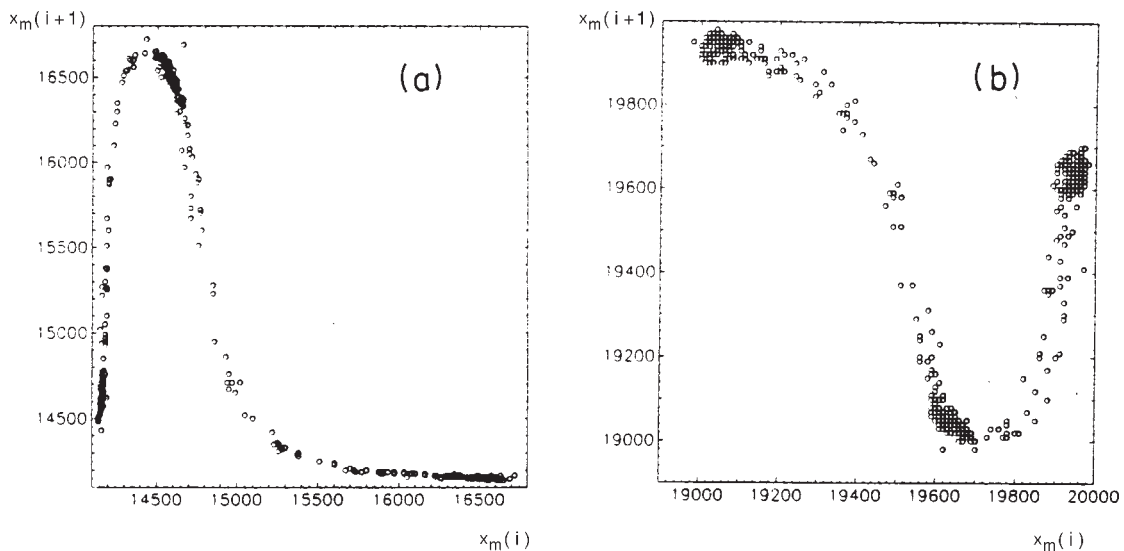


FIG. 50. First-return maps for (a) successive minima and (b) successive maxima in a Belousov-Zhabotinskii data set.

## X. EMBEDDING

A strange attractor is a geometric structure embedded in a space of dimension  $n \geq 3$ . To construct a strange attractor from a scalar data set  $x(t)$  it is necessary to construct vectors  $\mathbf{y}(t)$  with  $n$  components from the scalar  $x(t)$  in some way. A number of ways have been proposed. These are described below.

### A. Time-delay embedding

The default embedding involves creating an  $n$  vector by the map

$$\begin{aligned} x(t) \rightarrow y(t) &= (y_1(t), y_2(t), \dots, y_n(t)) \\ y_k(t) &= x(t - \tau_k), \quad k=1, 2, \dots, n. \end{aligned} \quad (10.1)$$

The parameters  $\tau_k$  are called the time delays. These are usually spaced equally (it is a matter of convenience) and expressed as multiples of a single parameter  $\tau$  called the time delay,

$$\tau_k = (k-1)\tau, \quad (10.2)$$

but this is not necessary. For a discretely sampled time series  $x(i)$  the embedding is

$$\begin{aligned} x(i) \rightarrow \mathbf{y}(i) &= (y_1(i), y_2(i), \dots, y_n(i)), \\ y_k(i) &= x(i - (k-1)d), \end{aligned} \quad (10.3)$$

where  $d$  is the delay.

The embedding theorem is based on the mathematics of manifolds (Whitney, 1936). If two manifolds of dimensions  $d_1$  and  $d_2$  are mapped into a space of dimension  $D$ , then typically (generically, see Gilmore, 1981) either

- (a) they do not intersect or
- (b) if they do intersect, their intersection is a manifold of dimension  $d = d_1 + d_2 - D \geq 0$ . Under perturbation, their intersection remains a manifold of dimension  $d$ .

If  $d_1 + d_2 - D < 0$ , then typically the two manifolds do not intersect. If they do, it is an accident (“nongeneric”) and this intersection is removed by an arbitrary perturbation. For example, two one-dimensional curves in a plane either do not intersect, or, if they do, intersect transversely at a point ( $1+1-2=0$ ). This intersection cannot be removed by a small perturbation. Alternatively, a one-dimensional curve may have nonremovable zero-dimensional self-intersections when mapped into a plane. However, a one-dimensional curve will typically not have self-intersections when mapped into  $R^n$ ,  $n > 2$ . Any self-intersections in this larger space can be removed by an arbitrarily small perturbation.

This theorem was applied to dynamical systems in the early 1980s (Packard *et al.*, 1980; Mañé, 1981; Takens, 1981). The basic idea is this: A dynamical system  $\dot{x} = F(x)$  over  $R^n$  generates motion in an  $n$ -dimensional manifold ( $R^n$ ). A generic scalar observable  $z(t) = g(x(t))$  can then be used to create a representation of the dynamics in  $R^k$  by the delay mapping (10.1). The

image of this map is contained in an  $n$ -dimensional submanifold in  $R^k$  if  $k \geq n$ . This manifold can undergo generic nonremovable self intersections if  $k$  is not sufficiently large. At such self-intersections the uniqueness theorem for ordinary differential equations is lost. To ensure that the mapping is an embedding (preserves the dynamics), self-intersections must be avoided so that the uniqueness theorem remains valid globally. This is guaranteed if  $k > 2n$  or  $k \geq 2n + 1$ .

The original version of the embedding theorem guaranteed that the dynamics of an  $n$ -dimensional dynamical system could be recovered by a  $k$ -dimensional embedding of a scalar observable, such as a coordinate, for  $k \geq 2n + 1$ . The original version of the embedding theorem was a differential embedding involving derivatives  $d^j x / dt^j$ ,  $j=0, 1, \dots, k-1$ . The  $j$ th derivative is approximated by a linear combination of  $j+1$  adjacent sample values. Therefore the delay embedding (10.3) is related to Whitney’s embedding by an affine transformation.

The actual dynamics occurs in a subspace of  $R^n$ , so that it might be anticipated that the bound  $k = 2n + 1$  is too conservative. If motion occurs on a strange attractor with a “fractal dimension”  $d_A$ , it might be anticipated that a better bound would be  $k > 2d_A$  or  $k = [2d_A] + 1$ . This result was shown to be true for  $d_A = D_0$  by Sauer, Yorke, and Casdagli (1991).

For the Lorenz system (Lorenz, 1963)  $n=3$ , so earlier estimates guaranteed an embedding for  $k=7$ . The Lorenz attractor has  $D_0 \approx 2.06$ , so that the tighter bound is  $k=5$ . However, since the Lorenz system is three dimensional, we would prefer an embedding with  $k=3$  ( $>2.06$ ). Though not guaranteed by the embedding theorem, it is not forbidden, either.

The time-delay embedding has several advantages over other embedding methods. One virtue of the time-delay embedding is that it can always be constructed, even if the embedding dimension is larger than necessary. Another very important virtue is that each coordinate in a delay embedding has the same signal-to-noise ratio. For other embeddings the signal-to-noise ratio usually decreases as additional coordinates are added.

This embedding method also has several disadvantages. One major disadvantage is that there is no obvious dynamical relationship between the coordinates, as already pointed out [see Sec. II.B, especially Eq. (2.16)]. A second major disadvantage is that the results of a topological analysis are not independent of the time-delay parameter. In Fig. 51 we show three time-delay embeddings of the Belousov-Zhabotinskii data. Figure 51(a) shows the embedding for a very small time delay. Figure 51(c) shows the embedding for a time delay comparable to a cycle time. This also provides an embedding, but the topological invariants of embedded orbits are different in the two embeddings. Figure 51(b) shows an embedding for some intermediate time delay. Roughly speaking, the attractor appears to be confined to a “fat” two-dimensional manifold that undergoes a self-intersection as the time delay is increased from  $\sim 0.01T$  (a) to  $\sim \frac{3}{4}T$  (c). At the self-intersection, invariance of the topological indices is lost. This self-intersection does not

violate Whitney's embedding theorem, which guarantees an embedding in dimension  $n \geq 7$ .

Dependence of topological invariants on the time delay has been pointed out in two recent studies. Mindlin and Solari (1995) studied a delay embedding where  $\tau_1 = 0$ ,  $\tau_2$  was fixed, and  $\tau_3$  was allowed to vary. They found values for  $\tau_3$  for which the attractor underwent apparent self-intersections and other regions without self-intersections. The topological invariants were different on different sides of the self-intersection regions. Worse, periodic orbits that had zero topological entropy in the differential phase-space embedding (which we will describe next) turned up after self-intersections with different symbolic names. These names suggest that these orbits have positive topological entropy. That there is no inconsistency is the consequence of a subtle theorem dealing with the topological properties of the map to the Poincaré section. That is, changing the time delay changes the boundary conditions on the mapping of the Poincaré section onto itself. This in turn changes the properties of braids in the flow. Mancho, Duarte, and Mindlin (1996) studied a parametrically forced oscillator and found results compatible with those shown in Fig. 51 and reported by Mindlin and Solari (1995).

The occurrence of self-intersections in this time-delay embedding is not a violation of either the weaker (Packard *et al.*, 1980; Mañé, 1981; Takens, 1981) or the stronger (Sauer, Yorke, and Casdagli, 1991) embedding theorem, since the actual dimension in which the attempted embedding occurred was less than the bound provided by either theorem. The result shows that three-dimensional embeddings are possible, but one must be very careful in interpreting the topological invariants that result, as they could depend on the parameters chosen for the embedding.

## B. Differential phase-space embedding

### 1. $x, \dot{x}, \ddot{x}$

Our background as physicists encourages us to look for cause-effect relations among the components of the embedding vector. To this end, we construct an embedding in which each component is the derivative of the previous component:

$$\begin{aligned} x(t) \rightarrow y(t) &= (y_1(t), y_2(t), y_3(t)) \\ &= (x(t), dx/dt, d^2x/dt^2). \end{aligned} \quad (10.4)$$

This embedding leads directly to a set of equations of motion and a canonical way to model the data

$$\begin{aligned} y_1 &= x(t) && \text{(definition of } y_1), \\ dy_1/dt &= y_2 && \text{(definition of } y_2), \\ dy_2/dt &= y_3 && \text{(definition of } y_3), \\ dy_3/dt &= f(y_1, y_2, y_3) && \text{(physics lives here)}. \end{aligned} \quad (10.5)$$

The entire modeling process reduces to attempts to construct one unknown scalar function:  $f(y_1, y_2, y_3)$ .

This differential embedding procedure has strengths and weaknesses. One strength is that it is Newtonian in

spirit, and leads directly to a simple modeling procedure. Furthermore, there is only one function to estimate rather than three.

A second strength is that the linking numbers can be computed by inspection in this embedding. In Fig. 52 we show two orbits projected into the  $x-\dot{x}$  plane, with  $\dot{x}$  out of the plane of the page. We compute the slopes at the intersection:

$$\text{slope} = \frac{d\dot{x}}{dx} = \frac{d\dot{x}/dt}{dx/dt} = \frac{y_3}{y_2}. \quad (10.6)$$

As a result

$$y_3 = \text{slope} \times y_2. \quad (10.7)$$

This means that the larger the slope at a crossing in the upper ( $y_2 > 0$ ) half plane, the nearer the observer. Conversely, the larger the slope in the lower half plane, the further from the observer. Thus all crossings in the upper half plane are left-handed and therefore negative by convention. All crossings in the lower half plane are positive.

Yet another nice feature of the differential phase-space embedding is the existence of a Poincaré section, and a simple one at that. In Fig. 53 we show the projection onto the  $y_2$ - $y_3$  subspace. It is a simple matter to show that the flow follows the indicated directions. All crossings of the  $y_3$  axis with  $y_2 = 0$  are to the right when  $y_3 > 0$  (since  $dy_2/dt = y_3$ ) and to the left when  $y_3 < 0$ . As a result, we can use the half plane consisting of the  $y_1$  axis with  $y_2 = 0$  and  $y_3 > 0$  as a Poincaré section. This observation can be phrased more simply as follows: a local maximum is always followed by a local minimum, which is followed by another local maximum.

The differential phase-space embedding has a serious weakness: it depends on construction of the second derivative. As a general rule of thumb, an order of magnitude is lost in the signal-to-noise ratio each time a derivative (or integral) is taken. Loss of two orders of magnitude degrades the embedding to the extent that the topological organization of unstable periodic orbits may be difficult to compute, even with very clean data sets.

### 2. $\int x, x, \dot{x}$

Rather than abandon the differential phase-space embedding in which the three components of the embedding vector  $\mathbf{y}(t)$  are differentially related to each other, we define  $y_1$  to be the integral of  $x(t)$  and  $y_3$  to be the derivative of  $x(t)$ . To avoid secular trends, we perform the embedding on the zero-mean data set  $x(t) - \langle x \rangle_t$ :

$$\begin{aligned} y_1(t) &= \int_{-\infty}^t (x(t') - \langle x \rangle_t) dt', \\ y_2(t) &= \frac{dy_1}{dt} = x(t), \\ y_3(t) &= \frac{dy_2}{dt} = \frac{dx}{dt}. \end{aligned} \quad (10.8)$$

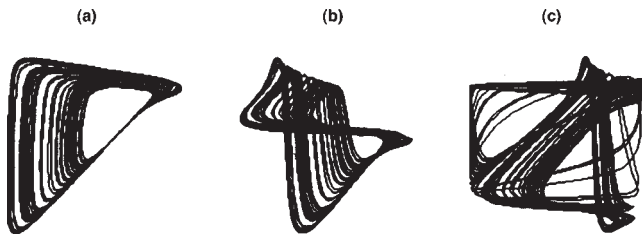


FIG. 51. Embedding attempts using three time delays. (a) Very small delay. (b) Intermediate delay. (c)  $\tau \sim \frac{3}{4}T$ . The attractor undergoes a self-intersection between (a) and (c). Topological invariants differ in the two embeddings (a) and (c).

In this embedding the signal-to-noise ratio of the components  $y_1$  and  $y_3$  is only about one order of magnitude smaller than that of  $y_2$ .

The integral-differential embedding suffers from the problem that long period (or secular) variations of the data create havoc with the component  $y_1(t)$ . Such long period variations are impossible to detect in delay embeddings and differential phase-space embeddings.

The problem can be removed by a low-frequency filter. Filtering can also be done in the time domain by integrating backwards over a small number of cycles:

$$y_1(t) = \int_0^{+\infty} x(t-t')e^{-t'/\tau} dt', \quad (10.9)$$

where  $\tau$  is a “memory time.” That is, the integration has a memory time of length  $\tau$ . The derivative of  $y_1$  must then be modified slightly:

$$\frac{dy_1}{dt} = x(t) - \frac{1}{\tau} y_1(t). \quad (10.10)$$

It is a simple matter to construct this embedding from the discretely sampled data set:

$$\begin{aligned} y_1(i) &= x(i) + e^{-1/\tau} y_1(i-1), \\ y_2(i) &= x(i), \\ y_3(i) &= x(i) - x(i-1). \end{aligned} \quad (10.11)$$

The beauty of this embedding is that it can be done on-line with simple circuit elements.

**C. Embeddings with symmetry**

The presence of symmetry in an attractor creates possibilities that we have not yet encountered. We illustrate these possibilities for the Lorenz equations. These equations are invariant under rotations by  $\pi$  radians about the  $z$  axis:

$$(x, y, z) \xrightarrow{R_z(\pi)} (-x, -y, +z). \quad (10.12)$$

This symmetry tells us that the  $x$  and  $y$  variables behave differently from the  $z$  variable. A differential phase-space embedding based on the  $z$  variable is shown in Fig. 54(a). It is clear from this figure that there is no simple *topological* transformation, nor any 1-1 algebraic transformation, that will map this attractor onto the

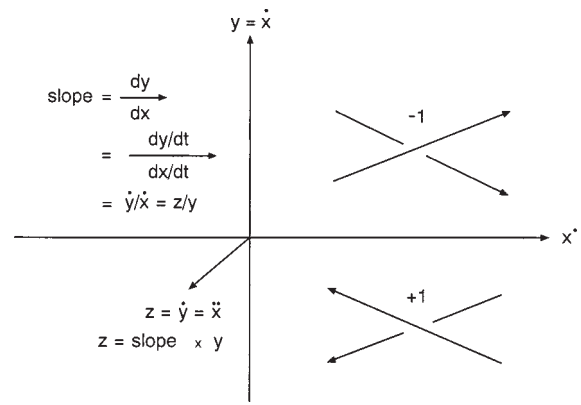


FIG. 52. Differential phase-space embedding. In this projection  $\ddot{x}$  is toward the observer. All crossings in the upper half plane are left handed; those in the lower half plane are right handed.

more familiar Lorenz attractor [see Fig. 16(c)]: one has two holes, the other only one.

On the other hand, a differential phase-space embedding based on the  $x$  or  $y$  variable has more possibilities. The projection onto the  $\dot{x}$ - $\dot{x}$  plane for Lorenz data is shown in Fig. 54(b). The embedding

$$\begin{aligned} y_1 &= x, \\ y_2 &= \dot{y}_1 = \dot{x}, \\ y_3 &= \dot{y}_2 = \ddot{x} \end{aligned} \quad (10.13)$$

has inversion symmetry:

$$(y_1, y_2, y_3) \xrightarrow{P} (-y_1, -y_2, -y_3). \quad (10.14)$$

As a result, it cannot be deformed to the Lorenz attractor, which has a rotation symmetry. On the other hand, the embedding

$$\begin{aligned} y_1 &= x, \\ y_2 &= \dot{y}_1 = \dot{x}, \\ y_3 &= \dot{y}_2^2 = 2y_2 \dot{y}_2 \end{aligned} \quad (10.15)$$

possesses symmetry under rotation through  $\pi$  radians about the  $z$  axis,

$$(y_1, y_2, y_3) \xrightarrow{R_z(\pi)} (-y_1, -y_2, +y_3), \quad (10.16)$$

suggesting that this embedding can be deformed to the familiar Lorenz attractor. We shall demonstrate this deformation explicitly in Sec. XII.

**D. Coupled-oscillator embeddings**

At the present time the methods of topological analysis are restricted to three-dimensional phase spaces because knots “fall apart” in higher dimensions. There is the hope that topological methods will be developed so that stretching and squeezing mechanisms can be identified in higher-dimensional spaces.

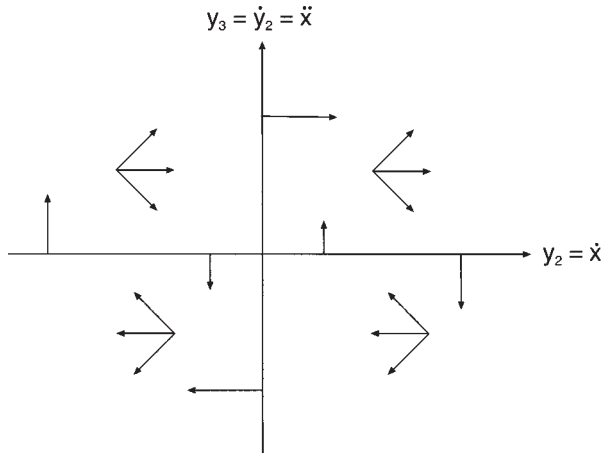


FIG. 53. Projection of the differential phase-space embedding onto the  $y_2$ - $y_3$  plane. This projection clearly shows the flow directions. Either half plane bounded by the  $y_1$  axis with  $y_2 = 0$  can serve as a Poincaré section. In fact, any half plane containing the  $y_1$  axis will serve as a Poincaré section.

It is not likely that the differential phase-space embedding technique can be extended much beyond three-dimensional phase spaces because of the signal-to-noise problem. Therefore we shall have to rely on other embedding methods. One natural fallback is the time-delay method. However, it is lacking in dynamics.

Another embedding method, with more dynamics, involves a combination of time delay and Hilbert transform pairs. In this procedure,  $4, 6, \dots, 2n$  dimensional embeddings are created from scalar data sets by the mapping

$$x(t) \rightarrow (z_1(t), z_2(t), \dots, z_n(t)). \quad (10.17)$$

Each  $z_j(t)$  is complex,

$$z_j(t) = x_j(t) + iy_j(t),$$

where  $y_j(t)$  is the Hilbert transform of  $x_j(t)$ . The complex variables are time-delay related to each other,

$$z_{j\pm 1}(t) = z_j(t \pm \tau),$$

where  $\tau$  is about  $\frac{1}{4}$  of the characteristic cycle time.

The motivation behind this coupled-oscillator representation is as follows: Each complex coordinate  $z_j(t)$  behaves more or less like the coordinates  $[x_j(t), y_j(t)]$  of a nonlinear oscillator. Successive oscillators  $z_j(t)$  and  $z_{j\pm 1}(t)$ , which are  $\pi/2$  radians out of phase, might be expected to interact strongly with each other.

This embedding possesses the strength of the time-delay embedding (equal signal-to-noise ratio in all real coordinates) as well as the strength of the differential phase-space embedding (strong dynamic coupling between  $x_j$  and  $y_j$ ; probably strong coupling between  $z_j$  and  $z_{j\pm 1}$ ). Its weakness is that modeling the dynamics will involve  $n$  complex functions of  $n$  complex variables:

$$\frac{dz_j}{dt} = f_j(z_1, z_2, \dots, z_n). \quad (10.18)$$

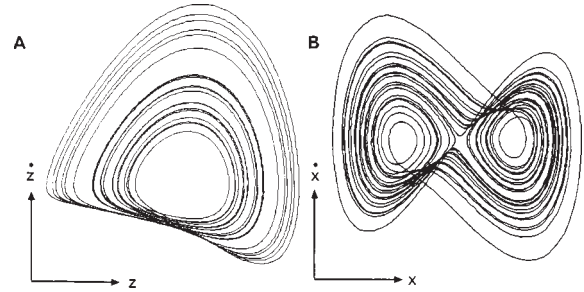


FIG. 54. Differential phase-space embeddings for the Lorenz system generated by (a)  $z$ -data and (b)  $x$ -data.

### E. Singular-value decomposition embeddings

As is apparent from Sec. VIII.D, the singular-value decomposition can also be used as an embedding tool (Broomhead and King, 1986). The  $n$  time-series  $v(j, \alpha)$  which can be constructed from a scalar time-series  $x(j)$ , can be used as embedding variables. Construction of these time series is shown explicitly for scalar data in Eqs. (8.7)–(8.9).

### F. Singular-value decomposition projections

On occasion time-series data arrive that are not scalar, but involve data fields in one, two, or even three space dimensions. Then we have the opposite problem of reducing the data to a small number of time-series coordinates. The singular-value decomposition has also been applied to do just that (Chauve and LeGal, 1992; Alvarez, 1996). This procedure has been shown explicitly in Eqs. (8.5) and (8.6). The spatial modes complementary to the time series are called empirical orthogonal functions. Projection of data fields onto a small number of time series, each coupled to an empirical orthogonal function, is the numerical equivalent of Galerkin projection of partial differential equations onto a set of ordinary differential equations for amplitudes, each of which is coupled to an analytic spatial mode.

## XI. HORSESHOE MECHANISM ( $A_2$ )

A moderate number of physical systems have already been studied by the topological methods described above. In many of the cases studied, chaotic behavior is generated by the same mechanism. This has been summarized as stretching and folding: the mechanism that generates the Smale (1967) horseshoe. In all such cases the squeezing mechanism is folding, as seen in the Rössler attractor. This mechanism accounts for chaotic behavior seen, for some range of control parameters, in the Belousov-Zhabotinskii reaction, the laser with saturable absorber, the laser with modulated losses, the NMR laser, the bouncing ball experiment, and a stringed instrument. We describe the analysis of one of these data sets (for the Belousov-Zhabotinskii reaction) in detail in Sec. XI.A. Features of other analyses not encountered in the Belousov-Zhabotinskii analysis are

treated in subsequent subsections. We describe the difference between a “robust” topological description and an “invariant” topological description in terms of a recent experiment. In the final subsection we return to the question of why this particular mechanism is so common and why we have designated it  $A_2$ .

### A. Belousov-Zhabotinskii reaction

We have carried out an extensive topological analysis of data generated by the Belousov-Zhabotinskii reaction (Mindlin *et al.*, 1991). The data were generated in experiments carried out by the Texas group (Roux, Simoyi, and Swinney, 1983; Richetti *et al.*, 1987; Argoul *et al.*, 1987). These data were studied in a topological context by Lathrop and Kostelich (1989) before methods were developed for extracting branched-manifold information, and the integer invariants that characterize such information, from chaotic data.

#### 1. Embedding

The data set that we analyzed consisted of 64K scalar measurements of  $\log[\text{Br}^-]$ , the logarithm of the bromine ion concentration. The sampling rate was uniform, with about 120 samples/cycle. The entire data set that we studied contained 543 cycles. The data were recorded in the range from about 14 000 to 20 000. The data set was very clean. This was determined directly by inspection and was verified by the absence of high-frequency terms in the power spectrum. The cycle time was determined by finding the average peak-to-peak distance (65,536/543~120), the highest frequency peak in the power spectrum, and the lowest delay peak in the close-returns histogram. A segment of the data set is shown in Fig. 55. By inspection, the system exhibits relaxation oscillations.

Our first attempt to analyze the data involved a differential phase-space embedding. The results are shown in Fig. 56(a). In this figure we plot  $dx/dt$ , as approximated by  $x(i+1) - x(i)$ , against  $x(i)$ . The difference  $x(i+1) - x(i)$  is about two orders of magnitude smaller than the signal. As can be seen, all crossings occur in the horizontal section of the plot and cannot be resolved. The second derivative was estimated by the second difference  $d^2x/dt^2 \sim x(i+1) - 2x(i) + x(i-1)$ . This was smaller than the signal by an additional two orders of magnitude, bringing it down to the noise level.

At this stage we knew the differential-embedding attempt would be defeated by the signal-to-noise problem. Our first attempt at an integral-differential embedding is shown in Fig. 56(b). This figure provides a plot of  $y_2(i) = x(i)$  vs  $y_1(i) = \sum_{j=1}^i x(j)$ . As the phase-space projection was being created, it was possible to clearly see the attractor drift slowly across the screen. (This is one of the virtues of using a small old computer for these analyses.) This was clearly a signal of nonstationarity. Two procedures were used to make the data stationary: low-frequency filtering and time-domain filtering. Low-frequency (Fourier) filtering actually returned a data set that was indistinguishable from the original at the reso-

lution of the screen display (20 000 – 14 000 = 6000 vs 500 pixels vertically). The integral and derivative coordinates were constructed from this filtered data set in both the time and frequency domains.

Frequency-domain and time-domain embedding led to indistinguishable strange attractors. Since time-domain filtering did not alter the data set, it was the preferred method, and the one used for this analysis. In this procedure, the embedding is created “on-line”:

$$\begin{aligned} y_1(i) &= \sum_{j \leq i} e^{-\lambda(i-j)} x(j) = x(i) + e^{-\lambda} y_1(i-1), \\ y_2(i) &= x(i), \\ y_3(i) &= x(i) - x(i-1). \end{aligned} \quad (11.1)$$

The beautiful embedding shown in Fig. 57 was produced in this way. Since the attractor has a hole in the center, a one-parameter family of Poincaré sections was available. The inset shows how this embedding can be performed on-line with simple circuit elements.

#### 2. Periodic orbits

Unstable periodic orbits were extracted from the data by the method of close returns. This method was initially applied to the flow data and resulted in close-returns plots of the type shown in Fig. 48. A few surrogates for periodic orbits were located this way. However, such close-returns plots were unwieldy because of the large size of the data set.

To facilitate the search for periodic orbits, we identified successive intersections (543 of them) with a Poincaré section. This information was used to create a first-return map. Two first-return maps are shown in Fig. 50. These were created for Poincaré sections defined by successive minima and successive maxima [ $y_3(i) = 0$ ]. Both return maps have a single critical point, which suggests strongly that a two-letter alphabet suffices to label orbits uniquely and that the template has two branches. Furthermore, the return-map data indicate a smooth fold deformation in phase space by the dynamics, so that one branch of the template is orientation preserving (0) and the other orientation reversing (1).

Period- $p$  orbits were located as described in Sec. IX.B.2. That is, we searched for sufficiently close intersections with the Poincaré section that were  $p$  periods apart. The corresponding segment of data was then extracted from the data file and considered a candidate for an unstable periodic orbit. The symbolic name of this surrogate orbit was determined by locating successive iterates of its initial point on the first-return plot. Following this procedure, we were able to locate and identify surrogate data segments for all the unstable periodic orbits shown in Table VII. We were also able to encode all but one of the data segments between the 543 intersections with the Poincaré section in terms of the two-letter alphabet. This encoding was ultimately used to locate three periodic orbits not located by the close-returns search.

The topological invariants of the surrogate unstable periodic orbits extracted from the data were computed.

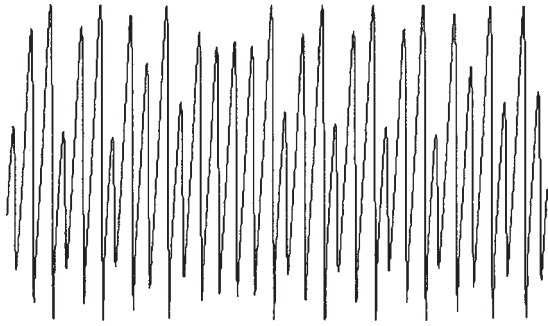


FIG. 55. A segment of the Belousov-Zhabotinskii time series on which the topological analysis was carried out.

In Fig. 58 we show a period-two and a period-three orbit extracted from the data. By counting the number of signed crossings, the self-linking numbers of these two orbits are  $-1$  and  $-2$ , respectively. In Fig. 58(c) these two orbits are superposed. Their linking number ( $-2$ ) is half the number of signed crossings of one with the other. These calculations are simple because all crossings in the upper half plane are negative, while those in the lower half plane are positive. The linking numbers for the unstable periodic orbits to period eight, extracted from the data, are summarized in Table VIII.

In Fig. 59 we show how the relative rotation rates for these two orbits were computed. The segments of the three orbits between the Poincaré section are numbered: (1,2,3) in temporal order for the period-three orbit, and (4,5) in order for the period-two orbit. A permutation matrix  $P$  is constructed for each orbit. This matrix summarizes the dynamics. Under forward-time evolution on the period-three orbit,  $1 \rightarrow 2 \rightarrow 3 \rightarrow 1 \dots$ . The direct sum of the two permutation matrices indicates how the five orbit segments are permuted under forward-time evolution.

The two orbits are superposed and a crossing matrix  $C$  is constructed. The matrix elements  $C(i,j)$  are the signed number of times orbit segment  $i$  crosses orbit segment  $j$ . For example, on its way from the Poincaré section defined by successive minima back to the Poincaré section, orbit segment 2 crosses in succession 3 ( $-1$ ), 5 ( $-1$ ), 4 ( $-1$ ), 1 ( $-1$ ), 1 ( $+1$ ), and 4 ( $+1$ ). Thus  $C(2,3) = -1$ ,  $C(2,5) = -1$ , and  $C(2,k) = 0$ , where  $k = 1, 2, 4$ . The crossing matrix is symmetric.

The crossing matrix contains linking and self-linking information on two orbits  $A$  and  $B$ . The linking number of two orbits is half the sum of the matrix elements in either off-diagonal block  $C(A,B)$  or  $C(B,A) = C(A,B)^T$ . The self-linking number is half the sum of the matrix elements in the appropriate block-diagonal submatrix  $C(A,A)$  or  $C(B,B)$ .

The crossing and permutation matrices can be used to compute the relative rotation rates as well. Initial conditions on segments  $i$  and  $j$  will cross  $C(i,j)$  times. After one period,  $i \rightarrow Pi, j \rightarrow Pj$ , so the initial conditions will cross  $(P^{-1}CP)(i,j)$  times. Since  $P$  is orthogonal,  $P^{-1} = P^T$ . After a full set of  $p_A \times p_B$  iterations, the total number of crossings is the sum of these similarity transformations. Thus

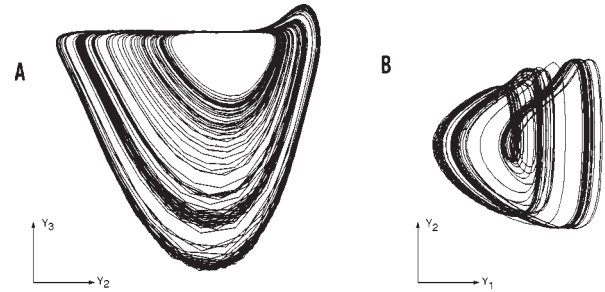


FIG. 56. (a) Projection of the differential phase-space embedding of the Belousov-Zhabotinskii data into the  $x$ - $\dot{x}$  plane. (b) Projection of the integral-differential phase-space embedding into the  $\int x$ - $x$  plane. Drift in the horizontal ( $y_1$ ) direction shows nonstationarity of the integral.

$$p_A \times p_B \times RRR = \sum_{k=0}^{p_A \times p_B - 1} (P^T)^k C P^k. \quad (11.2)$$

Here  $RRR$  is the matrix of relative rotation rates. For the period-two and period-three orbits, this matrix is shown in Fig. 59. From this matrix we see that the period-three orbit has self-relative rotation rates  $(-\frac{1}{3})^6 0^3$ , the period-two orbit has self-relative rotation rates  $(-\frac{1}{2})^2 0^2$ , and the period-two and period-three orbits have relative rotation rates  $(-\frac{1}{3})^6$ . The relative rotation rates for all surrogate orbits up to period eight extracted from the Belousov-Zhabotinskii data are summarized in Table IX. In fact, these results, particularly the self-relative rotation rates, are extremely useful in associating the correct symbol name to a data segment representing an unstable periodic orbit. For example, the self-relative rotation rates of the two different period-eight orbits clearly identifies  $8a$  as a member of the cascade  $(1_1 \rightarrow 2_1 \rightarrow 4_1 \rightarrow 8_1)$  and  $8b$  as the well-ordered orbit  $8_3$ .

### 3. Template identification

A template is identified algebraically by the linking numbers and local torsions of the period-one and period-two orbits. For the Belousov-Zhabotinskii data, these are the orbits 0, 1, and 01. Since there was no surrogate for the period-one orbit 0, template information must be extracted using a different low-period orbit. We used the next-lowest-period orbit 011 for this purpose.

If the local torsions of the period-one orbits 0,1 are  $l(0), l(1)$ , the local torsion of a period- $p$  orbit with  $p_0$  symbols 0 and  $p_1$  symbols 1 is  $p_0 l(0) + p_1 l(1)$ . We computed the local torsion for several low-period orbits. This was done by observing the “linking number” for two or more different surrogates for the same orbit. We observed directly that  $l(1) = -1$ . We also observed that  $l(01) = -1$  and  $l(011) = -2$  and so inferred that  $l(0) = 0$ . In addition, we saw no evidence of a nonzero global torsion in the embedding (Fig. 57). As a result, we identified the template matrix as

$$T = \begin{bmatrix} 0 & 0 \\ 0 & -1 \end{bmatrix},$$

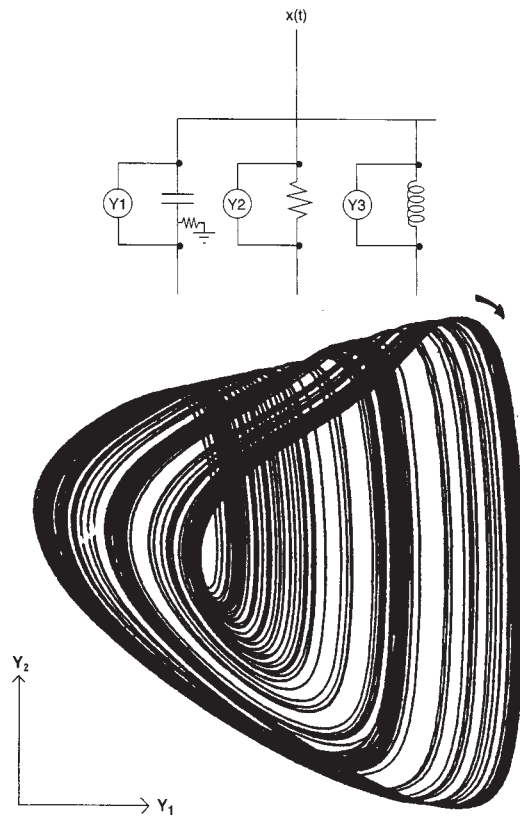


FIG. 57. Projection of the integral-differential phase-space embedding into the  $\int x$ - $x$  plane. The integral is carried out with exponentially decreasing memory. Inset shows how this embedding can be carried out on-line.

$$A = [0 \quad m], \quad m = +1. \quad (11.3)$$

To construct the array, we computed some linking numbers for both choices ( $m = \pm 1$ ). One choice ( $m = +1$ ) was compatible with the data; the other was not and was therefore rejected.

#### 4. Template verification

To verify the template identification, we computed linking numbers and relative rotation rates for all orbits extracted from the data. Each period- $p$  orbit was tentatively identified by a symbol sequence. Topological invariants were computed on the template for the symbol sequence.

The linking numbers and relative rotation rates computed for the symbol sequences listed in Table VII agreed with the linking numbers and relative rotation rates computed directly from the surrogates (Tables VIII and IX, respectively). All linking numbers, self-linking numbers, relative rotation rates, and local torsions are negative. The negative signs have not explicitly been included on Tables VII, VIII, and IX. This agreement provided the self-consistency check we needed to conclude that (a) the template identified from the low-period orbits was correct, and (b) the symbol sequence associated with each surrogate periodic orbit was correct. We repeat and emphasize a point made above. Identifying a template and naming surrogates for peri-

TABLE VII. Periodic orbits located in data from the Belousov-Zhabotinskii reaction by the method of close returns. The symbol  $M$  indicates the cut point between orientation-preserving and orientation-reversing branches of the first-return map. All topological indices are negative.

Orbit	Name	Symbolics	Local torsion	Self-linking
1	$1_1$	1	1	0
2	$2_1$	01	1	1
3	$3_1$	011	2	2
4	$4_1$	0111	3	5
5	$5_1$	01011	3	8
6	$6_2$	0110M1	3	9
7	$7_2$	0101011	4	16
8a	$8_1$	01010111	5	23
8b	$8_3$	01011011	5	21
9	$9_3$	$(01)^3 011$	5	28
10a	$10_6$	$(011)^2 0101$	6	33
10b	$10_6$	$(011)^2 0111$	7	33
11	$11_9$	$01(011)^3$	7	40
13a		$(01)^2 011010111$	8	62
13b		$(01)^3 0110111$	8	60
13c		$(011)^3 0101$	8	56
13d		$(011)^3 0111$	9	56
13e		$(01)^2 011011111$	9	62
14		$01(011)^4$	9	65
15		$01(011)^2 0111011$	10	78
16a		$(01)^3 (011)^2 0111$	10	89
16b		$(011)^4 0101$	10	85
16c		$(011)^4 0111$	11	85
16d		$(01)^2 (011)^2 011111$	11	91
17a		$(01)^3 01101(011)^2$	10	102
17b		$(011)^5 01$	11	96
17c		$(01)^2 01101(0111)^2$	11	108

odic orbits are not local problems: both must be settled simultaneously and consistently.

#### 5. Basis set of orbits

We used the method described in Sec. VI.C to construct a basis set of orbits for the strange attractor induced from the Belousov-Zhabotinskii data. Up to period eight, the basis set consists of the orbits  $7_2$ ,  $6_2$ , and  $8_3$ . These three orbits force all the other orbits of period  $p \leq 8$  found in the data. They also force three orbits not located by the method of close returns:  $6_1$ ,  $7_1$ , and  $8_2$ .

It is possible that the three orbits  $6_1$ ,  $7_1$ , and  $8_2$  were not located because they are not embedded in the attractor. It is also possible that they were not located because the phase-space point never wandered close enough to any of these orbits to evolve in its neighborhood for the full  $p (= 6, 7, 8)$  periods required to locate it by the method of close returns. In that case they would be located if the data set were longer.

To see if the existence of these three orbits was compatible with the data set, we searched for them using the

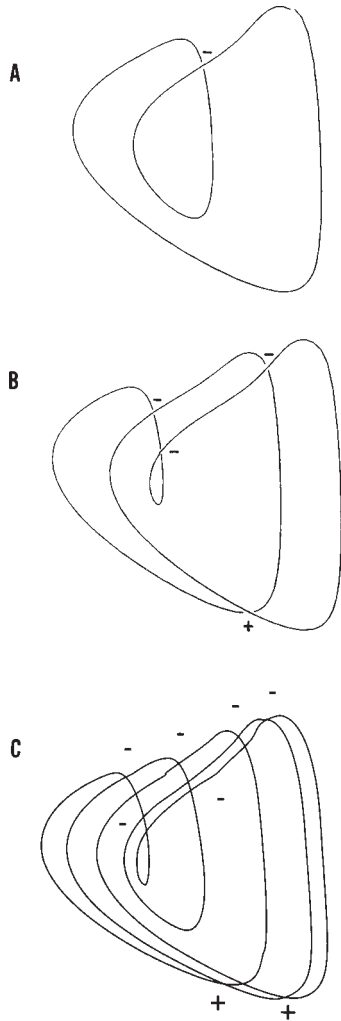


FIG. 58. (a) Period-two orbit and (b) period-three orbit extracted from the Belousov-Zhabotinskii data. Signed number of crossings is the self-linking number. (c) The two orbits are superposed to compute their linking number, which is half the signed number of crossings.

metric methods described in Sec. IX.C. For each orbit, we were able to locate segments in the data set that passed threshold tests and could be used as pieces of surrogate orbits. More convincingly, for each of the

TABLE VIII. Linking numbers for orbits extracted from the Belousov-Zhabotinskii data. All indices are negative.

		1	2	3	4	5	6	7	8a	8b
1	1	0	1	1	2	2	2	3	4	3
2	01	1	1	2	3	4	4	5	6	6
3	011	1	2	2	4	5	6	7	8	8
4	0111	2	3	4	5	8	8	11	13	12
5	01011	2	4	5	8	8	10	13	16	15
6	0110M1	2	4	6	8	10	9	14	16	16
7	0101011	3	5	7	11	13	14	16	21	21
8a	01110101	4	6	8	13	16	16	21	23	24
8b	01011011	3	6	8	12	15	16	21	24	21

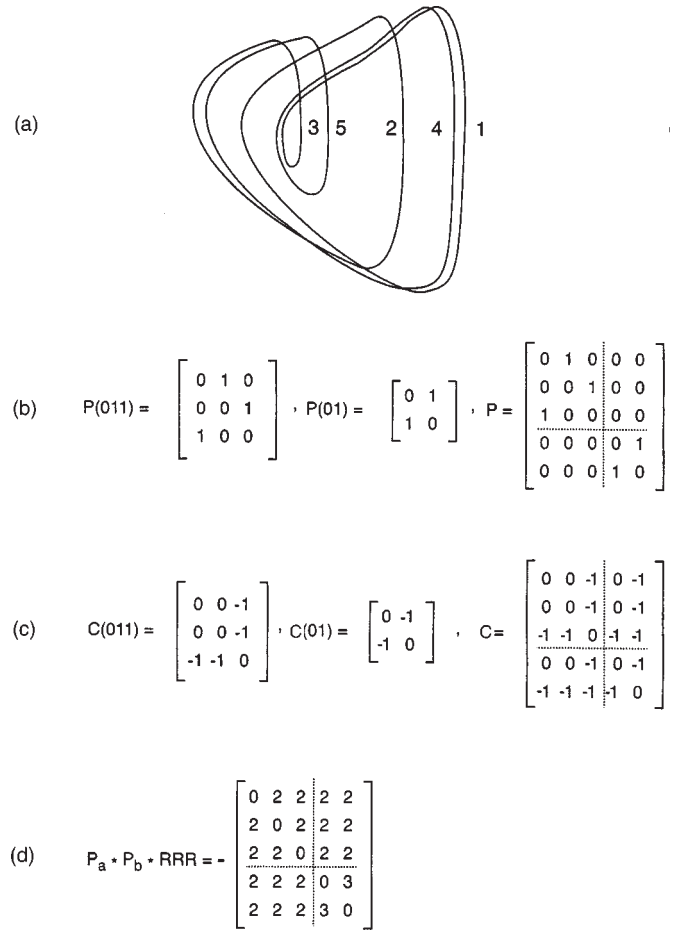


FIG. 59. (a) Period-three and period-two orbits. (b) Permutation matrices for these orbits and for all five orbit segments. (c) Crossing matrices for the two separate orbits and for all five orbit segments. (d) Matrix of relative rotation rates for 10 pairs of initial conditions.

three orbits only two segments from the data set were required, each representing two or more periods. We present the period-six orbit in Fig. 60(a). Since it would be easy to hide discontinuities, the ends of the orbit are made within a segment extracted from the data. The two end points are guaranteed to have equal values. The discontinuities associated with matching segments occur within the trace displayed, and are specifically indicated by arrows. They are smaller than the screen resolution. In Fig. 60(b) we present the phase-space plot of this orbit. The period-seven and -eight orbits behave similarly.

## 6. Modeling the dynamics

A standard procedure for creating models for a dynamical system  $\dot{y} = F(y; c)$  involves using the data to estimate the function  $F(y; c)$ . These functions are expanded as linear superpositions of basis functions  $\Phi_\beta(y)$ , and various methods are used to estimate the coefficients  $A_\beta$  in the general linear model

TABLE IX. Relative rotation rates for orbits extracted from the Belousov-Zhabotinskii data, to period 8. All relative rotation rates are negative.

	1	2	3	4	5	6	7	8a	8b
1	0								
2	$\frac{1}{2}$	$\frac{1}{2}0$							
3	$\frac{1}{3}$	$\frac{1}{3}$	$(\frac{1}{3})^2 0$						
4	$\frac{1}{2}$	$\frac{1}{2} \frac{1}{4}$	$\frac{1}{3}$	$(\frac{1}{2})^2 \frac{1}{4} 0$					
5	$\frac{2}{5}$	$\frac{2}{5}$	$\frac{1}{3}$	$\frac{2}{5}$	$(\frac{2}{5})^4 0$				
6	$\frac{1}{3}$	$\frac{1}{3}$	$\frac{1}{3}$	$\frac{1}{3}$	$\frac{1}{3}$	$(\frac{1}{3})^4 \frac{1}{6} 0$			
7	$\frac{3}{7}$	$\frac{5}{14}$	$\frac{1}{3}$	$\frac{11}{28}$	$\frac{13}{25}$	$\frac{1}{3}$	$(\frac{3}{7})^4 (\frac{2}{7})^2 0$		
8a	$\frac{1}{2}$	$\frac{1}{2} \frac{1}{4}$	$\frac{1}{3}$	$(\frac{1}{2})^2 \frac{3}{8} \frac{1}{4}$	$\frac{2}{5}$	$\frac{1}{3}$	$\frac{3}{8}$	$(\frac{1}{2})^4 (\frac{1}{4})^2 \frac{3}{8} 0$	
8b	$\frac{3}{8}$	$\frac{3}{8}$	$\frac{1}{3}$	$\frac{3}{8}$	$\frac{3}{8}$	$\frac{1}{3}$	$\frac{3}{8}$	$\frac{3}{8}$	$(\frac{3}{8})^7 0$

$$\frac{dy}{dt} = F(y;c) = \sum_{\beta} A_{\beta} \Phi_{\beta}(y). \tag{11.4}$$

There is no guarantee that a model of this general linear form will be a good model for the nonlinear dynamical system. However, until better modeling methods are proposed, such models will be adopted. Many different procedures exist for choosing the basis functions and carrying out estimation of the model parameters  $A_{\beta}$ . These have been discussed extensively in recent reviews (Abarbanel *et al.*, 1993; Abarbanel, 1996).

Most procedures involve a choice of functions  $\Phi_{\beta}(y)$ , together with an invariant measure on the attractor  $\rho(y)$ , which is estimated from the data and the embedding. With respect to this measure a natural inner product

$$g_{\beta\beta'} = \langle \Phi_{\beta} \Phi_{\beta'} \rangle = \int \Phi_{\beta}(y) \Phi_{\beta'}(y) \rho(y) dy \tag{11.5}$$

can be constructed. The parameters  $A_{\beta}$  in the general linear model (11.4) are then estimated by standard statistical techniques: the maximum likelihood or, more often, least-squares method. These involve computing the inverse of the matrix of overlap integrals, which can be delicate. If the functions  $\Phi_{\beta}$  are constructed to be orthonormal, say by the Gram-Schmidt procedure, then  $g_{\beta\beta'} = \delta_{\beta\beta'}$  and the matrix inversion is simple. However, the problem has then been pushed back to construction of the orthonormal basis set, which is then delicate.

To indicate the flavor of this delicacy, we sketch two examples. The first is classical. The Legendre polynomials  $P_n(x)$  can be constructed from the matrix of overlaps

$$g_{ij} = \langle x^i x^j \rangle = \int_{-1}^{+1} x^i x^j dx = \begin{cases} \frac{2}{i+j+1}, & i+j \text{ even,} \\ 0, & i+j \text{ odd.} \end{cases} \tag{11.6}$$

An LDU (lower triangular, diagonal, upper triangular) decomposition (Press *et al.*, 1986) is then used to rewrite the overlap,

$$g_{ij} = \sum_{\tau \leq \min(i,j)} L_{i\tau} D_{\tau} U_{\tau j}, \tag{11.7}$$

where  $L$  and  $U$  are lower and upper, respectively, triangular matrices with +1 on the diagonal. The diagonal matrix element  $D_{\tau}$  provides the normalization factor. The matrix elements of  $D$  decrease very rapidly ( $D_{\tau} \sim 10^{-7}$ ), making this numerical procedure for constructing these classical functions very sensitive to noise in the measure [ $\rho(x) = 1 + \text{noise}$ ].

As a second example, suppose we try to model data generated by the logistic map  $x_{j+1} = \lambda x_j (1 - x_j)$  by a model with basis set  $x_i, x_i^2, x_{i-1}, x_{i-1}^2$ :

$$x_{i+1} = Ax_i + Bx_i^2 + Cx_{i-1} + Dx_{i-1}^2. \tag{11.8}$$

Then, since  $x_i = \lambda x_{i-1} (1 - x_{i-1})$ , the basis set has a degeneracy, and any attempt to invert the matrix of overlaps  $g_{\beta\beta'}$  or orthonormalize the basis set is subject to instabilities due to this degeneracy among the basis vectors.

Rather than fight these singularities, we have developed a model-fitting procedure that effectively avoids them. More precisely, it explicitly exhibits degenerate directions in the space of basis vectors, including one direction in which  $dy/dt$  is degenerate with the expansion functions  $\Phi_{\beta}$ . The idea is to create a model in which the time derivative  $dy/dt$  is also treated as a basis vector ( $\Phi_0$ ), on the same footing as the other basis vectors  $\Phi_{\beta}$ . Then the desired equation (11.4) can be written as

$$B_0 \Phi_0 + \sum_{\beta} B_{\beta} \Phi_{\beta}(y) \sim 0, \tag{11.9}$$

with  $B_0 \neq 0$ . An  $N \times (1 + D)$  matrix is generated for the  $1 + D$  coefficients  $B_0$  and  $B_{\beta}$  from the  $N$  observations in the usual way (Draper and Smith, 1966). A singular-value decomposition is performed. Eigenvectors corresponding to nonzero (large) eigenvalues are not model candidates. Eigenvectors corresponding to small eigenvalues express degeneracies among the basis vectors, one of which is now  $dy/dt$ . To determine the appropriate eigenvector for the model, we search for the maximum of  $[\lambda(\alpha)/B_0(\alpha)]^2$ . For this eigenvector

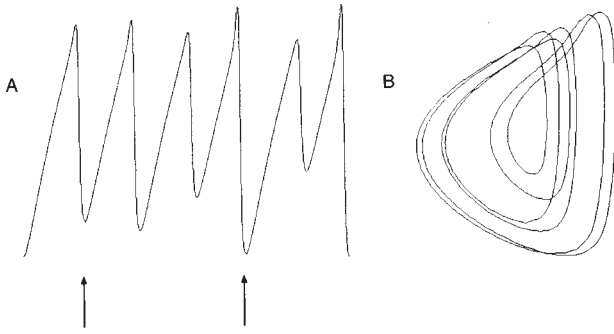


FIG. 60. (a) Surrogate orbit of period six reconstructed from the data using metric methods. Location of joins between different segments of data are indicated by arrows. (b) Embedding of this orbit in phase space.

$$B_0(\alpha) \frac{dy}{dt} + \sum_{\beta} B_{\beta}(\alpha) \Phi_{\beta}(y) \sim \epsilon. \quad (11.10)$$

The model (11.4) and (11.9) is then explicitly

$$\begin{aligned} \frac{dy}{dt} = F(y) &= \sum_{\beta} A_{\beta} \Phi_{\beta}(y) \\ &= \sum_{\beta} -\frac{1}{B_0(\alpha)} B_{\beta}(\alpha) \Phi_{\beta}(y) + \epsilon', \end{aligned} \quad (11.11)$$

where the stochastic term is  $\epsilon' = \epsilon/B_0(\alpha)$ .

This same eigenvalue procedure can be extended to create rational fractional models using as a basis set  $\Phi_0$ ,  $\Phi_{\beta}$ , and  $\Phi_0\Phi_{\beta}$  and defining a vector of the form

$$D_0\Phi_0 + \sum_{\beta} C_{\beta}\Phi_{\beta} + \sum_{\beta \neq 0} D_{\beta}\Phi_0\Phi_{\beta} + \epsilon. \quad (11.12)$$

Following the same procedure, we find a best fit model

$$\frac{dy}{dt} = \frac{-\sum_{\beta} C_{\beta}(\alpha) \Phi_{\beta}(y)}{D_0(\alpha) + \sum_{\beta \neq 0} D_{\beta}(\alpha) \Phi_{\beta}(y)} + \epsilon', \quad (11.13)$$

with least-squares residual  $[\lambda(\alpha)/D_0(\alpha)]^2$ .

This modeling procedure was applied to the Belousov-Zhabotinskii data in the embedding

$$\begin{aligned} \dot{y}_1 &= -\lambda y_1 + x(t), \\ \dot{y}_2 &= \dot{x} = y_3 \end{aligned} \quad (11.14)$$

to determine the single function  $f(y_1, y_2, y_3)$ , which determines the dynamics

$$\frac{dy_3}{dt} = f(y_1, y_2, y_3). \quad (11.15)$$

We used as a basis set the functions

$$\Phi_{\beta} = y_1^{\beta_1} y_2^{\beta_2} y_3^{\beta_3}, \quad (11.16)$$

with maximum degree  $\beta_1 + \beta_2 + \beta_3 \leq d$ . The total number of basis functions  $\Phi_{\beta}$  involved for a fit of maximum degree  $d$  is  $\binom{d+n}{3}$ , where  $n=3$ . For models of degree  $d=3,4,5$ , this number is 20,35,56. For rational fractional models of the type (11.12) and (11.13), with maximum degree  $d_n$  and  $d_d$  in the numerator and denominator, the eigenvector that determines the model has dimension  $\binom{d+n_n}{3} + \binom{d+n_d}{3}$ .

We have fitted the function  $f(y_1, y_2, y_3)$  to polynomial models with  $d=3,4,5$  and to rational fractional models with  $d_d = d_n - 1$ ,  $d_n = 3,4,5$ . In the cases studied the rational fractional models initially provided a closer approximation to the data than a polynomial model with  $d = d_n$ . However, the denominator in the rational fraction eventually went through zero, completely destroying any semblance of reasonable modeling. This occurs because the singular-value decomposition averages over data values. Data excursions to which Eq. (11.13) is very sensitive have very little effect on averages of the form (11.5), from which the singular-value decomposition is constructed.

In fact, polynomial models also show difficulty in accurately following the data. A polynomial model contains a large number of terms, all more or less of the same magnitude when evaluated on the attractor. The model requires that the sum of a large number of approximately equal terms be a small number.

## 7. Model validation

We have observed that free-running models of chaotic systems often either blow up or settle into a limit cycle or limit point (Alvarez, 1996). In the minority of circumstances in which a model generates chaotic data it is possible to test topological (qualitative) equivalence with the original experimental data.

To make a quantitative test of equivalence, we carried out a modification of the Fujisaka and Yamada (1983) test described earlier. The test that we used has been described by Pecora and Carroll (1990). In this test we define  $\mathbf{y}^m$  to be the model variables and  $\mathbf{y}^d$  to be the data variables. The original data set is  $x(i) = y_2(i)^d$ . We then construct a model as described in Sec. XI.A.6:

$$\frac{d\mathbf{y}^m}{dt} = F(\mathbf{y}^m). \quad (11.17)$$

In this model the function  $F$  is an eigenvector of a matrix after a singular-value decomposition. This model is driven by the data, which means we replace  $F(\mathbf{y}^m) = F(y_1^m, y_2^m, y_3^m)$  by  $F(y_1^m, x, y_3^m)$ . Then we compare  $y_1^m$  with  $y_1^d$  and  $y_3^m$  with  $y_3^d$ . This comparison is done for models of degree  $d=3,4,5$ . The results are shown in Fig. 61 for the case  $d=5$ .

In this figure the two time traces (a) are  $y_1^m(t)$  and  $y_1^d(t)$ . They are slightly displaced for purposes of comparison. The two traces (b) are  $y_3^m(t)$  and  $y_3^d(t)$ ; they are also purposely displaced. The straight diagonal line (c) is a plot of  $y_1^m(t)$  vs  $y_1^d(t)$ , while (d) is a plot of  $y_3^m(t)$  vs  $y_3^d(t)$ . Entrainment between  $y_1^m(t)$  and  $y_1^d(t)$  is easy. Entrainment between  $y_3^m(t)$  and  $y_3^d(t)$  is difficult. Plot (d) shows that the data entrain the model. That is, the model is a reasonably accurate representation of the dynamics.

For the model of degree four the plots look similar, except that plot (d) does not show entrainment quite as strongly. Models with  $d < 4$  were not entrained by the data.

Rational fractional models showed a higher degree of entrainment for substantial parts of the data set before they blew up because of denominator instability.

## B. Laser with saturable absorber

The laser with saturable absorber consists of a CO<sub>2</sub> laser with an absorbing cell placed inside the cavity. Various materials have been used as absorbers. The important point is that they are nonlinear media because they saturate as the beam intensity increases (Dangoisse *et al.*, 1988; Hennequin *et al.*, 1988; Lefranc, Hennequin, and Dangoisse, 1991).

A number of experimental data sets were taken on the laser with saturable absorber. The two different absorbers used were CH<sub>3</sub>I:He in the ratio 1:20 and OsO<sub>4</sub>:He in the same ratio. The physical (control) parameters that were varied from run to run included absorber pressure, discharge current, and frequency detuning. The laser was run under conditions that generated chaotic output signals. For each run data were sampled at ~80 samples/cycle. Long scalar time series, up to 32K 8-bit data, were stored in a microcomputer using a digital oscilloscope. A segment of one time series is shown in Fig. 62.

We analyzed about 25 runs from the laser under various operating conditions (Papoff *et al.*, 1992). The objective was to test the hypothesis that the topological organization of the strange attractor remained invariant under all changes in operating conditions. We were seeking experimental confirmation of our statement that, as control parameters are varied, (a) topological indices remain invariant and (b) the flow in phase space is directed over different parts of the branched manifold.

To test these claims a topological analysis was performed on each data set. We were able to extract at least four unstable periodic orbits from each data set. Each was identified by a symbol name drawn from the alphabet ( $L$ =large peak,  $S$ =small peak). The linking numbers of these orbits were computed and compared with those for orbits draped over a Smale horseshoe template under the identification  $L \leftrightarrow 1$  (orientation reversing),  $S \leftrightarrow 0$  (orientation preserving). For each run the strange attractor that was identified was a Smale horseshoe template that was independent of absorber and control parameter values.

We tested these results against four models that had been proposed to describe the system. Two (Lefranc, Hennequin, and Dangoisse, 1991; Zambon, 1991) were three-dimensional models, one (Hong *et al.*, 1989) was four-dimensional, and one (Hennequin *et al.*, 1988) was five-dimensional. In each model, in the chaotic regime there was one positive Lyapunov exponent, one zero exponent, and the remainder were negative. The four- and five-dimensional models were strongly contracting, so the Birman-Williams theorem could be applied to the model output. In each case the mechanism in the model that was responsible for generating chaotic behavior was

a homoclinic connection. As a result, all models were compatible with the result of the topological analysis of the data.

During the course of these analyses we made two observations. The first was that the unstable periodic orbits extracted from data sets seemed to occur in groups. That is, every time a certain orbit was found, a particular set of other orbits accompanied it. This observation encouraged us to study orbit-forcing relations in horseshoe dynamics. The end result was the horseshoe-implication diagram (Fig. 38). Furthermore, this led us to propose that the discrete classification of strange attractors (algebraic classification of branched manifolds for *hyperbolic* dynamics) could be further resolved by another discrete enumeration, a set of basis orbits whose presence forces the existence of all other orbits present. Finally, this led us to propose that routes to chaos could be discretely enumerated (to any finite period  $p$ ) on the horseshoe template, as well as other templates.

The second observation was that the symbol sequence in these data sets was almost predictable. If the symbol sequence is encoded with the numbers 0 and 1, and  $Q(P)$  is the number of symbols +1 after  $P$  periods, then we wondered if  $Q(P)/P$  was approximately constant as a function of  $P$ . This result was found in the Belousov-Zhabotinskii data, with  $Q(P)/P = \frac{2}{3} - \epsilon$  ( $\epsilon < 10^{-2}$ ). To investigate this question, we performed this test on a number of data files. In Fig. 63 we show these plots for the Belousov-Zhabotinskii data (left-hand side) and for three experimental data files for the laser with saturable absorber taken under different operating conditions (right-hand side).

## C. Laser with modulated losses

The laser with modulated losses was described in Sec. I. A number of data files from the laser with modulated losses and the laser with saturable absorber were difficult to analyze. A partial time trace from one of these files is shown in Fig. 64. The output consists of several peaks, with each group of peaks separated by a very low intensity output. So low, in fact, that all intensities measured during these dead time intervals wound up in the same last channel of the multichannel analyzer. As a result, there is no honest way to determine orbit-crossing information in these regions. One could impose the rule of thumb that the higher the peak, the lower the succeeding minimum. However, this is equivalent to putting in an answer "by hand." It would therefore be useful if a topological analysis could be carried out when topological information is missing.

### 1. Poincaré section mappings

Solari, Natiello, and Vazquez (1996) have provided a robust solution to the above problem. The solution depends on the existence of a Poincaré section and the ability to construct one. This is always possible for a scalar time series. The Poincaré section is associated with local maxima.

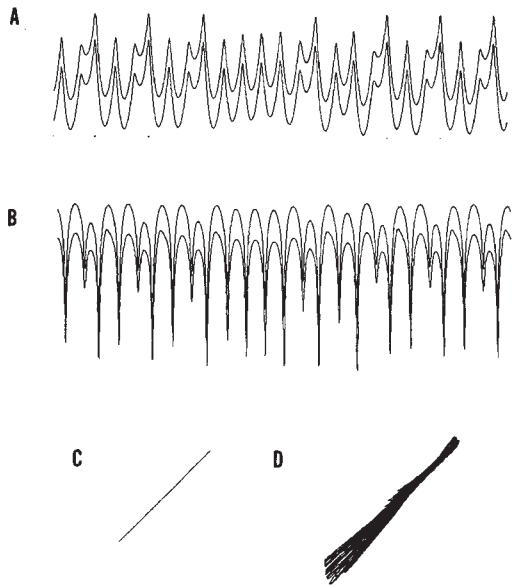


FIG. 61. Time traces of (a)  $y_1^m(t)$  and  $y_1^d(t)$  and (b)  $y_3^m(t)$  and  $y_3^d(t)$ . The traces are slightly offset for purposes of comparison. Plots of (c)  $y_1^m(t)$  vs  $y_1^d(t)$  and (d)  $y_3^m(t)$  vs  $y_3^d(t)$ . Calculations are done for a degree-five model of the Belousov-Zhabotinskii data. Results show entrainment.

Once a Poincaré section is constructed, a period-one return map becomes available. This is used to locate unstable periodic orbits by the usual methods. As usual, the more orbits the better. However, even one long-period ( $p > 4$ ) orbit is useful. At this point it is normally impossible to assign a symbol sequence to any of the orbits unless the return map is one dimensional. We assume it is not, as is the case for weakly dissipative systems.

This method proceeds by constructing a braid for the action of the map on periodic orbit(s). We illustrate the idea in Fig. 65. Here we show the five intersections of a period-five orbit with the Poincaré section. Assume that under forward iteration we have  $1 \rightarrow 2 \rightarrow 4 \rightarrow 3 \rightarrow 5 \rightarrow 1$ . This mapping deforms the Poincaré section, as indicated by its action on the links between adjacent points  $i$  and  $i+1$ . By connecting  $i$  to  $P(i)$  we create the outline of a flow in  $R^3$ . As more periodic orbits are included, the outline of the flow becomes clearer.

The key now is to project these flow lines onto a plane while keeping crossing information. This projection, shown in Fig. 65(c), shows the first three segments outlining a zero-torsion template branch. The other two segments lie in another template branch, which folds behind the first. The period-five orbit provides a skeleton that outlines a two-branch Smale horseshoe template. Additional periodic orbits can be added to this projection to fill out the details. Flow segments not belonging to periodic orbits can be introduced to determine the local torsion in some parts of the flow.

The projection of the segments in  $R^3$  representing the flow from section to section down to  $R^2$  plays the same role here as the identification (4.2) in the Birman-Williams theorem, which deflates flows in  $R^3$  down to

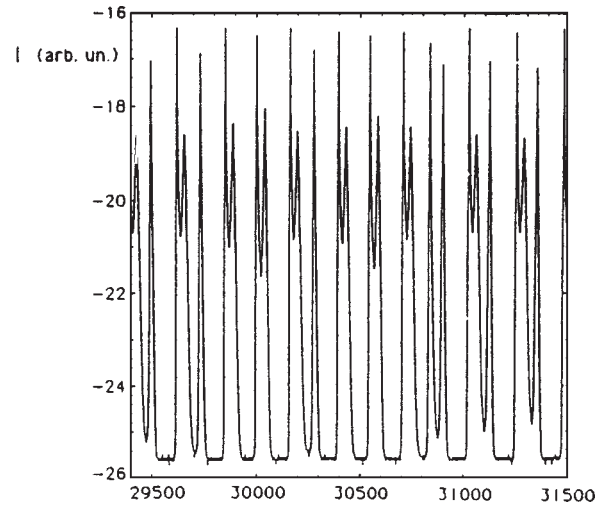


FIG. 62. A segment of time series from the laser with saturable absorber.

two-dimensional branched manifolds. This procedure is not completely equivalent to a topological analysis because global torsion information is lost (Solari and Gilmore, 1988). It is not always safe to assume that global torsion is zero: the systematic increase in global torsion is what provides regularity in the superstructure of the bifurcation diagram for the Duffing oscillator (Gilmore and McCallum, 1995). Horseshoe dynamics with systematically increasing global torsion has also been observed in laser experiments (Boulant *et al.*, 1997b; see Sec. XI.E).

## 2. Projection to a Poincaré section

Solari, Natiello, and Vazquez (1996) used a singular-value decomposition to project data from a laser with saturable absorber down to a Poincaré section. The procedure was as follows. Each peak in the data was located. The value of the intensity at the maximum and at  $k$  ( $\sim 20$ ) equally spaced points on both sides of the maximum was recorded. Since the signal usually wasn't recorded exactly at the peak, this information had to be interpolated. To these  $2k+1$  pieces of information one other piece of information was added: the distance to the next peak. Thus each of  $N$  peaks was identified by a point in a  $2k+2$  dimensional space, creating a data set  $Z(i,j)$  ( $1 \leq i \leq N$ ;  $1 \leq j \leq 2k+2$ ).

This  $N \times (2k+2)$  data matrix was then subjected to a singular-value decomposition. Normally only a small number of eigenvalues was sufficient. The  $d$  coordinates  $z_\alpha(i)$ ,  $\alpha = 1, 2, 3, \dots, d$ , for the  $i$ th peak in the Poincaré section were computed as overlaps with the  $2k+2$  dimensional eigenvectors  $v(j;\alpha)$ :

$$z_\alpha(i) = \sum_{j=1}^{2k+2} Z(i,j) v(j;\alpha), \quad \alpha = 1, \dots, d. \quad (11.18)$$

Then the return map is simply

$$z(i) \rightarrow z(i+1). \quad (11.19)$$

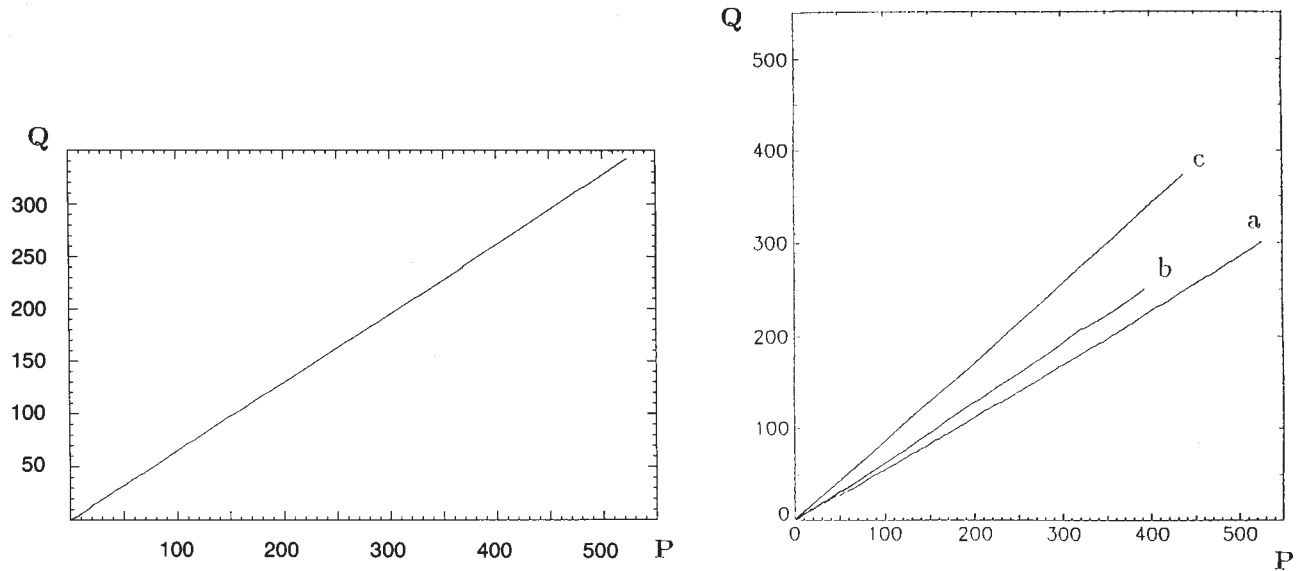


FIG. 63. Plot of the cumulative number of passes through orientation reversing branch as a function of total number of periods. Left-hand side: For Belousov-Zhabotinskii data. Right-hand side: For the laser with saturable absorber under three operating conditions (absorber, amplifier current, pressure): (a) ( $\text{CH}_3\text{I}:\text{He}$ , 10.9 mA, 0.1 mbar), (b) ( $\text{OsO}_4:\text{He}$ , 9.3 mA, 0.73 mbar), (c) ( $\text{OsO}_4:\text{He}$ , 9.3 mA, 0.47 mbar).

This return map was used to locate periodic orbits. These orbits were then projected down to  $R^2$  to construct the braid that outlined the template. This outline also provided the symbol name for the unstable periodic orbits.

### 3. Result

As with so many other systems, this analysis showed that chaotic behavior was generated by the stretching and folding mechanism characteristic of the Smale horseshoe. The deformation of the Poincaré section, as outlined by the braid (the more segments, the better), was then used to construct an estimate for the topological entropy of this map. The topological entropy is independent of the global torsion.

### D. Other systems exhibiting $A_2$ dynamics

A number of other experiments have been analyzed in which chaotic behavior is generated by the same stretching and folding mechanism. One of these is the NMR laser (Tufillaro *et al.*, 1991). We have used one of the period-four orbits extracted from this experimental data set to illustrate how relative rotation rates can be computed for driven dynamical systems simply by inspection (see Fig. 14). Data from a bouncing ball experiment (Tufillaro, Abbott, and Reilly, 1992; Tufillaro, 1994) also show a Smale horseshoe mechanism. So also do data generated by a stringed instrument (Tufillaro *et al.*, 1995). The analyses were carried out as described above.

### E. “Invariant” versus “robust”

Up to this point we have stated at various times that the topological (template) description of a strange attractor is “invariant” or “robust” under control-parameter variation, but we have not made a precise distinction between these two concepts. These two concepts are slightly different; we describe their differences in this section.

A strange attractor is the closure of an unstable invariant set. For the attractors studied so far, this is the outset of an unstable low-period (period-one) orbit or its surrogate, an unstable saddle fixed point. The branched manifold associated with the unstable invariant set has, in general, an infinite number of branches ( $A, B, C, D, \dots$ ), only a small number of which are explored by the flow.

In many situations only a small number (e.g.,  $B, C$ ) of branches are explored by the flow. As the control pa-

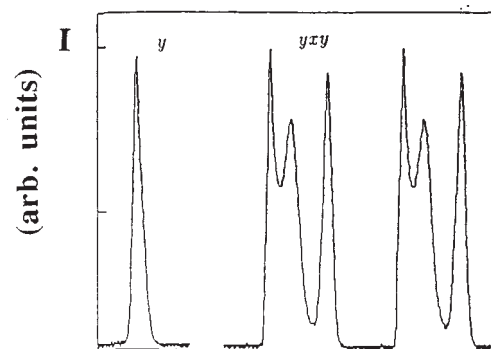


FIG. 64. Intensity trace for laser output, showing intervals of dead time between output spikes. These dead-time intervals make topological analyses difficult.

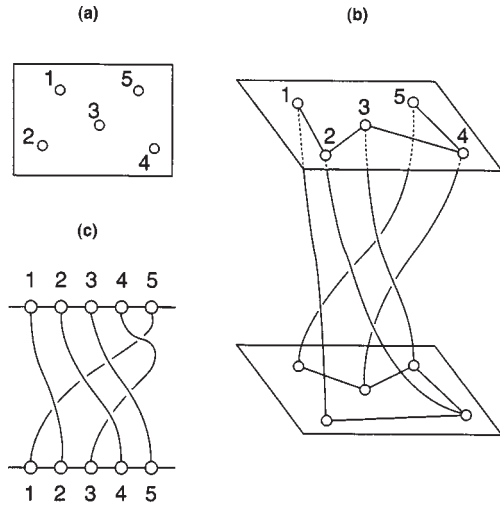


FIG. 65. (a) Five intersections of a period-5 orbit with a Poincaré section. (b) Flow lines from one section to itself. The flow deforms the phase space as indicated by the wrinkling of the segments connecting points in the Poincaré section. (c) Projection of the braid in (b) onto a plane  $R^2$ , keeping crossing information. The braid segments outline the template branches.

rameters are varied over a not-too-large range, the flow is pushed around but is confined to these branches. However, a larger change in control parameter values may cause the flow to explore new branches not previously explored (e.g.,  $D, E$ ) and to stop visiting branches previously explored (e.g.,  $B$ ). The changes in the control parameters cause changes in the template:  $(B, C) \rightarrow (C, D, E)$ . We say the underlying template is “robust” if it is unchanged under small control-parameter variations, but large control-parameter changes cause a change in the underlying template. We say the topological description is “invariant” if the underlying template is unchanged no matter how large the control-parameter variation is. In this case the underlying template  $(A, B, C, D, E, F, \dots)$  is invariant. Small changes in control parameters cause the flow to explore different regions of the two initially explored branches  $(B, C)$ , and larger changes force the flow to explore different regions  $(C, D, E)$  of the same invariant template.

This situation was discussed in detail for the Duffing oscillator by Gilmore and McCallum (1995) from a theoretical perspective (see Sec. XII) and first discussed in the context of an experiment by Boulant *et al.* (1997b). We now describe this experiment and its analysis.

The experiment was carried out on a  $\text{Nd}^{3+}$  doped-fiber laser. The laser consisted of a 4-in length of silicon optical fiber doped with 300 ppm  $\text{Nd}^{3+}$ . This fiber-optic cable was pumped by a laser diode operating at 810 nm. The equations describing the laser intensity  $I(t)$  and the population inversion  $D(t)$  are essentially [see Eq. (1.1)]

$$\begin{aligned} dI/dt &= I(D - 1), \\ dD/dt &= \gamma[A - D(1 + I)]. \end{aligned} \quad (11.20)$$

The pump was modulated sinusoidally,  $A = A(t) = A_0(1 + m \cos \omega t)$ , where in suitable dimensionless units  $A_0 = 2.7$  and  $m = 0.6$ . The control parameter for

this experiment was the modulation frequency  $\omega$ . The most important physical parameter for this experiment was the laser relaxation frequency  $\omega_\tau = 36$  kHz.

The response of this periodically modulated fiber laser varied as the modulation frequency  $\omega$  was slowly varied. Boulant *et al.* observed an alternation between chaotic and periodic behavior. Islands of chaotic behavior occurred around subharmonics of the relaxation frequency,  $\omega_{1/2} \sim 18$  kHz,  $\omega_{1/3} \sim 12$  kHz,  $\omega_{1/4} \sim 9$  kHz:

$$\omega_\tau \sim 2\omega_{1/2} \sim 3\omega_{1/3} \sim 4\omega_{1/4} \quad (\sim n\omega_{1/n}). \quad (11.21)$$

These islands of chaotic behavior did not overlap. They were connected by regions in which a single period-one orbit was observed.

The strange attractor within each island of chaotic behavior was analyzed. The first step involved estimation of the Lyapunov exponents. In each of the islands studied ( $n = 2, 3, 4$ )  $\lambda_1$  was positive,  $\lambda_2$  was zero, and  $\lambda_3$  was more negative than  $\lambda_1$  was positive:  $\lambda_3 < -\lambda_1$ . As a result, each strange attractor possessed a Lyapunov dimension  $d_L < 3$ . Furthermore,  $d_L$  remained less than three for each attractor while it existed as  $\omega$  was swept through  $\omega_{1/n}$ . This means that “most of the dynamical variables relax so quickly that they are enslaved by a few number of collective variables which are confined to a three-dimensional manifold” (Boulant *et al.*, 1997b). Thus, a topological analysis was possible for each of the strange attractors associated with the subharmonics  $\omega_{1/n}$ ,  $n = 2, 3, 4$ .

The unstable periodic orbits, to period five, extracted from the three chaotic data sets, are presented in Table X. For the orbits shown a two-branch template was sufficient to describe each attractor. The symbols  $x$  and  $y$  represent a passage through an orientation-preserving and -reversing (respectively) branch of the template. In each of the three cases studied the underlying template was a Smale horseshoe template. However, the global torsion (Solari and Gilmore, 1988) differed systematically from one attractor to the next. Specifically, the template matrix for the attractor in the subharmonic region  $\omega_{1/n}$  was

$$\begin{bmatrix} 0 & 0 \\ 0 & 1 \end{bmatrix} + (n-1) \begin{bmatrix} 2 & 2 \\ 2 & 2 \end{bmatrix}. \quad (11.22)$$

The global torsion for the attractors in  $\omega_{1/2}, \omega_{1/3}, \omega_{1/4}$  was 1, 2, 3 ( $n-1$ ). The corresponding templates are shown in Fig. 66.

Within an island of chaotic behavior, as the control parameter sweeps through  $\omega_{1/n}$  orbits are first created by saddle-node and period-doubling bifurcations as the strange attractor is formed. They are then destroyed by inverse period-halving and saddle-node bifurcations as the attractor is destroyed. During this “perestroika” the flow is “pushed around” on the template whose two branches are  $(x, y)$ . On entering the next island of chaotic behavior around the subharmonic  $\omega_{1/(n+1)}$ , periodic orbits are created for another strange attractor described by a different pair of branches.

In this description the template invariants are robust. They are unchanged while  $\omega$  is varied in a small range about  $\omega_{1/n}$ , but change (in a systematic way) for larger changes in  $\omega$ .

An alternative interpretation of these experimental results is possible. In this interpretation, we identify the three pairs of branches in the three regions as branches of a single “large” template. Each branch is labeled (uniquely here) by its local torsion. Thus, in the subharmonic region  $\omega_{1/2}$ , the orientation-preserving branch  $x$  has local torsion 2 while the orientation-reversing branch  $y$  has local torsion 3. In region  $\omega_{1/n}$ ,  $x$  has local torsion  $2(n-1)$  and  $y$  has local torsion  $2(n-1)+1$ . In Table X we present alternative names for the unstable periodic orbits according to this branch labeling scheme (e.g.,  $xy \rightarrow 23$  in  $\omega_{1/2}$ ;  $\rightarrow 45$  in  $\omega_{1/3}$ ;  $\rightarrow 67$  in  $\omega_{1/4}$ ). In this case the underlying “large” template is invariant. Changing the control parameters by a small amount forces the flow to explore new regions in one part (2,3) of the large template, and changing the control parameters by a larger amount forces the flow to explore different, adjacent branches (4,5) of the same “large” template.

Remark: This change in perspective, from robust to invariant, is not merely cosmetic in nature. It has predictive value. For example, the following predictions can be made (Gilmore and McCallum, 1995):

(i) The global torsion of the subset of the “large” template that is explored changes in a systematic way.

(ii) Between each pair of chaotic islands there are two stable and one unstable period-one orbits. They are “snaked” together. Their local torsions are closely related to the global torsions of the strange attractors that bound the regions of period-one behavior. Hysteresis will be observed in reversing the direction of sweep of the control parameter  $\omega$ .

(iii) If other control parameters are varied, the islands of chaotic behavior can begin to overlap (e.g.,  $\omega_{1/3}$  and  $\omega_{1/4}$ ). For these control-parameter values, periodic orbits will be built up from an alphabet consisting of four symbols [e.g., (4,5) and (6,7)]. Furthermore, orbit creation and annihilation must occur in a systematic way on this 4-branch subset of the “large” template.

(iv) For suitable control-parameter values, flows on reverse horseshoes (1,2),(3,4), . . . can occur. These have already been observed in experiments (Boulant *et al.*, 1997a).

(v) Flows over three (or more) adjacent branches should also be possible. These have been observed in simulations (Boulant *et al.*, 1997c).

It is possible to construct chaotic flows in which a very large number of branches [1,2,3, . . . ,  $n$  ( $n \rightarrow \infty$ )] are explored (Silnikov, 1965; Guckenheimer and Holmes, 1983). In this case, each branch is labeled uniquely by its local torsion. In other flows, local torsion does not serve to label distinct branches uniquely. In such cases the Birkhoff and higher signatures (Abraham and Shaw, 1984) provide a more refined description of the topology of the unstable invariant manifold and therefore the to-

TABLE X. Unstable periodic orbits extracted from three different strange attractors observed in the Nd<sup>3+</sup> fiber laser.

Period	$\omega_{1/2}$		$\omega_{1/3}$		$\omega_{1/4}$	
1	$x$		$y$	5	$y$	7
2	$xy$	23	$xy$	45	$xy$	67
3	$x^2y$	2 <sup>2</sup> 3			$xy^2$	67 <sup>2</sup>
4	$x^2y^2$	2 <sup>2</sup> 3 <sup>2</sup>	$xy^3$	45 <sup>3</sup>	$xy^3$	67 <sup>3</sup>
5			$xy^4$	45 <sup>4</sup>		
					$x^2y^3$	6 <sup>2</sup> 7 <sup>3</sup>
					$x^2yxy$	6 <sup>2</sup> 767
			$xyxy^2$	4545 <sup>2</sup>	$xyxy^2$	6767 <sup>2</sup>

political structure of the associated branched manifold. The Birkhoff index can change as the control parameters change.

## F. Why $A_2$ ?

We have already intimated (in Sec. XI.B) why the Smale horseshoe mechanism occurs so frequently in physical systems. Horseshoes occur in the neighborhood of homoclinic connections. When only one saddle appears to be present, the only kind of saddle connection possible is a homoclinic connection.

In fact, what is happening in each of the systems that we have analyzed is that the flow is controlled by a saddle with one real eigenvalue and one complex conjugate pair of eigenvalues. Usually the real eigenvalue is stable and the “spiral” eigenvalue is weakly unstable. The flow spirals away from this saddle. When it is far enough away, it enters the sphere of influence of another saddle. The flow approaches this other saddle along its stable direction(s) and leaves along the unstable direction(s). The outflow from this companion saddle is the action that produces the folding in the neighborhood of the organizing spiral saddle.

This process is evident in the Rössler attractor. There are two fixed points for this set of equations for all parameter values. These fixed points can be located by setting all time derivatives equal to zero. For interesting conditions the fixed points are real. For some range of parameter values they are complex. The transition from complex to real occurs in a fold catastrophe ( $A_2$ ) (Gilmore, 1981). At the bifurcation, the nonzero eigenvalues of the two degenerate critical points are identical. As the critical points move away from each other the nonzero eigenvalues do not change their stability type, while the zero eigenvalue becomes negative for one critical point and positive for the other. It appears that all autonomous dynamical systems we have described in this section are governed by two critical points, one of which organizes the motion and is responsible for stretching, the other of which is basically invisible and is

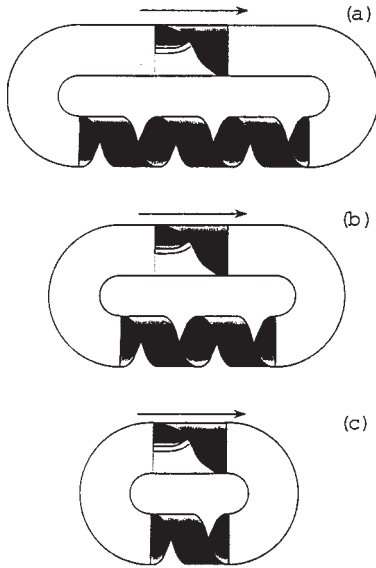


FIG. 66. Templates for the strange attractors of the fiber-optic laser. In the subharmonic regions  $\omega_{1/n}$  the template has global torsion  $n-1$ . Top to bottom:  $n=4,3,2$ . Reprinted with permission from G. Boulant *et al.*, 1997a.

responsible for squeezing (folding). These two saddles are created in an  $A_2$  (fold) catastrophe for some set of control-parameter values. This mechanism is suggested in Fig. 67.

## XII. LORENZ MECHANISM ( $A_3$ )

If the Rössler mechanism is the hydrogen-atom problem of nonlinear dynamics, then the Lorenz mechanism is its hydrogen molecule. In this section we will describe two types of systems that exhibit the Lorenz mechanism for generating chaotic behavior. We first describe a laser. More specifically, we describe a model for an optically pumped molecular laser. We then describe a fluid experiment that exhibits the characteristics modeled by the Lorenz equations.

### A. Optically pumped molecular laser

In 1975, Haken shocked the laser physics community by showing that one of the standard laser models was equivalent to the Lorenz equations in a certain limit. This stimulated a great deal of experimental and theoretical work that has not yet subsided.

Haken (1975) showed that the equations describing a coherently pumped, homogeneously broadened ring laser reduce to the Lorenz equations under the following conditions: (a) the atomic resonance is equal to a cavity resonance (zero detuning); (b) the rotating-wave approximation is made; (c) the field is uniform; and (d) the slowly varying envelope approximation is valid. This observation about the properties of a laser model introduced the ideas of nonlinear dynamics into the field of laser physics. It stimulated the use of lasers as tools to study nonlinear phenomena. Since the Haken-Lorenz model is so elementary, the questions were raised as to

whether (a) lasers actually behaved this way and (b) realistic models of lasers could be constructed that exhibited these properties.

Early experiments to address these questions were carried out by Lawandy and Koepef (1980), Lefebvre, Dangoisse, and Glorieux (1984), Weiss and Klisch (1984), Abraham *et al.* (1985), Harrison, Al-Saidi, and Biswas (1985), Harrison and Biswas (1985), Weiss (1985), and Weiss and Brock (1986). These experiments, and the theoretical descriptions of these experiments, were carried out on optically pumped molecular lasers. This class of lasers seemed most likely to operate in a regime compatible with dynamics of Lorenz type. The first review of this field was by Biswas *et al.* (1986). Thereafter, work on this problem accelerated. The first review was succeeded by many others: Abraham, Mandel, and Narducci (1988), Narducci and Abraham (1988), Weiss and Vilaseca (1991), Arecchi and Harrison (1993), Khanin (1995), and Roldán *et al.* (1997).

### 1. Models

An optically pumped molecular laser consists of a molecular gas ( $\text{NH}_3$ ,  $\text{CH}_2\text{F}_2$ ,  $\text{CH}_3\text{F}$ ,  $\text{HF}$ ,  $\text{HCOOH}$ , ...) confined to a laser cavity. The gas is coherently excited by another laser, typically a  $\text{CO}_2$  or  $\text{NO}_2$  laser. The molecule is excited to a vibrational state; lasing involves de-excitation through a rotational state. This produces an output signal in the range  $30 \mu\text{m}$  to  $1000 \mu\text{m}$ . Since both vibrational and rotational transitions occur, a minimum of three molecular levels is involved.

The dynamics is expressed in terms of an equation of motion for the electric field  $E(t)$  and the molecular density operator  $\rho$ . This is a  $3 \times 3$  Hermitian matrix ( $\rho^\dagger = \rho$ ,  $\text{Tr } \rho = 1$ ) describing the occupation probabilities and correlations among three molecular states  $|0\rangle$ ,  $|1\rangle$ , and  $|2\rangle$ . The dynamical equations for the molecular subsystem are

$$\begin{aligned}\dot{\rho}_{00} &= \gamma_0(n_0 - \rho_{00}) - 2\alpha \text{Im } \rho_{10} - 2\beta \text{Im } \rho_{20}, \\ \dot{\rho}_{11} &= \gamma_1(n_1 - \rho_{11}) + 2\alpha \text{Im } \rho_{10}, \\ \dot{\rho}_{22} &= \gamma_2(n_2 - \rho_{22}) + 2\beta \text{Im } \rho_{20}, \\ \dot{\rho}_{10} &= -[\gamma_{10} + i(\Delta_c + \dot{\phi})]\rho_{10} + i\alpha(\rho_{00} - \rho_{11}) - i\beta\rho_{12}, \\ \dot{\rho}_{20} &= -[\gamma_{20} + i\Delta_2]\rho_{20} - i\alpha\rho_{12} + i\beta(\rho_{00} - \rho_{22}), \\ \dot{\rho}_{12} &= -[\gamma_{12} + i(\Delta_c + \dot{\phi} - \Delta_2)]\rho_{12} + i(\alpha\rho_{02} - \beta\rho_{10}).\end{aligned}\quad (12.1)$$

In these equations, level zero is shared by the vibrational ( $2 \leftrightarrow 0$ ) and the rotational ( $1 \leftrightarrow 0$ ) transitions. The field evolution is coupled to the molecular evolution through

$$\begin{aligned}E(t) &= \alpha(t)e^{-i\phi(t)}, \\ \dot{\alpha} &= -\kappa\alpha + g \text{Im } \rho_{10}, \\ \dot{\phi} &= -g \text{Re } \rho_{10}/\alpha.\end{aligned}\quad (12.2)$$

The parameters in these equations have the following interpretation:

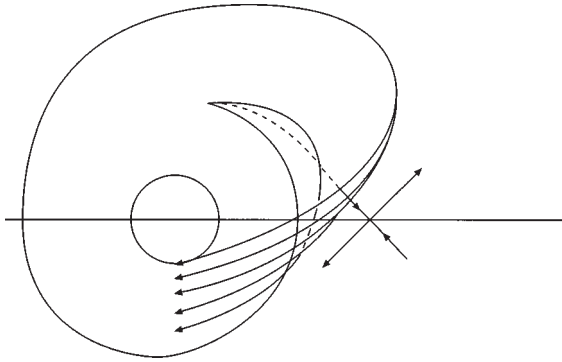


FIG. 67. Saddles and templates. A spiral saddle with one stable and two unstable directions organizes the rotational motion and is responsible for stretching. Its partner saddle with two stable and one unstable directions redirects the flow from its unstable direction to its stable directions, performing the squeezing (folding) that generates chaotic behavior.

- $\gamma_i$ : decay rate, level  $i$ ,
- $\gamma_{ij}$ : decay rate for transition  $i \leftrightarrow j$ ,
- $\Omega_2$ : pump frequency,
- $\omega_c$ : cavity resonance,
- $\Delta_2$ :  $\Omega_2 - \omega_{20}$  cavity detuning with respect to transition  $2 \leftrightarrow 0$ ,
- $\Delta_c$ :  $\omega_c - \omega_{20}$  cavity detuning,
- $g$ : unsaturated gain,
- $\kappa$ : cavity loss rate,
- $2\alpha$ : Rabi frequency of output field, and
- $2\beta$ : Rabi frequency of pump field.

The dynamical system (12.1) comprises a set of ten real ordinary differential equations. Dupertuis, Salomaa, and Siegrist (1986) showed that these equations reduce to the Lorenz equations when the following conditions are satisfied:

- (1) the fields are resonant ( $\Delta_c = \Delta_2 = 0$ );
- (2) the relaxation rates are all equal:  $\gamma_0 = \gamma_1 = \gamma_2$ ;
- (3)  $n_0 = n_1$  at equilibrium
- (4) the pump is weak:  $\beta \ll \gamma_i, \gamma_{ij}$ ;
- (5) the density matrix elements  $\rho_{02}, \rho_{12}$  can be adiabatically eliminated ( $\gamma_{01}, \gamma_{12} \gg \gamma_{01}$ ); and
- (6) the equation of motion for  $\rho_{22}$  can be decoupled ( $\gamma_{02}\gamma_{12} > |\alpha|^2$ ).

In an optically pumped laser operating under typical conditions, the pump line is much narrower than either the width of the vibrational transition or the Doppler linewidth of the thermal molecules. As a result, laser gain is velocity dependent. To make the model (12.1) more realistic, molecules were divided into 81 velocity groups. The gains and losses for each group were made velocity dependent. Under these Doppler-broadening conditions, the laser model consisted of 730 coupled ordinary differential equations. The question then is: does the dynamics of this high-dimensional system remain Lorenz-like?

This set of equations was numerically integrated under resonance-pump assumptions ( $\Delta_2 = 0$ ) under several conditions. The laser-output amplitude  $E(t)$  and intensity  $I(t) = |E(t)|^2$  were recorded and analyzed (Gilmore *et al.*, 1997; Roldán *et al.*, 1997).

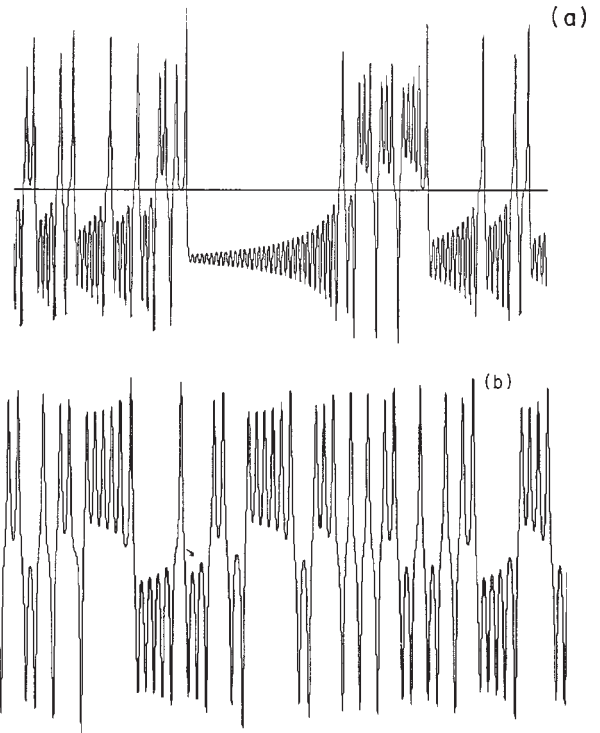


FIG. 68. Two time series obtained from the dynamical equations for the optically pumped molecular laser run under two different resonance-operating conditions.

## 2. Amplitudes

Under the resonance condition ( $\Delta_2 = 0$ ) the phase  $\phi$  changes by  $\pi$  whenever the field amplitude approaches zero. This phase change was incorporated in the field amplitude to give a real field  $E(t)$ . Time series obtained for two different operating conditions are shown in Figs. 68(a) and 68(b). In Fig. 68(a) the time trace behaves in the same way as the  $x$  and  $y$  variables for the Lorenz equations operating in the range  $r \sim 30$ . However, the behavior shown in Fig. 68(b) is slightly different. When the amplitude changes sign, the envelope of the oscillations first decreases before spiralling out again. These behaviors are topologically equivalent, although they are dynamically different.

We first study the properties of the time series shown in Fig. 68(a). An  $\dot{x}$  vs  $x$  ( $x = E$ ) projection of the standard embedding (10.4) is shown in Fig. 69. In this projection all crossings in the positive half plane are negative, while all in the lower half plane are positive. In the Lorenz attractor all crossings are positive. In addition, the standard embedding has inversion symmetry, while the Lorenz attractor is invariant under rotations by  $\pi$  radians about the  $z$  axis. Therefore there is no possibility that the standard embedding of this time series could be equivalent to the Lorenz equations.

In order to create an embedding that might be equivalent to the Lorenz equations, it is necessary that all crossings are positive. All crossings occur in the first quadrant ( $x > 0, \dot{x} > 0$ ) and the third quadrant ( $x < 0, \dot{x} < 0$ ). In order to create an embedding with the appropriate crossing and symmetry properties, we define the

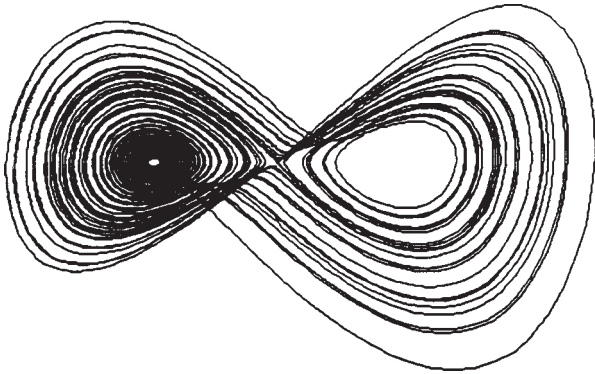


FIG. 69. Projection into the  $x$ - $\dot{x}$  plane of the time series shown in Fig. 68(a). All crossings occur in the first and third quadrants.

additional embedding variables  $y$  and  $z$  as follows:

$$\begin{aligned} y &= \dot{x}, \\ z &= -y\dot{y}. \end{aligned} \quad (12.3)$$

This embedding has the appropriate symmetry. In addition, at a crossing in the  $x$ - $y$  plane, we find

$$\begin{aligned} \text{slope} &= \frac{dy}{dx} = \frac{dy/dt}{dx/dt} = \frac{-z/y}{y}, \\ z &= -\text{slope} \times (y^2). \end{aligned} \quad (12.4)$$

As a result, all crossings are positive.

A caricature of the embedded data set is shown in Fig. 70(a). This is actually the branched manifold for the induced strange attractor. By rotating the right-hand lobe around the  $x$  axis by half a turn, with the top into the page, this branched manifold is deformed into the Lorenz branched manifold shown in Fig. 70(b).

To confirm that the strange attractor induced from the time series shown in Fig. 68(a) by means of the embedding (12.3) is equivalent to the strange attractor generated by the Lorenz equations, we followed the topological-analysis algorithm. A number of unstable periodic orbits were located by the method of close returns and identified by a symbol sequence (Gilmore *et al.*, 1997). The identification was easy in this case: a symbol  $L$  or  $R$  was assigned according to whether rotation was around the left- or right-hand focus. To period six, the orbits which we identified were  $LR$ ;  $L^2R$ ,  $LR^2$ ;  $L^3R$ ,  $LR^3$ ,  $L^2R^2$ ;  $L^4R$ ,  $LR^4$ ,  $L^3R^2$ ,  $LRLR^2$ ; and  $L^5R$ ,  $LR^5$ ,  $L^4R^2$ ,  $L^2R^4$ ,  $LRLR^3$ . The period-one orbits are the fixed points at  $(\pm x_0, 0, 0)$ . The linking numbers for these periodic orbits were computed and compared with those for the symbol sequence on the Lorenz template (Table II, augmented to period six). There were no discrepancies.

Although the embedding (12.3) used to induce the strange attractor from the time series is invariant under  $(x, y, z) \rightarrow (-x, -y, +z)$ , it was not obvious that the strange attractor itself had this symmetry. The attractor could lack symmetry for two reasons: (a) the underlying dynamics might not be symmetric (under  $E \rightarrow -E$ ) or (b) the time series might be too short to build up an

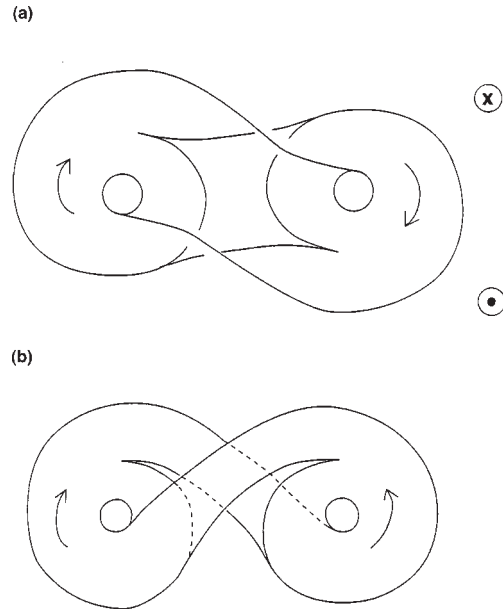


FIG. 70. (a) Branched manifold for the data set shown in Fig. 68(a) using the embedding (12.3). (b) Deforming the branched manifold by rotating the right-hand lobe half a turn, top into the page, produces a branched manifold that is equivalent to the right-handed Lorenz branched manifold.

invariant density that is symmetric to suitable statistical precision.

Two approaches can be taken to test for the presence of symmetry. One involves statistical procedures. This is less convincing than the one that we have adopted. Our test depends on the properties of a strange attractor: that embedded in it are unstable periodic orbits. If the attractor is symmetric, then conjugate orbits (under  $L \leftrightarrow R$ ) should be rotation related. We therefore compared the conjugate and self-conjugate orbits that were extracted from the data. These orbits include

$$\begin{aligned} LR &\leftrightarrow RL, \quad \text{self}, \\ L^2R &\leftrightarrow R^2L, \\ L^3R &\leftrightarrow R^3L, \\ L^2R^2 &\leftrightarrow R^2L^2, \quad \text{self}, \\ L^4R &\leftrightarrow R^4L, \\ L^5R &\leftrightarrow R^5L, \\ L^4R^2 &\leftrightarrow R^4L^2. \end{aligned} \quad (12.5)$$

In each of these cases, the rotated image of one orbit was indistinguishable from the image of its conjugate. In Fig. 71 we show the self-conjugate orbit  $L^2R^2$  and the conjugate orbit pair  $L^2R$  and  $R^2L$ . The  $x$  marks are fiducial marks, which allow unbiased comparisons to be made. This test produced convincing evidence that the induced attractor is in fact rotation symmetric and that the apparent lack of symmetry is due only to the relatively short length of the data set. We should remark that this is the only instance we have encountered where a data file containing more than about 100 cycles might

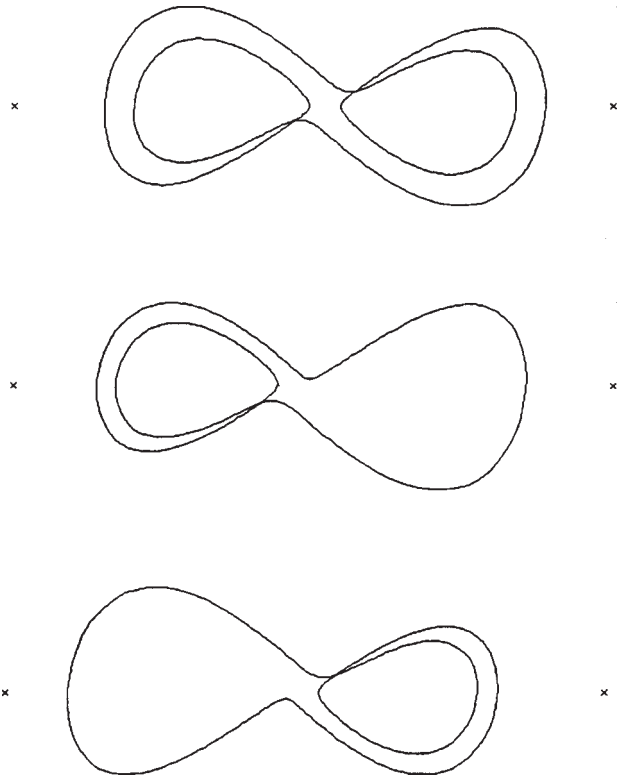


FIG. 71. Self-conjugate orbit  $L^2R^2$  and conjugate orbit pair  $L^2R$  and  $R^2L$  extracted from the time series shown in Fig. 68(a). These are invariant under rotations  $R_z(\pi)$ . The  $x$ 's are fiducial marks to allow unbiased comparisons.

have been useful. However, the problem of symmetry was resolved by relying on the properties of unstable periodic orbits in the strange attractor rather than its statistics.

We turn our attention now to the second time series shown in Fig. 68. When the amplitude changes phase, it first spirals in towards an unstable fixed point before it begins to spiral away. In fact, the unstable fixed points are surrounded by unstable limit cycles. These were extracted by the method of close returns and are the two period-one orbits  $L$  and  $R$ . This time series was treated in the same way as the time series shown in Fig. 68(a).

The branched manifold for the induced strange attractor is shown in Fig. 72(a). This differs from the branched manifold shown in Fig. 70(a) in that it has two folds, one in each of the flows from one lobe to the other. This branched manifold can be deformed by the rotation process illustrated in Fig. 70(b). The result is a branched manifold that is equivalent to the right-handed Lorenz attractor.

To verify that this identification is correct, we extracted the following unstable periodic orbits:  $L, R; LR; L^2R, LR^2; L^3R, LR^3, L^2R^2; L^4R, LR^4, L^2R^2L, R^2L^2L, L^3R^2, L^2R^3$ ; and  $L^5R, LR^5, L^3R^2L, R^3L^2L, L^2R^2LR$ . We could not find the orbits  $L^2R^4, R^2L^4$  to the precision used to find the other orbits. Many of these orbits had the same name as orbits found in the first data set. The presence of a fold merely served to push some crossings from the first or third quadrant

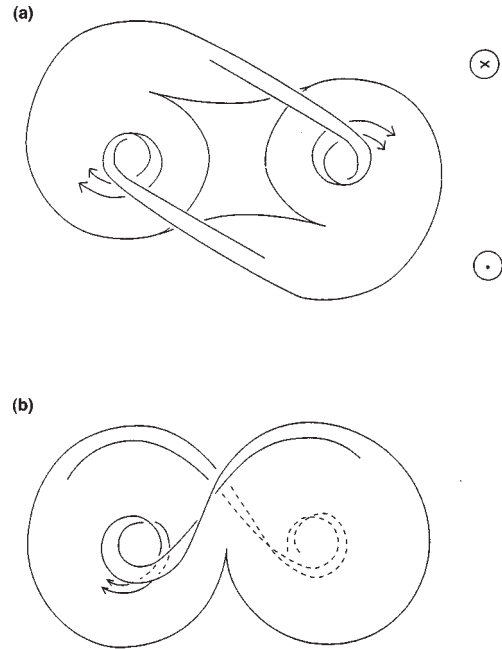


FIG. 72. (a) Branched manifold for the data set shown in Fig. 68(b) using the embedding (12.3). (b) Deforming the branched manifold by rotating the right-hand lobe half a turn, top into the page, produces a branched manifold that is equivalent to the right-handed Lorenz branched manifold.

into the fourth or second quadrant without changing their sign or therefore the linking numbers of the corresponding orbits. As a result, the orbits in the second data set had the same spectrum of linking numbers as those in the first data set. Thus both flows are topologically equivalent to the right-handed Lorenz flow when embedded according to Eq. (12.3).

We also tested for the symmetry of the induced attractor. The self-conjugate and conjugate pairs of orbits that were compared were

$$\begin{aligned}
 L &\leftrightarrow R, \\
 LR &\leftrightarrow RL, \quad \text{self}, \\
 L^2R &\leftrightarrow R^2L, \\
 L^3R &\leftrightarrow R^3L, \\
 L^2R^2 &\leftrightarrow R^2L^2, \quad \text{self}, \\
 L^4R &\leftrightarrow R^4L, \\
 L^2R^2L &\leftrightarrow R^2L^2L, \\
 L^3R^2 &\leftrightarrow R^3L^2, \\
 L^5R &\leftrightarrow R^5L, \\
 L^3R^2L &\leftrightarrow R^3L^2L.
 \end{aligned} \tag{12.6}$$

Orbit comparisons were very similar to those shown in Fig. 71. We therefore do not present any additional figures. The induced strange attractor is invariant under the rotation  $R_z(\pi)$ .

### 3. Intensities

Two intensity time series were also analyzed. These are shown in Figs. 73(a) and 73(b). A differential plot of  $dI/dt$  vs  $I(t)$  shows a simple fold, suggesting horseshoe dynamics for the intensity. However, the dynamical equations of motion involve the amplitude  $E$ , whose absolute square is the intensity. Therefore it was necessary

to extract square-root information from intensity data before a topological analysis was carried out.

In general the amplitude is complex, and phase information is lost in measuring the intensity. However, on resonance the phase undergoes rapid changes by  $\pi$  when the amplitude approaches zero sufficiently closely. These phase changes represent sign changes in the amplitude. To separate intensity minima where the phase changes rapidly from those where it does not, we plotted  $\sqrt{I(t)}$  vs  $t$ . This plot is shown in Fig. 74. When the minimum is  $I_0$ , the shape of the square root in the neighborhood of the minimum is

$$|E(t)| = \sqrt{I_0 + \Delta I(t)} \begin{cases} \xrightarrow{I_0 \neq 0} \sqrt{I_0} + \frac{1}{2\sqrt{I_0}} \Delta I(t) \text{ parabolic} \\ \xrightarrow{I_0 = 0} \sqrt{\Delta I(t)} \text{ linear.} \end{cases} \quad (12.7)$$

It is a simple matter to distinguish minima of  $\sqrt{I(t)}$  that are parabolic from those that are linear.

This test for sign assignment was implemented numerically. We chose the sign assignment that minimized the estimate of  $dE/dt \sim E_{i+1} - E_i$ . Specifically, at the  $i$ th element in the data field we defined

$$a_3 = \text{ISIGN} \times \sqrt{I_i}.$$

Then we tested the two differences

$$\begin{aligned} S1 &= |(+a_3 - a_2) - (a_2 - a_1)|, \\ S2 &= |(-a_3 - a_2) - (a_2 - a_1)|. \end{aligned} \quad (12.8)$$

After each test, we updated the variables according to  $a_3 \rightarrow a_2, a_2 \rightarrow a_1$ . Normally  $S1 < S2$  and there is no sign change. Whenever  $S1 > S2$ , we changed the phase  $\text{ISIGN} \rightarrow -\text{ISIGN}$ . Implementation of this algorithm is illustrated in Fig. 75. At the bottom of this figure we show the intensity data. At the top we show amplitude data extracted with the algorithm above. The differential embedding of this data set is shown projected onto

the  $x-\dot{x}$  plane ( $x = E$ ) in Fig. 76. The following unstable periodic orbits were extracted:  $L, R; LR; L^2R, LR^2; L^3R, LR^3, L^2R^2; L^4R, LR^4, L^2RLR, R^2LRL, L^3R^2;$  and  $L^5R, R^2L^2RL, R^3LRL$ . All self-conjugate orbits and conjugate pairs of orbits were invariant under rotations.

A similar analysis was carried out on the intensity data shown in Fig. 73(b), with identical results.

### B. Fluids

A simple fluid experiment has been designed and carried out that exhibits Lorenz dynamics. In this experiment a torus with a large radius  $R$  and a small radius  $r$  was filled with water (Creveling *et al.*, 1975; Gorman, Widmann, and Robins, 1984, 1986; Singer, Wang, and Bau, 1991). The bottom half was wrapped with a thermal heating ribbon, which generated a constant, uniform heat flux. The top half of the torus was surrounded by a water jacket, which kept that part of the torus surface at approximately the coolant temperature. Heat sensors were embedded within the torus at the 3 o'clock and 9 o'clock positions. The temperature difference was monitored as a function of time for different heating rates (inset, Fig. 77).

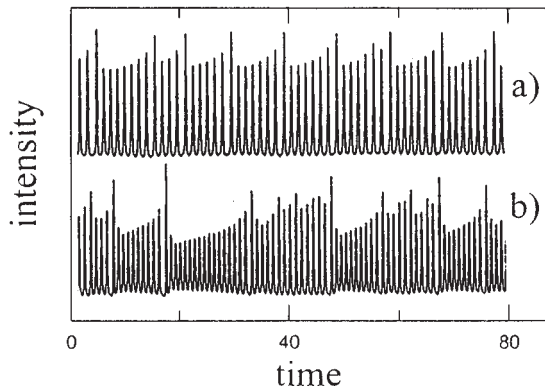


FIG. 73. Intensity output from an optically pumped molecular laser model under two operating conditions.

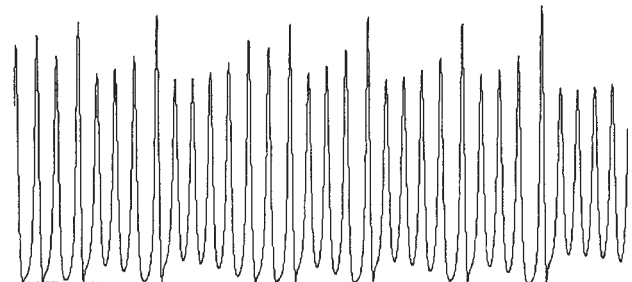


FIG. 74. Square root of intensity output in the top trace of Fig. 73.

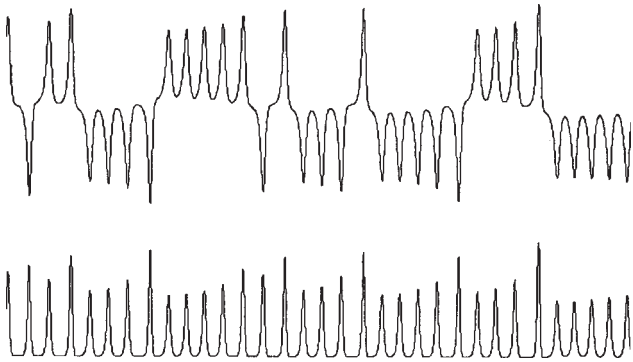


FIG. 75. Bottom: Segment of intensity data. Top: Conversion to amplitude data by implementing the algorithmic search for zero crossings.

The heated fluid in the bottom half of the torus was less dense than the cooler fluid in the top half. This density difference set up a thermal instability. For low heating, the fluid circulated in the clockwise or the counterclockwise direction. The direction of circulation can be determined from the temperature difference: if  $T_9 - T_3 > 0$ , the flow is clockwise [Fig. 77(a)].

As heating was increased, the rotation maintained its direction (either counterclockwise or clockwise) but became oscillatory. As heating was increased above a threshold, the direction of rotation changed unpredictably from counterclockwise to clockwise and back again [Fig. 77(c)].

The behavior shown in Fig. 77(c) is chaotic. An  $\dot{x}$  vs  $x$  ( $x = T_9 - T_3$ ) embedding will have the structure shown in Fig. 69. It is therefore possible to construct an embedding in which the attractor is equivalent to the strange attractor generated by the Lorenz system.

It is worthwhile to make a few remarks at this stage.

(i) The experimental apparatus has reflection symmetry in a vertical plane. It is this symmetry that forces the Lorenz ( $A_3$ ) mechanism rather than the Rössler mechanism ( $A_2$ ).

(ii) The identification of the thermal instability behavior observed in Fig. 77(c) with the Lorenz mechanism was made possible by observing the phase-space plot  $\dot{x}$

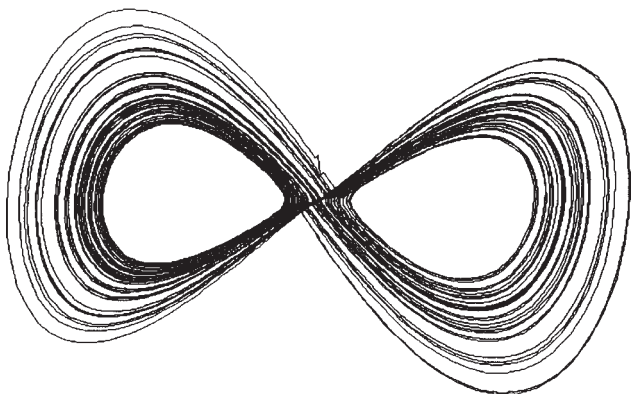


FIG. 76. Differential embedding of the amplitude data shown in Fig. 75.

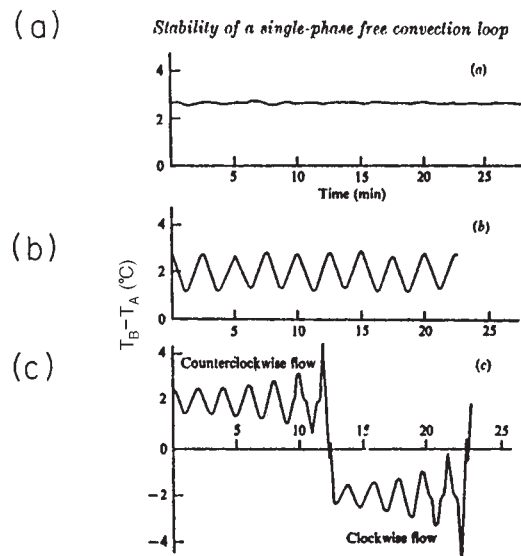
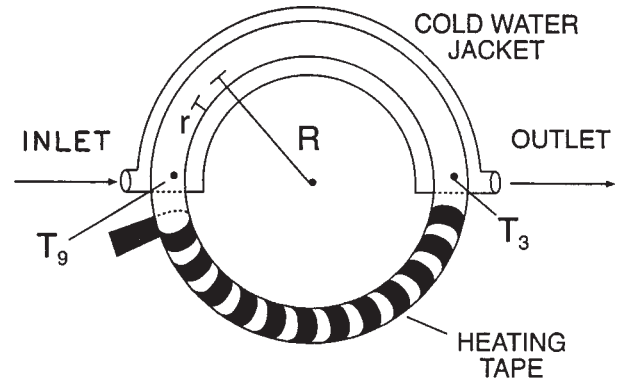


FIG. 77. Time series for temperature difference  $T_3 - T_9$  under three heat flow conditions. (a) Low heat flow: steady counterclockwise circulation. (b) Higher heat flow: oscillatory counterclockwise circulation. (c) Heating above instability threshold: chaotic behavior with unpredictable changes from counterclockwise to clockwise circulation. Top: experimental apparatus. Reprinted with permission from Creveling *et al.*, 1975. Copyright 1975 by American Institute of Physics.

vs  $x$ . In fact, we did not even have to perform this plot: the identification was made possible by inspecting the morphology (shape) of the time series alone. This is often possible for very dissipative systems.

### C. Induced attractors and templates

Strange attractors that are obtained by integrating ordinary differential equations are well defined. However, when we analyze chaotic data, the strange attractor that is obtained depends on (is “induced” from) the particular embedding employed.

To be explicit,  $x(t)$  data generated by the Lorenz equations can be used to induce a strange attractor either by the differential phase-space embedding (10.4) or the closely related embedding (12.4). The induced at-

tractors so obtained both provide a “faithful” (1-1) representation of the dynamics. But they are topologically inequivalent. The templates obtained from the two induced strange attractors are also inequivalent.

Attractors induced from the Lorenz variable  $z(t)$  or the laser intensity  $I(t) = |E(t)|^2$  show a simple fold. The induced attractor is a locally faithful but globally unfaithful ( $2 \rightarrow 1$  homomorphic image) representation of the original dynamics. The corresponding induced template is a Smale horseshoe template. The two inequivalent templates induced from  $x(t)$  by the embeddings (10.4) and (12.4) can be regarded as “double covers” of the Smale horseshoe template (Gilmore, 1974, 1996). At present, not much is known about covering templates and  $n \rightarrow 1$  locally faithful mappings of dynamics, strange attractors, and branched manifolds.

#### D. Why $A_3$ ?

The phase-space plots in this section all show three critical points very clearly. Two symmetric saddle foci at  $(x, \dot{x}) = (\pm x_0, 0)$  are separated by a regular saddle at the origin. On occasion the symmetric pair of critical points are inaccessible because they are shielded from the flow in phase space by unstable limit cycles.

The Lorenz model has three critical points. These may all be real, or two may be hidden in the complex “plane.” They are “unmasked” by a cusp catastrophe ( $A_3$ ) (Gilmore, 1981). In one-parameter unfoldings, it is typical to encounter only fold catastrophes. However, in the presence of symmetry, the cusp catastrophe is also generic. It is for this reason that physical systems whose dynamical equations of motion exhibit a symmetry may exhibit mechanisms leading to chaos that are more complicated than the  $A_2$  fold mechanism: that is to say, heteroclinic as opposed to homoclinic connections (Ott, 1993; Solari, Natiello, and Mindlin, 1996).

It is not an accident that the differential phase-space plot of the intensity  $I = |E|^2$  shows a fold while that of the amplitude  $E$  shows a heteroclinic connection. There is a  $2 \rightarrow 1$  relation between the amplitude and the intensity, just as there is a  $2 \rightarrow 1$  relation between the Lorenz branched manifold and the Rössler branched manifold. Dynamics on a Rössler branched manifold is locally isomorphic to dynamics on a Lorenz branched manifold, but globally two regions on a Lorenz attractor map to a single region of a Rössler attractor. Another way to state this is that the Lorenz system is a  $2 \rightarrow 1$  covering of the Rössler system. Letellier and Gouesbet (1995) have described multiple covers of the Rössler system.

### XIII. DUFFING OSCILLATOR

#### A. Background

Nonlinear oscillators have been studied extensively since the time of Duffing (1918) and van der Pol (1927). Early approaches to the study of driven damped nonlinear oscillators followed the classical route of perturba-

tion theory. These methods are reviewed in Minorsky (1962), Nayfeh (1973), and Mickens (1981).

With the availability of computers, nonlinear equations were numerically integrated and their study entered a descriptive phase in which salient features were pointed out. Such features included coexisting basins of attraction and rotational-flow properties in the neighborhood of stable periodic orbits. This approach is summarized in Hayashi (1964, 1975).

This phase in the study of nonlinear oscillators was followed by a phase that was both more quantitative and qualitative. Lauterborn and his colleagues (Parlitz and Lauterborn, 1985; Kurz and Lauterborn, 1987; Lauterborn and Steinhoff, 1988; Knop and Lauterborn, 1990; Parlitz *et al.*, 1990; Englisch and Lauterborn, 1991; Schefczyk *et al.*, 1991) studied a variety of nonlinear oscillators and found similar behavior among all of them. These included the Duffing, Morse, Toda, and bubble oscillators, as well as variants of them. In this approach the bifurcation diagram for a nonlinear oscillator was numerically constructed. Regions in the bifurcation diagram for which there were stable basins of attraction were outlined and identified by rational fractions. The fractions identified the local torsion of the stable periodic orbits in these basins. The bifurcation diagrams for the nonlinear oscillators studied were all more or less similar. Furthermore, these diagrams changed in an apparently systematic way as control parameters changed. Although algorithms were developed to predict how these rational fractions would change, the algorithms were empirical and not developed from a deeper understanding of the properties of these nonlinear oscillators.

The study of nonlinear oscillators moved into a new phase once it was realized that the Birman-Williams theorem could provide an accurate topological characterization of dynamics. With this in mind, Tufillaro, Solari, and Gilmore (1990) attempted to construct a template for the Duffing oscillator. This was done by integrating the Duffing equations and following the topological-analysis algorithm described in Sec. VII. The analysis of 16 orbits up to period five was sufficient to identify the underlying branched manifold as an iterated horseshoe template with four branches. In one sense this analysis was successful (a template was identified), but in another sense it was not. The analysis provided no information about why this particular stretching and squeezing mechanism was operative, nor did it provide information about how the branched manifold changed as the control parameters changed.

#### B. Flow approach

The limited success of the topological analysis carried out by Tufillaro, Solari, and Gilmore provoked us into searching for a better way to perform this analysis. This resulted ultimately in a deeper understanding of the properties of nonlinear oscillators and their bifurcation diagrams.

The procedure we adopted is implicit in the work of Poincaré (1892). We followed a neighborhood of phase

space as it evolved during one period under the action of the flow. During this period we were able to watch as the blob of initial conditions was deformed by stretching and squeezing in a way that was not too difficult to determine. This led to a tentative guess at an underlying branched manifold. To verify this guess a set of unstable periodic orbits was located in the strange attractor and identified by their symbol names. Their topological invariants were computed and compared to those for orbits with the same symbol name in the proposed template.

Before describing the procedure in detail, we first describe the Duffing equation. As a pair of first-order equations, they are

$$\begin{aligned}\dot{x} &= y, \\ \dot{y} &= -y/T - \partial V(x,t)/\partial x,\end{aligned}\quad (13.1)$$

$$V(x,t) = \frac{1}{4}x^4 - \frac{1}{2}x^2 - bx \sin(2\pi t/T). \quad (13.2)$$

These equations describe a periodically driven damped nonlinear oscillator. The driving term has period  $T$ . The equations are invariant under  $(x, \dot{x}, t) \rightarrow (-x, -\dot{x}, t + \frac{1}{2}T)$ . The dissipation over one period is  $e^{-\epsilon}$ . The strength of the driving term is  $b$ .

In the absence of driving ( $b=0$ ), the potential  $V = \frac{1}{4}x^4 - \frac{1}{2}x^2$  has two wells, one on the left and the other on the right. An initial condition in one well with kinetic energy less than the value of the potential at the origin will spiral down to the bottom of that well. The period of oscillation for this damped decay is roughly  $2\pi$ .

The driving term changes the relative height of the two wells. When  $b^2 > 2^2/3^3$ , during one cycle one of the wells completely disappears (in a fold catastrophe) for  $t = \frac{1}{4}T$ , and later, at  $t = \frac{3}{4}T$ , the other well completely disappears. This oscillation from a two-well state to a single-well state forces points in phase space from the neighborhood of one well to the neighborhood of the other and back again during the course of one period.

The analysis procedure that we adopted is described in Gilmore and McCallum (1995, see Fig. 4). The Duffing equations were integrated numerically. After transients died out,  $x$  and  $\dot{x}$  were recorded at five degree intervals for about 100 periods. The intersection of the strange attractor with each of 72 Poincaré sections, phase lagged by five degrees, was then constructed. By sweeping through these Poincaré sections we were able to animate the stretching and squeezing mechanisms that were operating to create the strange attractor. Animations of this type were created as the control parameter  $T$  was slowly increased. One of these animations is shown in Gilmore and McCallum (1995).

Between the physics described above and the animations constructed numerically, the following picture emerged. We begin with an open ellipse-shaped neighborhood in phase space that surrounds the strange attractor in the left-hand well. As time evolves, this open neighborhood rotates around the minimum in the left-hand well. As it rotates, it is stretched out in the direc-

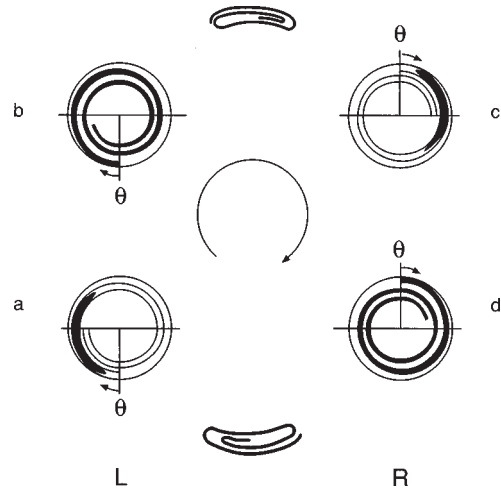


FIG. 78. Qualitative understanding of Duffing oscillator. (a) An elliptical open neighborhood in the left-hand well is (b) stretched out in the direction of motion during the first half period. When poured from the left-hand well to the right-hand well, it is squeezed into an elliptical neighborhood (c), which is a rotated image of (a). Stretching (d) and squeezing (a) continues.

tion of rotation, and it also spirals toward the bottom of the well. As the minimum of the well is raised by the time-varying potential, phase space in its neighborhood is squeezed. When the left-hand well disappears, the strange attractor, and the open neighborhood surrounding it, is “poured” into the right-hand well. In this well, one half period into the cycle, the attractor and the open set surrounding it appears as a rotated image of the initial conditions. This comes about because of the symmetry of the Duffing oscillator. This process is repeated. When the right-hand well is annihilated, the attractor is “poured” back into the left-hand well. This behavior is easily identified in animations. A caricature of this process is shown in Fig. 78. The number of rotations in each well is approximately  $\frac{1}{2}T/\tau$ , where  $\tau$  is the period of free oscillations.

### C. Template

It is possible to infer the appropriate branched manifold and template from the caricature presented in Fig. 78. The branched manifold is illustrated in Fig. 79. To keep this figure reasonably simple, we have constructed this branched manifold under the assumption that the number of rotations in each well is no more than three. As a result, the branched manifold has 9 ( $=3 \times 3$ ) branches. As the control parameter  $T$  increases, the number of rotations in each well, and therefore the number of branches, increases. However, if the unstable Lyapunov exponent for the map is  $\lambda_1$ , then the number of branches through which the strange attractor flows is about  $1 + \sqrt{\lambda_1}$  in each well, so the total number of branches required to describe the flow is about  $(1 + \sqrt{\lambda_1})^2$  (Gilmore and McCallum, 1995).

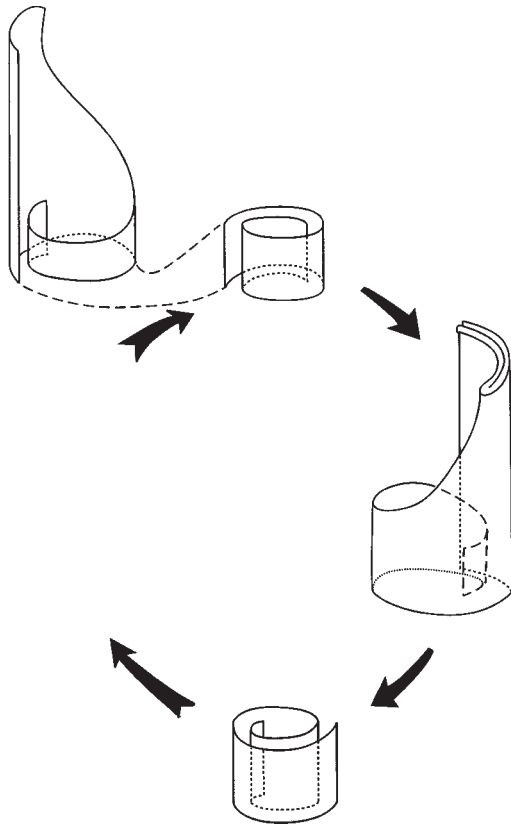


FIG. 79. Duffing branched manifold. The caricature in Fig. 78 can be used to construct a branched manifold for the Duffing oscillator. This branched manifold shows only three branches in each well.

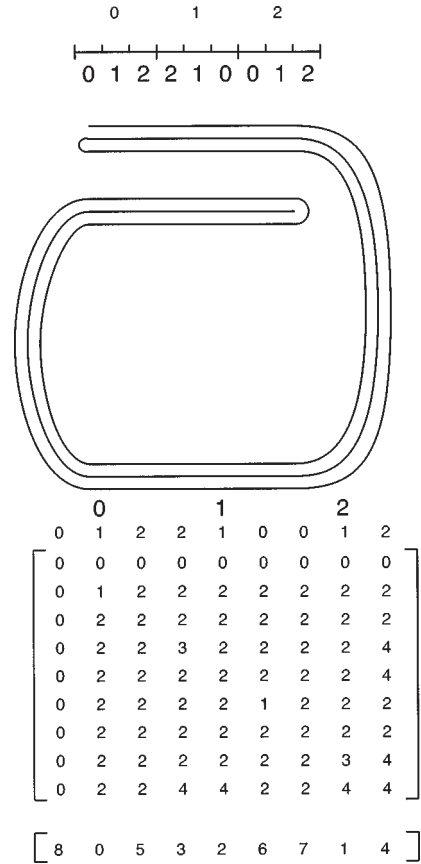


FIG. 81. Concatenation of a three-branched extended horseshoe template with itself. The resulting template has 9 branches. The Duffing template includes the two rotations by  $\pi$  radians induced by passing from one well to the other. This is represented by adding 2 to each matrix element above.

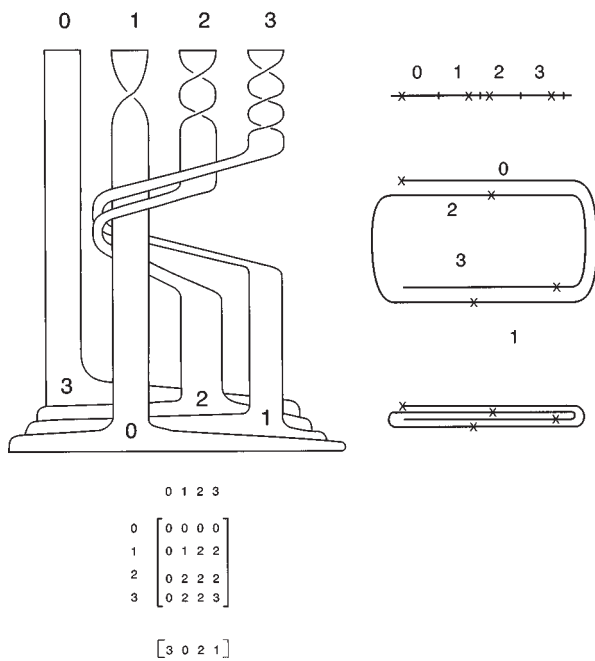


FIG. 80. Extended horseshoe. Template for a typical driven damped nonlinear oscillator is an extended horseshoe. The crosses show locations of period-one orbits.

The algebraic description of this template can now be constructed. We begin with a template for a nonlinear oscillator that exhibits damped rotation of the type that occurs in either well of the Duffing oscillator. Such a template is shown in Fig. 80. The template has four branches labeled 0, 1, 2, 3, where the integer describes the local torsion. The template matrix and array share systematics of construction that are easily deduced from the integers given. Driven damped nonlinear oscillators are typically characterized by this template (extended to sufficiently many branches). This has been observed in the fiber-optic laser (Boulant *et al.*, 1997b).

The Duffing oscillator has a symmetry that produces some complications. The stretching and squeezing described by the nonlinear oscillator template is followed by a half twist. The stretching and squeezing occurs again, and is followed by another half twist. As a result, the Duffing template can be produced by concatenating the extended horseshoe template (Fig. 80) with itself, including the half twists. In Fig. 81 we present the 9-branched template that results from concatenating the 3-branched horseshoe template with itself, ignoring the two half twists. The branches in each well are labeled by integers (0,1,2). The nine branches are labeled by two integers, which indicate the branch in each well that is traversed. To include both half twists, the integer 2 must

be added to all matrix elements.

As the period of the driving term increases, branches with larger local torsion must be included in the template. However, those with lower local torsion are no longer visited and can be omitted from the template description of the flow (“pruning” of unused template branches). As a result, as control parameters (e.g.,  $T$ ) change, the number of branches required to describe the flow remains more or less constant by virtue of new branches appearing and old branches disappearing. In this context, we recall a point made above. A strange attractor is the closure of the unstable invariant manifold of some appropriate invariant set. This invariant manifold has many branches, only a few of which are normally visited by a strange attractor under typical operating conditions. As operating conditions change, the flow extends over additional branches that were always present but not previously visited. The flow may also fail to visit branches that had previously been visited.

#### D. Orbit organization

As the period of the driving term increases, periodic orbits are created and annihilated in a systematic way. Upon creation the node is stable. It also becomes stable again just before annihilation in an inverse saddle-node bifurcation. When it is stable it “eats a hole” in the strange attractor. Its basin is often so large that most initial conditions fall asymptotically to the stable periodic orbit. A periodic “window” is then observed in the particular type of bifurcation diagram that plots a state-space variable against a control parameter. Many periodic windows appear. They have various widths, but most are too small to be seen without special care. Their order of appearance is also systematic. In fact, their order is governed to a large extent by the organization of periodic orbits in a horseshoe template.

We first discuss orbit organization for the typical nonlinear oscillator governed by an extended horseshoe template. Then we relate these results to the organization of periodic orbits in the Duffing equations.

##### 1. Nonlinear oscillator

As the control parameter  $T$  increases, the amount of rotation in the phase space increases. The amount of rotation in the neighborhood of an orbit is measured by its local torsion, which is determined by the relative rotation rates of that orbit. More specifically, the local torsion, or torsion in the neighborhood of an orbit, is the average of the relative rotation rates of the orbit and its partner at the bifurcation that creates it. For a saddle-node pair, this is the average of the relative rotation rates of the saddle and its node partner. For a period-doubled orbit, this is the average of the relative rotation rates between the daughter orbit and its mother.

On the horseshoe template with local torsion  $0,1$ , the local torsion of the orbit of period  $2^k$  is  $[2^k + (-1)^{k-1}]/3 \times 2^k$ . For a period-doubling cascade based

TABLE XI. Relative rotation rates for leading members of the primary series of well-ordered orbits. The fraction  $f = p/(q+2p)$  identifies a well-ordered orbit with  $q$  symbols 0 and  $p$  symbols 11 as equally spaced as possible. For the primary series:  $p$  is arbitrary,  $q=1$  (first half) or  $p=1$ ,  $q$  is arbitrary (second half). The two halves are dual under  $p \leftrightarrow q$  and  $11 \leftrightarrow 0$ . The self-dual orbit  $(p,q) = (1,1)$  has  $f=1/3$ . The table shows concentric organization. Orbits with lower local torsion are outside orbits with larger local torsion.

$f$	$f'$	3/7	2/5	1/3	1/4	1/5
		0111111	01111	011	0011	00011
3/7	0111111	3/7	2/5	1/3	1/4	1/5
2/5	01111	2/5	2/5	1/3	1/4	1/5
1/3	011	1/3	1/3	1/3	1/4	1/5
1/4	0011	1/4	1/4	1/4	1/4	1/5
1/5	00011	1/5	1/5	1/5	1/5	1/5

on a node with period  $p$  and local torsion  $\langle R \rangle$ , the local torsion of the orbit of period  $p \times 2^k$  is (Solari and Gilmore, 1988):

$$\text{local torsion} = \langle R \rangle + \frac{2^k + (-1)^{k-1}}{3 \times 2^k \times p}. \quad (13.3)$$

The other important class of orbits for which local torsions are easily available are the well-ordered orbits. These are all uniquely identified by a rational fraction  $0 < q/p < \frac{1}{2}$ , with  $p$  the period. For these orbits the local torsion is  $q/p$ .

The organization of periodic orbits among themselves can be determined from their relative rotation rates. The orbits 1, 01, 001 all have the same set of relative rotation rates with the period-four orbit 0001 ( $\frac{1}{4}$ , from Table III). This means that the three lower-period orbits can be deformed into each other without crossing the period-four orbit. This means that they occur inside the period-four orbit. By the same argument, 1 and 01 lie inside 001. These orbits are concentrically organized. In fact, all well-ordered orbits are concentrically organized. It is possible to show (Gilmore and McCallum, 1995) that two well-ordered orbits with self-relative rotation rates  $q/p$  and  $q'/p'$  have relative rotation rates with respect to each other:

$$RRR_{ij}(q/p; q'/p') = \min(q/p; q'/p'). \quad (13.4)$$

The organization is as follows: the smaller  $q/p$ , the further outside (see Fig. 3).

The largest windows in the bifurcation diagram belong to well-ordered orbits. In fact, they belong to a particular class of well-ordered orbits. These are Newhouse (1974) orbits and their duals. The Newhouse orbits of period  $p+2$  are defined by the fractions  $f=1/(p+2)$ . They have symbolic dynamics  $0^p 11$ . Their duals are obtained under  $0 \leftrightarrow 1^2$  and are identified with the rational fraction  $p/(2p+1)$ . Explicitly, the dual orbit has symbol sequence  $01^{2p}$ . The period-three orbit 011 is self-dual under this identification. The relative rotation rates for these two classes of orbits with  $p=1,2,3$  are shown in Table XI. These orbits are called the primary

series, since their windows are large and very noticeable.

As the control parameter  $T$  increases, the well-ordered orbits are created in saddle-node bifurcations “from inside to outside.” This means that the well-ordered orbits with larger fractional values are created before those with lower values. The width of the window decreases like some power of the period. Therefore the period-three window is the widest. In the bifurcation sequence, dual orbits are sequentially created with decreasing period and increasingly wide windows until the period-three window is created. Thus ends the first half of the primary series of windows. As  $T$  is further increased, the second half of the primary series is observed. This consists of a series of saddle-node bifurcations, which create Newhouse orbits with sequentially increasing period and decreasing window size.

Between windows in this primary series of well-ordered orbits there are windows belonging to all other well-ordered orbits. These are typically narrower than the primary-series windows. We call this series of windows the secondary series. The well-ordered orbits responsible for these windows can be constructed in a systematic way from the orbits in the primary series by Farey addition of the associated fractional values.

Finally, there is an abundance of non-well-ordered orbits. Each is created in a saddle-node bifurcation and is surrounded by a window that is very narrow. These windows are difficult to see. This series of windows is called a tertiary series.

The piece of the extended horseshoe template that consists of the two branches 1,2 is called the reverse horseshoe. There is a 1–1 correspondence between orbits on the direct horseshoe (0,1) and the reverse horseshoe (2,1). The correspondence involves replacing the symbol 0, wherever it occurs, by the symbol 2. There is also a duality in relative rotation rates and local torsions. If  $f=q/p$  is the rational fraction associated with a well-ordered orbit on the direct horseshoe, the relative rotation rate of the corresponding orbit on the reverse horseshoe is  $f' = 1 - f$ . Two well-ordered orbits with self-relative rotation rates  $f'_1 = 1 - f_1$  and  $f'_2 = 1 - f_2$  have mutual relative rotation rates:

$$RRR_{ij}(f'_1, f'_2) = \max(f'_1, f'_2) = 1 - \min(f_1, f_2).$$

These corresponding orbits are also concentrically organized. In a period-doubling cascade based on a node of period  $p$  with local torsion  $\langle R \rangle$ , the local torsion of the orbit of period  $p \times 2^k$  is given by

$$\text{local torsion} = \langle R \rangle - \frac{2^k + (-1)^{k-1}}{3 \times 2^k \times p}. \quad (13.5)$$

This differs from Eq. (13.3) by a minus sign.

Subsets of the extended horseshoe template involving two contiguous branches are homologs of the direct or reverse horseshoe template. In particular, the template built on branches with local torsion  $2k$  and  $2k+1$  is isomorphic to the direct horseshoe under the identification  $0 \leftrightarrow 2k, 1 \leftrightarrow 2k+1$ . In addition,  $2k$  must be added to each template matrix element and  $k$  to each relative rotation rate.

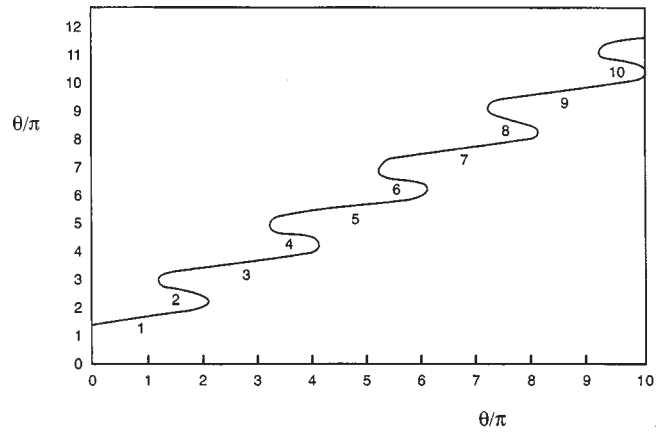


FIG. 82. Snakes. A snake of period-one orbits runs through the bifurcation diagram of a typical nonlinear oscillator which is described by an extended horseshoe template. Integers identify local torsion. Orbit creation occurs on direct horseshoes (branches 2 and 3) and annihilation occurs from reverse horseshoes (branches 3 and 4).

The template built on branches  $2k+1$  and  $2k+2$  is isomorphic to the reverse horseshoe template under the identification  $1 \leftrightarrow 2k+1, 2 \leftrightarrow 2k+2$ . A similar change must be made in the template matrix and relative rotation rates.

It is now possible to describe systematically the bifurcations that occur in a typical nonlinear oscillator as the period of the driving term is systematically increased. Fig. 82 shows a backbone of period-one orbits that occur in a nonlinear oscillator. The horizontal axis is  $2T/\tau$ , which describes how many half rotations a phase-space point makes around the bottom of a well during one period. The vertical axis measures the angle of rotation at which a period-one orbit will occur. This angle is measured in units of  $\pi$  radians. The period-one orbit “snakes” through this bifurcation diagram. Each branch of this orbit is labeled by an integer, which is the local torsion in the neighborhood of the orbit. This integer also defines a template branch and is used as a symbol to name periodic orbits that pass through this branch. As the control parameter is increased, period-one orbits are created in saddle-node bifurcations (e.g., 2 and 3; 4 and 5, . . .). They are also annihilated in inverse saddle-node bifurcations (e.g., 1 and 2; 3 and 4, . . .). The even branches are regular saddles. The odd branches are nodes. Along the nodal branches there is a great deal of activity. Orbits are created in saddle-node bifurcations. The lower-period well-ordered orbits are responsible for creating windows that can be observed. These windows occur in an organized way because the orbits are strictly organized. Before an odd branch is annihilated, all orbits created on it must first be destroyed. They are also annihilated in a systematic way, but from the reverse horseshoe. This process is then repeated on the next-higher nodal branch. The systematic behavior of the local torsion along branch 1 is shown in Fig. 83.

When a pair of period-one orbits is created (e.g., 0 and 1) in a saddle-node bifurcation, both have the same

LOCAL TORSION

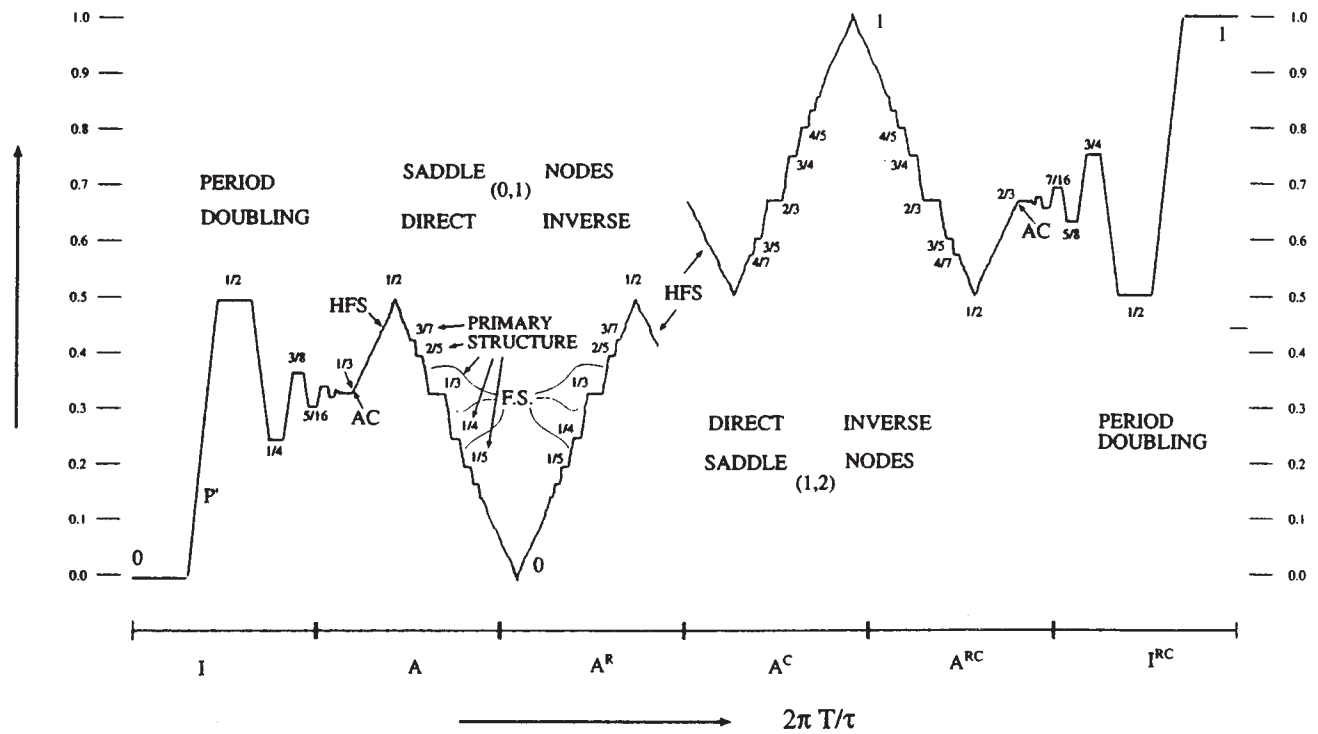


FIG. 83. Local torsion perestroika. Local torsion in a nonlinear oscillator changes in a systematic way as orbits are created on a direct horseshoe and annihilated from the reverse horseshoe.

local torsion, which is even (0). The node is stable. The torsion around the node increases to the next integer (1), at which point it becomes unstable to a period-doubling bifurcation. This initiates a cascade. The local torsion varies systematically throughout the cascade, as given in Eq. (13.3). Beyond the cascade the local torsion gradually rises from 1/3 to 1/2 as a large number of essentially invisible high-period non-well-ordered orbits are created in saddle-node bifurcations. Then the primary series of well-ordered orbits is created with decreasing local torsion. These consist of the dual and Newhouse orbits. These windows are interspersed with secondary and tertiary windows, which are generally unobservable.

When all three branches are involved in the flow, orbits involving all three symbols are created in saddle-node bifurcations. As the flow is shifted away from branch 0, orbits with a 0 are annihilated. A simple example illustrates how this occurs. On the direct horseshoe (0,1), the period-two orbit is 01. This is created from the period-one orbit 1 by a period-doubling bifurcation. Before branch 1 is annihilated, a saddle-node bifurcation must create the pair of period-two orbits 02 and 12. The pair 01 and 02 then undergo an inverse saddle-node bifurcation. Finally, the orbit 12 undergoes an inverse period-doubling bifurcation to create a stable form of the orbit 1 with local torsion 2. This then undergoes an inverse saddle-node bifurcation with the part of the snake labeled 2, which is created with that part of the snake labeled 3. The process then repeats.

2. Duffing template

The Duffing template is the second iterate of the extended horseshoe template. As a result, we can build on our knowledge of the systematics of the latter to determine the properties implied by the former. An orbit of period  $p$  in the Duffing oscillator can be identified by  $2p$  symbols  $(a_1 a_2)(a_3 a_4) \dots (a_{2p-1} a_{2p})$ , where  $a_j$  identifies a branch in the horseshoe template for the left well if  $j$  is odd and for the right well if  $j$  is even. An orbit is symmetric if the symbol sequence  $(a_{p+1} a_{p+2})(a_{p+3} a_{p+4}) \dots (a_{p-1} a_p)$  is the same as the original sequence. Otherwise the two form an asymmetric pair of orbits. Orbits with negative parity can initiate period-doubling cascades.

The Duffing template based on the regular horseshoe (0,1) has four branches (00), (01), (10), and (11). The period-one orbits (00) and (11) have even parity. The orbits (01) and (10) have odd parity and form an asymmetric pair. Each of these can initiate a period-doubling cascade. The first bifurcations for each orbit in the cascade are

$$\begin{aligned}
 (01) &\rightarrow (01)(11) \rightarrow (01)(11)(01)(01), \\
 (10) &\rightarrow (11)(10) \rightarrow (01)(01)(11)(10). \tag{13.6}
 \end{aligned}$$

As with the nonlinear oscillator, the most important orbits—from the point of view of observable windows created as control parameters are changed—are the sim-

TABLE XII. Relative rotation rates for leading members of the primary series of well-ordered orbits. Only nodes are shown. Orbits are in the reverse (5,6) horseshoe part of the Duffing template.

	$p'$	3	4	5	6	7	8
	Local torsion	$7-2/3$	$7-2/4$	$7-2/5$	$7-2/6$	$7-2/7$	$7-2/8$
$p$	symbolics						
3	(56)(65)(66)	19/3	26/4	33/5	40/6	47/7	54/8
4	(56)(66)	26/4	26/4	33/5	40/6	47/7	54/8
	(65)(66)						
5	(56)(66)(65)(66) <sup>2</sup>	33/5	33/5	33/5	40/6	47/7	54/8
6	(56)(66) <sup>2</sup>	40/6	40/6	40/6	40/6	47/7	54/8
	(65)(66) <sup>2</sup>						
7	(56)(66) <sup>2</sup> (65)(66) <sup>3</sup>	47/7	47/7	47/7	47/7	47/7	54/8
8	(56)(66) <sup>3</sup>	54/8	54/8	54/8	54/8	54/8	54/8
	(65)(66) <sup>3</sup>						

plest well-ordered orbits. We assume, for the following points that  $(a_1 a_2 \dots a_p)$  is a well-ordered horseshoe orbit:

$p$  is odd:  $(a_1 a_2 \dots a_p)^2$  is a well-ordered orbit for the Duffing oscillator. It has even parity, so does not initiate a cascade.

$p$  is even:  $(a_1 a_2 \dots a_p)$  is a well-ordered orbit for the Duffing oscillator of period  $p/2$ . If this orbit is asymmetric, then  $(a_2 \dots a_p a_1)$  is its symmetry partner. If the parity is odd, then both orbits can initiate cascades.

We illustrate these comments for horseshoe orbits with  $p=3$  and  $p=4$ .

$p=3$ : The two well-ordered orbits are 011 and 001. The second iterates are

$$\begin{aligned} (011)^2 &= (01)(10)(11) \quad \text{saddle,} \\ (001)^2 &= (00)(10)(01) \quad \text{node.} \end{aligned} \tag{13.7}$$

Both orbits are symmetric. The node undergoes a symmetry-breaking bifurcation to a symmetric pair of asymmetric period-three orbits with symbolic dynamics  $(00)(10)(11)$  and  $(01)(01)(10)$ .

$p=4$ : The two well-ordered orbits are 0011 and 0001. The second iterate of the saddle gives two saddles of period 2:

$$\begin{aligned} (0011)^2 &\rightarrow (00)(11)(00)(11) = ((00)(11))^2, \\ &\rightarrow (01)(10)(01)(10) = ((01)(10))^2. \end{aligned} \tag{13.8}$$

The second iterate of the node gives two nodes of period 2:

$$\begin{aligned} (0001)^2 &\rightarrow (00)(01)(00)(01) = ((00)(01))^2, \\ &\rightarrow (00)(10)(00)(10) = ((00)(10))^2. \end{aligned} \tag{13.9}$$

The second iterate of a well-ordered orbit on the (0,1) direct horseshoe defined by the rational fraction  $q/p$  is a well-ordered Duffing orbit with nonzero self-relative rotation rates  $1+2q/p$ . The 1 comes from the two half rotations on passing from one well to the other and back

again; the 2 is because the same rotation happens twice. The relative rotation rates of two such well-ordered Duffing orbits are given by

$$RRR_{ij}(q/p; q'/p') = \min(1+2q/p; 1+2q'/p'). \tag{13.10}$$

These orbits are therefore concentrically organized. As a result, all the organizational properties that are true for all nonlinear oscillators described by an extended horseshoe template are also true for the Duffing oscillator.

A similar result holds for the second iterate of a reverse horseshoe. For the Duffing template built from the reverse horseshoe (1,2), the orbits defined by  $1-q/p$  generate Duffing orbits with self-relative rotation rates  $1+2(1-q/p)$ . Two such orbits have relative rotation rates given by

$$\begin{aligned} RRR_{ij}(1-q/p; 1-q'/p') \\ = \max[1+2(1-q/p); 1+2(1-q'/p')]. \end{aligned} \tag{13.11}$$

For direct horseshoes  $(2N, 2N+1)$  and reverse horseshoes  $(2N+1, 2N+2)$ , the relative rotation rates are replaced by  $1+2(N+q/p)$  and  $1+2(N+1-q/p)$ , respectively. Thus, the organization of the well-ordered orbits on the horseshoe is preserved when these orbits are iterated to become well-ordered orbits on the Duffing template.

We used this information to identify the largest windows in several successive regions of the bifurcation diagram. First, the largest windows with periodic orbits were identified. The relative rotation rates of these orbits were determined by joining two initial conditions in a Poincaré section together and then sweeping through the sequence of Poincaré sections. Within each of the large windows, the self-relative rotation rates for the stable periodic orbit were all equal. This identifies the orbit as well ordered. Furthermore, the self-relative rotation rates are sufficient to identify the symbolic name of the orbit. In one region we found a series of adjacent windows containing stable periodic orbits  $(3^2 4^{p-2})^2$ ,  $p$

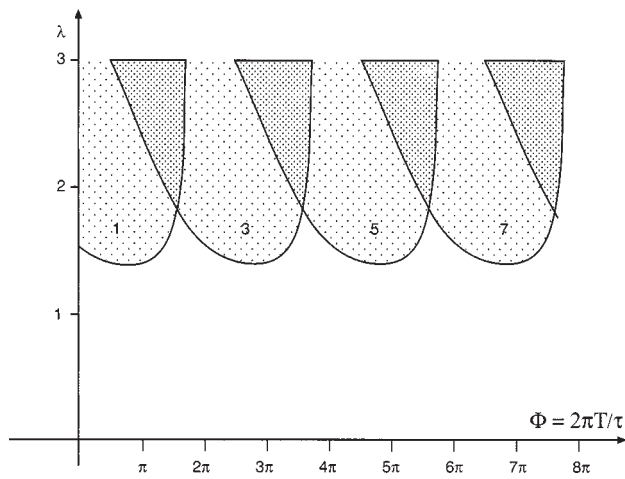


FIG. 84. Region in control-parameter space in which many bifurcations occur. The control parameters are the unstable Lyapunov exponent  $\lambda$  and the ratio of drive period to natural period. Each region can be identified by an odd integer, which is the local torsion of the node on which the bifurcation series is built.

$=3,4,\dots,8$ . These had self-relative rotation rates  $1 + 2(2 - 1/p) = 5 - 2/p$ . In the next bifurcation region we found a series of adjacent windows containing stable periodic orbits  $(5^2 6^{p-2})^2$ ,  $p=3,4,\dots,8$ . These had self-relative rotation rates  $1 + 2(3 - 1/p) = 7 - 2/p$ . Using a little care, we were able to follow these orbits outside their windows of stability so that we could compute their mutual relative rotation rates. The results for the reverse horseshoe built on the branches (5,6) are collected in Table XII.

The local torsions for the orbits  $(5^2 6^{p-2})^2$  are  $(19/3, 26/4, 33/5, 40/6, 47/7, 54/8)$  for  $p=3,4,5,6,7,8$ . This sequence of local torsions had previously been identified by Englisch and Lauterborn (1991). However, these authors did not identify the symbolic dynamics of the orbits responsible for the large windows. In addition, they did not attempt to predict the local torsions of the largest windows on the other side of the large period-three window. These are  $7 - 2p/(2p+1) = 6 + 1/(2p+1) = (19/3, 31/5, 43/7, 55/9, 67/11, 79/13)$  for  $p=3,4,5,6,7,8$ .

### E. Levels of structure

Four levels of structure have been identified in the bifurcation diagram of a typical nonlinear oscillator. These have been discussed at length above. We summarize the results here.

*Superstructure:* Bifurcation sequences are built on the period-one orbits with odd local torsion in the snake of period-one orbits (Fig. 84). These recur periodically as the period of the driving term is increased. This results in an alteration of regions in parameter space in which not many bifurcations occur and of other regions in which many bifurcations occur. These regions recur systematically, as shown in Fig. 84. The integer that identi-

fies the region is the local torsion of the period-one orbit that generates the bifurcations.

*Structure:* A series of large windows can be seen within each of the successive regions of superstructure shown in Fig. 84. The order in which the sequence of windows occurs is shown in Fig. 83. The windows first increase in width, reach a maximum associated with a period-three orbit, then decrease in width. All windows are associated with a special class of well-ordered orbits. These are the Newhouse orbits and their duals. The local torsions of these windows decrease from  $1/2$ , through values of  $p/(1+2p)$ , to  $1/3$  as  $p$  decreases from  $\infty$  to 1 and then continue to decrease from  $1/3$  to 0, through values of  $1/(q+2)$ , as  $q$  increases from 1 to  $\infty$ . The width of these windows is inversely proportional to some small power of the period of the stable orbit within the window.

*Fine structure:* Interspersed among the large windows are smaller windows associated with other well-ordered orbits which do not belong to the primary series of orbits. These well-ordered orbits are obtained by a ‘‘Farey construction’’ from the primary series of well-ordered orbits.

*Hyperfine structure:* Non-well-ordered orbits far outnumber the well-ordered orbits. Each time one of the former is created, a window appears in the bifurcation diagram. These windows are very narrow. As a result, it is very difficult to see the window of even the lowest-period non-well-ordered orbit, 00111, which has period five.

The systematic change in the local torsion as a function of increasing driving period is shown in Fig. 83. In this figure we also indicate where windows due to the primary series, and due to fine structure, appear.

## XIV. CONCLUSIONS

Three classes of tools now exist for the analysis of data generated by chaotic dynamical systems. These involve metric, dynamical, and topological invariants.

Metric methods depend on the computation of various dimensions  $D_q$  or scaling functions  $f(\alpha)$ . Dynamical methods rely on estimation of local and global Lyapunov exponents  $\lambda_j$  and dimensions  $d_L$ , as well as on entropy. These measures are invariant under coordinate transformations but not under changes in control-parameter values. They are difficult to verify independently, and no statistical theory yet exists that allows us to assign errors to these estimates. Finally, they provide no information on how to model the dynamics.

Topological methods involve determination of specific topological invariants. These include linking numbers and relative rotation rates for the unstable periodic orbits embedded in a strange attractor, as well as the topological indices describing the branched manifold that serves as a rigorous description (caricature) of the flow. These indices are essentially integer invariants, which (a) can be determined without error bars, (b) can be independently verified, (c) are independent of local coordinate transformations, (d) are independent of

changes in control parameter values, and (e) specify the stretching and squeezing mechanisms that generate the strange attractor and are responsible for the topological organization of all the unstable periodic orbits in it.

The basic tool for topological analysis was initially developed by Birman and Williams (1983a, 1983b) for three-dimensional dissipative dynamical systems. However, it also applies to “low-dimensional” dynamical systems. The strange attractors for such systems have Lyapunov exponents that obey  $\lambda_1 > \lambda_2 = 0 > \lambda_3 > \dots$ , where  $|\lambda_3| > \lambda_1$ . Strange attractors with this spectrum of Lyapunov exponents have a Lyapunov dimension,  $d_L$ , that obeys  $2 \leq d_L < 3$ . The topological-analysis method involves determining a caricature for the flow. Such a caricature is in fact the flow in the limit of infinite dissipation ( $\lambda_3 \rightarrow -\infty$ ). In this limit the strange attractor loses all thickness in the transverse direction and can be described by a two-dimensional branched manifold. The two dimensions describe the direction of flow and the direction of stretching. The singularities in the projection from the flow to the branched manifold describe the stretching and squeezing mechanisms that operate to generate chaotic behavior.

To identify a branched manifold, it is useful to first extract the unstable periodic orbits embedded in the strange attractor. In fact, there are no unstable periodic orbits in the chaotic time series used to create the strange attractor once an embedding has been chosen. Nevertheless, segments of the time series can often be found that mimic the behavior of nearby unstable periodic orbits so closely that they can be used as surrogates for the unstable periodic orbits. The organization of these unstable periodic orbits is then determined by computing the topological invariants of their surrogates: the linking and self-linking numbers and relative rotation rates. The underlying branched manifold can be identified from a subset of these surrogate orbits. A template-validation step then involves computing the topological invariants for all orbits supported by the template and comparing these invariants with those determined for the surrogate orbits extracted from the chaotic time series.

Templates describe hyperbolic strange attractors. We have yet to encounter such a structure, either in experimental data or numerical simulations. The strange attractors we have encountered are not hyperbolic and always possess fewer than the full set of unstable periodic orbits allowed by the branched manifold. Some orbits have been “pruned away.” However, the order in which pruning can occur is not arbitrary. There are topologically based rules determining to some degree the order in which orbit creation or annihilation by direct or inverse saddle-node or period-doubling bifurcations can occur. These are the forcing rules discussed in detail in Sec. VI. These rules provide a means for “unfolding” a template and enumerating the possible routes to chaos in a dynamical system. Figure 38 is an unfolding of the horseshoe template up to period eight. This figure has been used to determine the actual “operating state” of a dynamical system behaving chaotically due to the cre-

ation of a Smale horseshoe. This figure can also be used to distinguish all the different routes to chaos in dynamical systems governed by the formation of a Smale horseshoe, up to period eight.

The topological-analysis procedure provides a doubly discrete way to classify strange attractors. First, the underlying branched manifold or template that describes hyperbolic strange attractors is discretely classified by a set of integers, which can be extracted from chaotic data. At a second, more refined, level, the unfolding of the template that describes the nonhyperbolic strange attractors actually observed is determined by a basis set of orbits. This basis set is the second component of this doubly discrete classification of strange attractors. As control parameters are varied, the underlying template generally does not change (except when new branches are visited or old ones abandoned). Instead, it is the unfolding, or discrete basis set, that changes with control parameters.

Dynamical systems can be modeled in a number of different ways. These have been described in the extensive reviews by Abarbanel *et al.* (1993) and Abarbanel (1996). We have added only two new tools to their toolkit. One of these involves constructing a model as an eigenvector of a very specific real symmetric positive-semidefinite matrix. The other approach involves “thinking the unthinkable.” That is, we forego completely a global analytic model and numerically define the flow through various parts of phase space. In many instances the latter approach provides a far more detailed understanding of the dynamics than a global analytic model does.

Once again there is a validation step. The “goodness of fit” of a model generated from data can be assessed by the “symmetry restoration test.” That is, if the model provides a good representation of the dynamical system that generated the data, then the data will entrain the model output when a small linear perturbation is added to the model. It would be very nice to develop this entrainment test into a quantitative tool, so that it could be used in the same way that standard statistical tests (e.g.,  $\chi^2$  test) are used for deciding the outcome of hypothesis tests for general linear models.

The topological-analysis procedure has been applied to a number of experimental data sets. Some of these applications have been described in this review. Presently, these procedures can be carried out successfully, are informative, and describe how to model the flow.

What needs to be done in the future? The topological-analysis procedure described here is applicable only to low-dimensional dynamical systems. It is necessary to extend this procedure to higher-dimensional ( $d_L > 3$ ) dynamical systems. To do this, the following problems must be overcome:

*Embedding:* The differential phase-space embedding that we found so useful will not be useful in higher dimensions because of the signal-to-noise problem. The delay embedding does not suffer from this problem. However, it is a nonlocal coordinate transformation, and

one must be wary of dependence of “topological invariants” on the parameters of the embedding.

*Close returns:* The larger the value of  $n$  (“dimension”), the more difficult it is to locate unstable periodic orbits in a chaotic time series by the method of close returns. This is because, in a Poincaré section, a return can miss closing up in  $n-1$  directions. For three-dimensional dynamical systems ( $n=3$ ), we have been able to locate numerous unstable periodic orbits. We have been aided in large part by the fact that, effectively,  $n=d_L=2+\epsilon$  for the strange attractors we have analyzed. For systems with  $d_L>3$  it will become more and more difficult to locate surrogates for unstable periodic orbits.

*Topological organization:* We face the additional problem that unstable periodic orbits “fall apart” when embedded in spaces with  $n>3$ . Therefore we cannot compute their topological organization by the methods described above.

*Branched manifolds:* What is the generalization of 2-dimensional branched manifolds to higher dimensions? What do the caricatures of  $d_L>3$  flows look like? How can these higher-dimensional analogs of branched manifolds stretch, squeeze, and entangle each other?

Such questions must be addressed before it is possible to move to the next stage in the application of topological methods for the analysis of nonlinear dynamical systems.

## ACKNOWLEDGMENTS

The author wishes to thank the many friends and colleagues whose efforts, computations, discussions, and corrections have contributed to the present work. I specifically wish to thank my colleagues H. G. Solari, G. B. Mindlin, J. R. Tredicce, N. B. Tuffillaro, and M. A. Natiello for making significant contributions during the course of this work. I thank E. J. Kostelich and D. P. Lathrop for furnishing a Belousov-Zhabotinskii data set on which the analysis described in Sec. XI was carried out, and for their encouragement of our efforts. I have also benefited from very useful discussions with H. D. I. Abarbanel, N. B. Abraham, A. M. Albano, K. T. Alligood, F. T. Arecchi, E. Arimondo, D. Auerbach, S. Bielawski, J. S. Birman, P. D. Boyd, R. Brown, T. L. Carroll, P. Carter, D. Derozier, E. Eschenazi, P. Glorieux, C. Grebogi, T. Hall, J. F. Heagy, P. Holmes, X.-J. Hou, M. Lefranc, R. Lopez-Ruiz, J. W. L. McCallum, E. Ott, F. Papoff, U. Parlitz, L. M. Pecora, J. Plumecoq, T. Sauer, I. Schwartz, J. J. Sidorowich, H. B. Stewart, J. M. T. Thompson, L. S. Tsimring, R. A. Vilaseca, R. F. Williams, and J. A. Yorke.

## REFERENCES

Abarbanel, H. D. I., 1996, *Analysis of Observed Chaotic Data* (Springer, New York).  
 Abarbanel, H. D. I., R. Brown, J. J. Sidorowich, and L. S. Tsimring, 1993, *Rev. Mod. Phys.* **65**, 1331.

Abraham, N. B., D. Dangoise, P. Glorieux, and P. Mandel, 1985, *J. Opt. Soc. Am. B* **2**, 23.  
 Abraham, N. B., P. Mandel, and L. M. Narducci, 1988, in *Progress in Optics XXV*, edited by E. Wolf (North-Holland, Amsterdam), p. 1.  
 Abraham, R. H., and C. D. Shaw, 1984, *Dynamics, The Geometry of Behavior, Part III* (Ariel Press, Santa Cruz, CA).  
 Adams, C. C., 1994, *The Knot Book* (Freeman, New York).  
 Alligood, K. T., 1985, *Trans. Am. Math. Soc.* **292**, 713.  
 Alligood, K. T., T. D. Sauer, and J. A. Yorke, 1997, *Chaos: An Introduction to Dynamical Systems* (New York, Springer).  
 Alsedá, L., J. Llibre, and M. Misiurewicz, 1993, *Combinatorial Dynamics and Entropy in Dimension One* (World Scientific, Singapore).  
 Alvarez, R., 1996, Ph.D. thesis (Drexel University).  
 Arecchi, F. T., and R. G. Harrison, 1993, *Selected Papers on Optical Chaos* (SPIE Milestone Series, Vol. MS 75).  
 Arecchi, F. T., R. Meucci, G. P. Puccioni, and J. R. Tredicce, 1982, *Phys. Rev. Lett.* **49**, 1217.  
 Argoul, F., A. Arneodo, P. Richetti, J. C. Roux, and H. L. Swinney, 1987, *Acc. Chem. Res.* **86**, 119.  
 Arnol'd, V. I., 1968, *Russian Math. Surveys* **23**, 1.  
 Arnol'd, V. I., 1973, *Ordinary Differential Equations* (MIT, Cambridge, MA).  
 Arnol'd, V. I., 1975, *Russian Math. Surveys* **30**, 1.  
 Arnol'd, V. I., 1986, *Catastrophe Theory*, second edition (Springer, New York).  
 Atiyah, M., 1990, *The Geometry and Physics of Knots* (Cambridge University, Cambridge, England).  
 Auerbach, D., P. Cvitanovic, J.-P. Eckmann, G. Gunaratne, and I. Procaccia, 1987, *Phys. Rev. Lett.* **58**, 2387.  
 Beiersdorfer, P., J. M. Wersinger, and Y. Treve, 1983, *Phys. Lett. A* **96**, 269.  
 Bestvina, M., and M. Handel, 1992, *Ann. Math.* **135**, 1.  
 Birman, J. S., 1975, *Braids, Links, and Mapping Class Groups* (Princeton University, Princeton, NJ).  
 Birman, J. S., and R. F. Williams, 1983a, *Topology* **22**, 47.  
 Birman, J. S., and R. F. Williams, 1983b, *Contemp. Math.* **20**, 1.  
 Biswas, D. J., R. G. Harrison, C. O. Weiss, W. Klische, D. Dangoise, P. Glorieux, and N. M. Lawandy, 1986, in *Instabilities and Chaos in Quantum Optics*, edited by F. T. Arecchi and R. G. Harrison (Springer, Berlin), p. 109.  
 Block, L., and W. A. Coppel, 1992, *Dynamics in One Dimension*, Lecture Notes in Mathematics No. 1513 (Springer, New York).  
 Block, L., J. Guckenheimer, M. Misiurewicz, and L.-S. Yang, 1980, *Global Theory of Dynamical Systems*, edited by Z. Nitecki and C. Robinson, Lecture Notes in Mathematics No. 819 (Springer, New York), p. 18.  
 Bocko, M. F., D. H. Douglas, and H. H. Fruchty, 1984, *Phys. Lett. A* **104**, 388.  
 Boulant, G., S. Bielawski, D. Derozier, and M. Lefranc, 1997a, *Phys. Rev. E* **55**, R3801.  
 Boulant, G., M. Lefranc, S. Bielawski, and D. Derozier, 1997b, *Phys. Rev. E* **55**, 5208.  
 Boulant, G., M. Lefranc, S. Bielawski, and D. Derozier, 1997c, *Int. J. Bifurcation Chaos Appl. Sci. Eng.* (in press).  
 Broomhead, D. S., and G. P. King, 1986, *Physica D* **20**, 217.  
 Brown, R., N. Rulkov, and E. R. Tracy, 1994, *Phys. Rev. E* **49**, 3784.  
 Chauve, M. P., and P. LeGal, 1992, *Physica D* **58**, 407.  
 Coffman, K., W. D. McCormick, Z. Nosziczius, R. H. Simoyi, and H. L. Swinney, 1987, *J. Chem. Phys.* **86**, 119.

- Collet, P., and J.-P. Eckmann, 1980, *Iterated Maps on the Interval as Dynamical Systems* (Birkhäuser, Boston).
- Creveling, H. F., J. F. De Paz, J. Y. Baladi, and R. J. Schoenhals, 1975, *J. Fluid Mech.* **67**, 65.
- Cvitanovic, P., 1984, *Universality in Chaos* (Adam Hilger, Ltd., Bristol).
- Cvitanovic, P., G. H. Gunaratne, and I. Procaccia, 1988, *Phys. Rev. A* **38**, 1503.
- Dangoisse, D., A. Bekkale, F. Papoff, and P. Glorieux, 1988, *Europhys. Lett.* **6**, 335.
- DeMelo, W., and S. Van Strien, 1993, *One Dimensional Dynamics* (Springer, New York).
- Devaney, R., and Z. Nitecki, 1979, *Commun. Math. Phys.* **67**, 137.
- Draper, N. R., and H. Smith, 1966, *Applied Regression Analysis* (Wiley, New York).
- Duffing, G., 1918, *Erzwungene Schwingungen bei Veränderlicher Eigenfrequenz* (Vieweg, Braunschweig).
- Dupertuis, M. A., R. R. E. Salomaa, and M. R. Siegrist, 1986, *Opt. Commun.* **57**, 410.
- Eckmann, J.-P., and D. Ruelle, 1985, *Rev. Mod. Phys.* **57**, 617.
- Eckmann, J.-P., and D. Ruelle, 1987, *Europhys. Lett.* **4**, 973.
- Efron, B., 1979, *SIAM (Soc. Ind. Appl. Math.) Rev.* **21**, 460.
- Englisch, V., and W. Lauterborn, 1991, *Phys. Rev. A* **44**, 916.
- Eschenazi, E., H. G. Solari, and R. Gilmore, 1989, *Phys. Rev. A* **39**, 2609.
- Feigenbaum, M. J., 1978, *J. Stat. Phys.* **19**, 25.
- Feigenbaum, M. J., 1980, *Los Alamos Sci.* **1**, 4.
- Franks, J., and R. F. Williams, 1985, *Trans. Am. Math. Soc.* **20**, 241.
- Fujisaka, H., and T. Yamada, 1983, *Prog. Theor. Phys.* **69**, 32.
- Gaito, S. T., and G. P. King, 1990, in *Measures of Complexity and Chaos*, edited by N. B. Abraham, A. M. Albano, A. P. Passamante, and P. E. Rapp, Vol. 208 of NATO ARW Series B (Plenum, New York), p. 235.
- Ghrist, R. W., P. J. Holmes, and M. C. Sullivan, 1996, *Knots and Links in Three-Dimensional Flows* (unpublished).
- Gilmore, C., 1993a, *Int. J. Bifurcation Chaos Appl. Sci. Eng.* **3**, 583.
- Gilmore, C., 1993b, *J. Econ. Behav. Organ.* **22**, 209.
- Gilmore, R., 1974, *Lie Groups, Lie Algebras, and Some of Their Applications* (Wiley, New York).
- Gilmore, R., 1981, *Catastrophe Theory for Scientists and Engineers* (Wiley, New York).
- Gilmore, R., 1996, A program for dynamical systems theory, Drexel University, preprint (unpublished).
- Gilmore, R., and J. W. L. McCallum, 1995, *Phys. Rev. E* **51**, 935.
- Gilmore, R., R. Vilaseca, R. Corbálan, and E. Roldán, 1997, *Phys. Rev. E* **55**, 2479.
- Gioggia, R. S., and N. B. Abraham, 1983, *Phys. Rev. Lett.* **51**, 650.
- Golubitsky, M., and V. Guillemin, 1973, *Stable Mappings and Their Singularities* (Springer, New York).
- Gorman, M., P. J. Widmann, and K. A. Robins, 1984, *Phys. Rev. Lett.* **52**, 2241.
- Gorman, M., P. J. Widmann, and K. A. Robins, 1986, *Physica D* **19**, 255.
- Grassberger, P., and I. Procaccia, 1983, *Phys. Rev. A* **28**, 2591.
- Grebogi, C., E. Ott, and J. A. Yorke, 1983, *Physica D* **7**, 181.
- Guckenheimer, J., and P. J. Holmes, 1983, *Nonlinear Oscillations, Dynamical Systems, and Bifurcations of Vector Fields* (Springer, New York).
- Gunaratne, G. H., P. S. Linsay, and M. J. Vinson, 1989, *Phys. Rev. Lett.* **63**, 1.
- Haken, H., 1975, *Phys. Lett. A* **53**, 77.
- Hall, T., 1991, Ph.D. Thesis (Cambridge University).
- Hall, T., 1993, *Phys. Rev. Lett.* **71**, 58.
- Hall, T., 1994a, *Nonlinearity* **7**, 367.
- Hall, T., 1994b, *Nonlinearity* **7**, 861.
- Halsey, T. C., M. H. Jensen, L. P. Kadanoff, I. Procaccia, and B. I. Shraiman, 1986, *Phys. Rev. A* **33**, 1141.
- Hammel, S., 1990, *Phys. Lett. A* **148**, 421.
- Hao, B.-L., 1984, *Chaos* (World Scientific, Singapore).
- Harrison, R. G., I. A. Al-Saidi, and D. J. Biswas, 1985, *IEEE J. Quantum Electron.* **21**, 1491.
- Harrison, R. G., and D. J. Biswas, 1985, *Phys. Rev. Lett.* **55**, 63.
- Hayashi, C., 1964, *Nonlinear Oscillations in Physical Systems* (McGraw Hill, New York).
- Hayashi, C., 1975, *Selected Papers on Nonlinear Oscillations* (Nippon Printing and Publishing, Osaka).
- Hennequin, D., F. de Tomais, B. Zambon, and E. Arimondo, 1988, *Phys. Rev. A* **37**, 2243.
- Holmes, P. J., 1986, *Physica D* **21**, 7.
- Holmes, P. J., 1988, in *New Directions in Dynamical Systems*, edited by T. Bedford and J. Swift (Cambridge University, Cambridge, England), p. 150.
- Holmes, P. J., and R. F. Williams, 1985, *Arch. Ration. Mech. Anal.* **90**, 115.
- Hong, F. L., M. Tachikawa, T. Oda, and T. Shimizu, 1989, *J. Opt. Soc. Am. B* **6**, 1378.
- Jackson, E. A., 1990, *Perspectives in Nonlinear Dynamics* (Cambridge University, Cambridge, England).
- Kaplan, J. L., and J. A. Yorke, 1979, in *Functional Difference Equations and the Approximation of Fixed Points*, edited by H. O. Pietgen and H. O. Walther, Springer Lecture Notes in Mathematics No. 730 (Springer, Berlin), p. 204.
- Kaufmann, L. H., 1987, *On Knots* (Princeton University, Princeton, NJ).
- Khanin, Ya. I., 1995, *Principles of Laser Dynamics* (North-Holland, Amsterdam).
- King, G. P., and S. T. Gaito, 1992, *Phys. Rev. A* **46**, 3092.
- Klinker, T., T. W. Meyer-Ilse, and W. Lauterborn, 1984, *Phys. Lett. A* **101**, 371.
- Knop, W., and W. Lauterborn, 1990, *J. Chem. Phys.* **93**, 3950.
- Kocarev, L., Z. Tasev, and D. Dimovski, 1994, *Phys. Lett. A* **190**, 399.
- Kurz, T., and W. Lauterborn, 1987, *Phys. Rev. A* **37**, 1029.
- Lathrop, D. P., and E. J. Kostelich, 1989, *Phys. Rev. A* **40**, 4028.
- Lauterborn, W., and R. Steinhoff, 1988, *J. Opt. Soc. Am. B* **5**, 1097.
- Lawandy, N. M., and G. A. Koepf, 1980, *IEEE J. Quantum Electron.* **16**, 701.
- Lefebvre, M., D. Dangoisse, and P. Glorieux, 1984, *Phys. Rev. A* **29**, 758.
- Lefranc, M., and P. Glorieux, 1993, *Int. J. Bifurcation Chaos Appl. Sci. Eng.* **3**, 643.
- Lefranc, M., D. Hennequin, and D. Dangoisse, 1991, *J. Opt. Soc. Am. B* **8**, 239.
- Letellier, C., and G. Gouesbet, 1995, *Phys. Rev. E* **52**, 4754.
- Lorenz, E. N., 1956, *Statistical Forecasting Program* (Department of Meteorology, MIT, Cambridge, MA), Technical Report No. 1.
- Lorenz, E. N., 1963, *J. Atmos. Sci.* **20**, 130.
- Lorenz, E. N., 1980, *Ann. (N.Y.) Acad. Sci.* **357**, 282.

- Los, J., 1993, *Proc. London Math. Soc.* (3) **66**, 1.
- Mancho, A. M., A. A. Duarte, and G. B. Mindlin, 1996, *Phys. Lett. A* **221**, 181.
- Mañé, R., 1981, in *Dynamical Systems and Turbulence, Warwick, 1980*, edited by D. Rand and L.-S. Young, Lecture Notes in Mathematics No. 898 (Springer, Berlin), p. 230.
- Matorin, I. I., A. S. Pikovskii, and Ya. I. Khanin, 1984, *Sov. J. Quantum Electron.* **14**, 1401.
- Melvin, P., and N. B. Tuffillaro, 1991, *Phys. Rev. A* **44**, 3419.
- Metropolis, M., M. L. Stein, and P. R. Stein, 1973, *J. Comb. Theory, Ser. A* **15**, 25.
- Mickens, R. E., 1981, *Nonlinear Oscillations* (Cambridge University, Cambridge, England).
- Midavaine, T., D. Dangoisse, and P. Glorieux, 1986, *Phys. Rev. Lett.* **55**, 1989.
- Milnor, J., and W. Thurston, 1987, in *Dynamical Systems*, edited by J. C. Alexander, Lecture Notes in Mathematics No. 1342 (Springer, New York), p. 465.
- Mindlin, G. B., and R. Gilmore, 1992, *Physica D* **58**, 229.
- Mindlin, G. B., X.-J. Hou, H. G. Solari, R. Gilmore, and N. B. Tuffillaro, 1990, *Phys. Rev. Lett.* **64**, 2350.
- Mindlin, G. B., R. Lopez-Ruiz, H. G. Solari, and R. Gilmore, 1993, *Phys. Rev. E* **48**, 4297.
- Mindlin, G. B., and H. G. Solari, 1995, *Phys. Rev. E* **54**, 1497.
- Mindlin, G. B., H. G. Solari, M. A. Natiello, R. Gilmore, and X.-J. Hou, 1991, *J. Nonlinear Sci.* **1**, 147.
- Minorsky, N., 1962, *Nonlinear Oscillations* (Van Nostrand, Princeton, NJ).
- Narducci, L. M., and N. B. Abraham, 1988, *Laser Physics and Laser Instabilities* (World Scientific, Singapore).
- Nayfeh, A. H., 1973, *Perturbation Methods* (Wiley, New York).
- Newhouse, S. E., 1974, *Topology* **13**, 9.
- Oppenheim, A. V., and R. W. Schaffer, 1989, *Discrete-Time Signal Processing* (Prentice-Hall, Englewood Cliffs, NJ).
- Oseledec, V. I., 1968, *Trans. Mosc. Math. Soc.* **19**, 197.
- Ott, E., 1993, *Chaos in Dynamical Systems* (Cambridge University, Cambridge, England).
- Packard, N. H., J. P. Crutchfield, J. D. Farmer, and R. S. Shaw, 1980, *Phys. Rev. Lett.* **45**, 712.
- Papoff, F., A. Fioretti, E. Arimondo, G. B. Mindlin, H. G. Solari, and R. Gilmore, 1992, *Phys. Rev. Lett.* **68**, 1128.
- Parlitz, U., V. Englisch, C. Scheffczyk, and W. Lauterborn, 1990, *J. Acoust. Soc. Am.* **88**, 1061.
- Parlitz, U., and W. Lauterborn, 1985, *Phys. Lett.* **107A**, 351.
- Pecora, L. M., and T. L. Carroll, 1990, *Phys. Rev. Lett.* **64**, 821.
- Poincaré, H., 1892, *Les Methodes Nouvelle de la Mécanique Céleste* (Gauthier Villars, Paris).
- Poston, T., and I. N. Stewart, 1978, *Catastrophe Theory and Its Applications* (Pitman, London).
- Press, W. H., B. P. Flannery, S. A. Teukolsky, and W. T. Vetterling, 1986, *Numerical Recipes* (Cambridge University, Cambridge, England).
- Puccioni, G. P., A. Poggi, W. Gadoski, J. R. Tredicce, and F. T. Arecchi, 1985, *Phys. Rev. Lett.* **55**, 339.
- Richetti, P., P. De Keeper, J. C. Roux, and H. L. Swinney, 1987, *J. Stat. Phys.* **48**, 977.
- Roldán, E., G. J. de Valcárcel, R. Vilaseca, R. Corbálan, V. J. Martínez, and R. Gilmore, 1997, *Quantum Semiclassic. Opt.* **9**, R1.
- Rolfsen, D., 1976, *Knots and Links* (Publish or Perish, Berkeley, CA).
- Roux, J.-C., R. H. Simoyi, and H. L. Swinney, 1983, *Physica D* **8**, 257.
- Rössler, O. E., 1976a, *Phys. Lett. A* **57**, 397.
- Rössler, O. E., 1976b, *Z. Naturforsch. A* **31a**, 1664.
- Satija, I. I., A. R. Bishop, and K. Fesser, 1985, *Phys. Lett. A* **112**, 183.
- Sauer, T., 1992, *Physica A* **58**, 193.
- Sauer, T., J. A. Yorke, and M. Casdagli, 1991, *J. Stat. Phys.* **65**, 579.
- Scheffczyk, C., U. Parlitz, T. Kurz, W. Knop, and W. Lauterborn, 1991, *Phys. Rev. A* **43**, 6495.
- Schwartz, I. B., and H. L. Smith, 1983, *J. Math. Biol.* **18**, 233.
- Scott, S. K., 1991, *Chemical Chaos* (Oxford University, London).
- Shaw, R., 1981, *Z. Naturforsch. A* **36a**, 80.
- Shil'nikov, A. L., 1993, *Physica D* **62**, 338.
- Shimizu, T., and N. Morioka, 1980, *Phys. Lett. A* **76**, 201.
- Shinriki, M., M. Yamamoto, and S. Mori, 1981, *Proc. IEEE* **69**, 394.
- Šilnikov, L. P., 1965, *Sov. Math. Dokl.* **66**, 163.
- Singer, J., Y.-Z. Wang, and H. Bau, 1991, *Phys. Rev. Lett.* **66**, 1123.
- Smale, S., 1967, *Bull. Am. Math. Soc.* **73**, 747.
- Solari, H. G., E. Eschenazi, R. Gilmore, and J. R. Tredicce, 1987, *Opt. Commun.* **64**, 49.
- Solari, H. G., and R. Gilmore, 1988, *Phys. Rev. A* **37**, 3096.
- Solari, H. G., M. A. Natiello, and G. B. Mindlin, 1996, *Nonlinear Physics and Its Mathematical Tools* (IOP Publishing Ltd., Bristol).
- Solari, H. G., M. A. Natiello, and M. Vazquez, 1996, *Phys. Rev. E* **54**, 3185.
- Sparrow, C., 1982, *The Lorenz Equations* (Springer, New York).
- Takens, F., 1981, in *Dynamical Systems and Turbulence, Warwick, 1980*, edited by D. Rand and L.-S. Young, Lecture Notes in Mathematics No. 898 (Springer, Berlin), p. 366.
- Thom, R., 1975, *Structural Stability and Morphogenesis* (Benjamin-Addison Wesley, New York).
- Thompson, J. M. T., and H. B. Stewart, 1986, *Nonlinear Dynamics and Chaos* (Wiley, New York).
- Tredicce, J. R., N. B. Abraham, G. P. Puccioni, and F. T. Arecchi, 1985, *Opt. Commun.* **55**, 131.
- Tredicce, J. R., F. T. Arecchi, G. L. Lippi, and G. P. Puccioni, 1985, *J. Opt. Soc. Am. B* **2**, 173.
- Tredicce, J. R., F. T. Arecchi, G. P. Puccioni, A. Poggi, and W. Gadoski, 1986, *Phys. Rev. A* **34**, 2073.
- Tuffillaro, N. B., 1994, *Phys. Rev. E* **50**, 4509.
- Tuffillaro, N. B., T. Abbott, and J. Reilly, 1992, *An Experimental Approach to Nonlinear Dynamics and Chaos* (Addison-Wesley, Reading, MA).
- Tuffillaro, N. B., R. Holzner, L. Flepp, E. Brun, M. Finardi, and R. Badii, 1991, *Phys. Rev. A* **44**, 4786.
- Tuffillaro, N. B., H. G. Solari, and R. Gilmore, 1990, *Phys. Rev. A* **41**, 5717.
- Tuffillaro, N. B., P. Wyckkoff, R. Brown, T. Schreiber, and T. Molteno, 1995, *Phys. Rev. E* **51**, 164.
- Uezu, T., 1983, *Phys. Lett. A* **93**, 161.
- Uezu, T., and Y. Aizawa, 1982, *Prog. Theor. Phys.* **68**, 1907.
- van Buskirk, R., and C. Jeffries, 1985, *Phys. Rev. A* **31**, 3332.
- van der Pol, B., 1927, *Philos. Mag.* (7) **3**, 65.
- Waldner, F., R. Badii, D. R. Barberis, G. Broggi, W. Floeder, P. F. Meier, R. Stoop, M. Warden, and H. Yamazaki, 1986, *J. Magn. Magn. Mater.* **54–57**, 1135.

- Wedding, B., A. Gasch, and D. Jaeger, 1984, *Phys. Lett. A* **105**, 105.
- Weiss, C. O., 1985, *J. Opt. Soc. Am. B* **2**, 137.
- Weiss, C. O., and J. Brock, 1986, *Phys. Rev. Lett.* **50**, 413.
- Weiss, C. O., and W. Klisch, 1984, *Opt. Commun.* **57**, 2804.
- Weiss, C. O., and R. Vilaseca, 1991, *Dynamics of Lasers* (VCH, New York).
- Whitney, H., 1936, *Ann. Math.* **37**, 645.
- Wolf, A., J. B. Swift, H. L. Swinney, and J. A. Vastano, 1985, *Physica D* **16**, 285.
- Zambon, B., 1991, *Phys. Rev. A* **44**, R688.
- Zeeman, E. C., 1977, *Catastrophe Theory: Selected Papers 1972–1977* (Addison-Wesley, Reading, MA).